Summer 2014

Investigation of the influence of gravitational body force effects on critical heat flux for flow boiling with subcooled and two-phase inlet

Christopher Alan Konishi
Purdue University

Graduate School ETD Form 9
(Revised 01/14)

PURDUE UNIVERSITY
GRADUATE SCHOOL
Thesis/Dissertation Acceptance

This is to certify that the thesis/dissertation prepared

By Christopher Alan Konishi

Entitled

INVESTIGATION OF THE INFLUENCE OF GRAVITATIONAL BODY FORCE EFFECTS ON CRITICAL HEAT FLUX FOR FLOW BOILING WITH SUBCOOLED AND TWO-PHASE INLET

For the degree of Doctor of Philosophy

Is approved by the final examining committee:

Issam Mudawar

Jong Hyun Choi

Xiulin Ruan

Steven Collicott

To the best of my knowledge and as understood by the student in the *Thesis/Dissertation Agreement. Publication Delay, and Certification/Disclaimer (Graduate School Form 32)*, this thesis/dissertation adheres to the provisions of Purdue University's "Policy on Integrity in Research" and the use of copyrighted material.

Issam Mudawar

Approved by Major Professor(s): _____

_____

Approved by: David C. Anderson 08/12/2014

Head of the Department Graduate Program Date

INVESTIGATION OF THE INFLUENCE OF GRAVITATIONAL BODY FORCE EFFECTS ON CRITICAL HEAT FLUX FOR FLOW BOILING WITH SUBCOOLED AND TWO-PHASE INLET

A Dissertation

Submitted to the Faculty

of

Purdue University

by

Christopher Alan Konishi

In Partial Fulfillment of the

Requirements for the Degree

of

Doctor of Philosophy

December 2014

Purdue University

West Lafayette, Indiana

This dissertation is dedicated to the memory of my grandfather Alfred "Papa" Ferreira. My commitment to pursue a graduate education was solely driven by honoring a final promise made during our last conversation together. His guidance, encouragement and love for his family have continuously strengthened my will throughout my life to become a better person as he always portrayed. My grandfather spent his life helping others by "building things with his hands," I will continue on his legacy "building things with my mind."

ACKNOWLEDGEMENTS

I would like to acknowledge the following people who have helped me through my journey towards a higher education. First and foremost, I would like to thank my advisor, Dr. Issam Mudawar for his invaluable guidance and support. His dedication and enthusiasm towards conducting research and teaching truly inspired me to have a profound appreciation to discover and invent new ideas for engineering applications to better the world. I'm truly grateful for the support and involvement of my advisory committee members Dr. Jong Hyun Choi, Dr. Xiulin Ruan and Dr. Steven Collicott.

I would also like to express my sincere gratitude to my past advisor Dr. Weilin Qu for his inspiration and guidance. He initiated my interest in research of two-phase heat transfer and motivated me to pursue my Ph.D in mechanical engineering.

I also extend my sincere thanks to the following members at the NASA Glenn Research Center: Dr. Mohammad Hasan, Dr. Henry Nahra, Nancy Hall, Jeffrey Mackey and James Wagner. It was truly a privilege to work with such talented individuals and granted access to incredibly exciting projects driven to developing new space technologies.

I would also like to thank my fellow graduate students at the Boiling and Two-Phase Flow Laboratory: Hyoungsoon, Nikhin, Chirag, Sung-Min, Seunghyun, and Ilchung. Their support on and off campus has no doubt made the journey both rewarding and fun. Finally, I would like to express my thanks and gratitude to my parents and the rest of my family for their unwavering love and encouragement, which has continuously motivated me to never give up during my academics and life.

TABLE OF CONTENTS

Page

Page

Page

Page

LIST OF TABLES

LIST OF FIGURES

Figure Page

Figure Page

Figure Page

Figure Page

Figure Page

Figure Page

NOMENCLATURE

Symbols

A	cross-sectional area of flow channel
A_h	heated area of flow channel
A_w	area of wetting front
b	ratio of wetting front length to wavelength
Bo	Bond number
c	wave speed
c_p	specific heat at constant pressure
$C_{f,i}$	interfacial friction coefficient
C_o	distribution parameter in Drift Flux model
D	diameter
D_h	hydraulic diameter
f	friction factor
Fr	Froude number
g	gravity
g_e	Earth gravity
g_n	component of gravity normal to heated wall
$g_{//}$	component of gravity opposite to direction of fluid flow
g_z	vertical acceleration
G	mass velocity
h	heat transfer coefficient
h_{fg}	latent heat of vaporization
H	height of flow channel; layer thickness
H_f	mean thickness of liquid layer

Symbols

H_g	mean thickness of vapor layer
$H1$	heated wall 1
$H2$	heated wall 2
j	superficial velocity
k	wave number
L	heated length
L_d	development length of channel
L_e	exit length of channel
L_h	heated length of channel
$\dot{m}$	mass flow rate
$\dot{m}'_{fg}$	liquid evaporation rate between heated wall liquid and vapor layers
MAE	mean absolute error
p	pressure
P_e	electric power input to second preheater
P_i	interfacial perimeter
P_w	perimeter in contact with channel walls
q''	wall heat flux
q''_m	critical heat flux (CHF)
q''_w	wetting front lift-off heat flux
Q	volumetric flow rate
Re	Reynolds number
t	time
T	temperature
u_i	interfacial velocity
U	mean axial velocity
U_f	mean velocity of liquid layer
U_g	mean velocity of vapor layer
U_∞	rise velocity of slug bubble
W	width of flow channel

Symbols

We	Weber number
x_e	thermodynamic equilibrium quality
x_f	liquid mass flow fraction
y	coordinate normal to heated wall
z	axial distance
z_0	axial location where vapor layer velocity just exceeds liquid layer velocity
z^*	axial location for determining vapor thickness and critical wavelength in Interfacial Lift-off Model

Greek Symbols

α	vapor (area-based) void fraction
δ	vapor layer thickness
δ_h	thickness of heated wall
ε_f	liquid area fraction
η	interfacial perturbation
η_o	amplitude of interfacial perturbation
θ	flow orientation angle
λ	wavelength
μ	dynamic viscosity
n	kinematic viscosity
Π	dimensionless group
ρ	density
ρ''	modified density
σ	surface tension
t	shear stress
τ_i	interfacial shear stress
τ_w	wall shear stress

Subscripts

1	insulated wall liquid layer

Subscripts

2	middle vapor core
3	heated wall liquid layer
4	heated wall wavy-vapor layer
asy	asymptotic wall thickness
avg	average
b	bulk liquid
c	critical
d	developing
e	exit
exp	experimental (measured)
f	saturated liquid; bulk liquid
g	saturated vapor
h	heated wall
i	interface
in	inlet to heated portion of flow channel
k	phase k, $k = g$ or f
m	maximum (CHF)
min	minimum
max	maximum
n	normal to heated wall
o	outlet
sat	saturation
sub	subcooling
pred	predicted
preh	upstream of second preheater
w	wall; wetting front

ABSTRACT

Konishi, Christopher Alan. Ph.D., Purdue University, December 2014. Investigation of the Influence of Gravitational Body Force Effects on Critical Heat Flux for Flow Boiling with Subcooled and Two-Phase Inlet. Major Professor: Dr. Issam Mudawar, School of Mechanical Engineering.

Space agencies worldwide are being confronted with the challenges of more distant manned space missions, which will demand greater energy efficiency and reduced weight and volume. One method being considered to reduce the weight and volume is to replace present single-phase Thermal Control Systems (TCSs) with ones that rely on flow boiling and condensation. This transition will require a thorough understanding of the influence of reduced gravity on flow boiling and condensation, and the development of predictive tools for both. The primary purpose of the present study is to investigate the impact gravitational body force effects have on flow boiling heat transfer performance and critical heat flux (CHF). Two flow boiling investigations will be presented, where experimentation was conducted both on-ground and in microgravity conditions.

The terrestrial-based study explores the mechanism of flow boiling CHF for FC-72 in a rectangular channel fitted along one side with a heated wall. The flow is supplied as a two-phase mixture and the channel is tested at different orientations relative to Earth's gravity. High-speed video imaging is used to identify the complex flow boiling CHF trigger mechanism for different orientations, mass velocities and inlet qualities. It is shown that orientation has a significant influence on CHF for low mass velocities and small inlet qualities, with the orientations surrounding horizontal flow with downward-facing heated wall causing stratification of the vapor towards the heated wall and yielding very small CHF values. High mass velocities cause appreciable diminution in the

influence of orientation on CHF, which is evidenced by similar flow patterns and CHF trigger mechanism regardless of orientation. The Interfacial Lift-off Model is shown to predict the influence of orientation on CHF with good accuracy. Overall, this study points to the effectiveness of high mass velocities at combating buoyancy effects and helping produce CHF values insensitive to orientation.

It is also shown that the influence of orientation can be negated by simultaneously satisfying three separate criteria: overcoming the influence of gravity perpendicular to the heated wall, overcoming the influence of gravity parallel to the heated wall, and ensuring that the heated wall is sufficiently long to endure liquid contact. These criteria are combined to determine the minimum mass velocity required to negate gravity effects in both terrestrial and space applications. Exceeding this minimum is of paramount importance to space systems since it enables the implementation of the vast body of published CHF data, correlations and models developed from terrestrial studies for design of thermal management systems for space applications.

Determining flow boiling CHF using mechanistic models or empirical correlations requires careful validation with the aid of reliable databases. But, while many new databases are being made available in the literature, the methods used to detect CHF vary greatly, producing different CHF estimates for the same fluid and operating conditions. The variations in detection method are the result of both heated wall design and criteria used to terminate an experiment in response to wall temperature excursions. This study also investigates the interfacial phenomena preceding the occurrence of CHF for flow boiling with a finite inlet vapor void. Temporal records of the heated wall temperatures are used to track the complex transient response of the heated wall, and identify differences between temperature excursions associated with momentary localized dryout and those with true CHF. It is shown that the flow enters the channel fully separated, with a liquid layer sheathing all four channel walls surrounding a central vapor core. At high heat fluxes, a wavy vapor layer begins to form beneath the liquid layer adjacent to the heated wall, and cooling is provided mostly though wetting fronts associated with the wave troughs in accordance with the Interfacial Lift-off Model. However, depending on mass velocity, inlet quality and flow orientation, conditions may

arise that cause breakup of the heated wall liquid layer into ligaments that are entrained in the vapor core. This phenomenon causes localized dryout and wall temperature excursions at heat fluxes well below CHF, but the wall is able to recover from these excursions by a combination of reattachment of ligaments with the heated wall and lateral heat conduction within the wall itself. Recommendations are made concerning construction of the heated wall and CHF detection in pursuit of reliable CHF data.

The microgravity-based study investigates flow boiling of FC-72, which is simulated in a series of parabolic flight maneuvers. Flow boiling experiments are conducted in a rectangular channel fitted with two opposite heating walls. The operating conditions include liquid inlet velocities of 0.1 – 1.9 m/s, liquid mass velocities of 224.2 – 3347.5 kg/m^{2}s, and inlet suboolings of 2.8 – 8.1°C. The study includes both high-speed video analysis of interfacial features and heat transfer measurements. During a flight parabola, the heated wall temperatures decrease slightly as the aircraft enters the hypergravity ascent phase, then increase slightly during the microgravity phase, and decrease once again during the hypergravity descent. These temperature variations point to enhancement in flow boiling heat transfer with increasing gravity, and degradation in microgravity. For both single-sided and double-sided heating, interfacial behavior just before CHF is characterized by dominant wavy vapor layers covering the heated walls, where liquid is able to access the walls only in wetting fronts corresponding to the wave troughs. CHF is associated with successive lift-off of wetting fronts from the walls, consistent with the Interfacial Lift-off Model, which has been validated extensively in past studies using single-sided heating in both μg_e and 1 g_e. It is shown this model predicts μg_e double-sided flow boiling CHF with excellent accuracy. Additionally, the model points to convergence of CHF values for μg_e and 1 g_e for inlet velocities greater than about 1 m/s. Therefore, by maintaining velocities above this threshold allows designers of space systems to achieve inertia-dominated performance as well as to adopt prior data and correlations developed from terrestrial studies.

CHAPTER 1. INTRODUCTION

1.1 Importance of Two-Phase Flow and Heat Transfer to Future Space Missions

As the attention of space agencies worldwide is shifting to more complex and more distant missions, including manned missions to Mars, greater emphasis is being placed on efficiency of power utilization onboard both space vehicles and future planetary bases. A key tactic towards achieving this goal is to reduce the weight and volume of all subsystems. These include several components that are intended specifically for thermal management. One means to achieving this goal is to transition from single-phase to two-phase thermal management. By capitalizing upon the merits of latent heat of the working fluid rather than sensible heat alone, two-phase systems are expected to yield orders of magnitude enhancement in evaporation and condensation heat transfer coefficients compared to single-phase systems, which would result in drastic reductions in the weight and volume of thermal management hardware [1].

Thermal management plays a crucial role in supporting astronaut life onboard space vehicles and planetary bases. Thermal management systems are responsible for controlling the temperature and humidity of the environment using a Thermal Control System (TCS), and fall into three main categories [2]. *Heat acquisition* components acquire energy from a heat-producing source. *Heat transport* components move the energy from the heat acquisition component to heat rejection hardware. *Heat rejection* components reject the heat from the TCS to deep space by radiation. There are also other specialized subsystems, such as *refrigerator/freezer* components that provide cooling for science experiments and food storage, and *water recovery* components that transfer crew and system wastewater into potable water for crew and system reuse.

Understanding the influence of gravity on two-phase flow and heat transfer is crucial to the development of space power for future missions. For example, NASA's

Fission Power System (FPS) program aims to develop a fission system for use on advanced science missions, which would provide both very high power and very low mass to power ratio [3]. The Rankine cycle is one example of a high power system (>100 kW) that promises high thermal efficiency and enables high performance nuclear electric propulsion for distant cargo and human missions. But before the Rankine cycle can achieve fruition, the influence of microgravity on fluid physics must be well understood. This includes critical heat flux (CHF) in the boiler, and shear driven condensation heat transfer.

A key strategy in designing two-phase components for space missions is to develop tools that enable the prediction of flow conditions (*e.g.,* coolant flow rate) that would ensure insensitivity of evaporation or condensation to gravity [1,4,5] for the relevant gravity range important to a particular space system or mission, as illustrated in Figure 1.1. This would allow existing data, correlations, and models developed from ground-based 1 g_e studies to be employed with confidence for design of reduced gravity and microgravity thermal management systems.

Researchers employ a variety of techniques to assess the important influence of gravity on flow boiling CHF. These include conducting ground-based experiments at different flow orientations relative to Earth's gravity [4,5]. Microgravity is achieved in drop tower and drop shaft experiments, which provide a high degree of control of residual gravity, but are too short (less than 10 s) to achieve steady two-phase flow or to collect sufficient amounts of data for statistical analysis without a significant number of repetitive drops [2]. Aircraft parabolic flight tests offer significant advantages over drop tower and drop shaft tests, including longer test duration (up to 25 s), larger and more complex test packages, and ability of the experimenter to interact with the test [1]. Space Shuttle experiments provided an ideal testing environment because of the ability to accommodate long-duration experiments with good control of residual gravity. Since the recent abandonment of Space Shuttles, the International Space Station (ISS) has become the sole platform for conducting long duration microgravity experiments.

Researchers at the Purdue University Boiling and Two-Phase Flow Laboratory (PU-BTPFL) have been involved in several NASA-supported initiatives to explore the

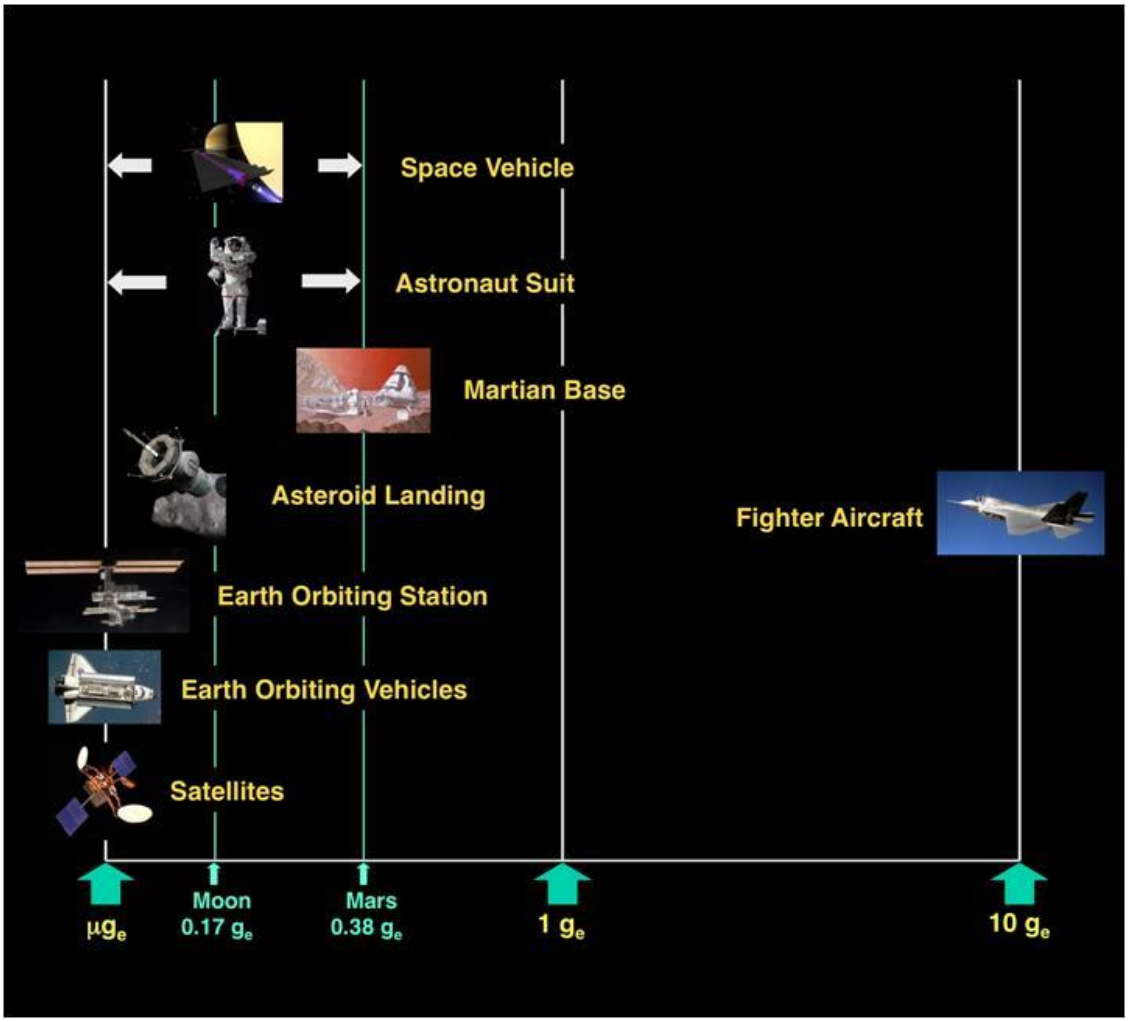

Figure 1.1: Examples of systems demanding predictive models of the effects of gravity on two-phase flow and heat transfer.

influence of gravity on both flow boiling and condensation. These studies are initiated with ground experiments, by exploring the effects of flow orientation relative to Earth's gravity [4,5]. The same hardware is then tested in parabolic flight experiments [1]. Both types of tests are used to assist the design of test hardware for future experiments onboard the ISS. The present study concerns flow boiling CHF findings from ground-based 1 g_e and microgravity μg_e experiments.

1.2 CHF in Terrestrial-Based Two-Phase Flow Boiling Systems

CHF is arguably the most important design and safety parameter for heat-flux-controlled two-phase flow systems. Depending on the working fluid and operating conditions, CHF occurrence can trigger physical meltdown, burnout, or another form of permanent physical damage to the heat-dissipating surface. But, while the importance of this phenomenon is clearly understood, there is considerable confusion about its trigger mechanism, experimental detection and measurement, and prediction.

A vast number of studies conducted mostly since the 1940s aimed at exploring these very issues. Because of the complexity of hydrodynamic and thermal characteristics of flow boiling, the primary contribution from most studies has been the accumulation of CHF data and development of empirical correlations applicable to specific fluids, flow geometries and operating conditions. Despite the great value of these contributions, two-phase system designers are often confronted with great difficulty predicting CHF with acceptable accuracy. As explained by Mudawar [6], the primary reason behind this difficulty can be explained as follows for the special case of flow boiling in tubes. A typical CHF correlation for tube flows takes the form

$$\frac{q''_m}{Gh_{fg}} = f\left(\frac{\rho_f}{\rho_g}, \frac{G^2 L}{\sigma \rho_f}, \frac{c_{p,f}\Delta T_{sub}}{h_{fg}}, \frac{L}{D}, \frac{G}{\rho_f \sqrt{g_e D}}, ..\right) = f\left(\Pi_1, \Pi_2, \Pi_3, \Pi_4, \Pi_5, ..\right) \begin{cases} \Pi_{1,min} < \Pi_1 < \Pi_{1,max} \\ \Pi_{2,min} < \Pi_2 < \Pi_{2,max} \\ \Pi_{3,min} < \Pi_3 < \Pi_{3,max} \\ \Pi_{4,min} < \Pi_4 < \Pi_{4,max} \\ \Pi_{5,min} < \Pi_5 < \Pi_{5,max} \\ \quad . \\ \quad . \end{cases} \tag{1.1}$$

Unlike single-phase heat transfer coefficient correlations that generally consist of one dependent parameter (Nusselt number) as a function of only two independent parameters (Reynolds and Prandtl numbers), CHF correlations are far more complex. Eq. (1.1) shows (i) CHF correlations consist of a dimensionless group that is a function of numerous independent dimensionless groups, and (ii) each independent group is valid over a finite range. Furthermore, because of the high cost of conducting two-phase experiments compared to their single-phase counterparts, CHF data from individual sources are comparatively sparse, and coverages of the individual independent parameters quite limited. Therefore, when a CHF database is consolidated from different sources in pursuit of CHF correlation, the resulting database is restricted to narrow ranges of many parameters, and the CHF correlation is valid over a very small region of the multidimensional space representing all independent parameters. Because of this limitation, thermal system designers are often forced to employ correlations beyond the parameter ranges for which these correlations are recommended. This is undoubtedly one of the primary reasons for inaccurate CHF predictions.

The alternative to empirical correlations is to develop theoretical models based on dominant CHF trigger mechanisms. The saturated pool boiling CHF model by Zuber *et al.* [7] is arguably the best example of a successful theoretical formulation for boiling applications. Unfortunately, CHF in flow boiling is significantly more complicated and exhibits different forms depending on working fluid and operating conditions.

1.2.1 CHF Trigger Mechanisms and Models

Despite the confusion concerning the precise mechanism for CHF, researchers concur that, for heat-flux-controlled systems, CHF is associated with a sharp rise in wall temperature and appreciable reduction in local heat transfer coefficient resulting from inadequate liquid access to the wall. Two different terms that are commonly used to describe specific types of CHF are *Dryout* and *Departure from Nucleate Boiling* (DNB) [8]. Dryout occurs in high quality flows exhibiting an annular flow boiling regime. Here, the heat supplied to the fluid causes gradual thinning of the annular liquid film, and the term 'dryout' is used to describe complete evaporation of the liquid film as the cause

for CHF. DNB is more prevalent with subcooled inlet conditions and higher mass velocities, and corresponds to loss of liquid access to the heated wall despite the existence of adequate liquid elsewhere in the tube's cross section. In general, dryout represents a milder form of CHF and is encountered at lower heat fluxes. DNB, on the other hand, corresponds to higher wall heat fluxes and results in faster wall temperature excursion and therefore higher potential for physical damage to the heated wall.

Four different CHF models have been proposed for flow boiling in tubes: *Boundary Layer Separation, Bubble Crowding, Sublayer Dryout,* and *Interfacial Lift-off*, which are illustrated schematically in Figure 1.2. The Boundary Layer Separation Model [9,10] is based on analogy between wall fluid injection – transpiration - into a single-phase boundary layer and vapor effusion at the wall in flow boiling. In the case of single-phase fluid injection, the velocity profile across the boundary layer is diminished, and becomes vanishingly small once the injection velocity reaches a threshold value, which causes the boundary layer to separate from the wall. By analogy, the Boundary layer Separation Model is based on the premise that CHF occurs when the rate of vapor effusion normal to the heated wall reaches a threshold value that causes appreciable reduction in the liquid velocity gradient, and eventual separation of the liquid from the wall. The Bubble Crowding Model [11,12] is based on the observation that liquid access to the wall is greatly impeded by a thick layer of oblong vapor bubbles. Here, CHF is assumed to occur when turbulent fluctuations in the core liquid flow become too weak to support liquid penetration across the thick bubbly wall layer and provide adequate liquid to the wall. The Sublayer Dryout Model [13] is based on the depiction of a wall that is covered with oblong vapor bubbles that trap liquid sublayers with the wall. CHF is postulated to occur when the heat supplied at the wall exceeds the enthalpy of replenishment liquid from the bulk region. The more recent Interfacial Lift-off Model [14-17] is based on the observation that, during vigorous boiling, the vapor coalesces into a fairly continuous wavy vapor layer. Before CHF, bulk liquid is capable of reaching the heated wall and providing adequate cooling in the wave troughs. CHF is postulated to occur when intense vapor production in the troughs causes the wavy interface to be lifted

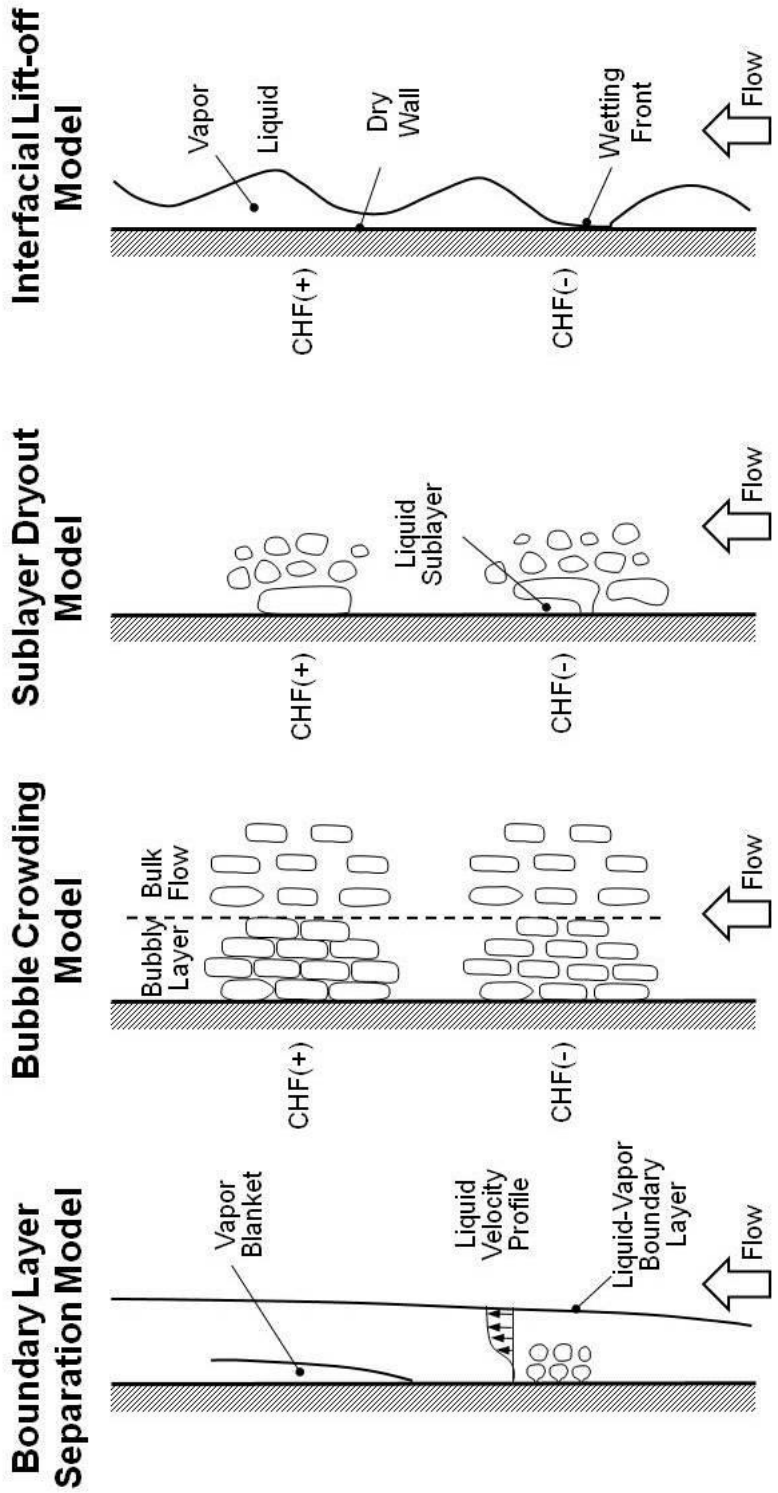

Figure 1.2: Trigger mechanisms for flow boiling CHF according to different models.

off the wall, extinguishing liquid supply to the wall. The Interfacial lift-off model has been especially effective at predicting CHF for flow boiling in microgravity [1].

1.2.2 Differences in Methods of Detecting and Measuring Flow Boiling CHF

Developing reliable CHF correlations and mechanistic models requires systematic methods for CHF detection and measurement. Surprisingly, there is great uncertainty in the heat transfer literature concerning the precise definition of CHF, evidenced by differences in the experimental methods adopted for CHF detection. These differences are responsible for drastic differences in measured CHF [18]. Following are the more popular methods for CHF detection:

(a) First measureable degradation in flow boiling heat transfer, indicated by a slope change of the upper portion of the nucleate boiling region of the boiling curve [19-21].

(b) Rise in heated wall temperature above a fixed level dictated by the experimenter [22,23], followed by either manual or automatic power shut-off.

(c) Appreciable unsteady temperature rise of any portion of the heated wall [24,25].

(d) Allowing sufficient, albeit short period of time for the heated wall to recover from any brief, localized temperature excursion, then increasing heat flux until the wall temperature escalates uncontrollably [26].

Aside from detection method, CHF magnitude can also be greatly influenced by the thickness, δ_h, and thermal properties (k_h, ρ_h, $c_{p,h}$) of the heated wall [27]. For example, some investigators employ extremely thin electrically heating walls (*e.g.,* semitransparent gold film sputtered on a quartz wall) for CHF measurement [28-30]). The concern with this type of heated wall construction is that it may be too thin to permit momentarily dry portions of the wall to be cooled by lateral conduction to other adequately cooled portions. Theoretically speaking, very thin walls may falsely detect CHF even in the low heat flux region of nucleate boiling once dryout occurs, say, beneath a single growing bubble. Very thin heating walls are both unrepresentative of practical surfaces and known to yield CHF values considerably smaller than those of practical walls. To achieve reliable CHF measurement, a sufficient heated wall thickness is required. Figure 1.3 illustrates this phenomenon by the variation of CHF for FC-72 with

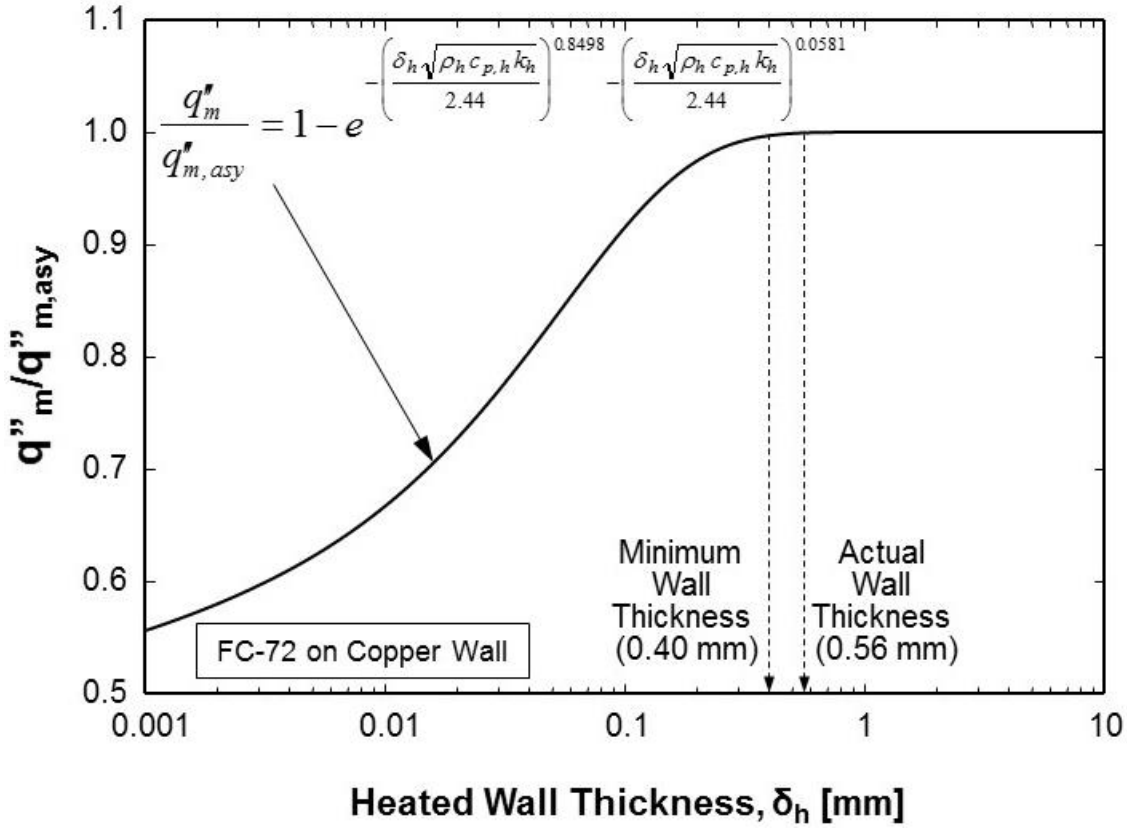

Figure 1.3: Effect of wall thickness on CHF, and determination of wall thickness to attain CHF values that are representative of metallic walls of practical interest. Adapted from Zhang *et al*. [1].

copper wall thickness [1]. It shows very thin walls yield unusually small CHF values, and CHF increasing with increasing thickness up to 0.4 mm, above which it assumes a constant asymptotic value that is representative of practical walls. Hence, it is important to employ a wall thickness for CHF measurement that falls within the asymptotic range.

1.3 Gravity Effects in Terrestrial-Based Boiling Systems

The influence of gravity is exasperated in a two-phase system by the large density difference between liquid and vapor. This difference plays a crucial role in dictating the motion of vapor relative to liquid, thereby influencing heat transfer effectiveness. Flow boiling CHF is an important heat transfer design parameter that exhibits complex variations with the magnitude of gravitational field. The challenge in designing a thermal management system is to make certain that the prevailing boiling heat flux is safely below CHF, which explains the importance space system design engineers place on precise determination of the influence of both flow conditions and gravity on CHF. This is especially the case for high-flux, heat-flux-controlled electronic and power devices, where CHF occurrence can lead to device burnout or other forms of permanent damage. This risk explains a recent surge in the number of published articles addressing means to enhance CHF using a variety of configurations, including spray [31-34], jet [35-38], and micro-channel cooling schemes [32,39-42], and surface enhancement techniques [43].

1.3.1 Influence of Orientation on Flow Boiling CHF

Vertical upflow is a preferred orientation for flow boiling systems because it enables buoyancy to move vapor in the same direction as the liquid flow. This imparts flow stability to the system and helps achieve relative high CHF values by aiding vapor removal from, and liquid replenishment of the heated wall. This explains why the majority of published studies on flow boiling CHF are conducted in the vertical upflow orientation. While different mechanisms have been proposed for flow boiling CHF [9-13], photographic evidence points to a dominant *Wavy Vapor Layer Regime* commencing along the heated wall as CHF is approached, and CHF being triggered by an *Interfacial Lift-off Mechanism* [4,5,14-17], which will be discussed later.

Flow boiling CHF for all other orientations can be highly complicated by the manner in which buoyancy influences the vapor and liquid flows both along the flow channel and perpendicular to the heated wall. Figure 1.4 is used as a guide to explain the influence of flow orientation on CHF for a flow channel that is heated along one side. Shown are eight channel flow orientations, with the flow radiating outwards, and the placement of the heated wall, indicated by a black rectangular strip.

1.3.2 Influence of Buoyancy along the Flow Channel

The influence of buoyancy *along* the channel is especially problematic for vertical downflow, $\theta = 270°$. Here, buoyancy opposes the liquid forces – both drag and shear - and flow behavior is therefore a function of the relative magnitude of buoyancy and liquid forces. Zhang *et al.* [4,5] showed that the vertical downflow orientation results in one of three possible CHF regimes. At very low flow rates, buoyancy exceeds liquid forces, causing the vapor to flow backwards (vertically upwards) along the channel with CHF associated with a *Vapor Counterflow Regime* and *Flooding* and CHF values are quite small. Increasing the flow rate increases the relative magnitude of the liquid forces, and a particular flow rate is reached that causes a balance between the two opposing forces, causing the vapor to stagnate along the channel. Here, CHF is associated with a *Stagnation Regime*, and corresponding CHF values are vanishingly small. A further increase in flow rate causes the liquid forces to exceed buoyancy, and the vapor to flow concurrently with the liquid. CHF for these conditions is associated with a *Separated Concurrent Vapor Flow Regime*, and CHF values are appreciably greater than those for the *Vapor Counterflow* or *Stagnation Regimes*. In the limit of a very high flow rate, the liquid forces render any buoyancy effects negligible, and CHF values for vertical upflow and vertical downflow converge. Clearly, high flow rate is an effective means to negating the influence of buoyancy on both flow behavior along the channel and CHF magnitude.

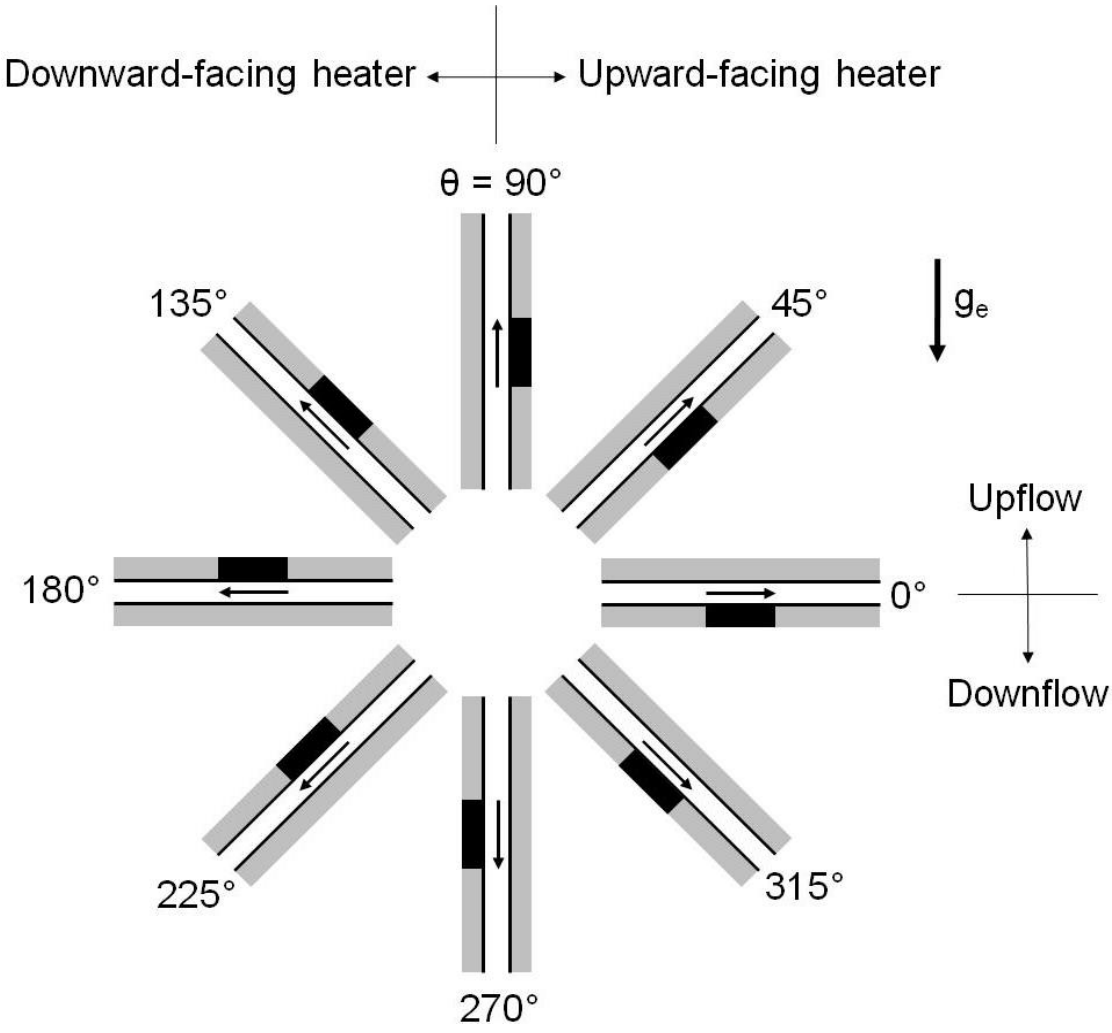

Figure 1.4: Flow orientation nomenclature (heated wall is indicated by a black rectangular strip).

1.3.3 Influence of Buoyancy Perpendicular to the Heated Wall

The influence of buoyancy perpendicular to the heated wall is most noticeable for horizontal flow orientations with the heated wall pointing upwards, θ = 0°, and downwards, θ = 180° [4,5]. For θ = 0° and small flow rates, small bubbles that nucleate along the heated wall tend to coalesce together to form larger vapor bubbles, which are driven by buoyancy across the channel to the opposite adiabatic wall. Here, CHF is associated with a *Pool Boiling Regime*. For θ = 180° and small flow rates, buoyancy causes the vapor to stratify above the liquid and adjacent to the heated wall. Clearly, this *Stratification Regime* impedes liquid access to the heated wall, resulting in very low CHF values. By greatly increasing the flow rate for both horizontal orientations, the flow behavior at CHF begins to resemble that for vertical upflow, θ = 90°. Furthermore, CHF values for θ = 0° and 180° at high flow rates converge with those for vertical upflow, θ = 90°. The convergence of CHF values for different orientations at high flow rates has been confirmed in several prior studies [44-47].

1.3.4 Importance of Wavy-Layer Regime

Figure 1.5 shows CHF data for FC-72 measured by Zhang *et al.* [5] in a flow velocity–orientation plane. The data are grouped into the six aforementioned CHF regimes for which representative photographs are also depicted in Figure 1.5. Notice that all CHF regimes other than the *Wavy Vapor Layer Regime* are encountered at low velocities, while the *Wavy Vapor Layer Regime* is dominant at high velocities regardless of orientation. Interestingly, the *Wavy Vapor Layer Regime* is prevalent in the vertical and near-vertical upflow orientations, θ = 90 and 135°, respectively, even at low velocities.

In a subsequent study, Zhang *et al.* [1] performed similar flow boiling experiments in parabolic flight to simulate microgravity. In the absence of buoyancy, the *Wavy Vapor Layer Regime* was observed over the entire range of velocities, Figure 1.6(a), including low velocities that resulted in the other more complex CHF regimes in 1 g_e experiments.

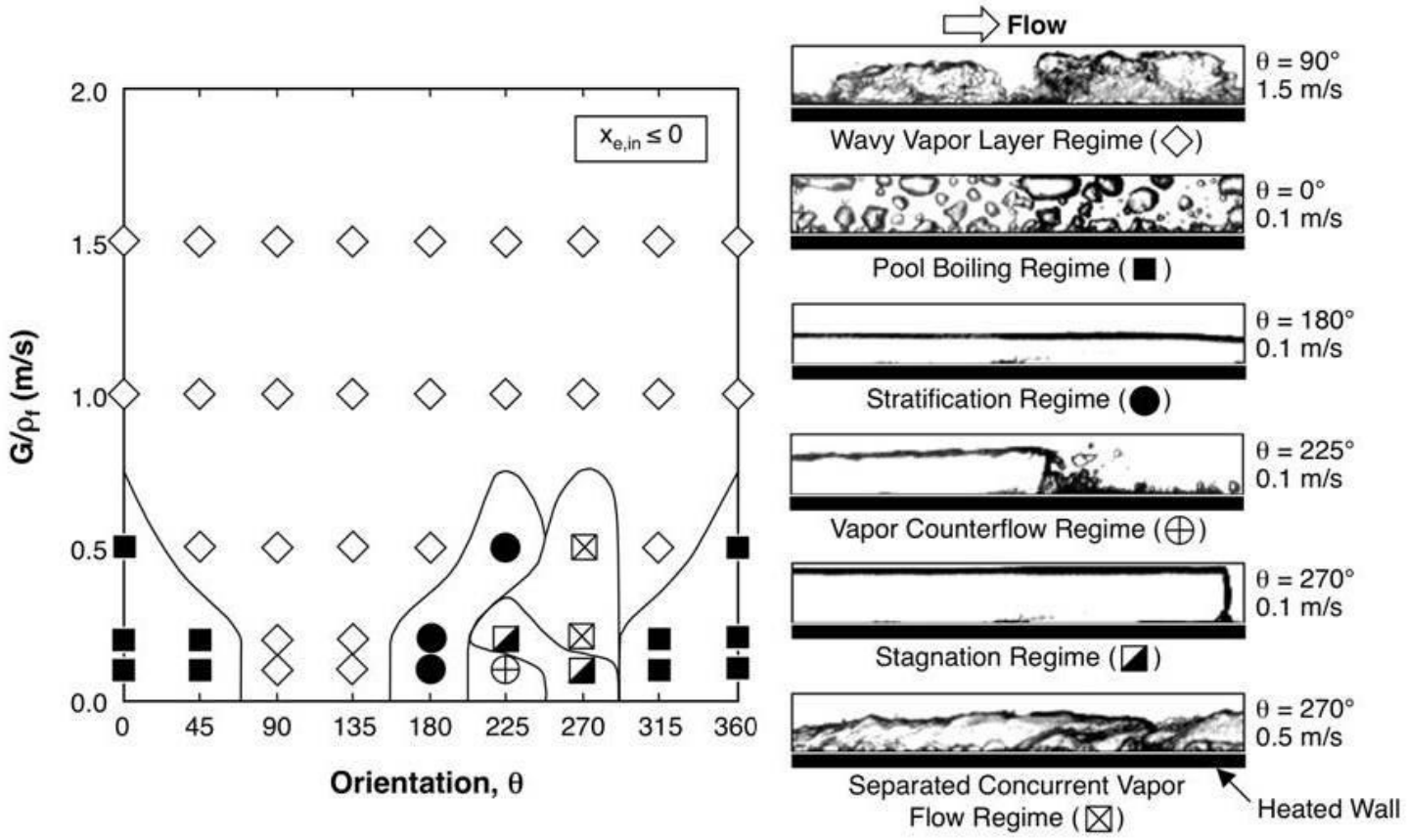

Figure 1.5: CHF regime map for FC-72 and photos of representative CHF regimes. Adapted from Zhang *et al.* [5].

Interestingly, the *Wavy Vapor Layer Regime* has been observed at 1 g_e even in saturated pool boiling. While CHF for a horizontal upward-facing heated wall follows the classical depiction of Zuber *et al.* [7], tilting the wall to near vertical orientations resulted in a wavy vapor layer pattern [48,49] as shown in Figure 1.6(b). The same behavior was observed in pool boiling along a downward-facing convex surface in 1 g_e [50] as shown in Figure 1.6(c).

1.3.5 Threshold Flow Rate for Flow Boiling CHF

Clearly, increasing flow rate in channel flow boiling precipitates uniformity in interfacial behavior before CHF, with the *Wavy Vapor Layer Regime* occurring along the heated wall, and CHF triggered by the *Interfacial Lift-off Mechanism* regardless of orientation.

The discussion above concerns working fluid that is supplied to the channel in pure liquid state, *i.e.,* with $x_{e,in} \leq 0$. Recently, Kharangate *et al.* examined flow boiling CHF with the fluid entering the channel as a two-phase mixture ($x_{e,in} \geq 0$) in vertical upflow [26] and horizontal flow with the heated wall facing upwards [51]. Despite the complicated flow patterns caused by the incoming two-phase mixture, CHF for both orientations was predicted with good accuracy using the *Interfacial Lift-off Mechanism* employed by Zhang *et al.* for pure liquid inlet conditions ($x_{e,in} \leq 0$) in conjunction with the *Wavy Vapor Layer Regime* both at different flow orientations in 1 g_e [4,5] and in microgravity [1]. The authors of the present study extended the work of Kharangate *et al.* for all flow orientations [52]. They proved that, for two-phase mixture inlet conditions ($x_{e,in} \geq 0$), high flow rates cause appreciable diminution in the influence of orientation on CHF. This behavior was explained by the higher mass velocities increasing the magnitude of shear and drag forces compared to buoyancy, especially for high inlet qualities.

The studies by Zhang *et al.* [1,4,5], Kharangate *et al.* [26,51], and Konishi *et al.* [52] all point to the existence of a threshold flow rate above which virtually identical CHF values are measured for all orientation. This threshold is of paramount importance to future space systems since, by operating the thermal management system at a flow rate

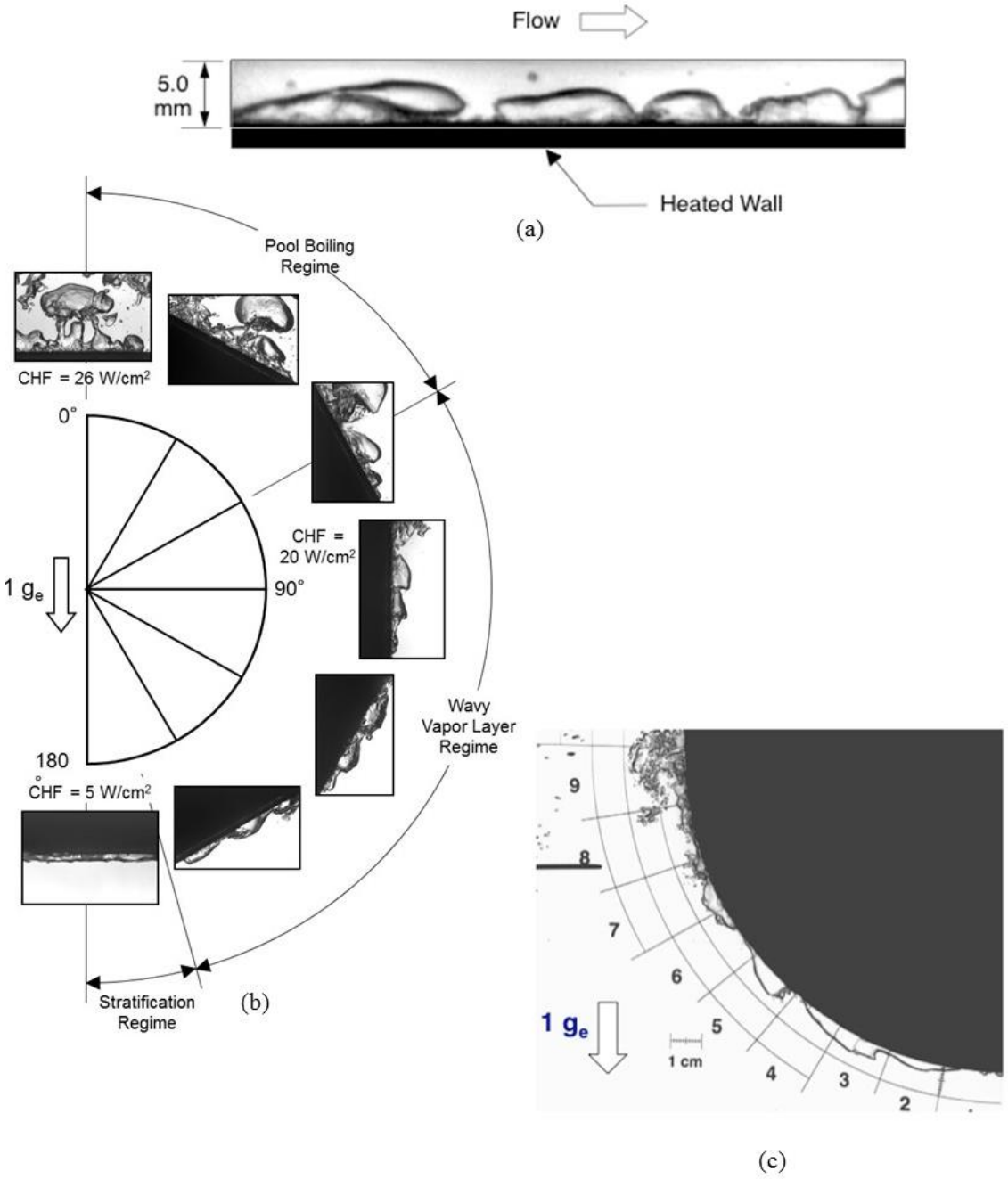

Figure 1.6: Wavy vapor layer CHF regime for (a) flow boiling of FC-72 in microgravity at 0.25 m/s inlet velocity [1], (b) pool boiling of PF-5052 at different wall orientations at 1 g_e [48,49], and (c) pool boiling of FC-87 along a downward-facing convex wall at 1 g_e [50].

that exceeds this threshold, one is able to utilize, with confidence, the vast body of published CHF data, correlations and models developed from ground-based studies for design of reduced gravity thermal management systems.

1.4 Transition from Pool Boiling to Flow Boiling in Microgravity

The vast majority of microgravity boiling research performed to date has been focused on pool boiling. The original intent in pool boiling studies was to develop fundamental understanding of the influence of microgravity on such phenomena as boiling incipience, bubble nucleation, growth and coalescence, nucleate boiling heat transfer, and, most importantly, CHF [2]. Spanning over 60 years, most of these studies point to the danger of enormous bubble growth because of the absence of an effective force to remove the bubble from the heated wall. This also points to the danger of abrupt occurrence of CHF at relatively low heat fluxes. These complications render the implementation of pool boiling in space systems very impractical.

Recently, there have been urgent calls to shift the focus of microgravity research from pool boiling to flow boiling in order to achieve both the high heat transfer coefficients and high CHF values required for space applications [2,3]. In the absence of a body force to remove vapor bubbles from the boiling wall, flow boiling can augment CHF in microgravity by relying on bulk liquid motion to flush bubbles away before they coalesce into large insulating vapor masses, and to replenish the wall with bulk liquid. Despite these highly acknowledged merits of flow boiling, very few microgravity flow boiling experiments have been performed to date. This can be attributed to the high complexity and high cost of flow boiling microgravity test facilities compared to those intended for pool boiling. Flow boiling facilities are typically much larger, include many more components, and demand greater power. They also require a longer microgravity test duration to achieve steady state, which makes them difficult to implement in drop towers, drop shafts, sounding rockets and parabolic flight aircraft.

The Appendix provides a review of published literature concerning two-phase flow and heat transfer in reduced gravity. This encompasses the different methods and platforms dedicated to exploring the influence of reduced gravity, including ground flow

boiling experiments performed at different orientations relative to Earth gravity, as well as adiabatic two-phase flow, pool boiling, flow boiling and CHF reduced gravity experiments. Discussed in this review are key mechanisms, correlations and models from these studies, as well as implementation of the same tools in design of thermal management systems in future space missions.

1.5 Overall Flow Boiling Study Objectives

The present study is a part of a NASA-supported partnership between the Purdue University Boiling and Two-Phase Flow Laboratory (PU-BTPFL) and NASA Glenn Research Center that was initiated in 2012 with the goal of developing the Flow Boiling and Condensation Experiment (FBCE) for the International Space Station (ISS). The long-term objectives of this effort are to: (a) obtain flow boiling and condensation databases in microgravity, (b) develop an experimentally validated, mechanistic model for flow boiling critical heat flux (CHF) in microgravity, and criteria to predict the minimum flow rate required to ensure gravity-independent CHF, and (c) develop an experimentally validated, mechanistic model for condensation in microgravity, and criteria to predict the minimum flow rate required to ensure gravity-independent annular condensation. This study concerns the flow boiling portion of the project.

The overall study is composed of two separate experimental investigations driven by the underlying goal to explore the effects of gravitational body force on flow boiling heat transfer and CHF. One experimental study examines the influence of orientation on CHF for flow boiling with two-phase inlet conducted in terrestrial conditions. Another study investigates subcooled flow boiling heat transfer and CHF performance in microgravity conditions.

1.5.1 Objectives of Terrestrial-Based Study

This study is a continuation of the ground-based studies of flow boiling CHF for different orientations begun by Zhang *et al.* [4,5] for subcooled and saturated liquid inlet conditions, and the more recent vertical and horizontal studies by Kharangate *et al.* [26,51] for saturated two-phase mixture inlet conditions. The present study is focused on

saturated two-phase mixture inlet conditions similar to those in [26,51], but covers all flow orientations relative to Earth's gravity. Saturated inlet conditions are important for space applications where a number of heat dissipating electronic or power modules are cooled in series using a single two-phase flow loop. While upstream modules can take advantage of subcooled flow boiling, both the sensible and latent heat of the coolant are gradually depleted, and the downstream modules may be exposed to a two-phase mixture. In the present study, experiments are conducted by boiling FC-72 along a rectangular channel fitted with a heated wall along one side. High-speed video imaging is used to capture interfacial behavior at wall heat fluxes up to and including CHF. The primary objectives of the ground-based study are to:

(1) Identify CHF mechanisms associated with different orientations for varying mass velocity and inlet quality.
(2) Explore the effectiveness of the Interfacial Lift-off Model in predicting the new CHF data.
(3) Investigate the interfacial phenomena preceding the occurrence of CHF.
(4) Identify differences between temperature excursions associated with momentary localized dryout and true CHF using temporal records of the heated wall temperatures,
(5) Discuss extensive video records of flow boiling CHF that were captured at different flow rates, inlet qualities and flow orientations.
(6) Develop a systematic criteria for assessing the influence of gravity on flow boiling CHF and, more specifically, for negating the influence of gravity altogether.

1.5.2 Objectives of Microgravity-Based Study

Overall, the influence of body force on two-phase heat transfer appears to be highly dependent on mass velocity, inlet quality and heat flux, which also dictate flow pattern. Amongst the collection of microgravity boiling studies presented in Appendix A, findings by different investigators often appear contradictory to one another. Although microgravity boiling research has been conducted since the late 1950s, there is a severe shortage of data for two-phase heat transfer in microgravity. The microgravity study fills

this gap by providing detailed heat transfer data for boiling of FC-72 in a rectangular channel fitted with two heated walls positioned opposite of each other, where one or both heated walls could be activated during testing. The data are also complemented by extensive high-speed video records that capture interfacial behavior for different flow velocities and wall heat fluxes. The primary objectives of the microgravity-based study are to:

(1) Explore the experimental methods used, heat transfer data trends, and interfacial behavior.
(2) Address the events just before CHF, during the CHF transient, and immediately following CHF.
(3) Develop a mechanistic CHF model for a double-sided heated rectangular channel and explore the model's effectiveness in predicting the new CHF data.

CHAPTER 2. EXPERIMENTAL METHOD

2.1 Terrestrial Saturated Flow Boiling Facility

The following flow boiling facility was constructed and operated by the PU-BTPFL. It is designed to perform on-ground experiments investigating the influence of orientation on CHF for flow boiling with an inlet vapor void. Descriptions of the overall facility and test procedure are discussed below.

2.1.1 Fluid Conditioning Loop

Figure 2.1 shows a schematic of the two-phase flow loop that is configured to condition the working fluid, FC-72, to the desired pressure, mass velocity, and quality at the inlet to the main flow boiling test module. The bulk of the FC-72 liquid is contained in a reservoir that is fitted with both an electrical immersion heater and a water-cooled condensation coil. Prior to testing, the FC-72 is de-aerated by vigorous boiling with the aid of the immersion heater. The non-condensable gases are purged to the ambient using a vacuum pump as the FC-72 is recaptured by condensation in the upper part of the reservoir. The coolant is circulated through the flow loop using a gear pump. Exiting the pump, the coolant passes through a filter followed by a turbine flow meter. The liquid then enters two in-line electric heaters - preheaters - connected in series before entering the flow boiling module. Each of the in-line heaters is powered by a 115-W variac to regulate power input to the liquid. The first preheater raises the liquid temperature to a level close to, but below saturation temperature, while the second preheater heats the fluid to a saturated mixture with a prescribed quality at the inlet to the flow boiling module. The quality at the inlet to the flow boiling module is determined from measurements of liquid temperature, T_{preh}, and pressure, p_{preh}, upstream of the second preheater, and electrical power input, P_e, to the second preheater according to the relation

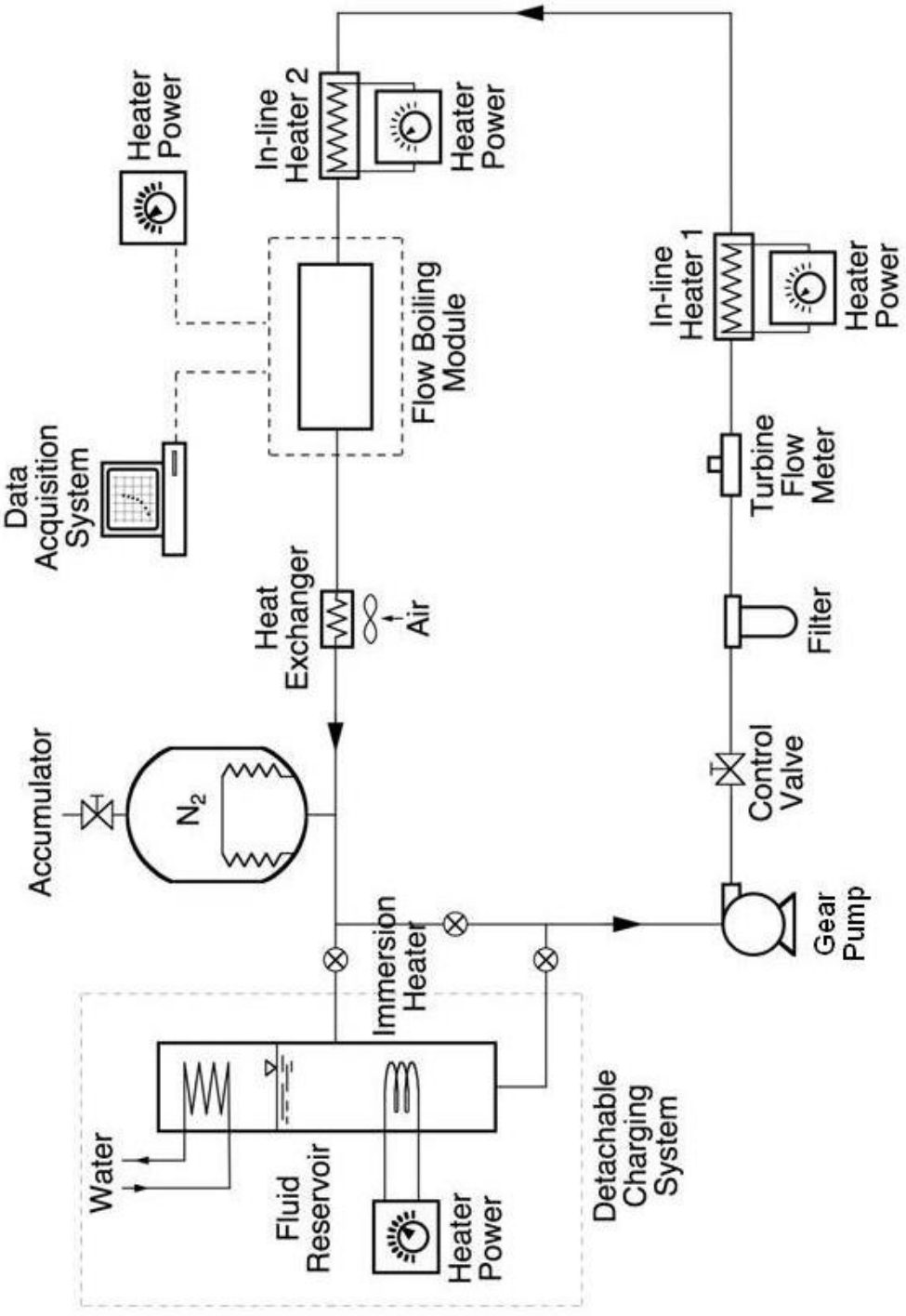

Figure 2.1: Schematic of ground-based two-phase flow loop.

$$x_{e,in} = -\frac{c_{p,f}\left(T_{sat} - T_{preh}\right)}{h_{fg}} + \frac{P_e}{\dot{m}h_{fg}}. \quad (2.1)$$

In Eq. (2.1), T_{sat} is the coolant saturation temperature corresponding to the pressure measured upstream of the preheater.

Exiting the flow boiling module, the two-phase mixture is passed through an air-cooled heat exchanger to return the fluid to liquid state. A nitrogen-filled accumulator is situated between the heat exchanger and the reservoir to provide a controlled reference pressure point for the entire loop. The accumulator contains stainless steel bellows that accommodate any expansion or contraction of the FC-72.

2.1.2 Flow Boiling Test Module

The flow boiling test module is designed to conduct flow boiling CHF measurements and allow video motion analysis of the two-phase flow along a uniformly heated wall. As shown in Figure 2.2, the flow boiling module consists of two transparent polycarbonate plastic (Lexan) plates that are bolted together between two stainless steel support plates; the purpose of the latter plates is help prevent buckling of the plastic plates or fluid leaks. A rectangular flow channel is formed by milling a 5.0-mm high by 2.5-mm wide slot into the top plastic plate. A portion of the opposite plastic plate is milled out to insert a 0.56-mm thick, 6.5-mm wide and 101.6-mm long oxygen-free copper plate that serves as heated wall for the flow boiling module. The heated plate is positioned 106 hydraulic diameters from the inlet to help ensure fully developed flow at the upstream edge of the heated wall. A honeycomb insert is affixed upstream of the channel inlet to break up any large inlet eddies and help straighten the flow. A flexible Teflon cord is trapped in an o-ring groove between the two plastic plates to prevent any leaks. The interface between the copper plate and the lower plastic plate is sealed with high-temperature silicone rubber.

The test module is mounted on an aluminum bracket that features a 0-360° swivel. This bracket, along with the flow loop components, power and instrumentation cabinets, and data acquisition system, are mounted in a single rigid aluminum frame.

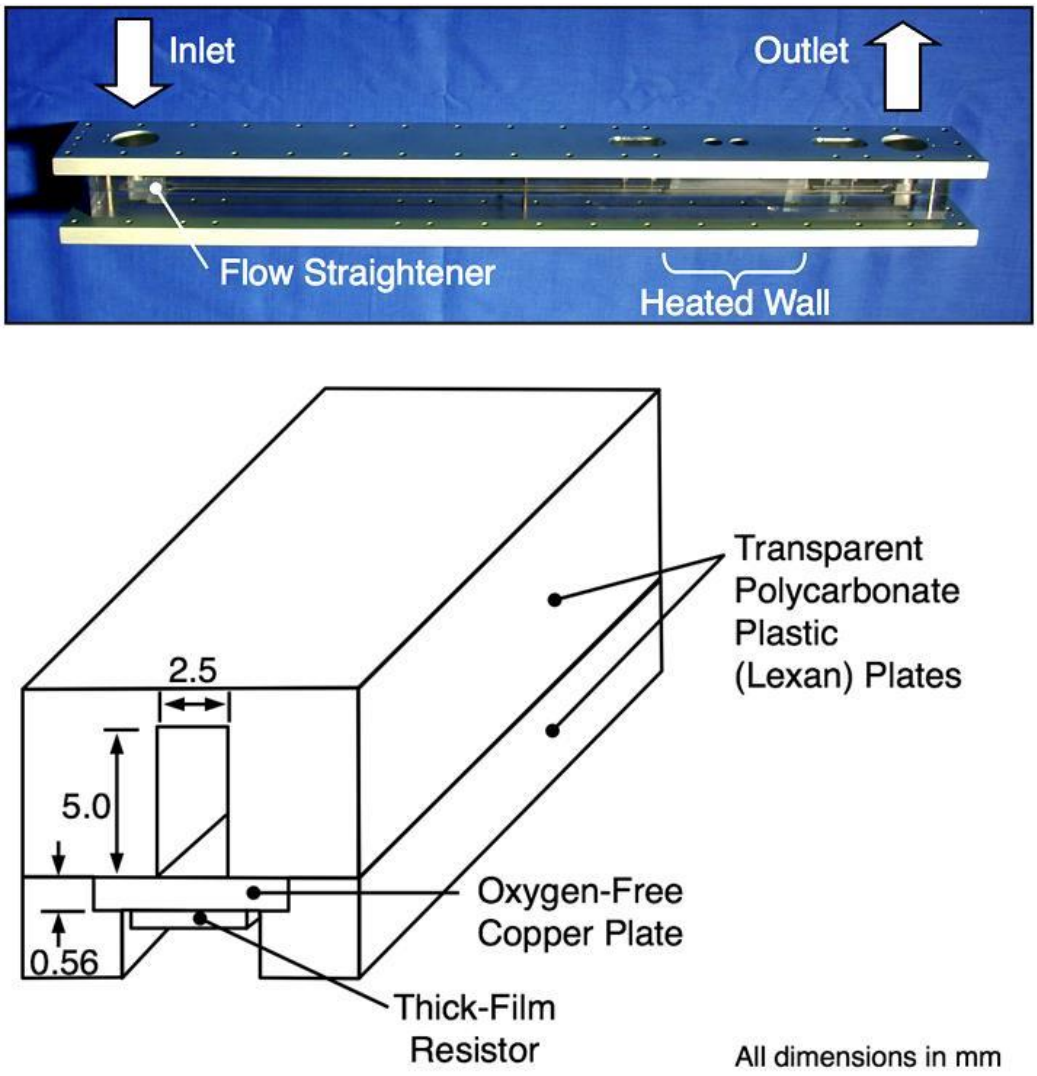

Figure 2.2: Flow channel assembly.

2.1.3 Heated Wall Construction

Originally designed for parabolic flight microgravity experiments [1], the heated wall consists of six 4.0-mm wide by 16.1-mm long, thick-film resistors that are soldered to the underside of the copper plate, Figure 2.3(a), and connected in parallel to a single 115-volt ac variac. The heated wall temperature is measured by five type-K thermocouples that are inserted into small holes in the copper plate between the resistors at the axial locations indicated in Figure 2.3(b).

One of the primary challenges in selecting an optimum thickness for the copper plate is to simultaneously satisfy two crucial criteria. The first is to minimize wall thickness in pursuit of fast temperature response to achieve steady state temperatures following a small power increment within a typical parabola (~ 17–23 s) [1]. The second is to ensure that the measured CHF is representative of practical walls. As shown in Figure 1.3, the minimum thickness that precludes CHF dependence on wall thickness for boiling of FC-72 on copper is 0.40 mm, which is why a thickness of 0.56 mm is used [1].

2.1.4 Flow Visualization Techniques

Analysis of interfacial features along the flow channel is achieved with a high-speed Photron Fastcam Ultima APX video camera with a shutter speed of 1/20,000 s, which is fitted with a high magnification Nikon Micro-Nikkor 105 mm f/8D autofocus lens. Video capture is achieved at a frame rate of 4000 fps, with the heated channel backlit using a high intensity light source that is diffused across a Mylar sheet. As shown in Figures. 2.4(a) and 2.4(b), the camera is aimed normal to the side of the flow channel, and the imaging is repeated in 20-mm long inlet, middle, and outlet portions of the heated wall.

2.1.5 Operating Conditions and Measurement Accuracy

Flow boiling tests are performed in eight flow orientations as illustrated in Figure 1.4. For all the orientations, the flow radiates outwards, and the placement of the heated wall (indicated by a black rectangular strip), along with the flow orientation, produce predominantly upflow or downflow with the heated wall facing either upwards or

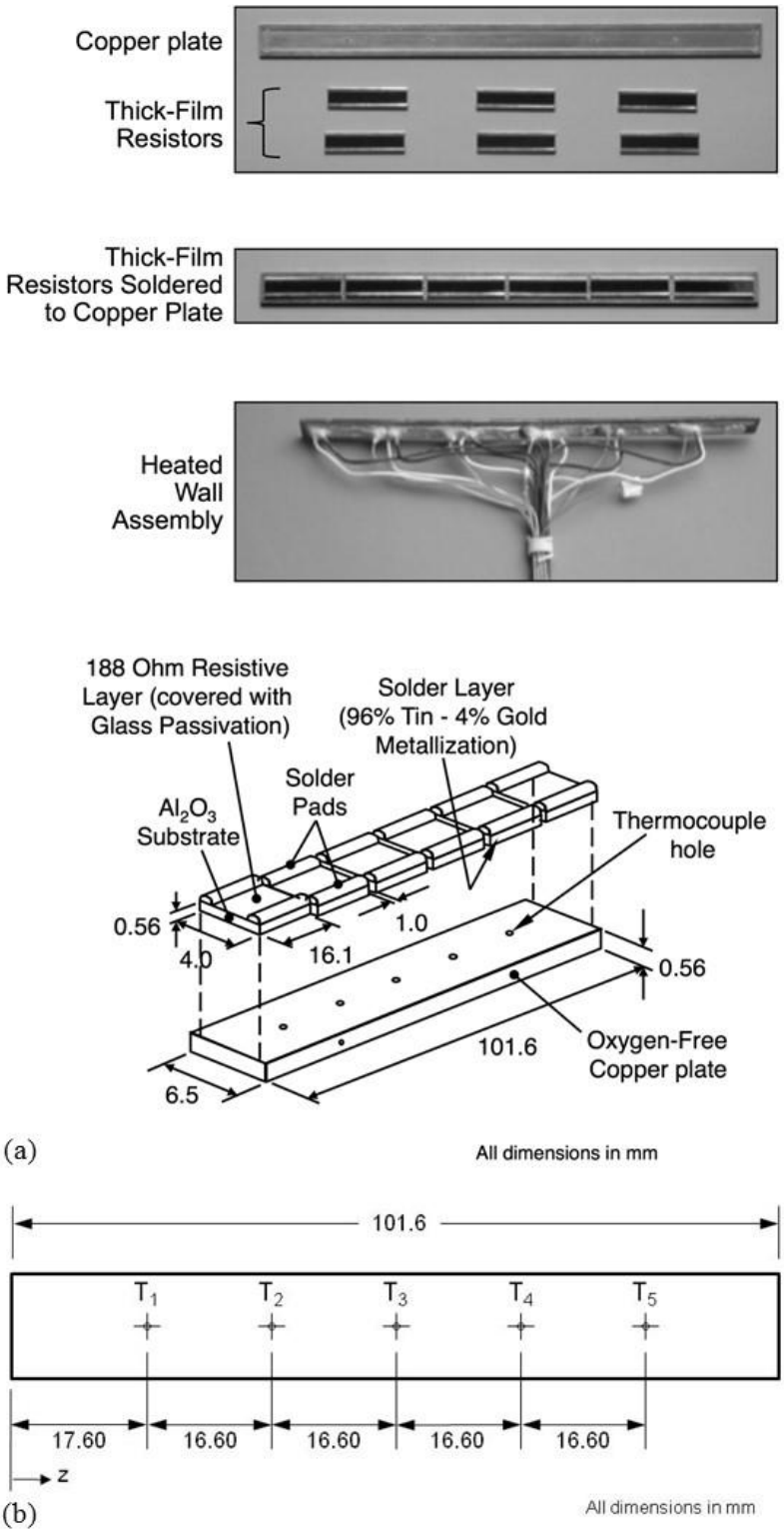

Figure 2.3: (a) Construction of heated wall. (b) Axial locations of heated wall thermocouples.

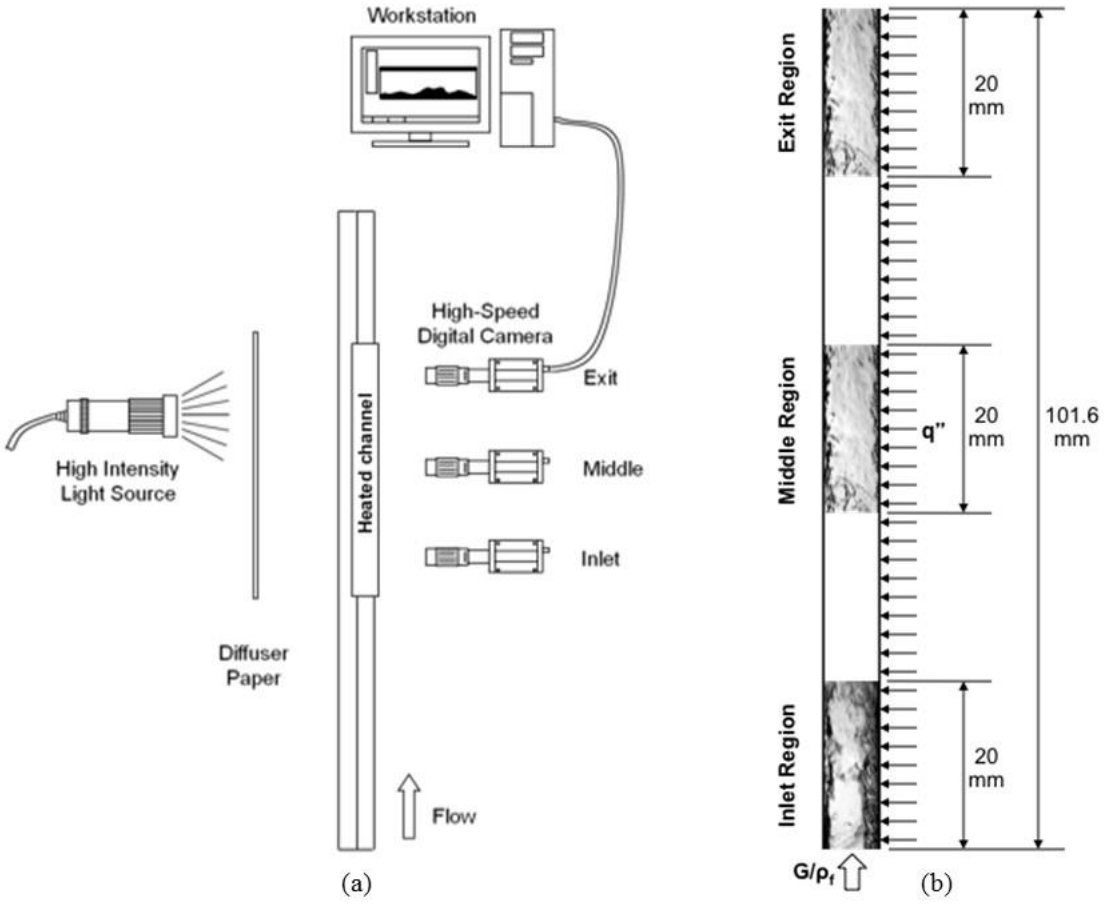

Figure 2.4: (a) Flow visualization setup. (b) Axial spans of video capture regions of the heated wall.

downwards relative to Earth's gravity. For each orientation, tests are attempted at nine values of mass velocity, with G/ρ_f = 0.126, 0.224, 0.315, 0.398, 0.542, 0.712, 0.850, 0.995 and 1.130 m/s. Pressure at the outlet from the heated wall is held constant at 103 kPa (15 psia) for all the tests. For each mass velocity, the inlet temperature and outlet pressure are first adjusted to desired values, and the preheater power, P_e, is progressively increased to span an inlet quality range of $x_{e,in}$ = 0.01-0.19.

During the tests, the electrical power input to the heated wall is increased in small increments and the electrical power, flow rate, temperature and pressure measurements are recorded only after conditions in the flow boiling channel and entire flow loop reach steady state. This procedure is repeated up to CHF, which takes the form of a sudden unsteady rise in wall temperature initiated at any of the wall thermocouple locations.

Pressure is measured both upstream and downstream of the heated wall of the flow boiling module as well as at other locations along the loop by pressure transducers having an accuracy of 0.01%. Temperatures are measured along the heated wall as well as upstream and downstream of the heated wall and at various points along the loop using type-K thermocouples with an uncertainty of 0.3 °C. The uncertainty in the heat flux measurement is 0.2%.

2.2 Microgravity Subcooled Flow Boiling Facility

A second facility was constructed to perform subcooled flow boiling experiments in reduced gravity. Operation and construction of the test facility and critical components were coordinated by the NASA Glenn Research Center in Cleveland, OH. Details of the test facility and operation in simulated microgravity conditions are discussed below.

2.2.1 Fluid Conditioning Loop

Microgravity is achieved in this study by flying a complete flow boiling facility in a series of parabolic maneuvers onboard Zero-G Corporation's modified Boeing 727 aircraft. Figure 2.5(a) shows a schematic of the two-phase flow loop that is used to deliver the working fluid, FC-72, to the Flow Boiling Module (FBM) at desired pressure, temperature, and flow rate. Made by 3M Company, FC-72 is a dielectric liquid with a

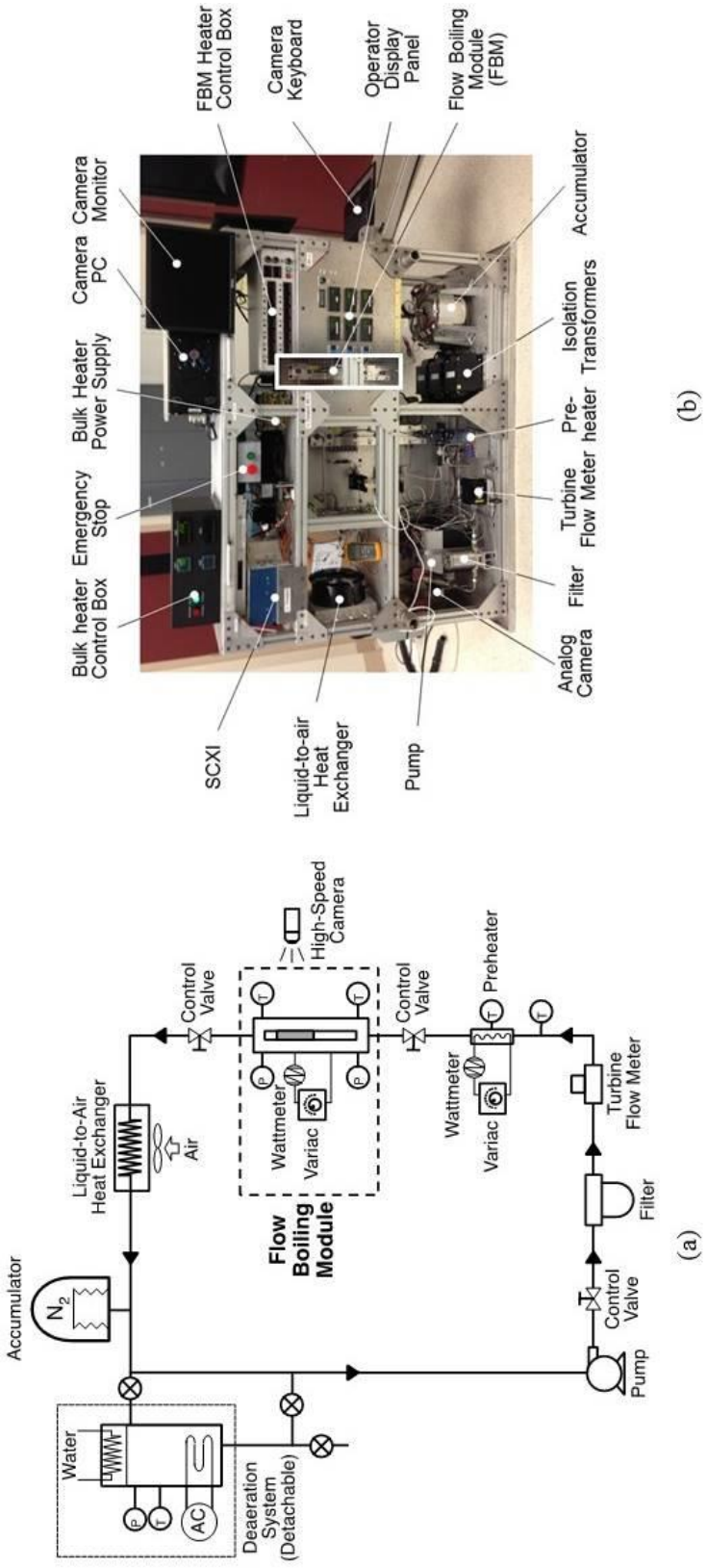

Figure 2.5: (a) Schematic diagram of flow loop. (b) Photo of parabolic flight facility.

relatively moderate saturation temperature 56 °C at atmospheric pressure. A secondary deaeration system is used to rid the FC-72 from any non-condensable gases prior to a series of tests. The deaeration is achieved by vigorously boiling FC-72 liquid for 30 minutes using immersion heaters situated near the bottom of a stainless steel reservoir. The mixture of FC-72 vapor and non-condensables is passed over the surfaces of a water cooled condenser, where most of the FC-72 vapor is recaptured by condensation, while the non-condensables are purged to the ambient. The deaeration system is then fully disconnected from the flow loop prior to loading the facility onto the aircraft.

The deaerated FC-72 is circulated through the closed flow loop with the aid of a magnetically coupled pump. FC-72 liquid exiting the pump is passed through a control valve, particulate filter, and turbine flow meter. It then enters a Watlow CAST X-500 circulation heater, where the liquid temperature is raised to the desired level, before entering the FBM. The liquid is heated along the FBM, and converted to a two-phase mixture. The mixture exiting the FBM is returned to liquid state after passing through a liquid-to-air heat exchanger. Located downstream of the heat exchanger is a nitrogen-filled accumulator which is used to set a reference pressure point for the loop.

The entire flow boiling parabolic flight facility, including the flow loop components, data acquisition system, power and instrumentation cabinets, and high-speed camera, are mounted onto a rigid extruded aluminum frame as shown in Figure 2.5(b).

2.2.2 Flow Boiling Module (FBM)

The FBM is designed to simultaneously enable thermal measurements and conduct high-speed video motion analysis of interfacial features. As shown in the exploded view in Figure 2.6(a), the FBM consists of three transparent polycarbonate plastic (Lexan) plates that are bolted together between two aluminum support plates. The purpose of the support plates is to prevent buckling of the plastic plates and help prevent fluid leaks during the aircraft experiments. A rectangular flow channel is formed by cutting a 5.0-mm high by 2.5-mm wide slot into the central axis of the channel sidewall plate. Both the outer channel top and bottom plastic plates are milled out to insert 15.5-mm wide, 114.6-mm long and 1.04-mm thick oxygen-free copper slabs that serve as

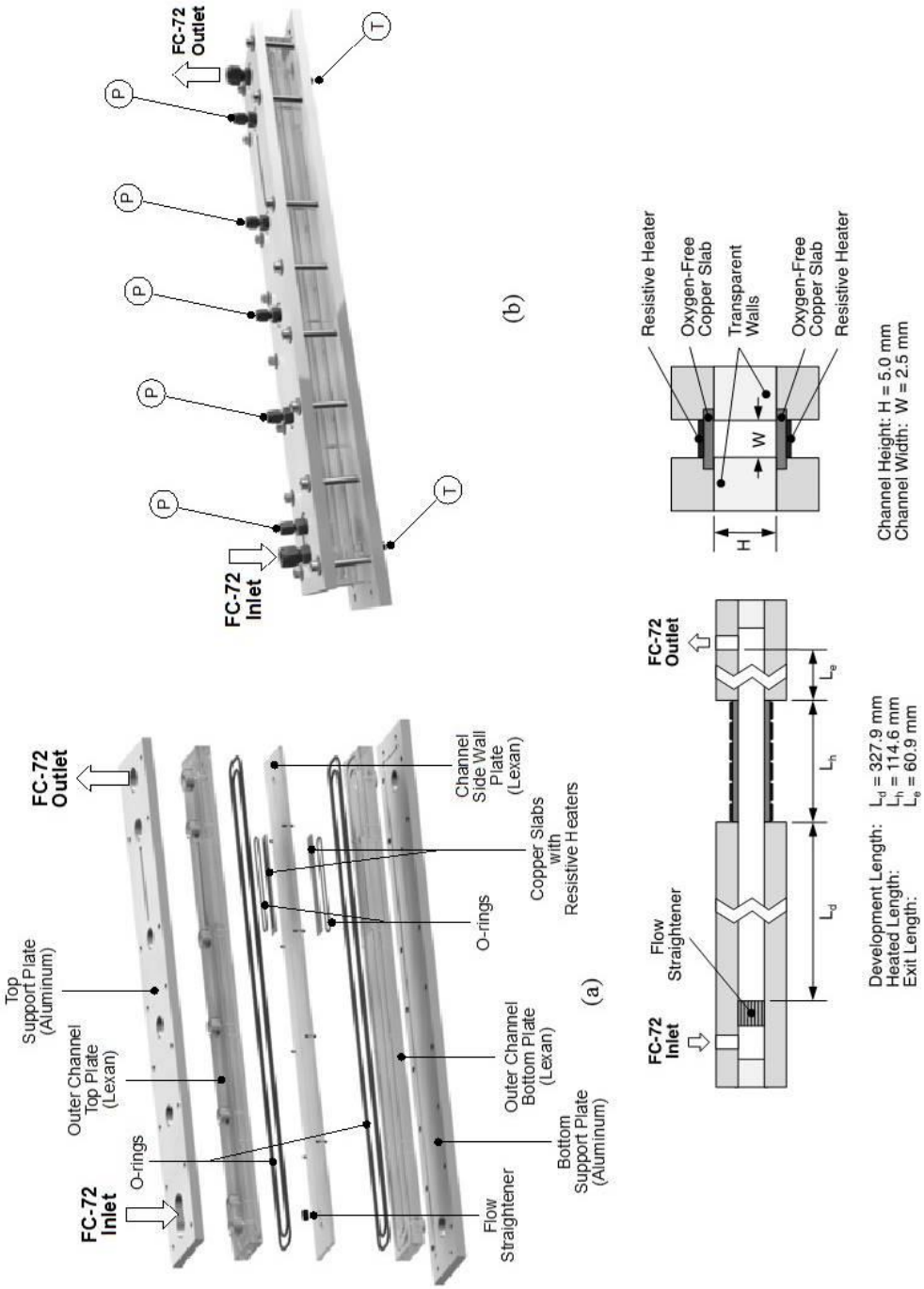

Figure 2.6: (a) Exploded view of Flow Boiling Module (FBM). (b) Assembled view of FBM. (c) Key dimensions of flow channel.

heating walls for the FBM. O-rings are inserted in grooves milled around the perimeter of the copper plates in both the outer top and bottom plastic plates. There are two additional o-rings between the channel sidewall plate and outer top and bottom plastic plates. These o-rings ensure a leak-proof assembly.

Figure 2.6(b) depicts an assembled view of the FBM. Static pressure is measured at various locations along the central axis of the flow channel using four pressure taps in the top plastic plate placed equidistantly between the FC-72 inlet port and immediately upstream of the copper heating slabs, with an additional pressure tap placed downstream of the copper slabs. Type-E thermocouples are inserted in the middle of the flow channel through the bottom plastic plate near the inlet and outlet FC-72 ports.

Shown in Figure 2.6(c) is a honeycomb flow straightener affixed upstream at the channel inlet to break any eddies and help straighten the flow. An entry development length 100 times the channel hydraulic diameter provides a hydrodynamically fully developed flow prior to reaching the copper heating slabs. Indicated in Figure 2.6(c) are key dimensions of the channel, including flow development length, L_d = 327.9 mm, heated length, L_h = 114.6 mm, and exit length, L_e = 60.9 mm, in addition to the height, H = 5.0 mm, and width, W = 2.5 mm of the channel's cross-section. Notice that the flow is heated along the shorter dimension, W, of the flow channel. The heated portion of the channel consists of the two copper slabs, placed opposite to one another, with the central transparent polycarbonate plate providing sidewalls for the rectangular flow area. The FBM is fixed securely to the facility's aluminum frame in a vertical position perpendicular to the floor of the aircraft.

2.2.3 Heated Wall Construction

As shown in Figure 2.7(a), each heated wall consists of six 4.5-mm wide and 16.14-mm long thick-film resistors. Soldered in series to the backside of the copper slab, each resistor has a resistance of about 188 Ω, and each set of seven resistors per copper slab is connected electrically in parallel. Power to the resistors is supplied from a variable voltage transformer. The FBM heater control box depicted in Figure 2.5(b) allows the user to supply heat to either or both heated walls at a time. As shown in

Figure 2.7(b), two sets of seven Type-E thermocouples are inserted into shallow holes along the centerline of each copper plate between the resistors. One set is used for temperature measurements, and the other to activate a relay that cuts off power supply once CHF is detected. The thermocouples temperatures are designated as $T_{wm,,n}$, where m represents the heated wall (*H1* or *H2*) and n the axial thermocouple location.

A key concern in the present experiments is to measure true CHF that is representative of practical engineering surfaces. As discussed by Zhang *et al.* [1], this measurement required a minimum heated wall thickness that is dependent on the heat diffusion properties of the wall material. As shown in Figure 2.7(c), CHF for FC-72 on a copper wall is both quite small and dependent on wall thickness for thicknesses below 0.4 mm. Above 0.4 mm is the asymptotic range, where CHF is both constant and independent of wall thickness. This is the desired range representative of practical surfaces. While any thickness larger than 0.4 mm is adequate, use of a very large thickness is also undesirable because this would preclude the ability of the heated wall temperatures to reach steady state during the μg_e phase of a parabola of 15-22 s. Therefore, a wall thickness of 1.04 mm is used. Figure 2.7(d) shows actual temporal records of wall temperatures measured in the inlet, middle, and downstream regions of the heated copper walls and corresponding gravity record for a mean FC-72 inlet velocity of U = 0.5 m/s and $\Delta T_{sub,in}$ = 3-7°C. These results indicate steady state conditions are achieved during the μg_e phase of the parabola.

2.2.4 Flow Visualization Techniques

A Sentech STC-CMB2MCL high-speed camera is used to capture the two-phase interfacial features along the heated portion of the flow channel. A fixed frame rate of 2,217 frames per second (fps) and a pixel resolution of 2040 x 156 are used to capture the entire heated length for each test run. Each video image sequence consists of 3000 frames, or 1.353 s of flow visualization data per test run. Illumination is provided from the backside of the flow channel by two Cree LEDs, with a light shaping diffuser (LSD) situated between the LEDs and the channel to enhance illumination uniformity.

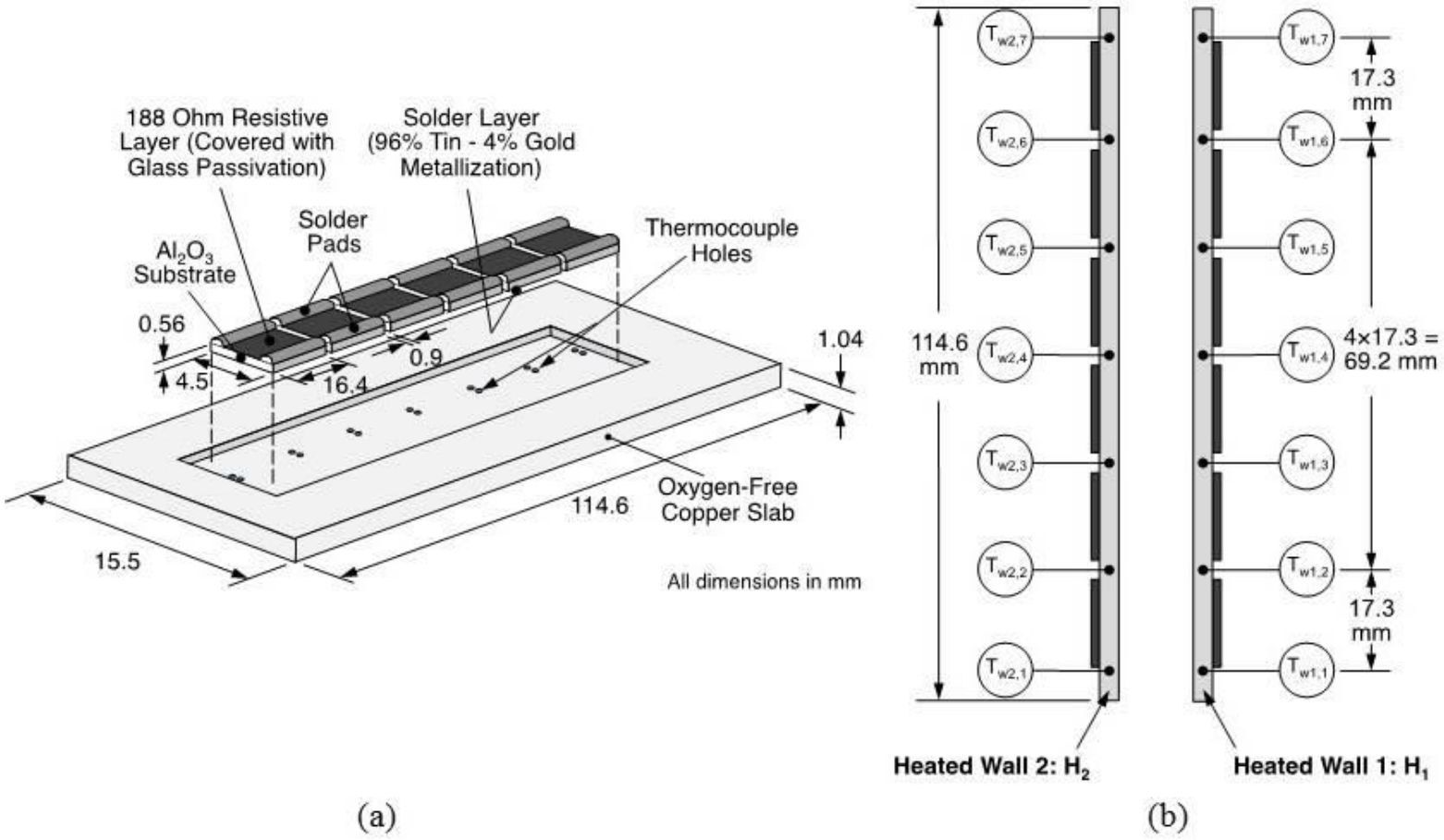

Figure 2.7: (a) Construction of heated wall and thick-film resistors. (b) Thermocouple layout in two heated walls.

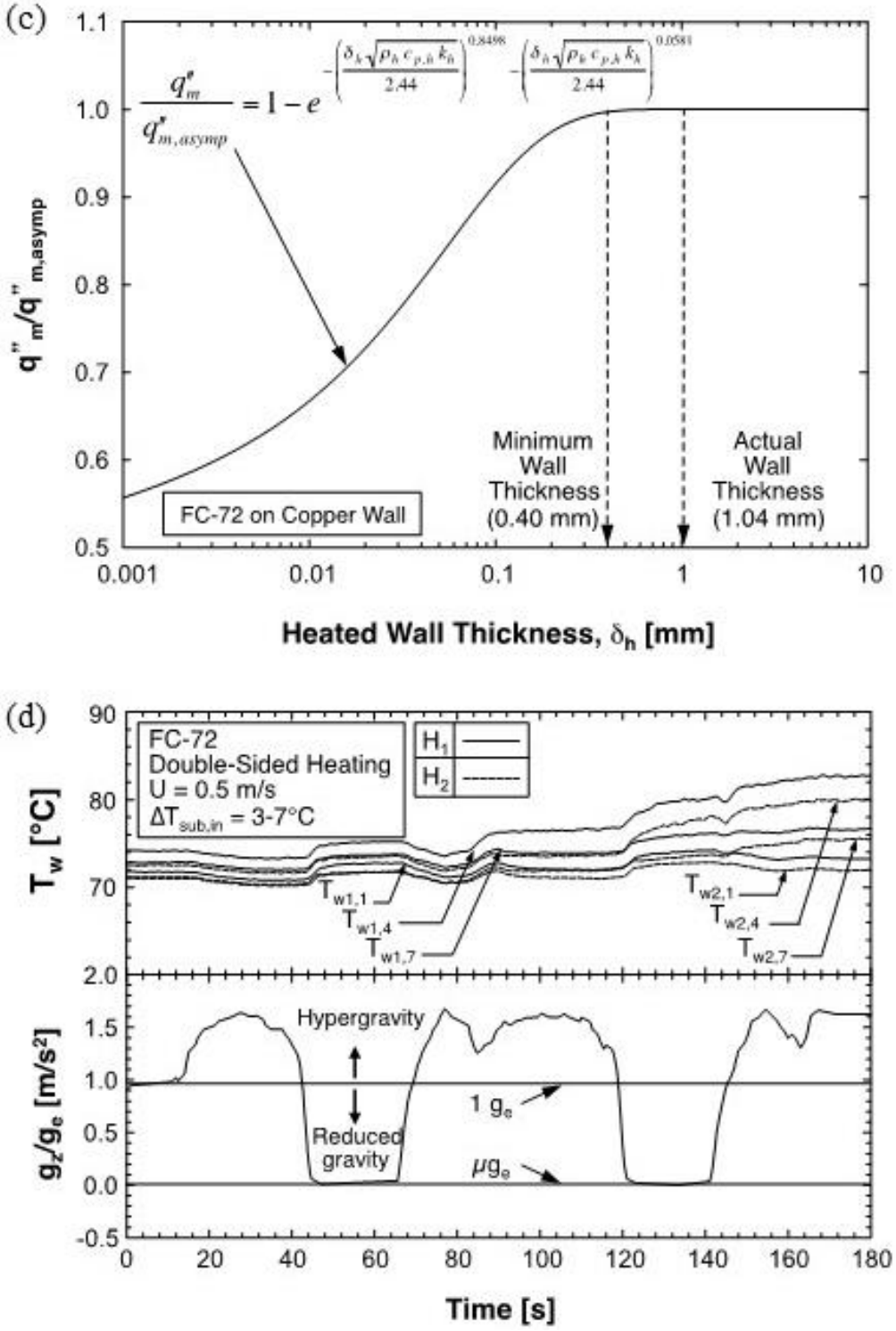

Figure 2.7: (c) Minimum heated wall thickness requirement [1]. (d) Temporal records of heated walls' thermocouples and gravity during series of parabolas.

It should be noted that the captured high-speed images suffer from two physical issues that cause distortion and defocus. The first is barrel distortion caused by the camera lens. As shown in Figure 2.8(a), the images are obtained starting at pixel element (0,0) and ending at pixel element (2040, 156) to produce images 2040 pixels horizontally by 256 pixels vertically. The apparent curvature seen in the images is an artifact of forming the image on the pixel elements near the edge of the field of view. The second noticeable issue is the defocus or 'fuzzy' sections near the top and bottom of a boiling image. As depicted in Figure 2.8(b), the copper heaters are recessed into the top and bottom polycarbonate plates so the bubbles seen near these extremes are being viewed through additional polycarbonate material that has been machined but not optically polished.

2.2.5 Operating Conditions and Measurement Accuracy

As indicated earlier, the flow boiling experiments were conducted in simulated reduced gravity conditions onboard Zero-G Corporation's modified Boeing 727 parabolic flight aircraft. Four flights were performed, with a series of 40 parabolic maneuvers executed during each flight. As shown in Figure 2.7(d), a single parabolic maneuver is initiated as the aircraft ascends in altitude, entering a hypergravity phase (1.5 g_e to 1.8 g_e). The μg_e phase is initiated as the aircraft reaches the zenith of the parabolic trajectory, lasting approximately 15-22 s, before entering another hypergravity phase during altitude descent.

The operating conditions for the study are as follows: FC-72 inlet mean liquid velocity of $U = G/\rho_f = 0.1 - 1.9$ m/s, liquid mass velocity of $G = 224.2 - 3347.5$ kg/m^{2}s, inlet temperature of $T_{in} = 56.5 - 64.7$°C, inlet subooling of $\Delta T_{sub,in} = 2.8 - 8.1$°C, and outlet pressure of $P_o = 118.2 - 148.3$ kPa (17.1 – 21.5 psi). The desired flow conditions are set by adjusting various components of the flow loop prior to a parabolic maneuver. Once inlet conditions to the FBM are achieved, power is supplied to the FBM's copper wall resistors before each parabola and held constant throughout the μg_e phase of the parabola. The high-speed camera is manually triggered to record approximately 10 s into the μg_e phase. Immediately after the μg_e duration, heat flux to the FBM heaters is

increased 1–5 W/cm^2, and this process is continued for each subsequent parabola until CHF is detected. A Labview program is developed in conjunction with a NI SCXI-1000 data acquisition system to record all instrument data throughout the flow boiling facility, and a special fail-safe feature is implemented into the program to automatically cut off power input to the resistive heaters should any of the measured temperatures exceed 150°C. This safety feature is intended to prevent any breakdown of the FC-72, which may lead to formation of the toxic compound perfluoroisobutene (PFiB).

Flow boiling tests were performed on three days of parabolic flight where both copper heated walls were activated in the FBM, and on one day where only one heated wall was activated. It should be noted that during two of the three days with both wall heated activated, unexpected technical problems with the flow boiling facility arose resulting in sporadic loss of wall temperature signals. Any of the data from tests where these anomalies occurred are excluded from data processing or presentation.

Fluid and wall temperatures throughout the flow boiling facility are measured with type-E thermocouples having an accuracy of ±0.5°C. STS absolute pressure transducers having an accuracy of ±0.05% are used to measure pressures at several locations along the FBM and the flow loop. The Flow Technology turbine flow meter has an accuracy of ±0.1%.

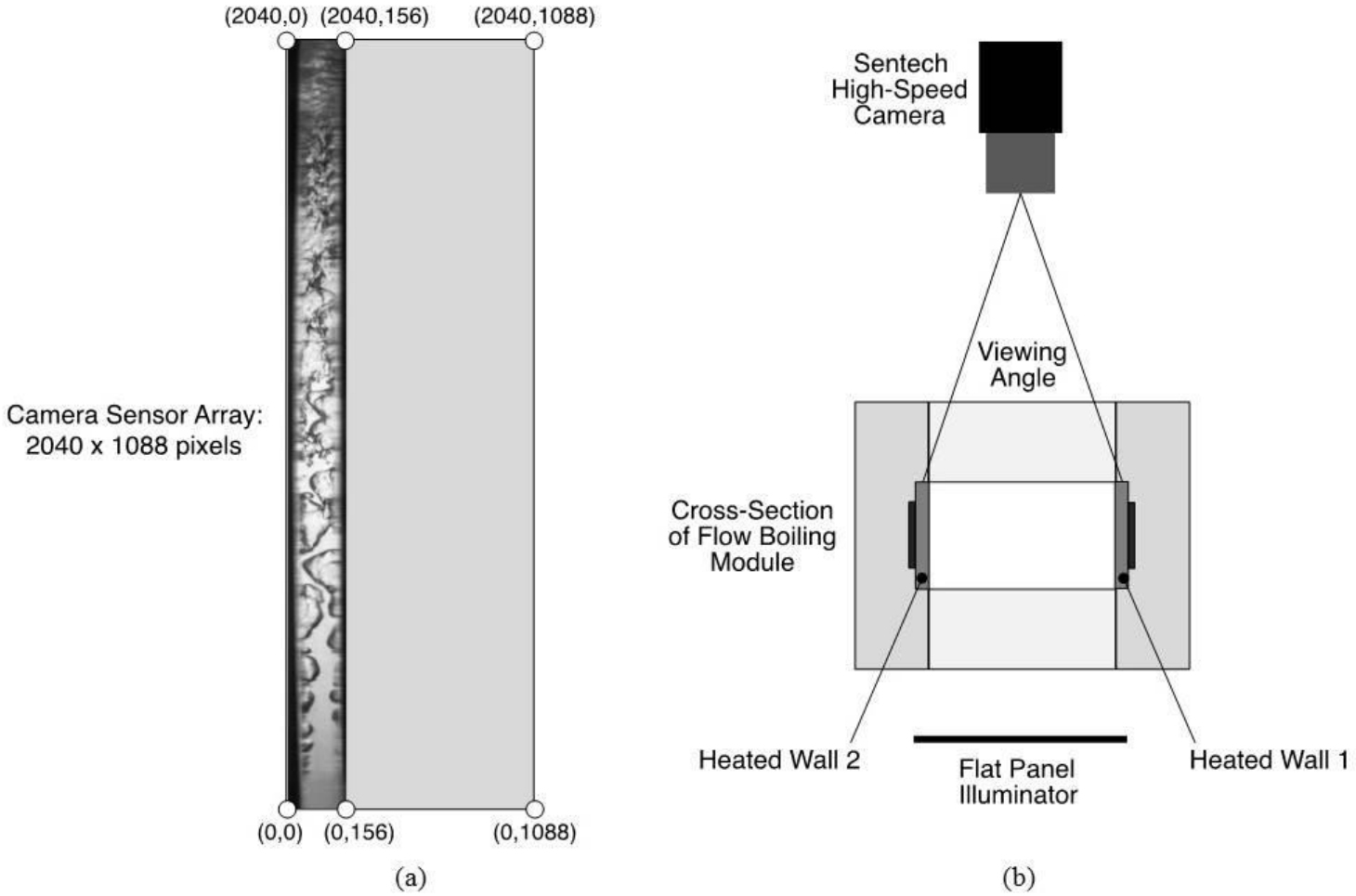

Figure 2.8: (a) Resolution of high-speed video camera image encompassing entire heated region of flow channel. (b) Viewing angle of camera and back lighting.

CHAPTER 3. TERRESTRIAL FLOW BOILING CHF WITH INLET VOID

3.1 Flow Visualization Results

Emphasis during the flow visualization experiments is placed on capturing interfacial behavior at conditions that precede CHF in order to identify the CHF trigger mechanism. These conditions are captured at about 95% CHF (termed CHF- hereafter) to avoid the risk of physical wall burnout.

Figure 3.1(a) shows a polar composite of photos captured in the outlet region of the heated portion of the channel at CHF- for $G/\rho_f = 0.224$ m/s and inlet quality of $x_{e,in} = 0.01$. There are similarities in CHF mechanism corresponding to certain ranges of orientation angles. The first range includes $\theta = 315°$, 0°, and 45°, orientations surrounding horizontal flow with upward-facing heated wall. Buoyancy causes clear separation between the phases at the channel inlet, with the vapor residing above the liquid, and this separation persists along the heated portion of the channel. At CHF-, there is appreciable vapor production within the liquid layer flowing along the heated wall. CHF appears to be triggered by the vapor beginning to separate the liquid layer from the wall. For $\theta = 90°$, corresponding to vertical upflow, the flow enters the flow separated, with liquid covering both the heated wall and opposite insulated wall, as well as the front and back walls, surrounding a central vapor core. This pattern persists along the heated portion of the channel, but with the liquid layer along the heated wall undergoing appreciable vapor production. Here too, CHF occurs when the vapor production causes separation of the liquid layer adjacent to the heated wall. For $\theta = 135°$, 180° and 225°, orientations surrounding horizontal flow with downward-facing heated wall, there is clear stratification of vapor above liquid, which starts at the channel inlet and persists along the heated portion of the channel. With the vapor layer covering the heated wall, CHF for these orientations is quite small, especially for $\theta = 225°$, which

culminates in a vanishingly small CHF value of only 1.85 W/cm^2. For θ = 270°, corresponding to vertical downflow, like vertical upflow, the flow enters the flow with liquid covering the heated wall, opposite insulated wall, and front and back walls, surrounding a central vapor core. This pattern also persists along the heated portion of the channel, and CHF occurs when vapor production begins to separate the liquid layer adjacent to the heated wall. Despite seemingly identical flow patterns, there is a fundamental difference between the flows for θ = 90° and θ = 270° because of the buoyancy serving to assist vapor removal along the channel for the former and resist the vapor removal for the latter. This difference is responsible for the θ = 270° orientation producing lower CHF, 10.3 W/cm^2, compared to that for θ = 90°, 13.7 W/cm^2.

Interfacial flow behavior for θ = 270° is especially complex for flow boiling systems. In a previous study by Zhang *et al.* [4] involving CHF with the coolant entering the channel in pure liquid state, three possible CHF regimes were observed at θ = 270° at low flow velocities. At 0.1 m/s, strong buoyancy effects overcame any drag or shear forces exerted by the liquid, causing the vapor to flow backwards (*i.e.,* vertically upwards) along the channel. As the flow velocity was increased, a balance was achieved between the buoyancy and liquid forces, causing the vapor to stagnate along the channel. Increasing the liquid velocity further caused the liquid drag and shear forces to exceed buoyancy, and the vapor to flow concurrently with the liquid. Interestingly, only the third concurrent vapor flow regime is observed in the present study, apparently because of the increasing magnitude of effective liquid velocity and therefore the liquid drag and shear forces when the fluid is supplied to the channel as a two-phase mixture rather than pure liquid.

Figure 3.1(b) shows a polar composite of photos captured in the outlet region of the heated portion of the channel at CHF- for a higher mass velocity with G/ρ_f = 0.398 m/s and inlet quality of $x_{e,in}$ = 0.01. There appears to be appreciable diminution of the influence of buoyancy for all orientations. Here, interfacial behavior appears to be virtually identical for all orientations and similar to that for θ = 90° for the lower mass velocity in Figure 3.1(a).

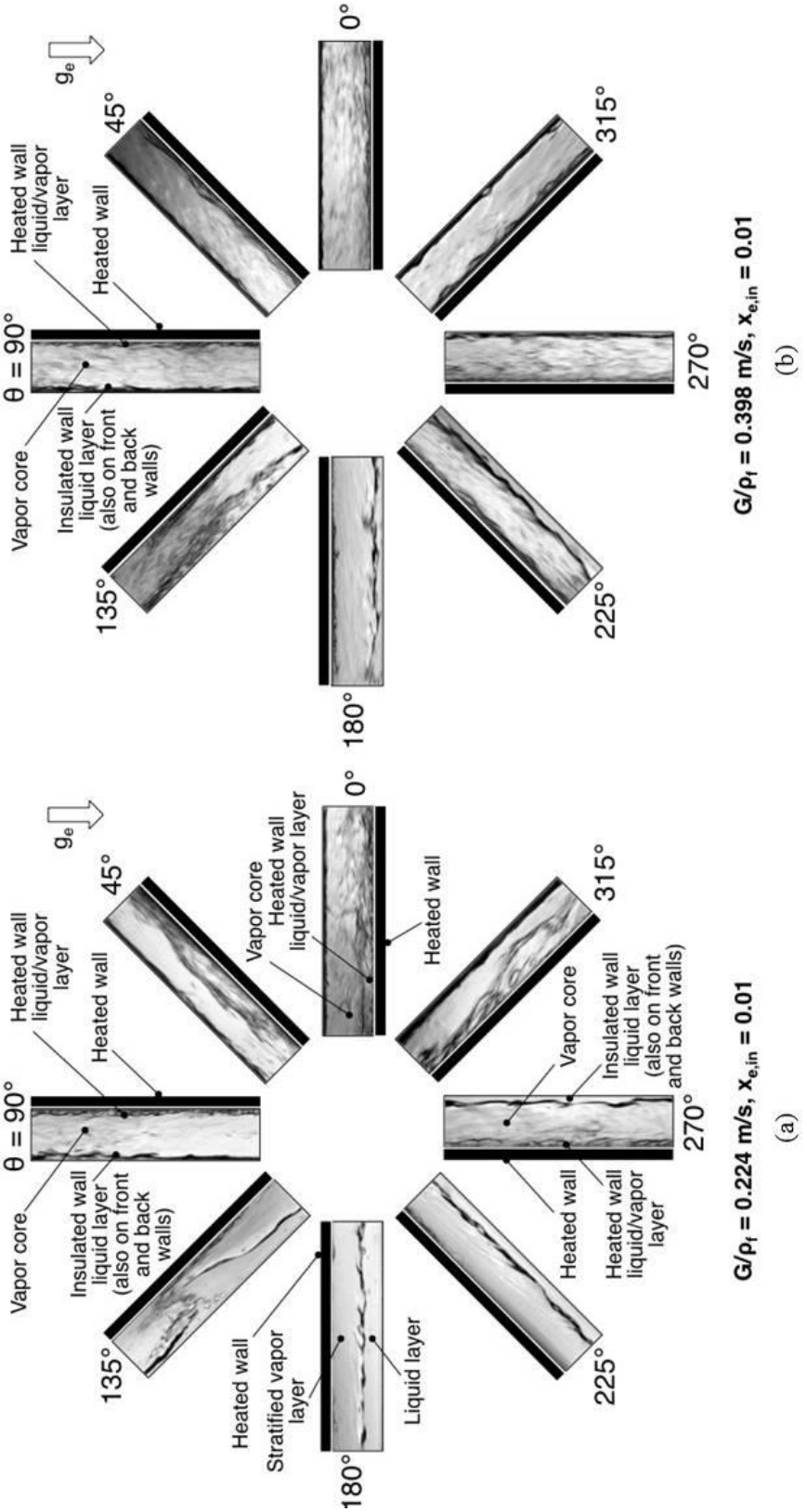

Figure 3.1: Photos of interfacial behavior captured in the outlet region of the heated portion of the channel at CHF- for different flow orientation for (a) G/ρ_f = 0.224 m/s and $x_{e,in}$ = 0.01, and (b) G/ρ_f = 0.398 m/s and $x_{e,in}$ = 0.01.

Figures 3.2(a) and 3.2(b) show schematic diagrams representing interfacial behavior observed at CHF- for G/ρ_f = 0.224 and 0.398 m/s, respectively, at $x_{e,in}$ = 0.01. To simplify the schematic representations, only orientations corresponding to 90° orientation increments are shown. Cross-sectional depictions are provided for the flow both upstream and downstream of the heated portion of the channel.

For G/ρ_f = 0.224 m/s, Figure 3.2(a), and θ = 0°, the flow enters the channel stratified, with the vapor flowing above the liquid. At CHF-, intense vapor effusion at the heated wall begins to separate the liquid layer, ultimately causing unsteady rise in the wall temperature. At θ = 90°, the flow enters the channel with a thin liquid layer sheathing all four walls of the channel, surrounding a central vapor core. At CHF-, vapor effusion along the heated wall begins to separate the wall layer adjacent to the heated wall. Notice that, unlike the flow at θ = 0°, a thin liquid film continues to sheath the three insulated walls of the channel even at CHF-. At θ = 180°, the flow enters the channel stratified but unlike θ = 0°, the vapor is now adjacent to the heated wall. The heated wall receives minor cooling from remnants of liquid that are broken off the liquid layer and able to reach the top heated wall, but CHF is fairly small because of the limited access of liquid to the heated wall. For θ = 270°, the flow enters the channel separated, with a wall liquid layer surrounding a central vapor core. At CHF-, the momentum of vapor perpendicular to the heated wall causes separation of the liquid layer adjacent to the heated wall. Overall, the interfacial behavior at θ = 270° appears similar to that at θ = 90°, however, as will be discussed later, these orientations produce different CHF values because of the liquid shear and drag forces exerted in the same direction as buoyancy at θ = 90° but opposite to buoyancy at θ = 270°.

Figure 3.2(b) shows schematics for CHF- at G/ρ_f = 0.398 m/s and $x_{e,in}$ = 0.01. Notice here that the interfacial behavior is similar for all orientations and reminiscent of that observed at θ = 90° for G/ρ_f = 0.224 m/s. This points to the effectiveness of high flow velocities at overcoming the influence of orientation. The similarity in interfacial behavior for different orientations at G/ρ_f = 0.398 m/s is indicative of (a) similarity in CHF mechanism and (b) diminution of the influence of orientation, but does not

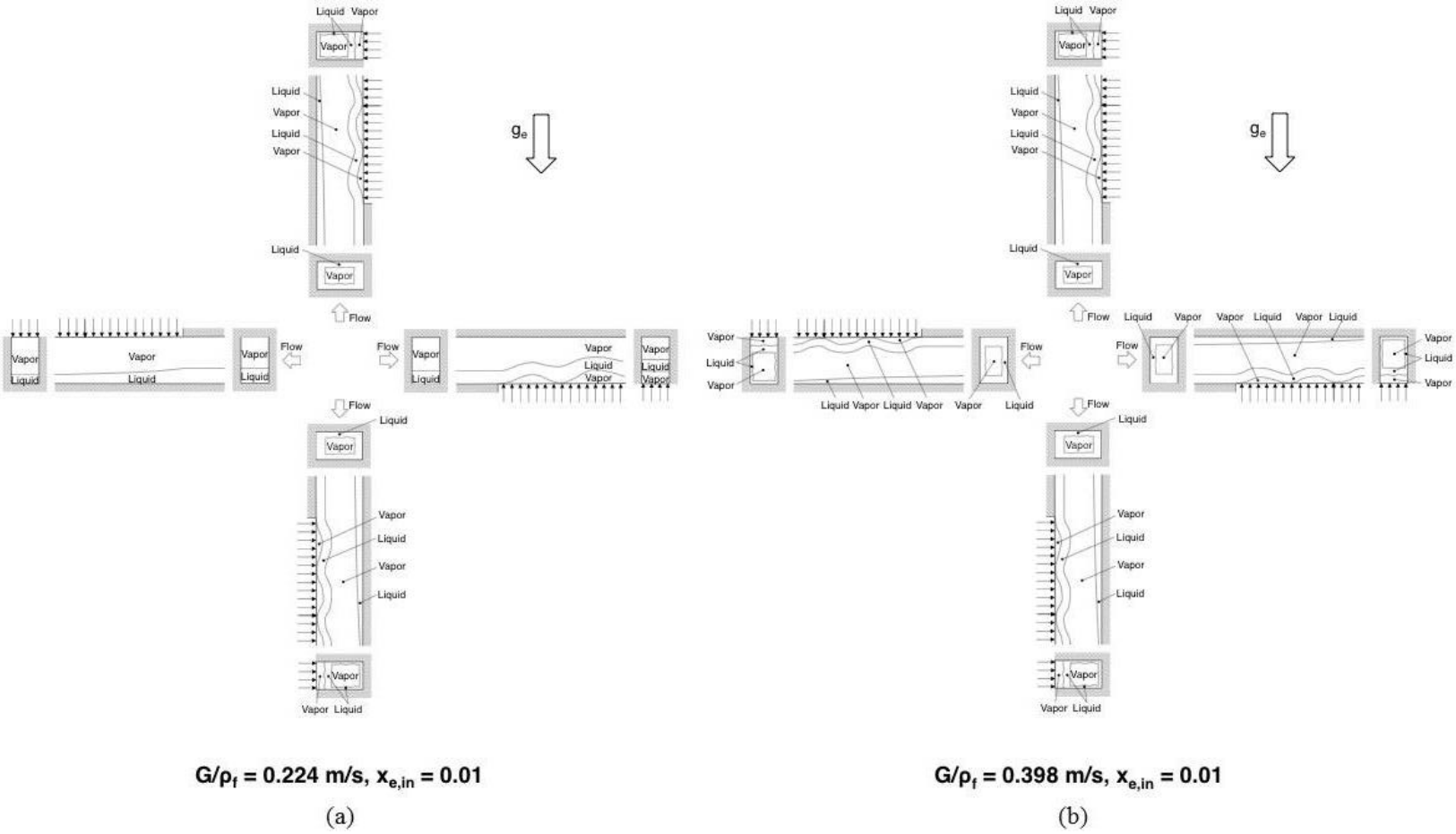

Figure 3.2: Schematic representation of interfacial behavior at CHF- for different flow orientations for (a) $G/\rho_f = 0.224$ m/s and $x_{e,in} = 0.01$, and (b) $G/\rho_f = 0.398$ m/s and $x_{e,in} = 0.01$.

necessarily translate to equal CHF values for this mass velocity. This important issue of CHF magnitude will be discussed later.

As will be discussed later, the inlet region plays a crucial role in CHF development. Figure 3.3 depicts video images of the inlet region for different orientations at $x_{e,in}$ = 0.01 and zero wall heat flux, 50% CHF and 95% CHF for G/ρ_f = 0.224 and 0.398 m/s. For the upward facing heated wall orientations, θ = 315, 0, and 45°, and zero heat flux, a vapor layer is shown residing above a liquid layer due to buoyancy. At 50% CHF, bubbles are shown nucleating and coalescing together within the liquid layer adjacent to the heated wall. Buoyancy appears to drive the coalescent bubbles to the liquid-vapor interface, where they are released into the vapor layer above. For the same orientations, there are visible differences between interfacial conditions at G/ρ_f = 0.224 m/s versus 0.398 m/s. The higher shear stresses associated with the higher velocity appear to thin the heated wall liquid layer and cause axial stretching of the coalescent vapor layers. This behavior is indication of the aforementioned diminution of the influences of buoyancy and orientation in general on interfacial behavior. At 95% CHF, there is a clear separation of the liquid layer from the heated wall and formation of a vapor layer between the liquid and the heated wall. For the vertical upflow orientation, θ = 90°, zero heating results in a flow pattern consisting of a liquid layer sheathing both the heated wall and opposite insulating wall, surrounding a central vapor core, with the interface of the liquid layer marred by roll waves, especially for G/ρ_f = 0.224 m/s. At 50% CHF, bubbles are shown forming in the liquid layer adjacent to the heated wall, coalescing together, and bursting into the vapor core. For the downward heated wall orientations, θ = 135°, 180°, and 225°, with zero heat flux, a vapor layer is shown stratified by buoyancy against the heated wall above a liquid layer, with the interface in between marred by roll waves. Despite this stratification, remnants of liquid deposited from the wavy interface onto the heated wall appear to form thin patches of liquid along the heated wall. At 50% CHF, bubbles form along the heated wall within the liquid patches, which appear to serve as the sole, albeit weak source for wall cooling. At 95% CHF, there is appreciable loss of liquid at the heated wall because of the loss of liquid patches by evaporation. As discussed later, these orientations are associated with

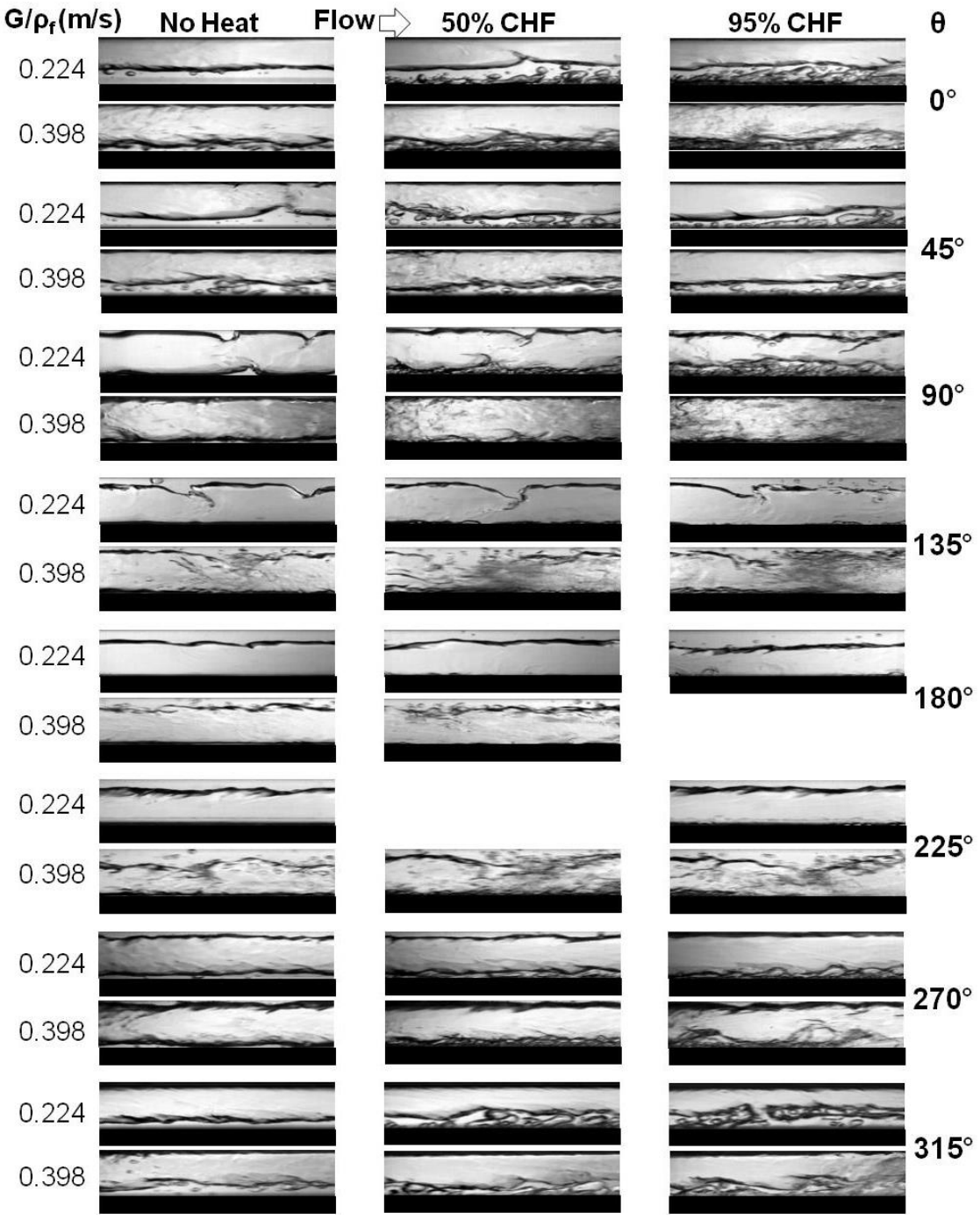

Figure 3.3: Video images of flow boiling in inlet region for different orientations at $x_{e,in}$ = 0.01 and zero wall heat flux, 50% CHF and 95% CHF at G/ρ_f = 0.224 and 0.398 m/s. Missing images correspond to conditions for which video images are not available. The heated wall is indicated by a rectangular black strip.

unusually low CHF values, especially for G/ρ_f = 0.224 m/s. For the vertical downflow orientation, θ = 270°, the flow appears to resemble that for vertical upflow, θ = 90°. However, given that the direction of buoyancy is opposite to that of liquid shear and drag forces for θ = 270°, CHF values for θ = 270° are smaller than for θ = 90° as will be discussed next.

3.2 CHF Results

Figure 3.4(a) shows a polar plot of CHF data measured at all orientations for velocities ranging from G/ρ_f = 0.126 to 1.130 m/s and an inlet quality of $x_{e,in}$ = 0.01. Notice how the influence of orientation is very pronounced for the two lowest velocities of G/ρ_f = 0.126 and 0.224 m/s, especially at θ = 225°, where CHF values are vanishingly small. The middle velocity of G/ρ_f = 0.398 m/s marks the onset of diminution of orientation effects. The influence of orientation decreases further for the two higher velocities of G/ρ_f = 0.712 and 1.130 m/s, despite a persistent residual influence, with orientations involving a combination of upflow and/or upward-facing heated wall (θ = 0°, 45° and 90°) producing higher CHF than downflow and/or downward-facing heated wall (θ = 180°, 225° and 270°).

Figure 3.4(b) shows a polar plot of CHF data for velocities ranging from G/ρ_f = 0.126 to 0.712 m/s at a much greater inlet quality of $x_{e,in}$ = 0.19. Like Figure 3.4(a), the influence of orientation for the lowest velocity of G/ρ_f = 0.126 m/s is very pronounced, yielding a vanishingly small CHF value for θ = 225°. But unlike Figure 3.4(a), the effect of orientation is noticeably weakened for G/ρ_f = 0.224 m/s at $x_{e,in}$ = 0.19 compared to $x_{e,in}$ = 0.01. The influence of orientation decreases further for the two higher velocities of G/ρ_f = 0.398 and 0.712, despite the afore-mentioned residual influence of orientation. Comparing Figs. 3.4(a) and 3.4(b) shows that, for equal G/ρ_f, increasing inlet quality reduces the sensitivity of CHF to orientation, which can be explained by the higher velocities of individual layers of the flow at higher $x_{e,in}$ greatly increasing the magnitude of shear and drag forces compared to buoyancy.

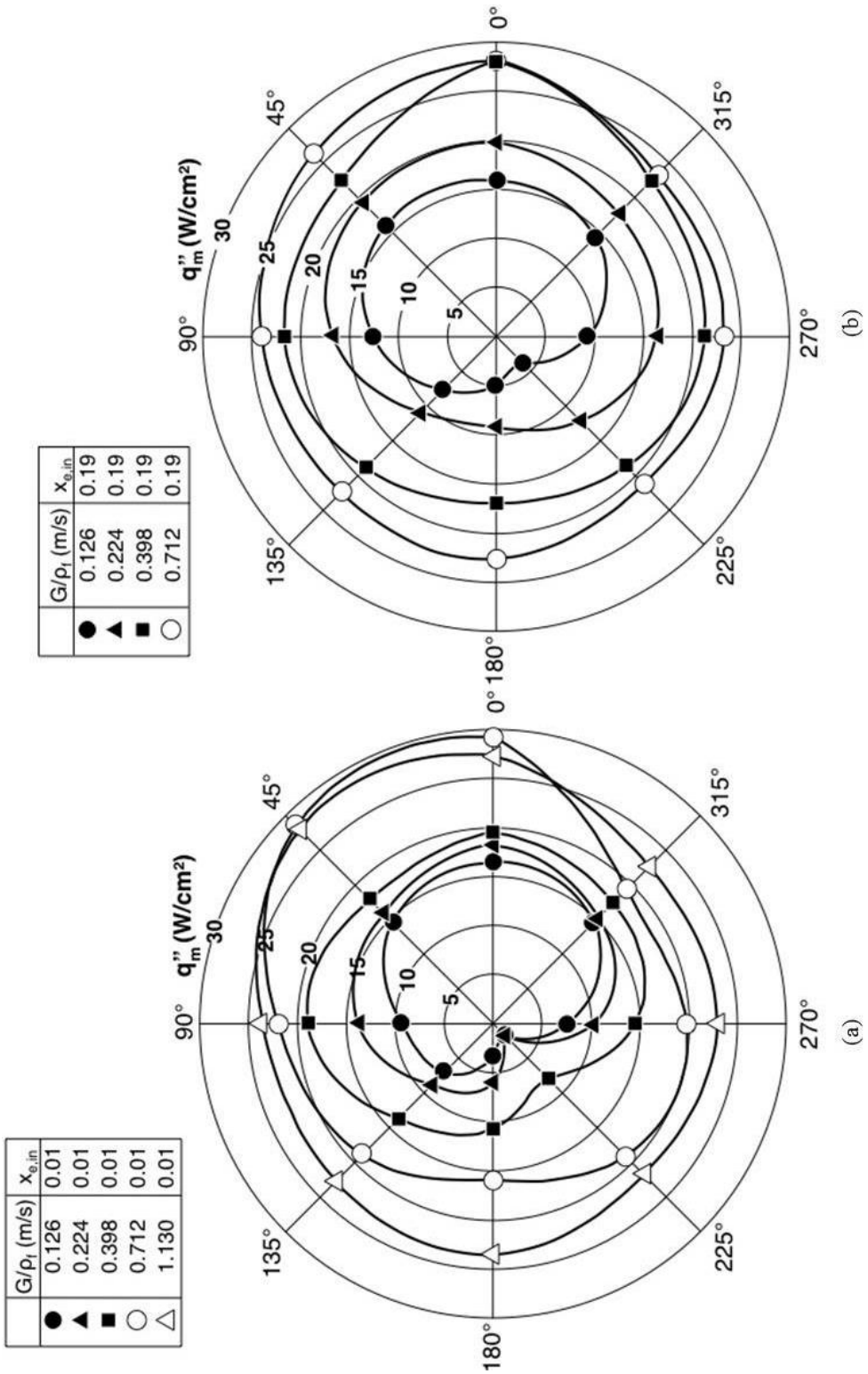

Figure 3.4: Variation of CHF with orientation for different mass velocities at (a) $x_{e,in} = 0.01$ and (b) $x_{e,in} = 0.19$.

3.3 CHF Prediction Method

3.3.1 Determination of Liquid and Vapor Liquid Layer Velocities and Thicknesses

As discussed earlier, CHF occurrence is a strong function of the relative magnitude of forces influencing the motion of individual liquid and vapor layers both along the channel and perpendicular to the heated wall. Determining the magnitude of these forces requires the determination of velocities and thicknesses of the individual layers. In this study, these parameters are determined using the control volume method, which consists of applying mass, momentum and energy conservation laws to control volumes encompassing the liquid and vapor phases separately as well as the combined flow. The control volume method proved highly effective in predicting two-phase behavior for separated flows in several past studies [1,4,5,14-17,26,48,49,51,53].

The video images described earlier show different flow patterns prevailing at CHF- for different velocities, inlet qualities and orientations. Because of the long-term focus of this study of determining CHF for flow boiling in microgravity, as well as determining minimum flow conditions that would cause appreciable diminution of the influence of gravity, the present control volume analysis is based on the flow pattern depicted in Figure 3.2(b), which is encountered at higher velocities irrespective of orientation.

The separated flow pattern observed at CHF- at relatively high velocities and depicted in Figure 3.2(b) consists of a flow entering the channel with a liquid film sheathing all four channel walls surrounding a central vapor core. Along the heated wall, the liquid layer begins to separate from the wall as a vapor layer begins to form underneath. Figure 8 shows a more detailed rendering of the same flow pattern, and identifies the individual layers of the separated flow along the heated wall: liquid layer 1 along the three adiabatic walls of the channel, central vapor layer 2, liquid layer 3 adjacent to, but separated from the heated wall, and vapor layer 4 at the heated wall beneath liquid layer 3. Unlike similar recent formulations by Kharangate *et al.* [26,51], the present separated flow model accounts for the varying influence of gravity for the different orientations.

The separated flow model is applied first to the adiabatic region upstream of the heated wall, and afterwards to the heated portion of the channel. For the adiabatic region, momentum conservation for the vapor and liquid portions of the channel yields

$$G^2 \frac{d}{dz}\left[\frac{x_{e,in}^2}{\rho_g \alpha_{in}}\right] = -\alpha_{in}\frac{dp}{dz} \mp \frac{\tau_i P_i}{A} - \rho_g \alpha_{in} g_e \sin\theta \tag{3.1}$$

and

$$G^2 \frac{d}{dz}\left[\frac{(1-x_{e,in})^2}{\rho_f (1-\alpha_{in})}\right] = -(1-\alpha_{in})\frac{dp}{dz} - \frac{\tau_{w,f} P_{w,f}}{A} \pm \frac{\tau_i P_i}{A} - \rho_f (1-\alpha_{in}) g_e \sin\theta, \tag{3.2}$$

respectively, where $x_{e,in}$ is the inlet velocity obtained from Eq. (2.1), α_{in} the inlet void fraction, $\tau_{w,f}$ the wall shear stress for the liquid layer, τ_i the interfacial shear stress, $P_{w,f}$ the channel perimeter, and P_i are the perimeter of liquid-vapor interface. The ± sign of the interfacial shear terms allows for any variations in the direction of the shear stress, depending on local velocity differences between the two layers.

Neglecting any property variations, mass and energy conservation result in $x_e = x_{e,in}$ for the adiabatic region. Equations (3.1) and (3.2) are solved simultaneously using an iterative procedure to determine α_{in}. Equations for the wall and interfacial shear stresses are similar to those utilized in the analysis of the heated section, which are discussed below. These stresses are functions of flow velocities, which are themselves functions of the void fraction.

Using Figure 3.5 as a guide, the inlet mass flow fraction of liquid layer 1 along the insulated walls can be expressed in terms of the channel dimensions as

$$x_{f1,in} = \frac{W+2H}{2W+2H}(1-x_{e,in}). \tag{3.3}$$

Similarly, the inlet mass flow fraction of liquid layer 3 can be expressed as

$$x_{f3,in} = \frac{W}{2W+2H}(1-x_{e,in}). \tag{3.4}$$

Because of the prevailing saturated conditions, heat transfer between the vapor core and the liquid layers is assumed negligible, which implies the flow quality of the vapor core is conserved ($x_2 = x_{e,in}$).

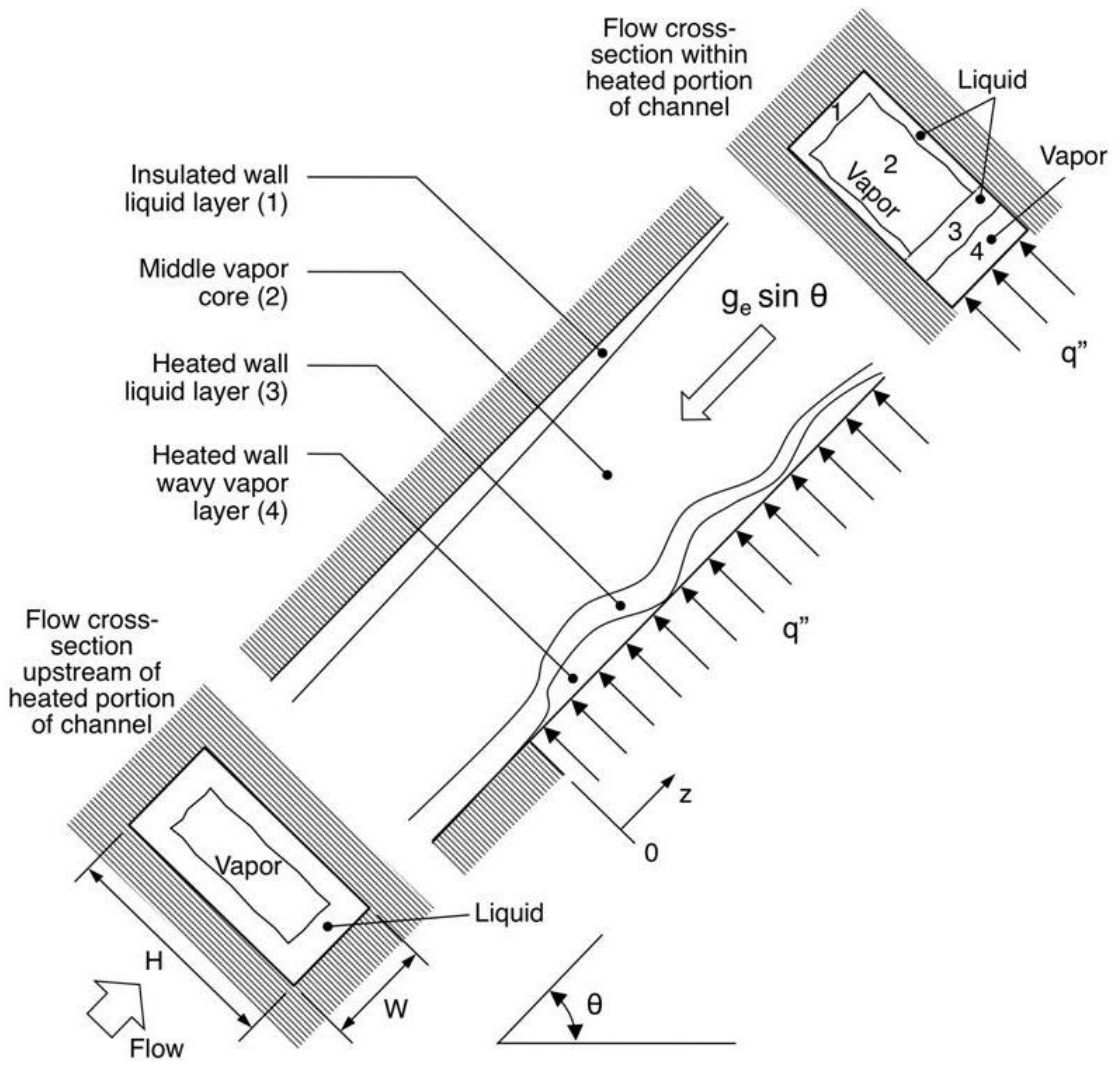

Figure 3.5: Schematic of different separated layers at CHF- for high mass velocities.

Similar relations are derived for the inlet area fraction of the liquid layer along the adiabatic walls (layer 1) and adjacent to heated wall (layer 3), respectively,

$$\varepsilon_{f1,in} = \frac{W+2H}{2W+2H}\left(1-\alpha_{in}\right), \tag{3.5}$$

and

$$\varepsilon_{f3,in} = \frac{W}{2W+2H}\left(1-\alpha_{in}\right). \tag{3.6}$$

Applying conservation of mass for the entire heated section results in $d\dot{m}/dz$, which implies both $\dot{m}$ and G are constant. Because of the prevailing saturated conditions, the temperature gradients between the four fluid layers are neglected. This implies the mass flow rates of the insulated wall liquid layer ($x_{f1}\dot{m}$) and central vapor core ($x_2\dot{m}$) are both constant, which also implies that both x_{f1} and x_2 are constant. The growth of the vapor layer (4) in contact with the heated wall is the result of evaporation of the heated wall liquid layer (3), which implies $x_{f3} = x_{f3,in} - x_4$. Mass conservation yields the following relation for liquid evaporation rate along the interface between layers 3 and 4.

$$\dot{m}'_{fg} = GA\frac{dx_4}{dz}. \tag{3.7}$$

The next step in the implementation of the model is to apply momentum conservation to the insulated wall liquid layer (1), central vapor layer (2), heated wall liquid layer (3), and heated wall vapor layer (4), which yields, respectively,

$$G^2\frac{d}{dz}\left[\frac{x_{f1}^2}{\rho_f\varepsilon_{f1}}\right] = -\varepsilon_{f1}\frac{dp}{dz} - \frac{\tau_{w,f1}P_{w,f1}}{A} \pm \frac{\tau_{i12}P_{i12}}{A} \mp \frac{\tau_{i13}P_{i13}}{A} - \rho_f\varepsilon_{f1}g_e\sin\theta, \tag{3.8}$$

$$G^2\frac{d}{dz}\left[\frac{x_2^2}{\rho_g\alpha_2}\right] = -\alpha_2\frac{dp}{dz} \mp \frac{\tau_{i12}p_{i12}}{A} \pm \frac{\tau_{i23}p_{i23}}{A} - \rho_g\alpha_2 g_e\sin\theta, \tag{3.9}$$

$$G^2\frac{d}{dz}\left[\frac{x_{f3}^2}{\rho_f\left(1-\varepsilon_{f1}-\alpha_2-\alpha_4\right)}\right]+\dot{m}_{fg}^{'}u_{i34}$$
$$=-\left(1-\varepsilon_{f1}-\alpha_2-\alpha_4\right)\frac{dp}{dz}-\frac{\tau_{w,f3}P_{w,f3}}{A}\pm\frac{\tau_{i13}P_{i13}}{A}\mp\frac{\tau_{i23}P_{i23}}{A} \quad (3.10)$$
$$\pm\frac{\tau_{i34}P_{i34}}{A}-\rho_f\left(1-\varepsilon_{f1}-\alpha_2-\alpha_4\right)g_e\sin\theta,$$

and
$$G^2\frac{d}{dz}\left[\frac{x_4^2}{\rho_g\alpha_4}\right]-\dot{m}_{fg}^{'}u_{i34}=-\alpha_4\frac{dp}{dz}-\frac{\tau_{w,g4}P_{w,g4}}{A}\mp\frac{\tau_{i34}P_{i34}}{A} \quad (3.11)$$
$$-\rho_g\alpha_4 g_e\sin\theta$$

Table 3.1 provides relations for x_{f1}, x_2, x_{f3} and x_4 that are used in the above equations. In Eqs. (3.8)-(3.11), $\tau_{w,f1}$, $\tau_{w,f3}$, $\tau_{w,g4}$ are, respectively, the wall shear stresses for the insulated wall liquid layer, heated wall liquid layer, and heated wall vapor layer, and τ_{i12}, τ_{i13}, τ_{i23}, and τ_{i34} are the interfacial shear stresses between the insulated wall liquid layer and vapor core, insulated wall liquid layer and heated wall liquid layer, vapor core and heated wall liquid layer, and heated wall liquid layer and heated wall vapor layer, respectively, $P_{w,f1}$, $P_{w,g2}$, $P_{w,f3}$, and $P_{w,g4}$ are the wall perimeters of the insulated wall liquid layer, vapor core, heated wall liquid layer, and heated wall vapor layer, respectively, P_{i12}, P_{i13}, P_{i23}, and P_{i34} are the interfacial perimeters between the insulated wall liquid layer and vapor core, insulated wall liquid layer and heated wall liquid layer, vapor core and heated wall liquid layer, and heated wall liquid layer and heated wall vapor layer, respectively.

The vapor generated at the heated wall is assumed to have no initial stream-wise velocity [26], therefore contributing no stream-wise momentum to the adjacent heated liquid layer. Relations for the wall shear stress for each phase are provided in Table 3.1. Also included in Table 3.1 are relations for all the interfacial shear stresses.

Applying energy conservation to a control volume encompassing the entire cross-sectional area of the channel yields

$$\frac{dx}{dz}=\frac{dx_4}{dz}=\frac{q''W}{\dot{m}h_{fg}}. \quad (3.12)$$

Table 3.1: Summary of relations used in conjunction with the control-volume model.

Quality relations for individual layers:

$$x_{f1} = \frac{\rho_f U_{f1} \varepsilon_{f1}}{G},\ x_2 = \frac{\rho_g U_{g2} \alpha_2}{G} = x_{e,in},\ x_{f3} = \frac{\rho_f U_{f3}\left(1-\varepsilon_{f1}-\alpha_2-\alpha_4\right)}{G},\ x_4 = \frac{\rho_g U_{g4} \alpha_4}{G}$$

Wall shear stress relations:

$$\tau_{w,k,j} = \frac{1}{2}\rho_k U_{k,j}^2 f_{k,j}$$

$$f_{k,j} = C_1 + \frac{C_2}{\mathrm{Re}_{D,k,j}^{1/C_3}} = C_1 + \frac{C_2}{\left(\frac{\rho_k U_{k,j} D_{k,j}}{\mu_k}\right)^{1/C_3}}$$

where $k = f$ or g, and j = 1-4. $C_1 = 0$, $C_2 = 16$ and $C_3 = 1$ for laminar flow ($\mathrm{Re}_{D,k,j} \leq 2100$), $C_1 = 0.0054$, $C_2 = 2.3 \times 10^{-8}$ and $C_3 = -2/3$ for transitional flow ($2100 < \mathrm{Re}_{D,k,j} \leq 4000$), and $C_1 = 0.00128$, $C_2 = 0.1143$ and $C_3 = 3.2154$ for turbulent flow ($\mathrm{Re}_{D,k,j} > 4000$) [54], where $D_{k,j} = 4A_{k,j}/P_{k,j}$

Interfacial shear stress relations:

$$\tau_{i12} = \frac{C_{f,i}}{2}\rho_g\left(U_{f1}-U_{g2}\right)^2,\ \tau_{i23} = \frac{C_{f,i}}{2}\rho_g\left(U_{g2}-U_{f3}\right)^2,\ \tau_{i34} = \frac{C_{f,i}}{2}\rho_g\left(U_{f3}-U_{g4}\right)^2,\ \tau_{i13} = \frac{C_{f,i}}{2}\rho_g\left(U_{f1}-U_{f3}\right)^2$$

where $C_{f,i} = 0.5$ [15]

3.3.2 Hydrodynamic Instability of Liquid-Vapor Interface along the Heated Wall

As depicted in Figure 3.2(b), CHF for high velocities is preceded by the formation of a wavy vapor layer beneath the heated wall liquid layer. Velocity differences between the two layers result in instability of the interface in-between. Therefore conditions at CHF- can be described by classical instability theory [42,55,56]. As shown in Figure 3.6, deformation of the liquid-vapor interface is assumed to follow the sinusoidal wave form

$$\eta(z,t) = \eta_o e^{ik(z-ct)}. \tag{3.13}$$

where η_o represents the wave amplitude ($\eta_o = \delta$), k the wave number ($k = 2\pi/\lambda$), and c the wave speed. The real part of Eq. (3.13) represents the actual liquid-vapor interface while the imaginary part is used to establish a criterion for interfacial instability. Any perturbation normal to the interface produces a pressure difference across the interface that can be expressed as

$$p_{f3} - p_{g4} = -\left\lfloor \rho_{f3}^{"}\left(c - U_{f3}\right)^2 + \rho_{g4}^{"}\left(c - U_{g4}\right)^2 + \left(\rho_f - \rho_g\right)\frac{g_n}{k} \right\rfloor k\,\eta_o e^{ik(z-ct)}, \tag{3.14}$$

where $\rho_{f3}^{"} = \rho_f \coth\left(k H_{f3}\right)$ and $\rho_{g4}^{"} = \rho_g \coth\left(k H_{g4}\right)$, which are 'modified density' terms, and g_n is the component of gravity acting normal to the heated wall. The mean liquid and vapor thicknesses, H_{f3} and H_{g4}, found in the modified density terms are obtained from the control volume model and are given, respectively, by

$$H_{f3} = \left(1 - \varepsilon_{f1} - \alpha_2 - \alpha_4\right)H \tag{3.15}$$

and

$$H_{g4} = \alpha_4 H. \tag{3.16}$$

The pressure difference across the interface is balanced by the surface tension force,

$$p_f - p_g \approx \sigma \frac{\partial^2 \eta}{\partial z^2} = -\sigma\,\eta_o k^2 e^{ik(z-ct)}. \tag{3.17}$$

Combining Eqs. (3.14) and (3.17) yields the following expression for the wave speed,

$$c = \frac{\rho_{f3}^{"} U_{f3} + \rho_{g4}^{"} U_{g4}}{\rho_{f3}^{"} + \rho_{g4}^{"}} \pm \sqrt{\frac{\sigma k}{\rho_{f3}^{"} + \rho_{g4}^{"}} - \frac{\rho_{f3}^{"}\rho_{g4}^{"}\left(U_{g4} - U_{f3}\right)^2}{\left(\rho_{f3}^{"} + \rho_{g4}^{"}\right)^2} - \frac{\left(\rho_f - \rho_g\right)}{\left(\rho_{f3}^{"} + \rho_{g4}^{"}\right)}\frac{g_e \cos\theta}{k}}, \tag{3.18}$$

where the terms under the radical represent the effects of different momentum or force terms. The first term accounts for the surface tension force, and this effect is always

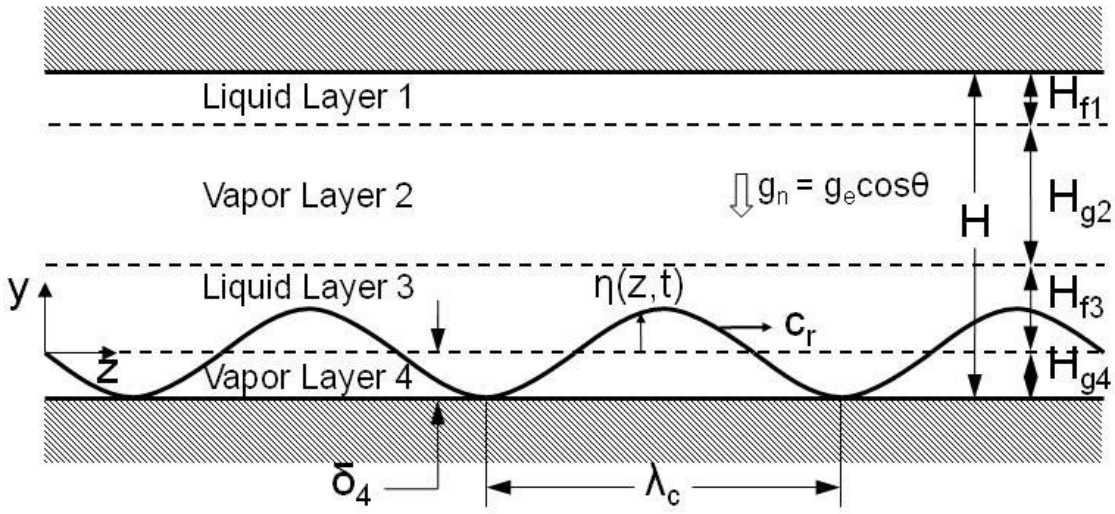

Figure 3.6: Schematic of interfacial lift-off model: wavy vapor layer formation along heated wall at CHF-.

stabilizing to the interface. The second term accounts for velocity difference between the heated vapor and liquid layers, which is destabilizing. The third term accounts for the effect of the component of gravity perpendicular to the heated wall, and this effect is stabilizing when the flow orientation places the vapor above the liquid, and destabilizing otherwise.

Should the destabilizing effects in Eq. (3.18) become dominant, the expression under the radical become negative, and the wave speed acquires both real and imaginary components, $c = c_r + i\, c_i$, where the imaginary component is given by

$$c_i = \sqrt{\frac{\rho''_{f3}\rho''_{g4}\left(U_{g4}-U_{f3}\right)^2}{\left(\rho''_{f3}+\rho''_{g4}\right)^2} + \frac{\left(\rho_f-\rho_g\right)}{\left(\rho''_{f3}+\rho''_{g4}\right)}\frac{g_e\cos\theta}{k} - \frac{\sigma k}{\rho''_{f3}+\rho''_{g4}}}\,, \tag{3.19}$$

The critical wavelength, λ_c, defined as the wavelength of a neutrally stable wave ($c_i = 0$), can be determined by setting the radical in Eq. (3.19) equal to zero.

$$k_c = \frac{2\pi}{\lambda_c} = \frac{\rho''_{f3}\rho''_{g4}\left(U_{g4}-U_{f3}\right)^2}{2\sigma\left(\rho''_{f3}+\rho''_{g4}\right)} + \sqrt{\left[\frac{\rho''_{f3}\rho''_{g4}\left(U_{g4}-U_{f3}\right)^2}{2\sigma\left(\rho''_{f3}+\rho''_{g4}\right)}\right]^2 + \frac{\left(\rho_f-\rho_g\right)g_e\cos\theta}{\sigma}}\,. \tag{3.20}$$

One important practical implication of Eq. (3.20) is that for very high velocity conditions, λ_c will approach the limit

$$\lambda_c = \frac{2\,\pi\,\sigma\left(\rho''_{f3}+\rho''_{g4}\right)}{\rho''_{f3}\,\rho''_{g4}\left(U_{g4}-U_{f3}\right)^2}\,. \tag{3.21}$$

irrespective of body force, which is consistent with the trend of CHF- versus orientation for high velocities depicted in Figures 3.4(a) and 3.4(b).

3.3.3 Modified Interfacial Lift-Off Criterion

The Interfacial Lift-off Model recently presented by Kharangate *et al.*[4] is modified to account for the effects of body force. CHF is postulated to occur when the momentum of vapor emanating from wetting fronts on the heated wall overcomes the pressure force caused by the interfacial curvature. This results in the interface in the wetting front detaching from the heated wall, which precludes any further liquid access

within the wetting front. The heat flux in the surrounding wetting fronts increases to compensate for the reduced liquid access. The surrounding wetting fronts now become more prone to lift-off because of the increased normal vapor momentum. Eventually more wetting fronts are lifted, preventing any appreciable liquid access to the heated wall, and CHF ensues.

Illustrated in Figure 3.7, the lift-off flux is determined by equating the pressure force pushing the interface towards the heated wall to the vapor momentum pushing the interface away from the heated wall. The vapor momentum $\rho_g U_{g4,n}^2$ emanating from a wetting front of length $b\lambda_c$ is opposed by the pressure difference

$$\overline{p_{f3} - p_{g4}} = \frac{4\pi\sigma\delta_4}{b\lambda^2}\sin(b\pi). \tag{3.22}$$

Previous studies [57] have shown that the ratio of wetting front length to critical wavelength is given by $b = 0.2$. The velocity of vapor in the wetting front normal to the heated wall can be determined by equating the heat input from the wall through the wetting front to the latent heat of the normal vapor flow.

$$q_w'' A_w = \rho_g U_{g4,n} A_w h_{fg}, \tag{3.23}$$

where A_w is the area of the wetting front. Equating the vapor momentum, $\rho_g U_{g4,n}^2$, to the pressure difference given by Eq. (3.22), and introducing Eq. (3.23), yield the following expression for the lift-off heat flux in the wetting front,

$$q_w'' = \rho_g h_{fg} \sqrt{\frac{\overline{p_{f3} - p_{g4}}}{\rho_g}} = \rho_g h_{fg} \left[\frac{4\pi\sigma}{\rho_g} \frac{\sin(b\pi)}{b} \right]^{1/2} \frac{\delta^{1/2}}{\lambda_c}. \tag{3.24}$$

The critical heat flux, q_m'', is based on the entire heated area. Because the heat flux, q_w'', in Eq. (3.24) is based on wetting front area, CHF can be determined from the relation

$$q_m'' = b q_w''. \tag{3.25}$$

Previous studies [38] proved the existence of a continuous upstream wetting region, z^*, defined as $z^* = z_o + \lambda_c(z^*)$, where z_o is the distance from the leading edge of the heated wall to the location where the vapor velocity just overcomes the liquid velocity. Hydrodynamic instability generates the wavy interface at z^*, downstream from which the wavy vapor layer begins to propagate along the heated wall.

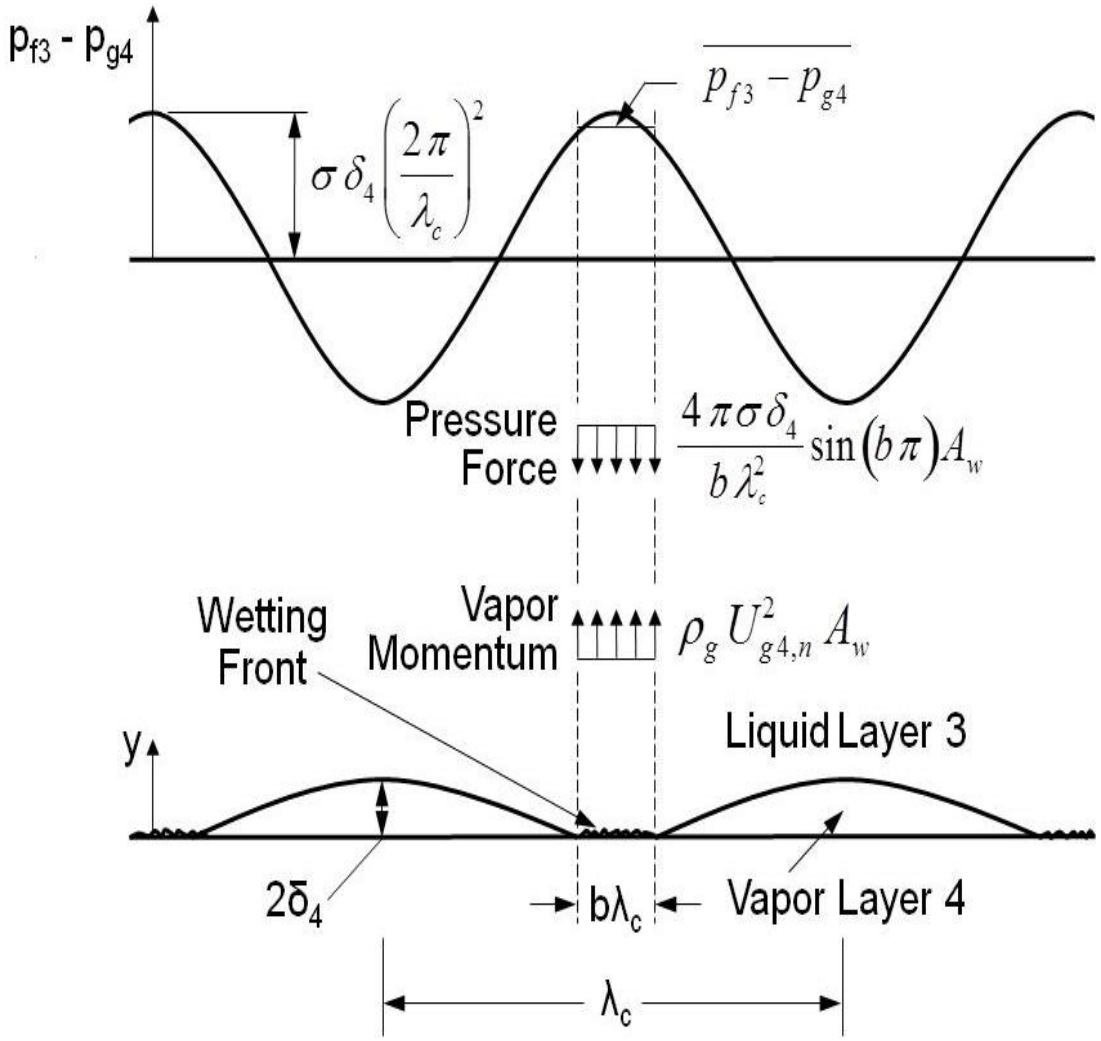

Figure 3.7: Schematic of interfacial lift-off of wetting front at CHF-.

Combining Eqs. (3.24) and (3.25) gives the following relation for CHF,

$$q''_m = \rho_g h_{fg} \left[\frac{4\pi\sigma b \sin(b\pi)}{\rho_g} \right]^{1/2} \left. \frac{\delta_4^{1/2}}{\lambda_c} \right|_{z^*} . \tag{3.26}$$

where, as discussed earlier, $b = 0.2$, and δ_4 is the thickness of vapor layer 4; both δ_4 and λ_c are calculated at z^*.

Calculation of CHF using a combination of the control volume model and the interfacial lift-off model requires an iterative numerical scheme. Key inputs for the control volume model are mass velocity, G, pressure at the inlet to the heated wall, p_{in}, inlet quality, $x_{e,in}$, and inlet void fraction α_{in}. This scheme is initiated with a guessed value for CHF, which is used in the control volume model to predict the velocities and area fractions for all four layers of the flow for every Δz axial increment from the upstream edge of the heated wall. The control volume model relations are solved simultaneously along the heated wall with the aid of a 4-th order Runge-Kutta numerical scheme using saturated fluid properties that are updated for each Δz increment based on local pressure. The outputs of the control volume model are then used in the instability analysis to determine the critical wavelength, λ_c, and z^*, which requires another series of iterations. Finally, the calculated parameters are used in Eq. (3.26) to calculate a new CHF value. The entire calculation scheme is now repeated using the newly calculated CHF value. Further iteration is attempted until the CHF value used in the control volume model and predicted CHF value converge.

3.4 Model Predictions

Figures 3.8(a) and 3.8(b) show predictions of the liquid layer velocity at the inlet to the heated portion of the channel, $U_{f,in}$, for $x_{e,in} = 0.01$ and $x_{e,in} = 0.19$, respectively. Because the flow enters the channel as a two-phase mixture, the mixture density is significantly smaller than the liquid density. This yields a liquid velocity significantly greater than G/ρ_f, which is the mean velocity for pure liquid at the inlet. Comparing Figures. 3.8(a) and 3.8(b) shows the liquid velocity increases with increasing $x_{e,in}$ because of the significantly lower mixture density at higher $x_{e,in}$. Notice that there is appreciable influence of flow orientation on $U_{f,in}$ for $x_{e,in} = 0.01$ and $G/\rho_f = 0.126$ and 0.224 m/s, but

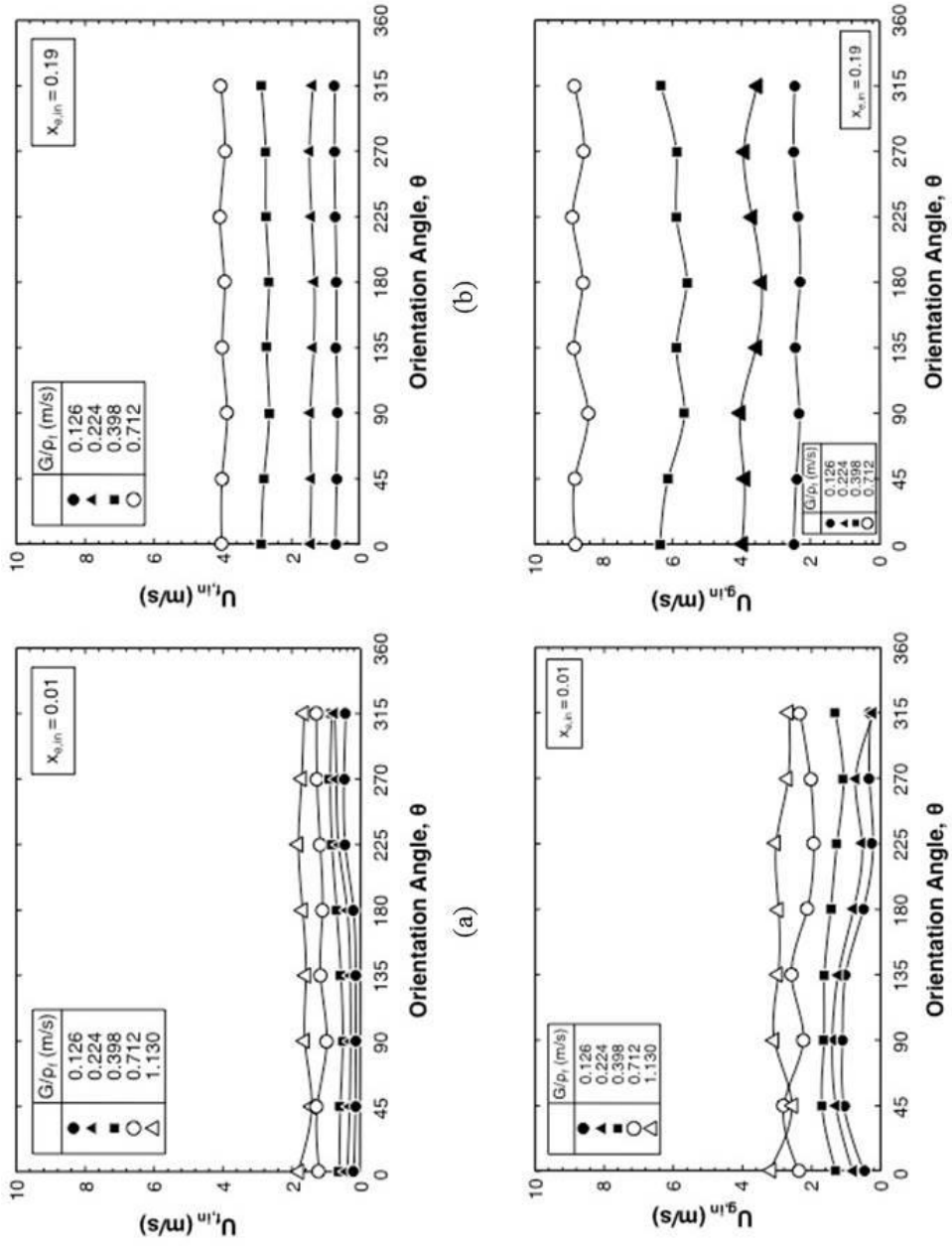

Figure 3.8: Variation of predicted mean liquid velocity at inlet to heated wall for (a) $x_{e,in} = 0.01$ and (b) $x_{e,in} = 0.19$, and predicted mean vapor velocity for (c) $x_{e,in} = 0.01$ and (d) $x_{e,in} = 0.19$.

this influence is much weaker for $x_{e,in}$ = 0.01 and G/ρ_f = 0.712 and 1.130 m/s. For $x_{e,in}$ = 0.19, the influence of orientation is fairly weak for the entire range of G/ρ_f. These trends can be explained by the dominance of fluid inertia compared to buoyancy as $x_{e,in}$ and G/ρ_f are increased.

Figures 3.8(c) and 3.8(d) show predictions of the vapor core velocity at the inlet to the heated portion of the channel, $U_{g,in}$, for $x_{e,in}$ = 0.01 and $x_{e,in}$ = 0.19, respectively. Here too, the vapor velocity is significantly greater than G/ρ_f, especially for $x_{e,in}$ = 0.19, and the influence of flow orientation is fairly weak for G/ρ_f = 0.712 and 1.130 m/s at $x_{e,in}$ = 0.01, and for the entire range of G/ρ_f at $x_{e,in}$ = 0.19.

Figure 3.9 shows the variation of critical wavelength, λ_c, with flow orientation for an intermediate inlet quality value of $x_{e,in}$ = 0.11. The critical wavelength is determined using Eq. (3.20) with the liquid and vapor velocities and different layer thicknesses predicted by the separated flow model at z^* using measured CHF values. It is important to note that hydrodynamic instability of the liquid-vapor interface adjacent to the heated wall is crucial to maintaining the wetting fronts that provide liquid access to the wall. Notice in Figure 3.9 the existence of a broad region of flow orientations between θ = 90° and 270° and low values of G/ρ_f, where the interface is stable. This region encompasses downward-facing heated wall orientations, where buoyancy causes stratification of vapor towards the heated wall, and CHF values are comparatively small. The Interfacial Lift-off Model is valid for velocities and orientations where the interface is unstable. For the unstable region, the wavelength increases with decreasing G/ρ_f, meaning wetting fronts are remote from one another for low velocities. Notice how the highest velocity of G/ρ_f = 0.712 m/s produces two important effects: (a) an unstable interface for all flow orientations, and (b) greatly reduced sensitivity of the critical wavelength to flow orientation. This demonstrates the importance of inertia at overcoming buoyancy effects and helping produce CHF values that are insensitive to flow orientation.

As indicated earlier, the Interfacial Lift-off Model is valid for flow conditions and orientations that produce an unstable interface and the separated four-layer flow pattern depicted in Figure 3.2(b). This excludes low velocities especially in combination with orientations associated with downflow and downward-facing heated wall.

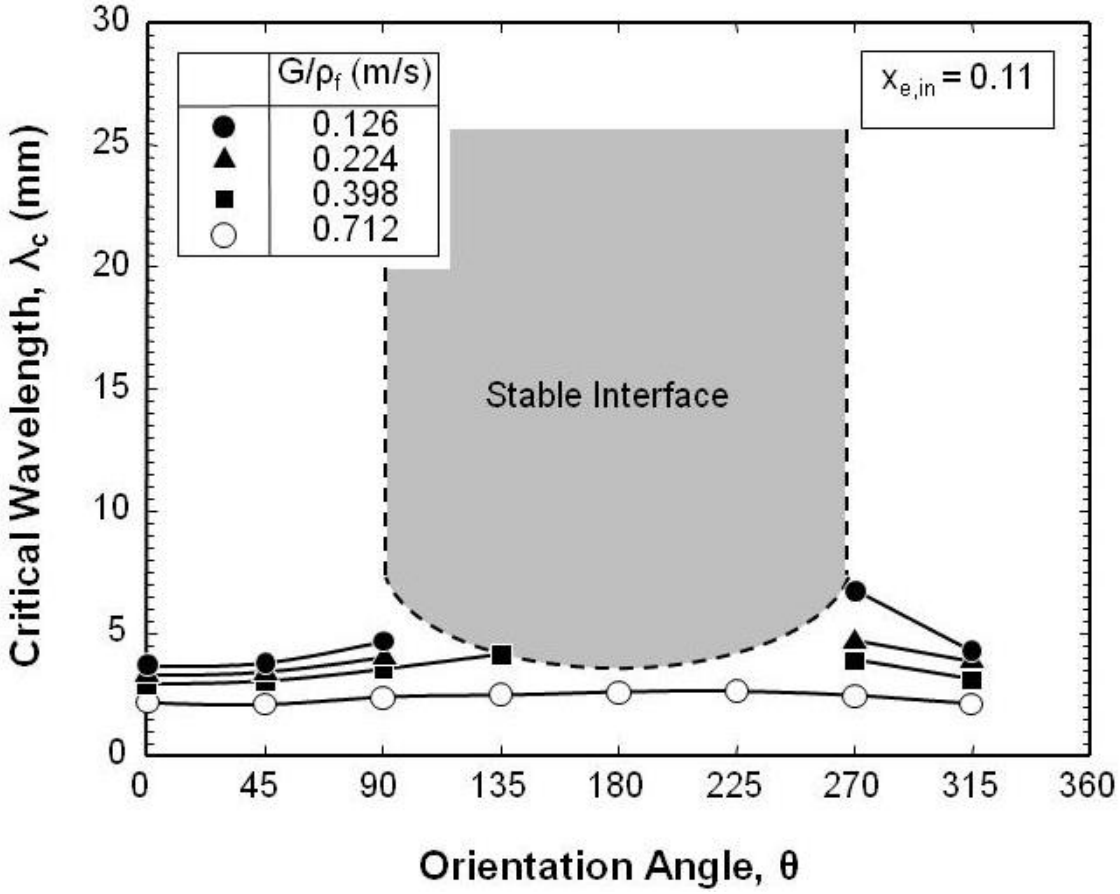

Figure 3.9: Variation of predicted critical wavelength at z^*, calculated using measured CHF, for $x_{e,in} = 0.11$.

Figures 3.10(a) and 3.10(b) compare the model predictions with experimental data for two operating conditions: G/ρ_f = 0.995 m/s and $x_{e,in}$ = 0.01, and G/ρ_f = 0.542 and $x_{e,in}$ = 0.11, respectively, and all orientations. These plots show good agreement in both trend and magnitude, evidenced by MAE values of 13.4% and 17.4%, respectively, where

$$MAE = \frac{1}{M}\sum \frac{\left|q''_{m,exp} - q''_{m,pred}\right|}{q''_{m,exp}} \times 100\%. \tag{3.27}$$

Notice how CHF is highest for θ = 0° - 45° and 315° - 360°, orientations that produce a buoyancy force that assists vapor removal and liquid replenishment at the heated wall. Conversely, CHF is lowest for θ = 135° - 225°, where buoyancy promotes vapor blanketing of the heated wall and hinders the liquid replenishment.

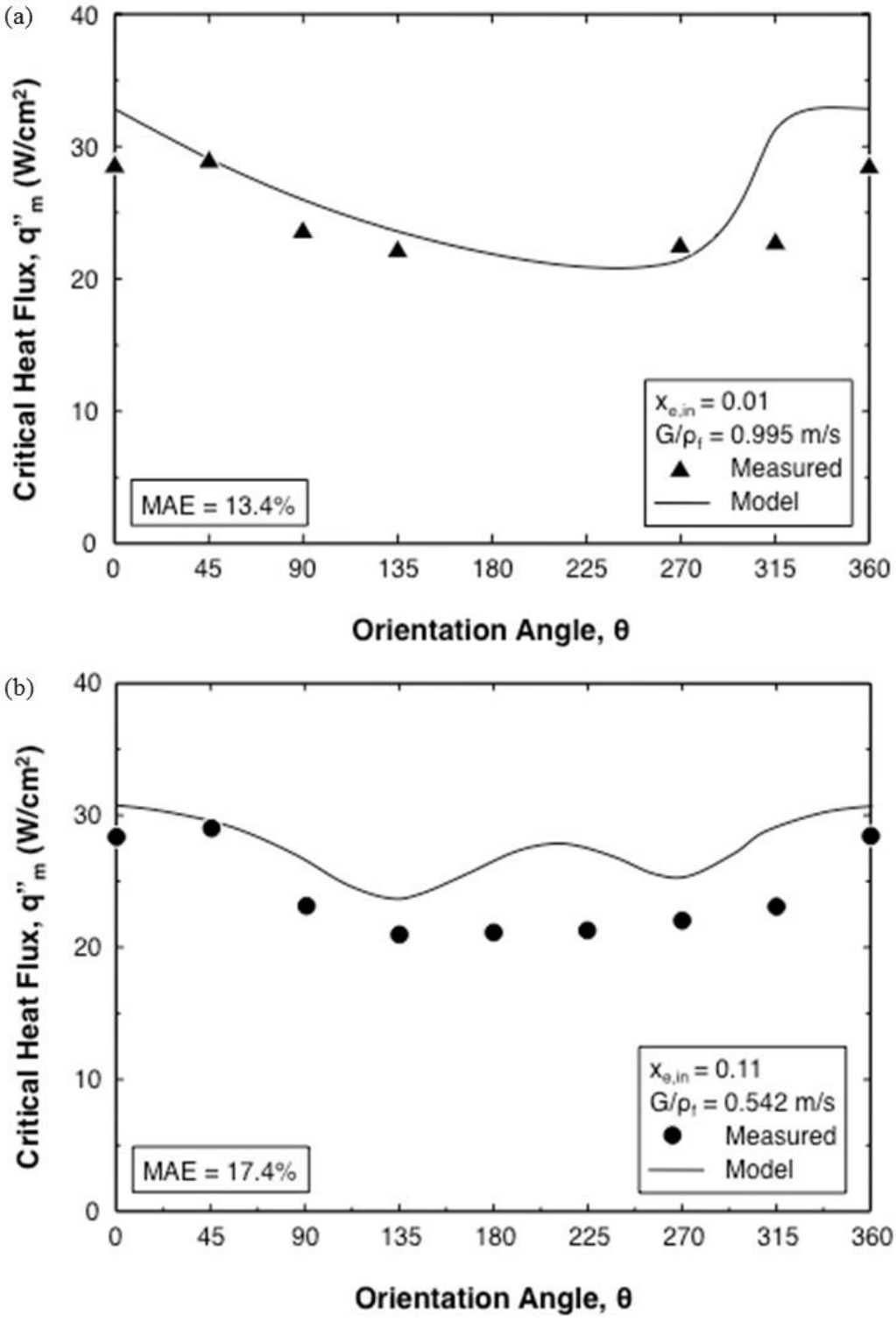

Figure 3.10: Comparison of measured and predicted CHF for: (a) $x_{e,in} = 0.01$ and $G/\rho_f = 0.995$ m/s, and (b) $x_{e,in} = 0.11$ and $G/\rho_f = 0.542$ m/s.

CHAPTER 4. LOCALIZED DRYOUT VERSUS CHF

4.1 Transient Heat Transfer Results

Another goal associated with the ground-based flow boiling study is to track the complex thermal transients associated with CHF occurrence for saturated inlet conditions with a finite vapor void. The experiments involved increasing the wall heat flux in small increments and measuring the ensuing temporal variations in wall temperatures. As CHF is approached, localized regions of dryout are observed, but wall temperatures sometimes incurred momentary unsteady excursions that subsided after a finite waiting period. Ultimately, CHF is identified by a fast, uncontrolled rise in any of the wall temperatures.

4.1.1 Typical Transient Behavior Leading to CHF

Figure 4.1 shows a composite plot of temporal records of the heated wall thermocouple signals, heat transfer coefficients at the same axial locations as the thermocouples, and input wall heat flux for G/ρ_f = 0.398 m/s, $x_{e,in}$ = 0.19 and θ = 45°. These characteristics are representative of CHF occurrence for most operating conditions. The upstream thermocouple is represented by T_1, which is followed by T_2, T_3, T_4 and T_5, with T_5 representing the most downstream thermocouple. The corresponding local heat transfer coefficient at any thermocouple T_i is derived from the simple relation $q'' = h\left(T_i - T_{sat}\right)$. Contrary to the notion that wall temperatures should increase along the heated wall, Figure 4.1 shows wall temperatures are highest at T_1 and for the most part decrease along the flow direction. This behavior can be explained by (i) the vapor core maintaining a fairly constant temperature equal to T_{sat}, and (ii) axial vaporization increasing the velocities of the flow layers, causing a stream-wise increase in the heat transfer coefficient. Notice that CHF is detected downstream by a sharp unsteady rise in the wall temperature starting at T_5 and T_4.

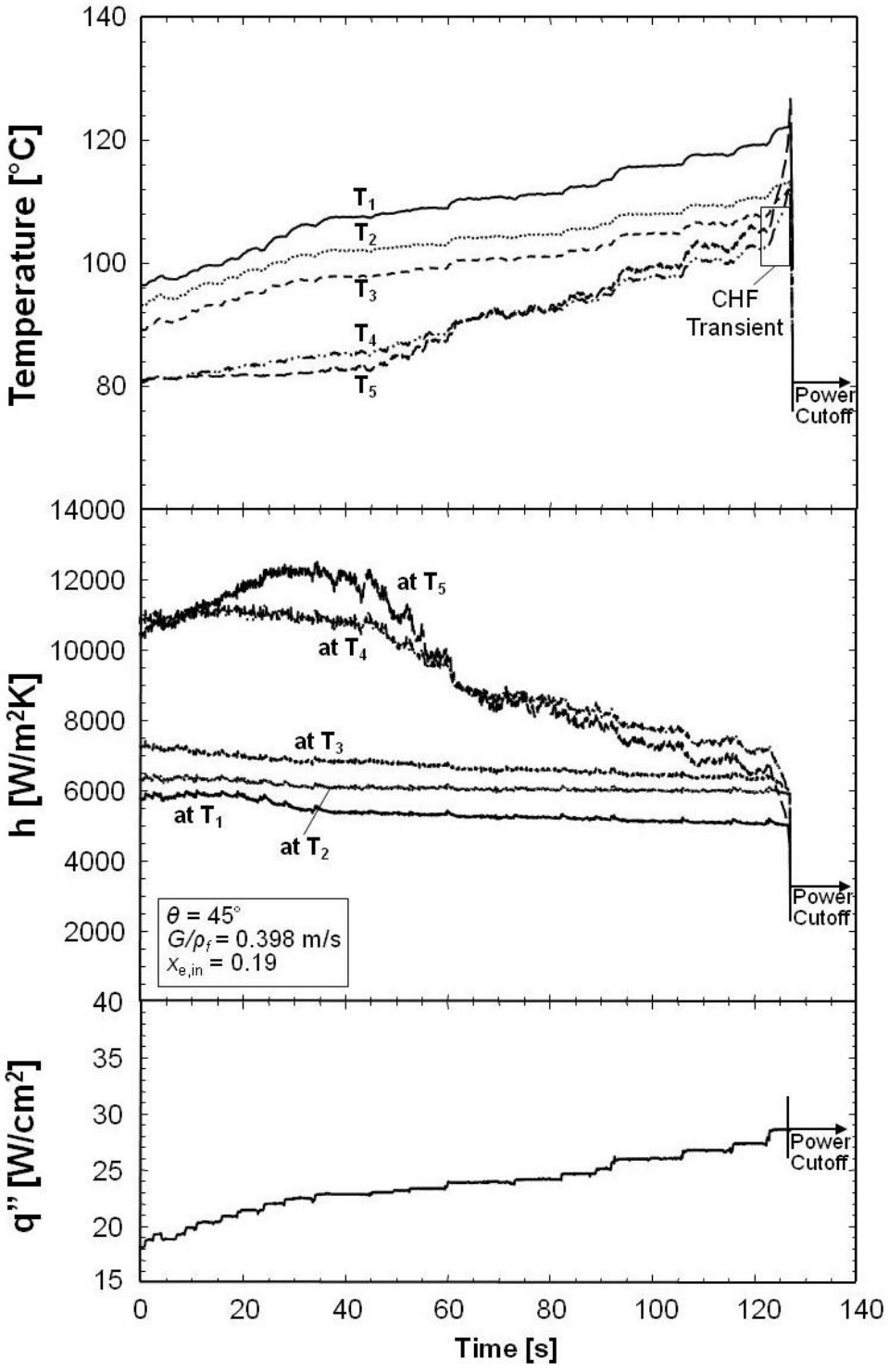

Figure 4.1: Temporal records of wall temperatures, heat transfer coefficients and input wall heat flux for $G/\rho_f = 0.398$ m/s, $x_{e,in} = 0.19$ and $\theta = 45°$.

4.1.2 Dryout Anomalies Prior to CHF

Pre-CHF anomalies were encountered only with upward-facing heated wall orientations (θ = 315°, 0° and 45°). The dryout typically occurred in the inlet region for low inlet mass velocities of $G/\rho_f \leq 0.315$ m/s, and the outlet region for mid-range velocities of $0.542 \geq G/\rho_f \geq 0.315$ m/s. All other orientations and inlet conditions displayed transient characteristics similar to those shown in Figure 4.1.

Figure 4.2 shows a composite plot of temporal records for G/ρ_f = 0.224 m/s, $x_{e,in}$ = 0.01 and θ = 315°. Notice how momentary dryout is first detected at T_1 and, to a lesser extent, T_2 after the wall heat flux is increased by a small increment then held constant. Without increasing the heat flux, T_1 begins to level off and decrease slightly before reaching steady state. The wall heat flux is then increased in several small increments, each followed by an adequate waiting period, with all the wall temperatures increasing gradually to new steady state levels with no spikes. Eventually, CHF is detected near the outlet by a sudden uncontrolled temperature rise commencing at T_5 and T_4 with no signs of temperature recovery. These trends point to a very important aspect of CHF detection. Given the large difference in wall heat flux between the time the first dryout is detected at T_1 and the time CHF actually occurs, identifying the temperature spike at T_1 as CHF would undoubtedly lead to a measurable error (~ 7.5%) in the measured CHF.

Figure 4.3(a) shows a representative photo of interfacial behavior immediately after the temperature spike at T_1. Figure 4.2(b) shows corresponding idealized representations of interfacial behavior based on observations from multiple video images. Before dryout, intense boiling initiates a series of vapor patches mimicking a wavy vapor layer 4 beneath liquid layer 3 adjacent to the heated wall. Cooling of the wall is still possible through wetting fronts between the vapor patches. Increasing the wall heat flux causes separation - lift-off - of the liquid-vapor interface in the wetting fronts, resulting in a continuous vapor layer. This explains the temperature spike at T_1 and corresponding sharp decrease in the heat transfer coefficient upstream. The interfacial lift-off is also responsible for formation of elongated liquid ligaments – remnants of the near-heated-wall liquid layer – that are carried downstream. Restoration of steady conditions at T_1 following the spike can be explained by reattachment of the liquid ligaments with the

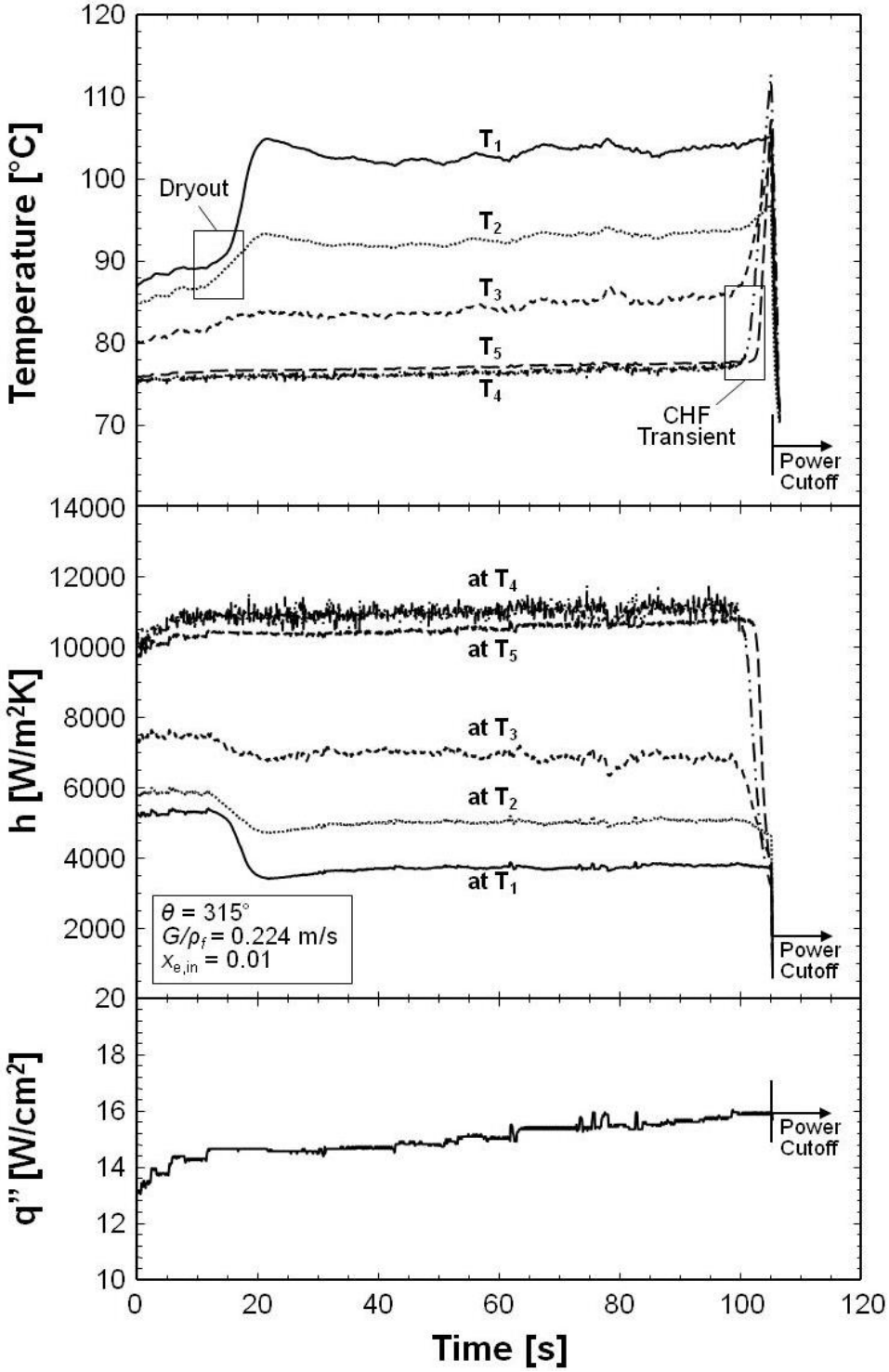

Figure 4.2: Temporal records of wall temperatures, heat transfer coefficients and input wall heat flux for $G/\rho_f = 0.224$ m/s, $x_{e,in} = 0.01$ and $\theta = 315°$.

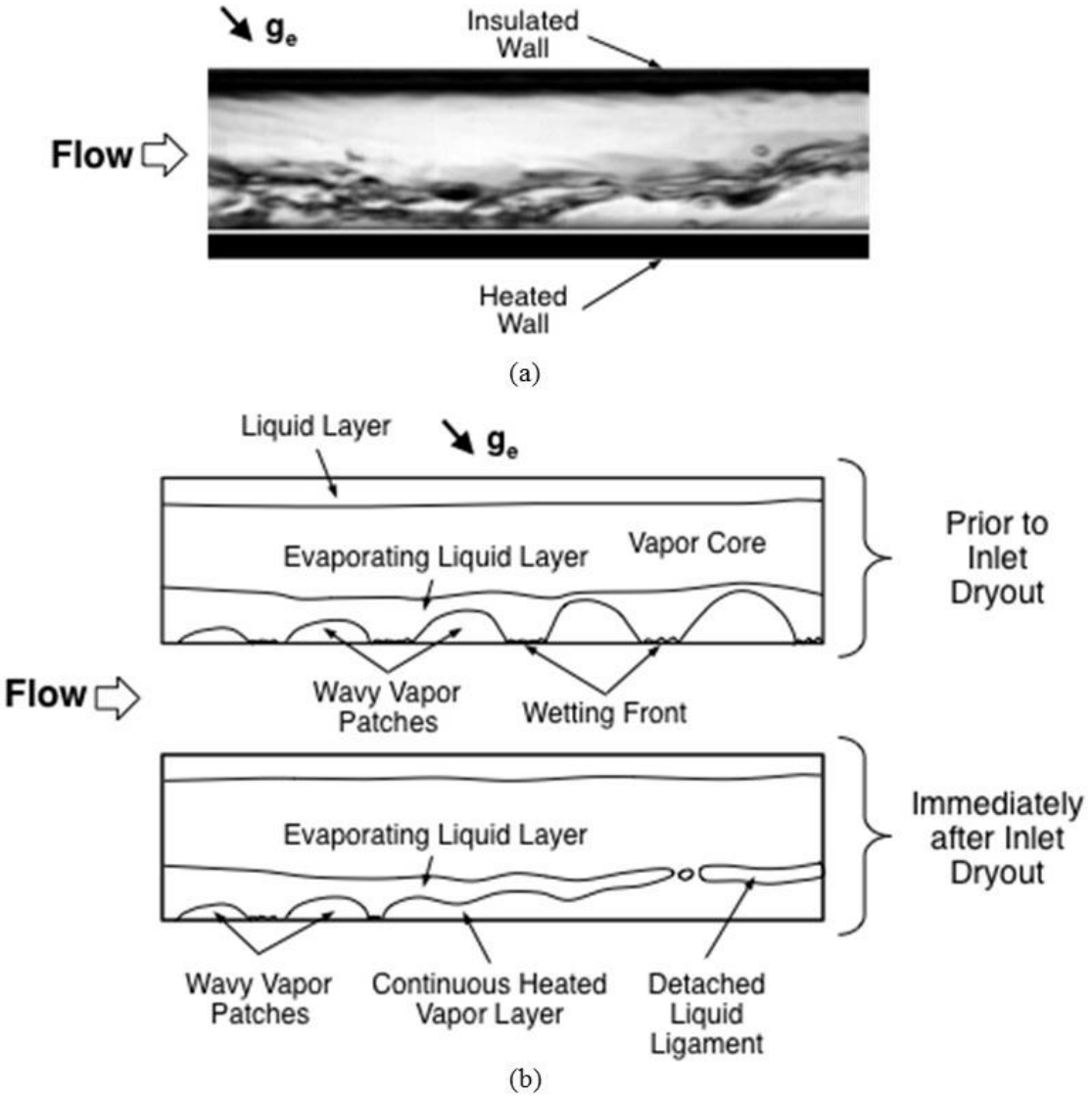

Figure 4.3: (a) Photo of the flow in the inlet region for $G/\rho_f = 0.224$ m/s, $x_{e,in} = 0.01$ and $\theta = 315°$ immediately after inlet dryout. (b) Idealized representation of the flow prior to, and immediately after the inlet dryout.

heated wall downstream. This rewetting effect causes re-initiation of wetting fronts downstream. Favorable cooling conditions at these downstream wetting fronts cause heat from the upstream vapor-insulated region to be conducted axially through the wall to the middle and outlet regions. This behavior provides support for the need to have adequate wall thickness to support lateral heat conduction and avoid pre-mature CHF detection. Another reason for the downstream heat transfer enhancement is the increase in velocities of all the flow layers because of evaporation.

Figure 4.4 shows a composite plot of temporal records for G/ρ_f = 0.398 m/s, $x_{e,in}$ = 0.11 and θ = 45°. In this case, momentary dryout is encountered in the outlet region of the heated wall and detected by thermocouples T_4 and T_5. The dryout is initiated at 40 s, with T_5 indicating significantly higher temperatures than T_4. The spike reaches peak temperature – peak dryout - around 47 s before subsiding back to post-dryout steady-state at 63 s. Notice that the electrical power input is held constant during the entire dryout episode. Between the initial and peak dryout, the local heat transfer coefficient at T_5 drops from 12,000 to 4500 W/m^{2}K in 5 s, then rises sharply between peak and post dryout to a value about 20% below where it started. Increasing electrical power input in small increments after the dryout episode causes incremental rise in T_4 and T_5, and corresponding monotonic decreases in the heat transfer coefficients at T_4 and T_5 until CHF is ultimately detected in the outlet region. Notice that the local heat transfer coefficients in the inlet region display far greater dependence on the wall heat flux than at T_4 and T_5. It is interesting to note that incorrectly identifying the dryout episode as CHF would result in a CHF value of 22.9 W/cm^2 instead of the true value of 28.5 W/cm^2.

Figure 4.5(a) shows schematic representations of the interfacial behavior observed in the inlet region for G/ρ_f = 0.398 m/s, $x_{e,in}$ = 0.11 and θ = 45°. The characteristic wavy vapor layer regime is observed throughout the inlet region. Wetting fronts are established consistently at the same axial distance, z^*, from the leading edge of the heated wall. The schematics show a wetting front, labeled 1, forming upstream and propagating along the heated wall as a second wetting front 2 is formed at z^*. The wetting fronts are formed between vapor patches mimicking a wavy vapor layer with uniform wavelength λ.

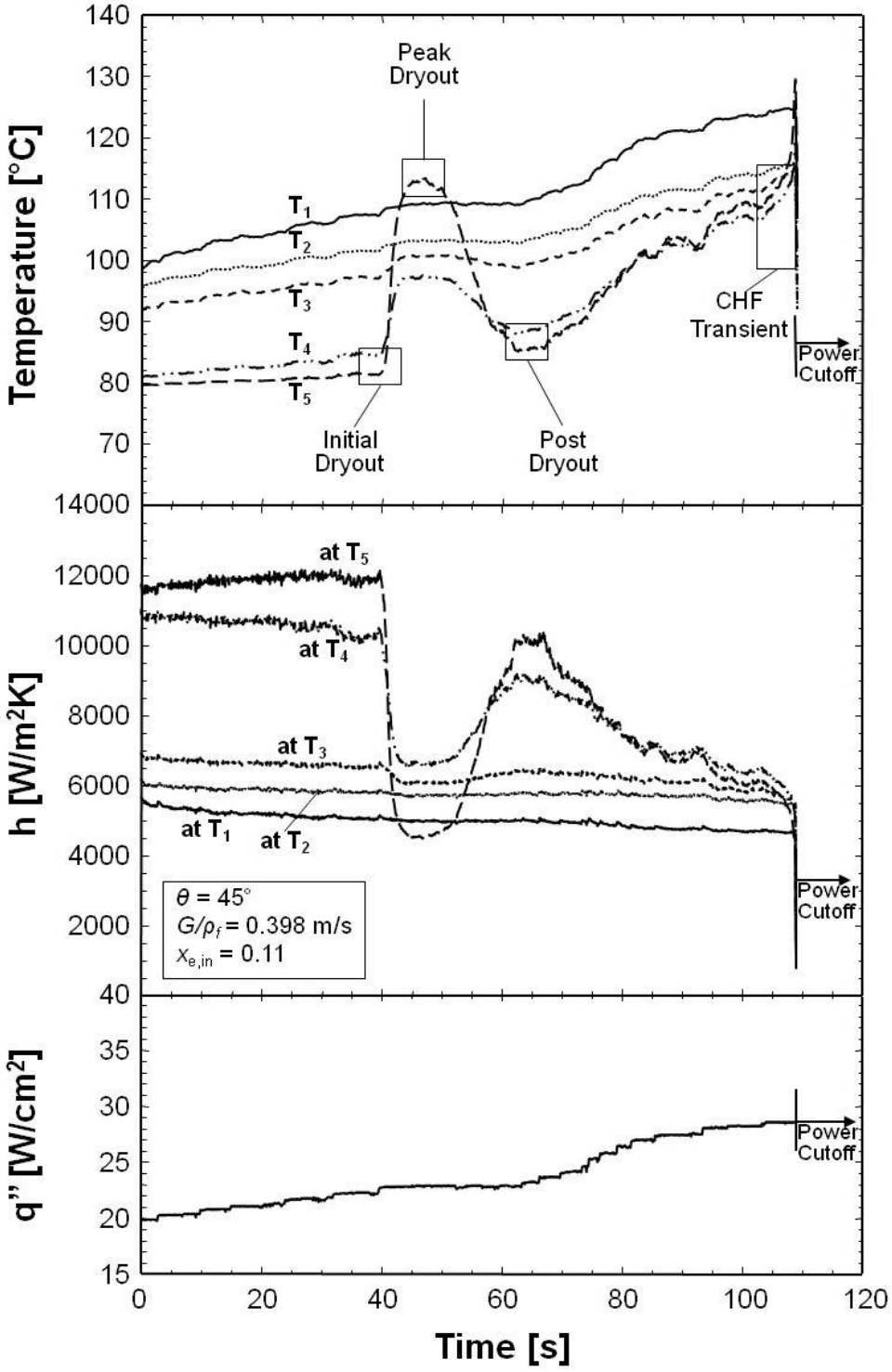

Figure 4.4: Temporal records of wall temperatures, heat transfer coefficients and input wall heat flux for $G/\rho_f = 0.398$ m/s, $x_{e,in} = 0.11$ and $\theta = 45°$.

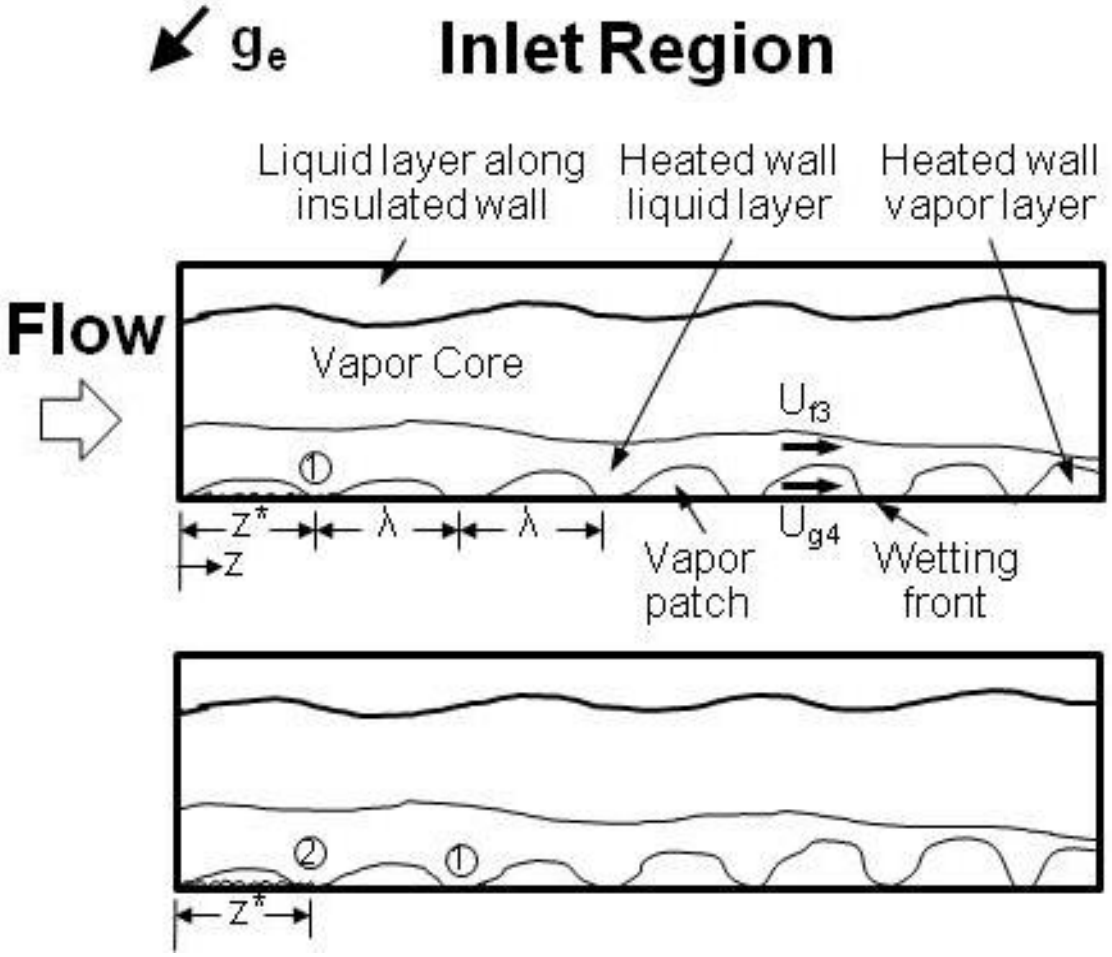

Figure 4.5(a): Illustration of flow behavior during the dryout episode for G/ρ_f = 0.398 m/s, $x_{e,in}$ = 0.11 and θ = 45° in the inlet region.

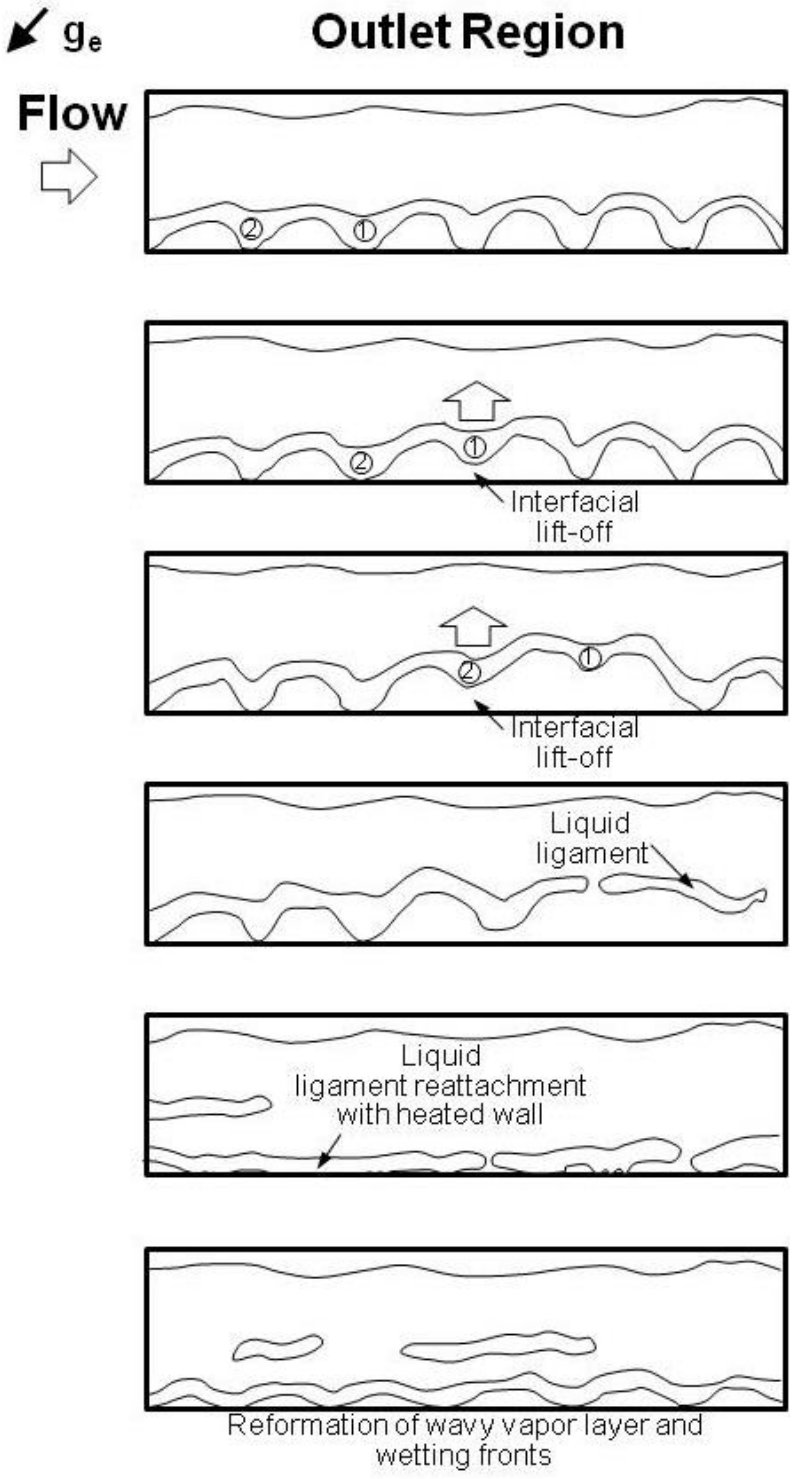

Figure 4.5(b): Illustration of flow behavior during the dryout episode for G/ρ_f = 0.398 m/s, $x_{e,in}$ = 0.11 and θ = 45° in the outlet region.

Figure 4.5(b) shows schematics of the flow behavior in the outlet region during the temporary dryout episode captured in Figure 4.4. Notice that the liquid layer adjacent to the heated wall suffers appreciable thinning due to both evaporation and increased shear stresses resulting from axial acceleration of the flow layers. The dryout episode is initiated with wetting front 1 lifting from the heated wall, causing the vapor patches upstream and downstream of 1 to merge into a single longer vapor patch. With a larger portion of the heated wall now insulated, more heat is concentrated in wetting front 2, causing lifting of 2 as well. This action causes the liquid layer to shatter into liquid ligaments that are entrained in the vapor core. The temporary dryout is terminated when the vapor core shear forces cause liquid ligaments to reattach with the heated wall, restoring the wavy vapor layer and wetting front formations. CHF is achieved at a later time when these newly established wetting fronts begin to lift from the heated wall.

4.2 Separated Model Predictions

Using the separated four-layer model summarized in Section 3.3.1, the thicknesses and velocities of the various layers comprising the flow are computed for three sets of operating conditions to provide further insight into the dryout phenomena discussed thus far.

Figures 4.6(a)-4.6(c) show variations of computed area fractions of the four layers along the heated portion of the flow channel at CHF- for G/ρ_f = 0.398 m/s, θ = 0° and different inlet qualities. The area fractions are segregated by $\left(\varepsilon_{f1} + \alpha_2\right)$ for the combined insulated wall liquid layer and vapor core, $\left(1 - \varepsilon_{f1} - \alpha_2 - \alpha_4\right)$ for the heated wall liquid layer, and α_4 for the heated wall wavy vapor layer.

For $x_{e,in}$ = 0.0143 and α_{in} = 0.344, Figure 4.6(a) shows the heated wall vapor layer's mean thickness increases in the axial direction because of evaporation. This causes the thickness of heated liquid layer to decrease monotonically, creating greater susceptibility to breakup into ligaments downstream. The model also shows the flow areas of the insulated wall liquid layer and vapor core decreasing axially due to the increasing shear stresses.

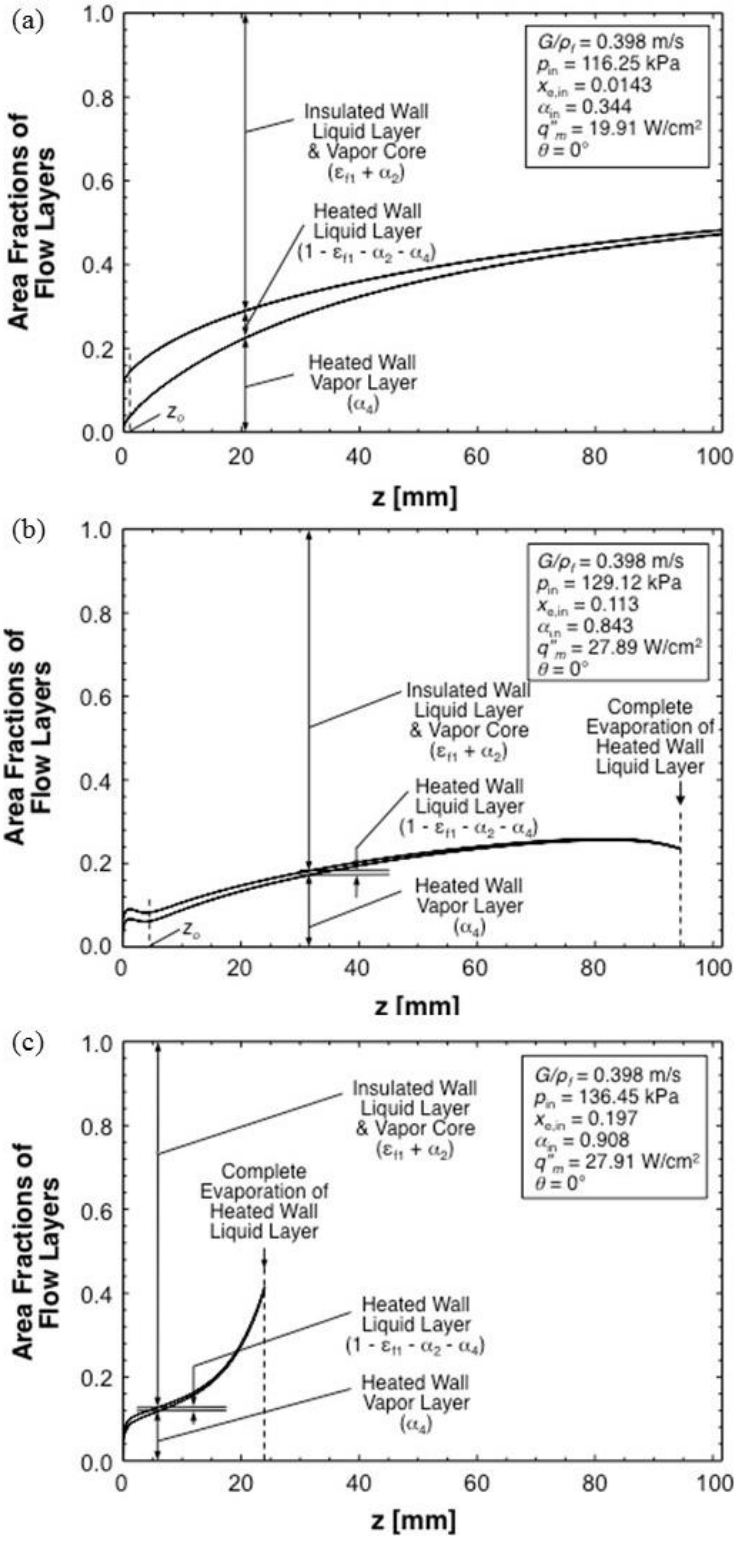

Figure 4.6: Separated four-layer model predictions of area fractions for $G/\rho_f = 0.398$ m/s, $\theta = 0°$ and (a) $x_{e,in} = 0.0143$, (b) $x_{e,in} = 0.113$, and (c) $x_{e,in} = 0.197$.

For higher inlet qualities of $x_{e,in}$ = 0.113 and α_{in} = 0.843, Figure 4.6(b) shows the combined insulated wall liquid layer and vapor core area fraction, $\left(\varepsilon_{f1} + \alpha_2\right)$, occupies the majority of the channel's cross-sectional area. The heated wall liquid layer is much thinner compared to $x_{e,in}$ = 0.0143, Figure 4.6(a), and is completely evaporated at z = 94 mm, before the end of the heated wall. For the highest inlet qualities of $x_{e,in}$ = 0.197 and α_{in} = 0.908, Figure 4.6(c) shows further thinning of the heated wall liquid layer and complete evaporation even further upstream, at 24 mm. The predicted thinning and complete evaporation of the heated wall liquid layer may help explain the aforementioned tendency of this layer to break apart into liquid ligaments and cause temporary pre-CHF dryout.

Figures 4.7(a)-(c) shows variations of computed phase velocities of the four layers along the heated portion of the flow channel at CHF- for G/ρ_f = 0.398 m/s and θ = 0° at different inlet qualities. Due to the fluid entering the heated portion of the channel with a finite vapor void, the two-phase mixture enters the heated channel region with velocities of the liquid film sheathing the four channel walls, U_{f1}, and vapor core, U_{g2}, that are greater than G/ρ_f. Shown in Figure 4.7(a) for $x_{e,in}$ = 0.0143 and α_{in} = 0.344, the vapor core velocity is significantly higher than that of the liquid layer along the insulated and heated walls. The velocities of the insulated walls' liquid layer, U_{f1}, and vapor core, U_{g2}, show comparatively minor variations along the heated portion of the channel. However, the velocity of heated wall wavy vapor layer, U_{g4}, increases drastically from the leading edge of the heated wall due to evaporation of the heated wall liquid layer 3. The velocity of the heated wall liquid layer, U_{f3}, also increases sharply, mostly because of the increasing shear stresses. Location z_o in Fig. 13(a) indicates where U_{g4} just surpasses U_{f3}.

Figure 4.7(b) shows velocity predictions for the different layers for higher inlet qualities of $x_{e,in}$ = 0.113 and α_{in} = 0.843. The increased inlet vapor void produces very high inlet velocities for the vapor core, U_{g2}, and insulated walls' liquid layer, U_{f1}. However, U_{g2} and U_{f1} show little variation along the heated portion of the channel. Strong axial velocity increases are predicted for the heated wall liquid layer, U_{f3}, and heated wall wavy vapor layer, U_{g4}. Two interesting observations are (i) U_{f3} surpassing U_{g3} and (ii) full evaporation of the heated wall liquid layer 3 downstream.

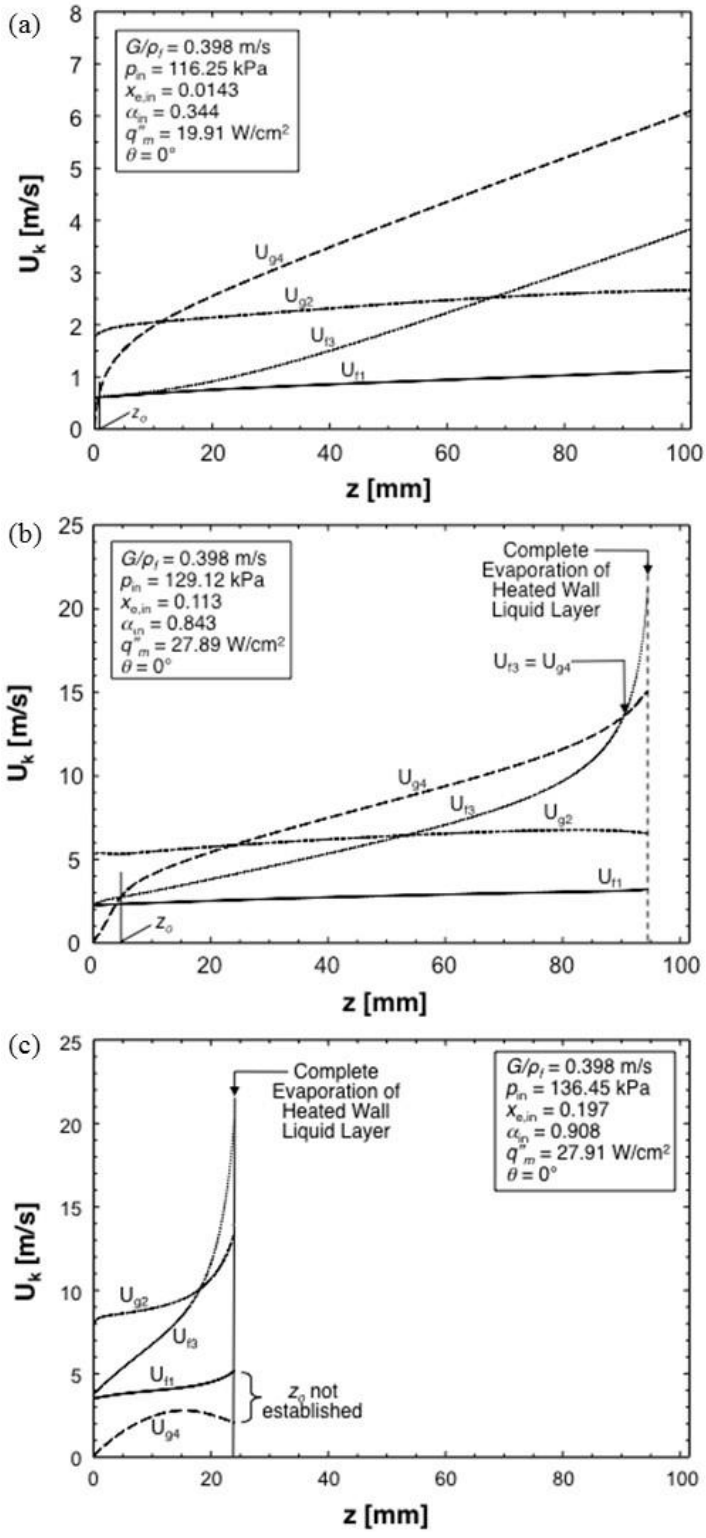

Figure 4.7: Separated four-layer model predictions of layer velocities for G/ρ_f = 0.398 m/s, θ = 0° and (a) $x_{e,in}$ = 0.0143, (b) $x_{e,in}$ = 0.113, and (c) $x_{e,in}$ = 0.197.

Figure 4.7(c) shows velocity predictions for $x_{e,in}$ = 0.197 and α_{in} = 0.908. Here, the velocity of the heated wall wavy vapor layer, U_{g4}, never surpasses that of the heated liquid layer, U_{f3}. Additionally, U_{f3} is shown exceeding U_{g4}, and the heated wall liquid layer fully evaporated over a small fraction of the heated length.

These predictions of area ratios and velocities for the different flow layers provide valuable insight into the pre-CHF anomalies. First, they identify the thinning and eventual evaporation of the heated wall liquid layer as the primary cause for these occurrences. They also point to lateral conduction along the heated wall as essential to channeling heat from momentary dry regions to adequately cooled regions, especially during the pre-CHF dryout episodes. This in turn points to the need to use an adequately thick and thermally conducting heated wall to obtain reliable CHF data. It is recommended that future CHF studies adopt the minimum heated wall thickness criterion discussed earlier to help ensure consistency between CHF databases.

CHAPTER 5. ASSESSMENT OF BODY FORCE ON FLOW BOILING CHF

5.1 CHF Regime Maps

Figures 5.1(a) and 5.1(b) summarize all CHF- regimes discovered from the ground-based flow boiling study for $x_{e,in} = 0.01$ in a mass velocity - orientation plane for the inlet and outlet regions, respectively. Shown in Figure 5.1(a) are three clearly identifiable CHF- regimes for the inlet region, with the *Pool Boiling Regime* prevailing for the two lowest mass velocities at $\theta = 45°$, the *Stratification Regime* for the lowest mass velocity at $\theta = 135°$, 180° and 225°, and the *Wavy Vapor Layer Regime* for all other mass velocities and orientations. Figure 5.1(b) shows, for the outlet region, the *Stratification Regime* prevailing for the same orientations as the inlet region and lowest mass velocity, and the *Wavy Vapor Layer Regime* for all other mass velocities and orientations. Overall, Figures 5.1(a) and 5.1(b) show that all regimes other than the *Wavy Vapor layer Regime* are encountered in downward-facing heated wall orientations and at low mass velocities, where the influence of buoyancy is most pronounced.

Comparing the present CHF- regime maps for $x_{e,in} = 0.01$, Figures 5.1(a) and 5.1(b), with those of Zhang *et al.* [5] for $x_{e,in} \leq 0$, Figure 1.5, shows that $x_{e,in} > 0$ offers greater resistance to buoyancy, evidenced by a transition to the *Wavy Vapor Layer Regime* at lower mass velocities.

5.1.1 CHF Regimes at Low Mass Velocity

At low mass velocities, CHF values are generally low and buoyancy results in complex boiling regimes. The subcooled CHF regime map, Figure 1.5, will serve as a guideline to identify any similarities or differences in CHF behavior for the present study corresponding to $x_{e,in} > 0$ with the CHF behavior captured by Zhang *et al.* [5] for $x_{e,in} \leq 0$. Figures 5.2(a)-5.2(h) show the vapor development at the inlet and middle regions at

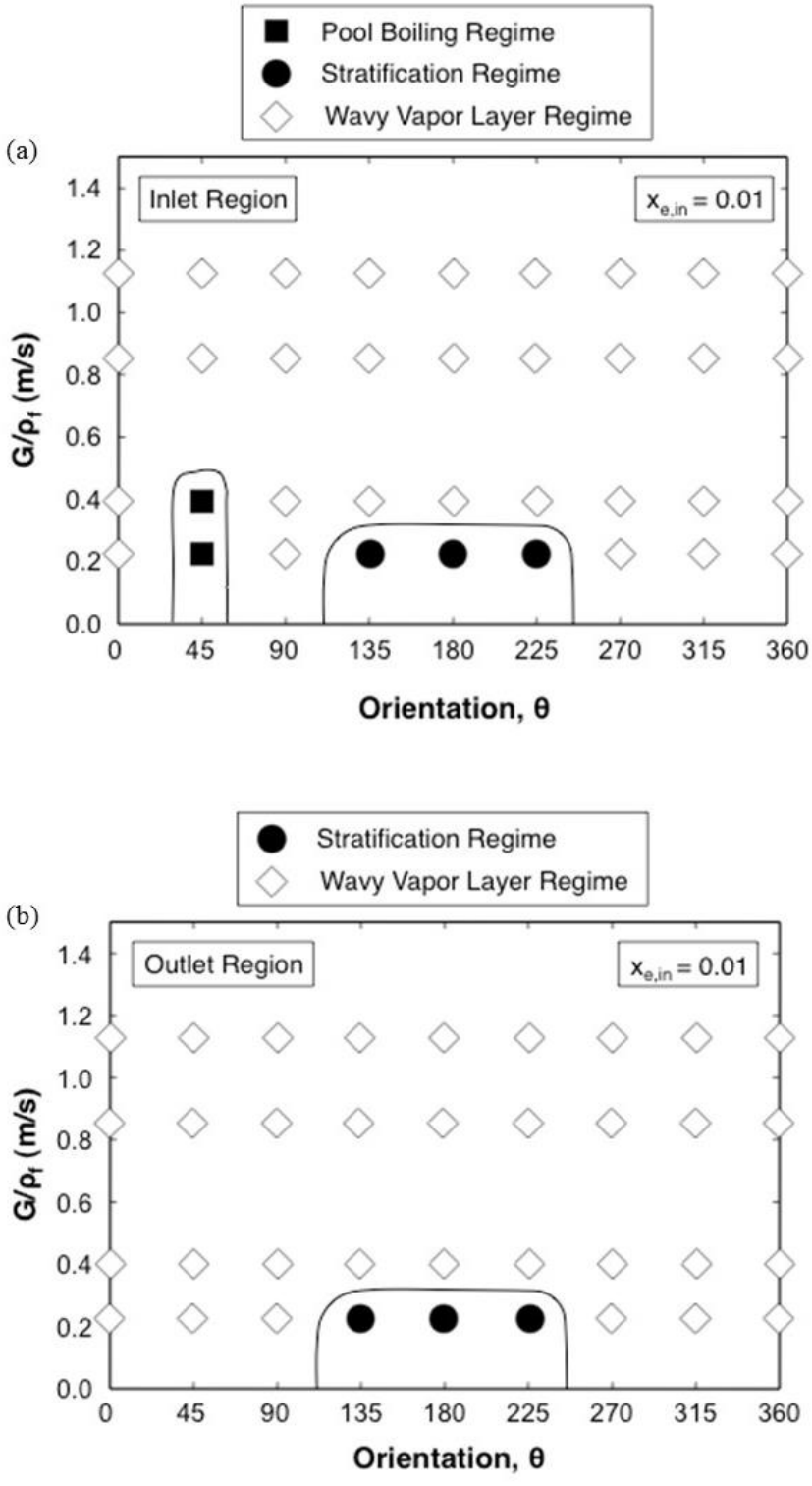

Figure 5.1: CHF regime map for $x_{e,in} = 0.01$ for (a) inlet region and (b) outlet region.

CHF- (just prior to CHF) for all orientations at $G/\rho_f = 0.224$ m/s and $x_{e,in} = 0.01$. For each orientation in Figure 5.2, fifteen sequential video frames are presented for each of the inlet and middle regions; the time elapsed between consecutive frames is 0.0006 s. Zhang *et al.* [5] identified a *Pool Boiling Regime* for all upward-facing heated wall orientations ($\theta = 0°$, 45° and 315°) at low mass velocities with $x_{e,in} \leq 0$. For the present study, corresponding to $x_{e,in} > 0$, the flow for the upward-facing heated wall orientations enters the heated portion of the channel fully separated, with a liquid layer covering the heated wall and a thick vapor layer residing atop. For $\theta = 0°$ and 315°, the *Pool Boiling Regime* is replaced by the *Wavy Vapor Layer Regime*, Figures 5.2(a), as a thick wavy vapor layer begins to form along the heated wall beneath the liquid layer. Interestingly, Zhang *et al.* encountered the *Wavy Vapor Layer Regime* at $\theta = 0°$ and 315° only at high mass velocities. This difference in CHF- behavior can be explained by the finite inlet void fraction in the present study producing higher flow velocities and higher shear stresses. The liquid layer adjacent to the heated wall is now sandwiched between the central vapor core and newly developed wavy vapor layer, and breaks apart in the middle region in the form of liquid ligaments, which provide partial wetting of the heated wall downstream.

The *Pool Boiling Regime* is encountered in the present study only at $\theta = 45°$ as depicted in Figure 5.2(b) for the inlet region. Here too, the flow enters the heated portion of the channel fully separated, with the heated wall covered with a liquid layer beneath a thick vapor layer. Because of the relatively low liquid velocity, bubbles that nucleate along the heated wall are removed by buoyancy towards the vapor-liquid interface where they are released into the vapor layer. Farther downstream in the middle region, the increased void fraction increases the velocities of the liquid and vapor layers, causing vapor bubbles to coalesce along the heated wall into a fairly continuous wavy vapor layer beneath the liquid layer. The liquid layer is now sandwiched between the heated wall vapor layer and the vapor layer above. The liquid layer is gradually consumed in the flow direction, with ligaments occasionally breaking off and providing wetting for the heated wall downstream.

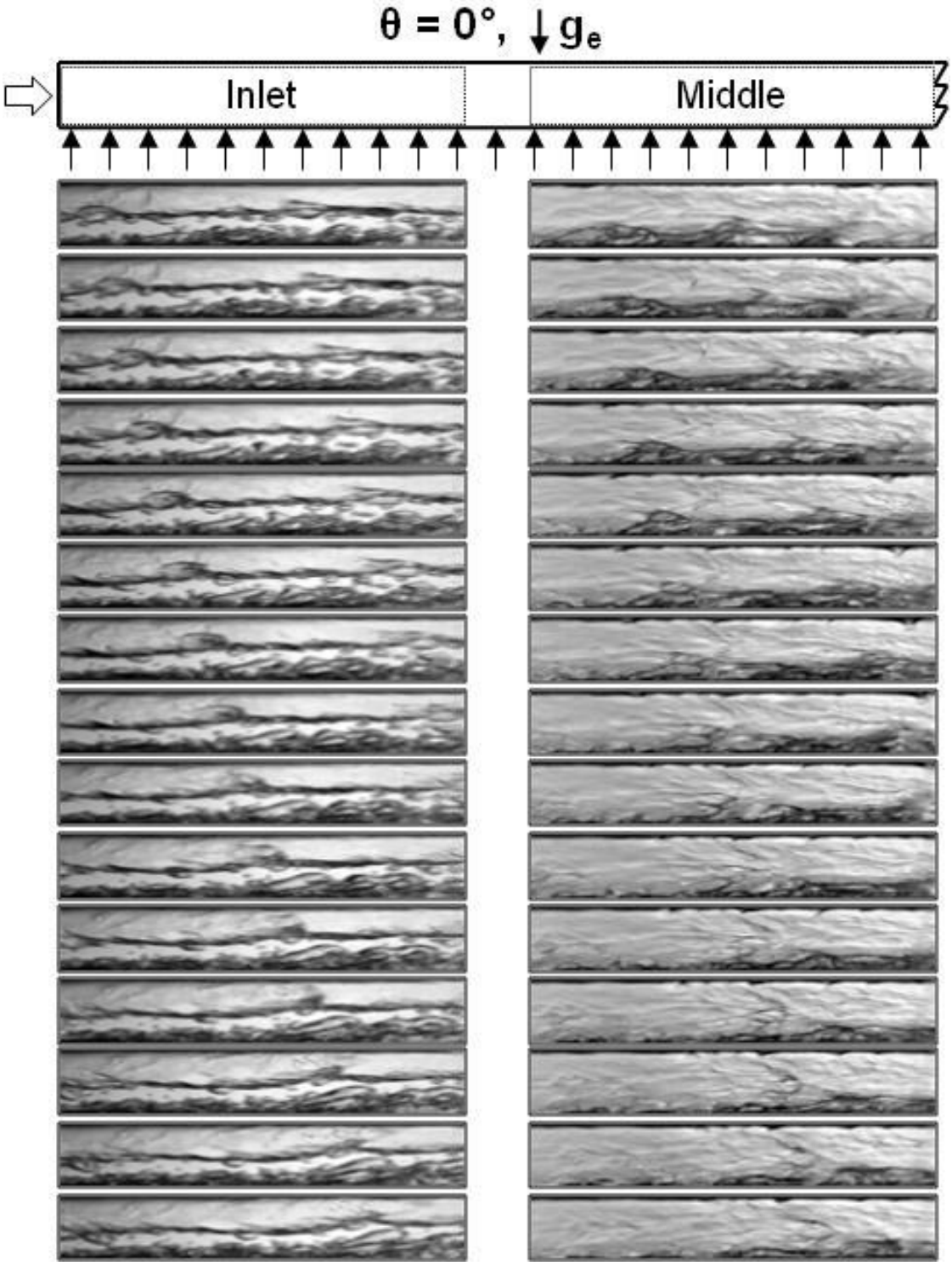

Figure 5.2(a): Sequential images of two-phase flow in inlet and middle regions of heated wall captured at CHF- for G/ρ_f = 0.224 m/s and $x_{e,in}$ = 0.01 for θ = 0°.

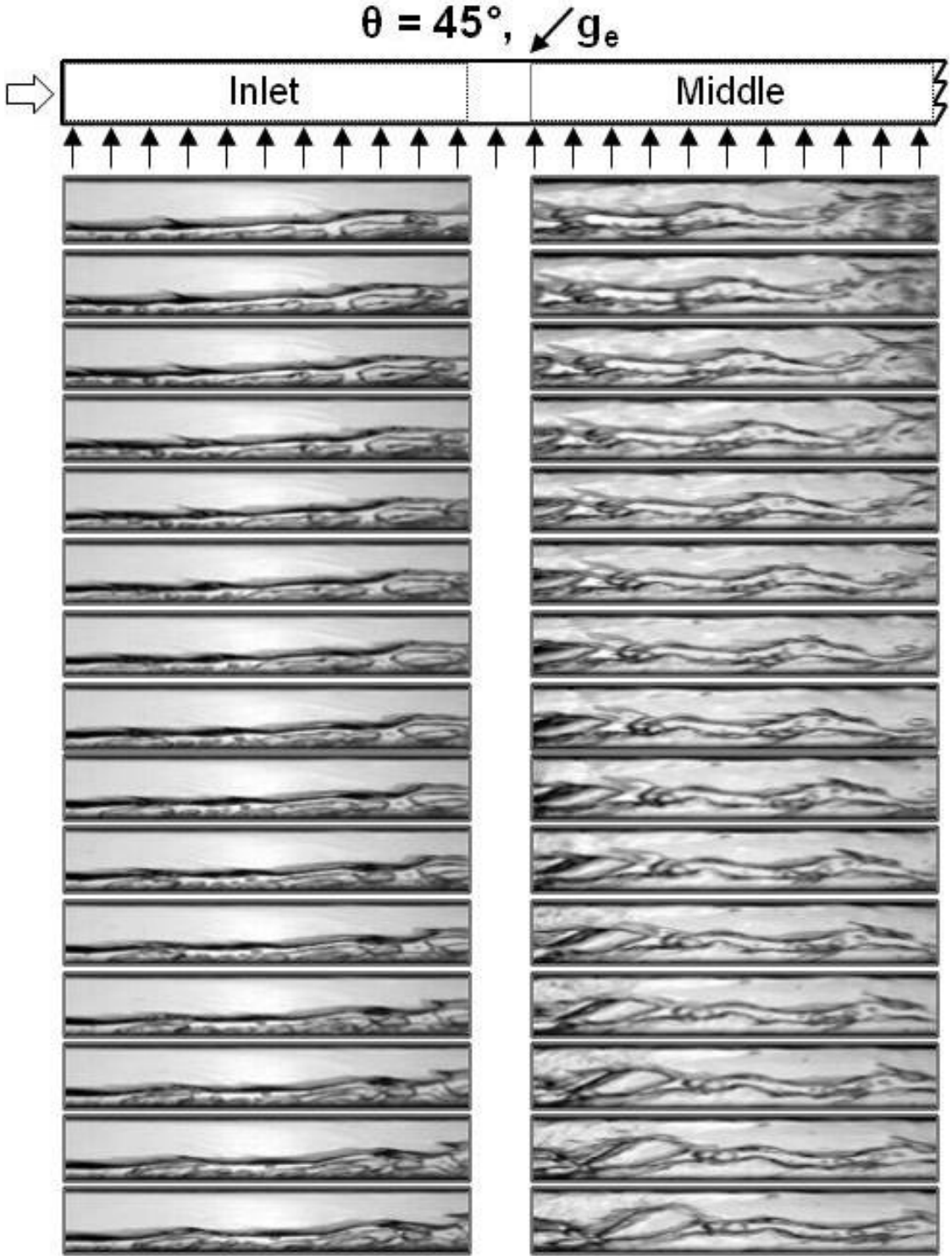

Figure 5.2(b): Sequential images of two-phase flow in inlet and middle regions of heated wall captured at CHF- for G/ρ_f = 0.224 m/s and $x_{e,in}$ = 0.01 for θ = 45°.

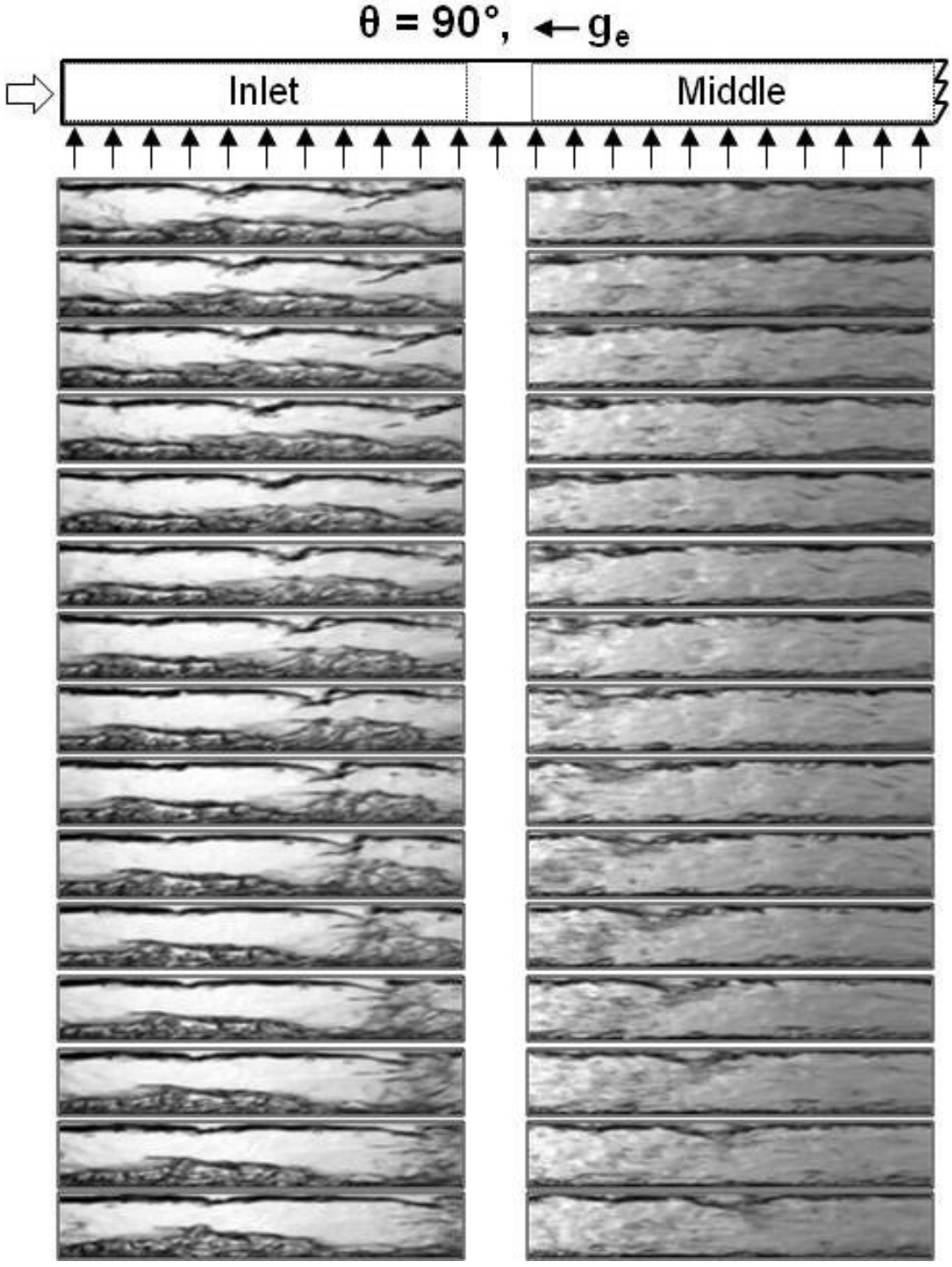

Figure 5.2(c): Sequential images of two-phase flow in inlet and middle regions of heated wall captured at CHF- for $G/\rho_f = 0.224$ m/s and $x_{e,in} = 0.01$ for $\theta = 90°$.

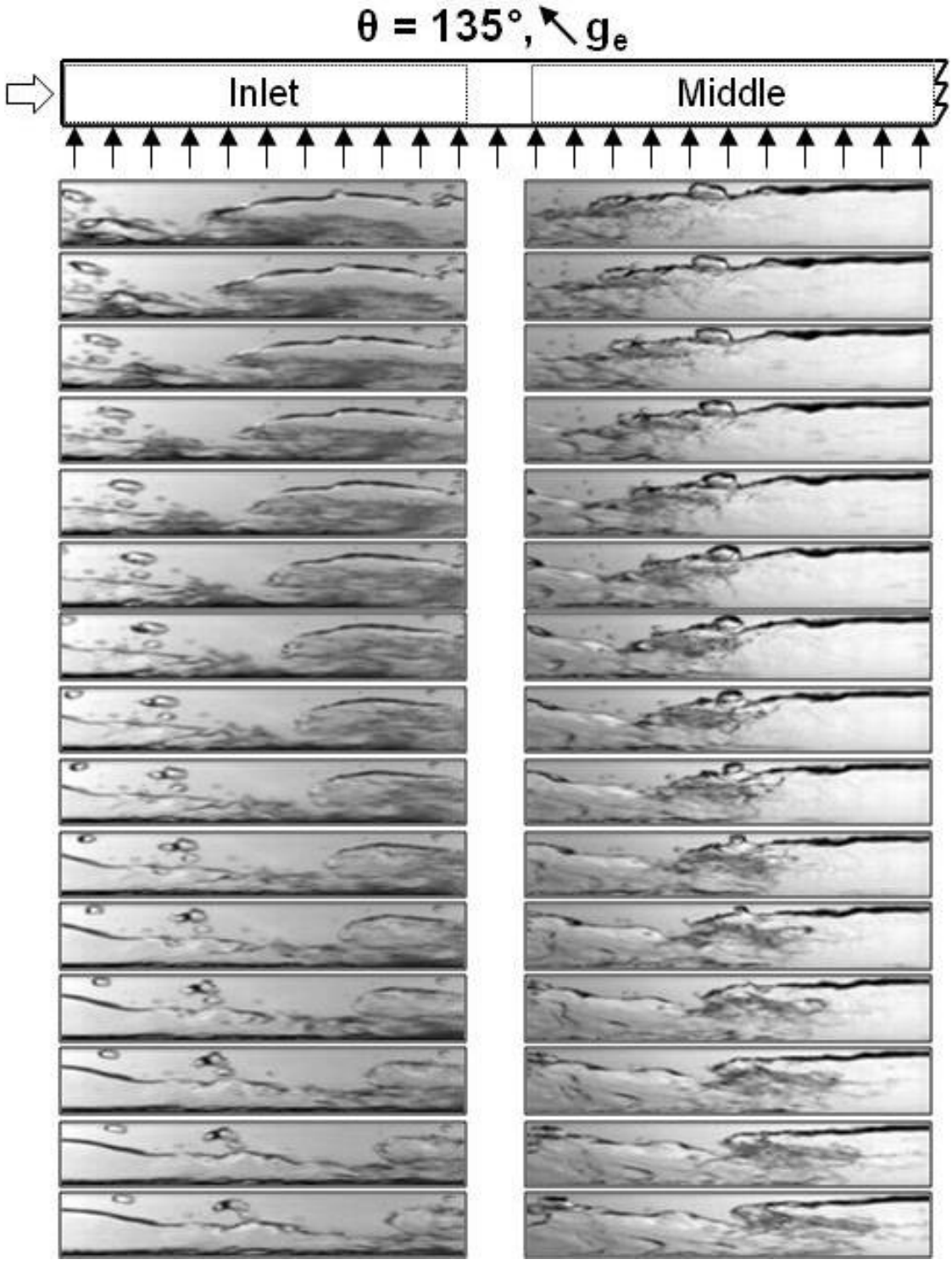

Figure 5.2(d): Sequential images of two-phase flow in inlet and middle regions of heated wall captured at CHF- for G/ρ_f = 0.224 m/s and $x_{e,in}$ = 0.01 for θ = 135°.

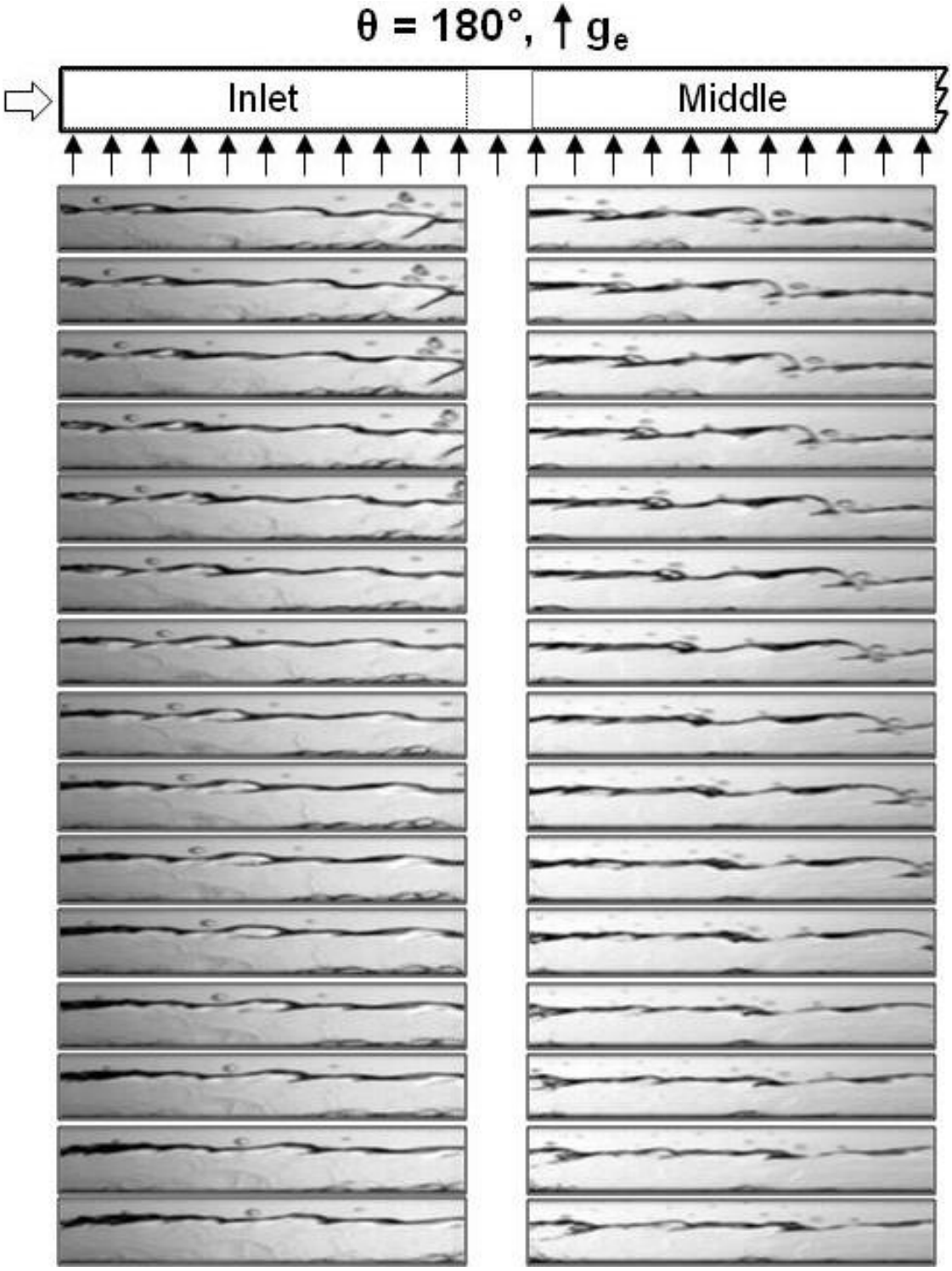

Figure 5.2(e): Sequential images of two-phase flow in inlet and middle regions of heated wall captured at CHF- for G/ρ_f = 0.224 m/s and $x_{e,in}$ = 0.01 for θ = 180°.

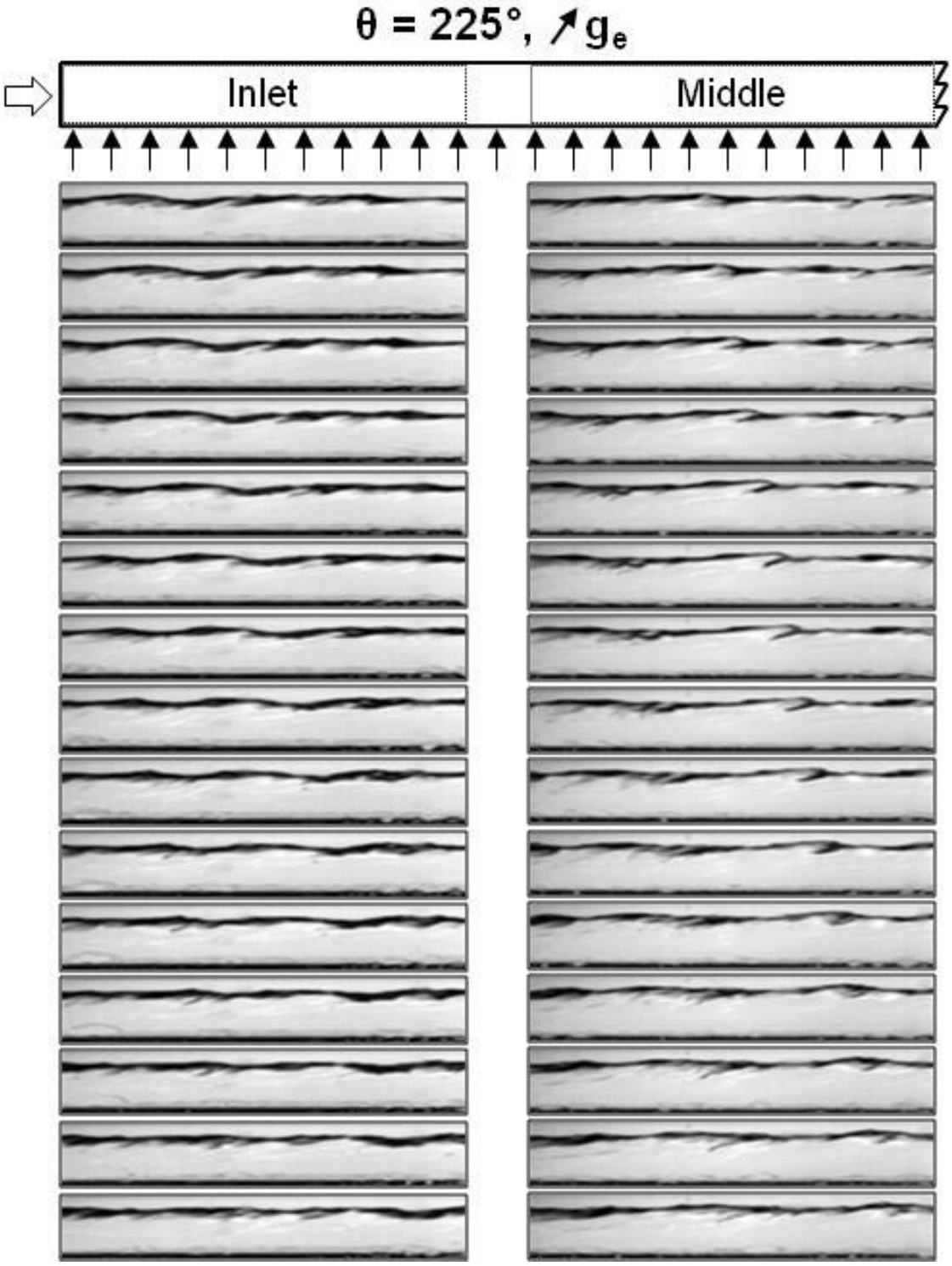

Figure 5.2(f): Sequential images of two-phase flow in inlet and middle regions of heated wall captured at CHF- for G/ρ_f = 0.224 m/s and $x_{e,in}$ = 0.01 for θ = 225°.

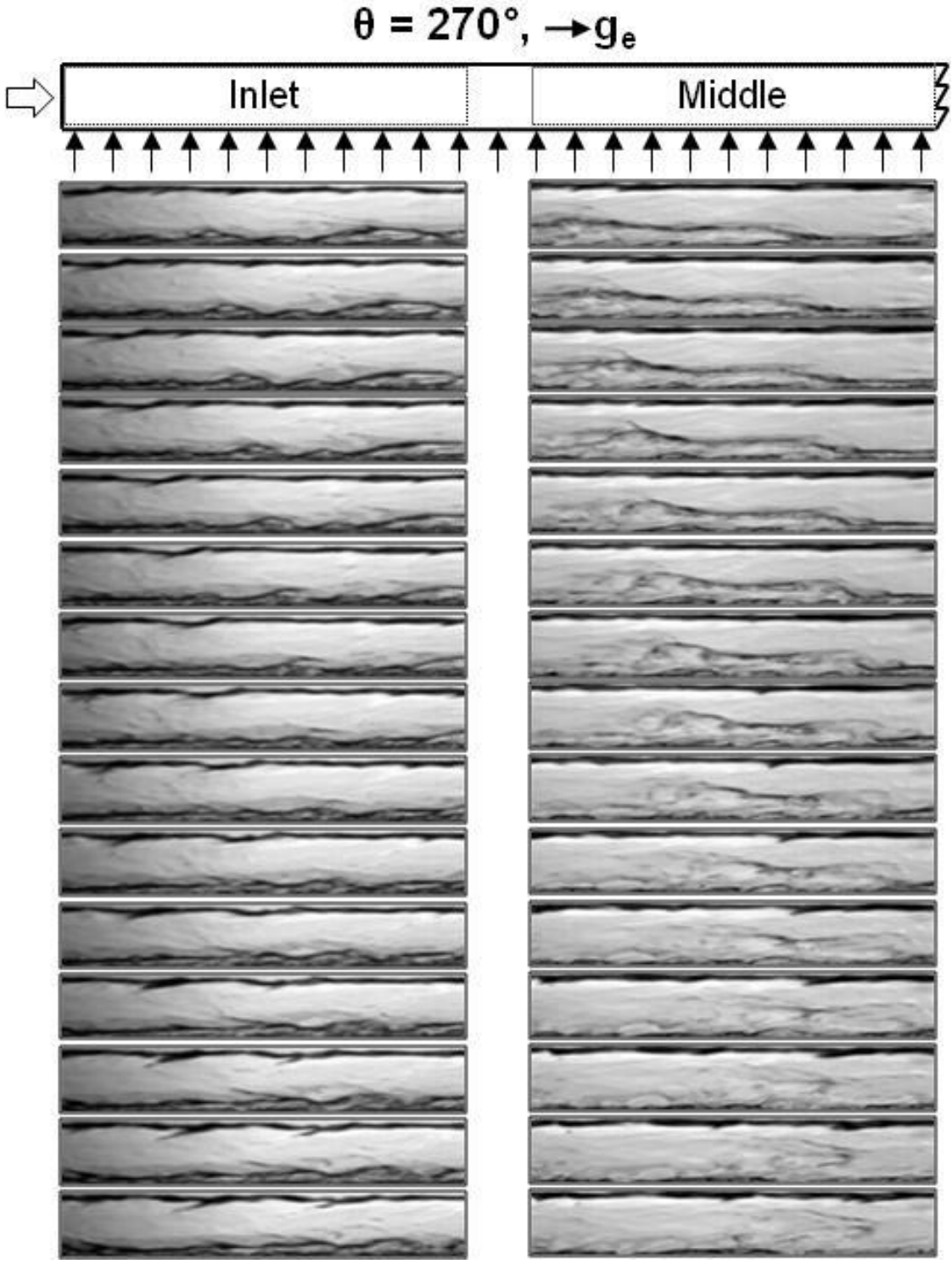

Figure 5.2(g): Sequential images of two-phase flow in inlet and middle regions of heated wall captured at CHF- for G/ρ_f = 0.224 m/s and $x_{e,in}$ = 0.01 for θ = 270°.

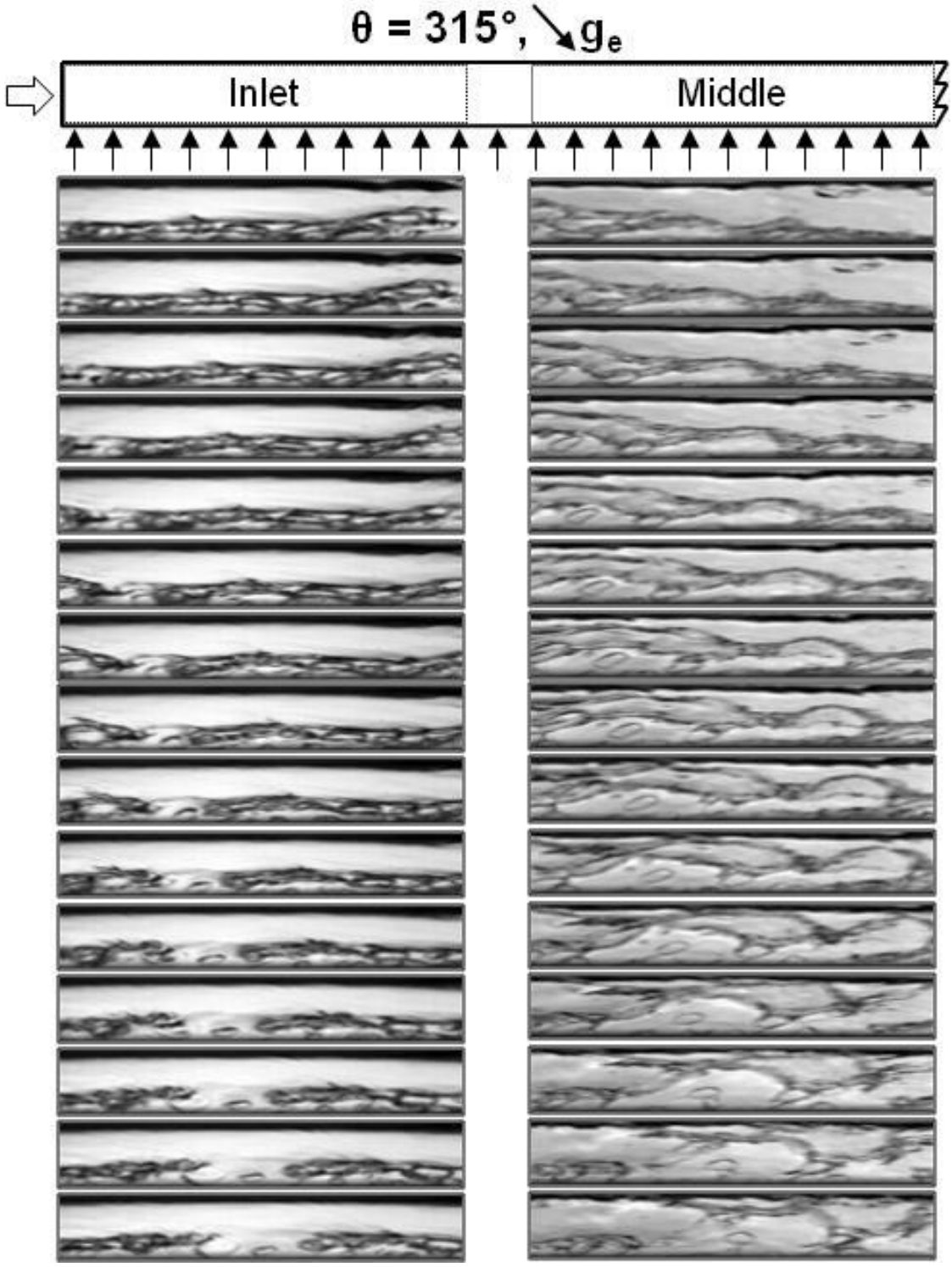

Figure 5.2(h): Sequential images of two-phase flow in inlet and middle regions of heated wall captured at CHF- for G/ρ_f = 0.224 m/s and $x_{e,in}$ = 0.01 for θ = 315°.

Figure 5.2(c) shows the interfacial behavior at CHF- for vertical upflow, $\theta = 90°$. Here, the flow entering the heated portion of the channel consists of a liquid layer covering all four channel walls, surrounding a central vapor core. At CHF-, vapor is generated within the liquid layer in contact with the heated wall, causing separation of the liquid layer in the inlet region. The vapor layer also persists along the heated wall in the middle region. This behavior is reminiscent of the *Wavy Vapor Layer Regime* identified by Zhang *et al.* [5] for $\theta = 90°$ and $x_{e,in} \leq 0$. Farther downstream, the separated liquid layer adjacent to the heated wall suffers appreciable thinning due to an axial increase in shear stresses brought upon by the axial acceleration associated with phase change.

Figure 5.2(d) shows sequential images for CHF- at $\theta = 135°$. Here, the flow enters the heated portion of the channel with vapor stratified against the heated wall, and liquid flowing against the opposite insulated wall at low velocity. This behavior is characteristic of the *Stratification Regime*. But unlike the other stratified regimes corresponding to $\theta = 180°$ and 225°, CHF- at $\theta = 135°$ is associated with appreciable interfacial waviness. With the liquid separated from the heated wall, this orientation yields a low CHF of only 8.90 W/cm^2.

For the horizontal downward-facing heated wall orientation, $\theta = 180°$, and downflow with a downward-facing heated wall, $\theta = 225°$, CHF- at $G/\rho_f = 0.224$ m/s and $x_{e,in} = 0.01$ follows a clear *Stratification Regime* as depicted in Figures 5.2(e) and 5.2(f), respectively. Here, the flow is well separated, with a vapor layer stratified along the heated wall, preventing the liquid beneath to access the heated wall. This behavior results in low CHF values and the stratified vapor layer is initiated immediately at the inlet. Relatively small velocity differences between the liquid and vapor layers impart stability to the liquid-vapor interface, ensuring clear separation and stratification of the vapor layer, and limited access of liquid to the heated wall. Interestingly, the behavior depicted in Figure 5.2(f) for $\theta = 225°$ yields an unusually small CHF of only 1.85 W/cm^2.

Figure 5.2(g) shows CHF- behavior for vertical downflow, $\theta = 270°$. Like vertical upflow, $\theta = 90°$, the flow entering the channel at $\theta = 270°$ is comprised of a liquid layer that covers all four channel walls surrounding a central vapor core. Vapor production within the liquid layer in contact with the heated wall causes separation of the

liquid layer in the inlet region, which is consistent with the *Wavy Vapor Layer Regime*. While this CHF- behavior may appear to resemble that observed at θ = 90°, there are appreciable differences between the two orientations, with the buoyancy aiding the vapor removal for θ = 90° and resisting the flow for θ = 270°. This difference is manifest in the middle region where a much thicker vapor layer for θ = 270° contributes to more significant wall dryout. It should be noted here that Zhang *et al.* [29] identified three distinct CHF regimes for $x_{e,in} \leq 0$ at θ = 270°: (i) *Vapor Counterflow Regime* at very low mass velocities, where buoyancy exceeds liquid forces, (ii) *Stagnation Regime,* where the two forces are equal, and (iii) *Separated Concurrent Vapor Flow Regime*, where liquid forces exceed buoyancy. Interestingly, the *Vapor Counterflow Regime* and *Stagnation Regime* were never observed in the present study corresponding to $x_{e,in} > 0$. This is apparently the result of the greatly increased flow velocities when the flow enters the channel as a two-phase mixture.

Figure 5.3 provides additional details concerning CHF- at θ = 135° for a very low mass velocity of G/ρ_f = 0.126 m/s and $x_{e,in}$ = 0.01. Here, the flow enters the channel with vapor stratified against the heated wall in accordance with the *Stratification Regime*, with liquid flowing against the opposite insulated wall at very low velocity. The large velocity difference between the vapor and liquid renders the interface highly unstable in the middle region, where the interfacial amplitude increases greatly and the interfacial waves cause liquid droplets and ligaments to be deposited onto the heated wall. Interestingly, this liquid replenishment mechanism caused this orientation to produce the highest CHF of all the downward-facing heated wall orientations for G/ρ_f = 0.126 m/s.

5.1.2 CHF Regimes at Intermediate Mass Velocity

Figure 5.4(a)-5.4(h) show sequential images for all orientations at G/ρ_f = 0.398 m/s and $x_{e,in}$ = 0.01. Because of the relatively high mass velocity, there is greater interfacial instability for all upward-facing heated wall orientations of θ = 315°, 0°, and 45°, and better replenishment of the heated wall by liquid ligaments downstream, and therefore higher CHF than those corresponding to G/ρ_f = 0.224 m/s and $x_{e,in}$ = 0.01. CHF- for these orientations is consistent with the *Wavy Vapor Layer Regime.* For

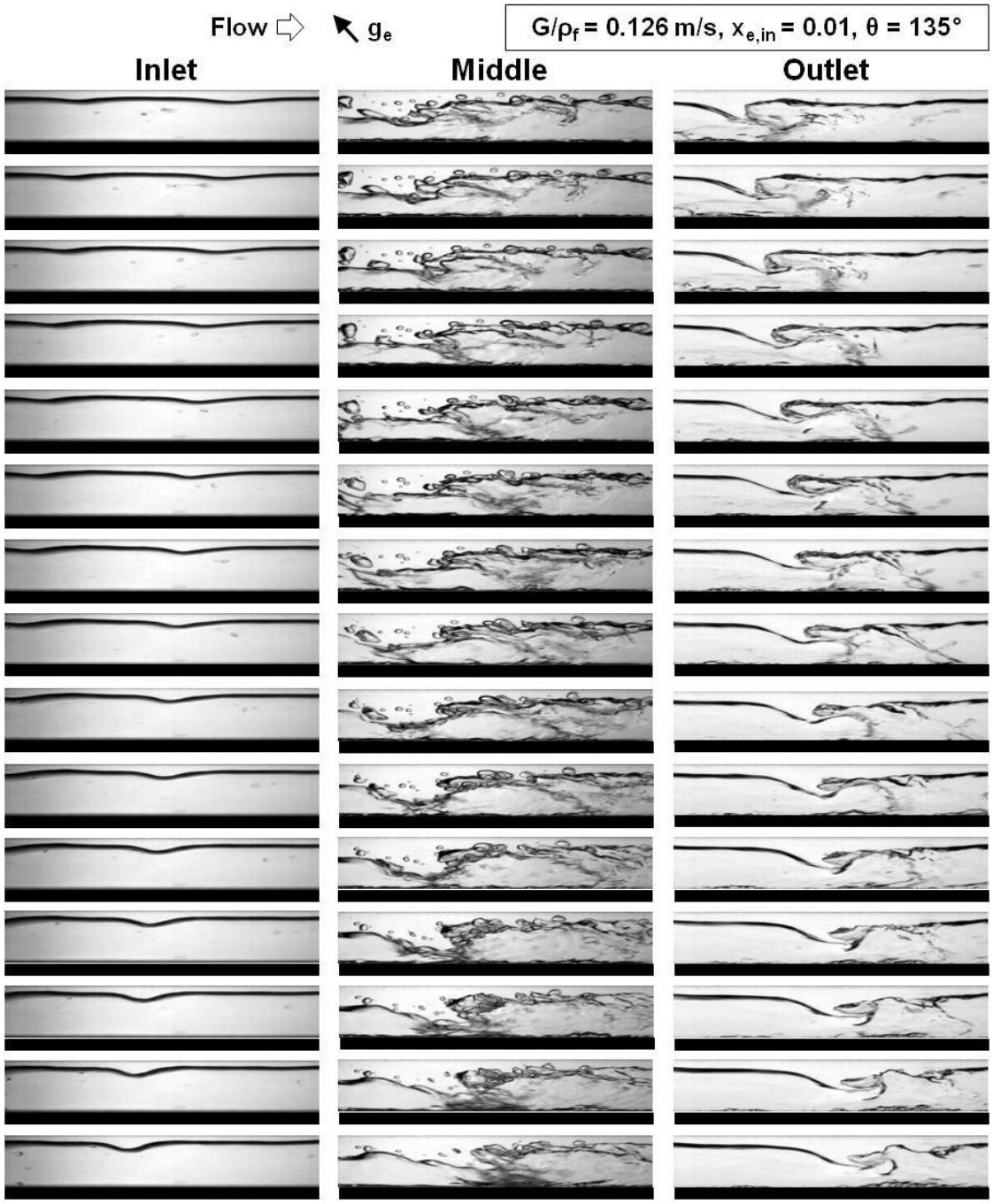

Figure 5.3: Sequential images of inlet, middle, and outlet regions depicting *Stratification Regime* with interfacial waves observed at CHF- for θ = 135°, G/ρ_f = 0.126 m/s and $x_{e,in}$ = 0.01. The heated wall is indicated by a rectangular black strip.

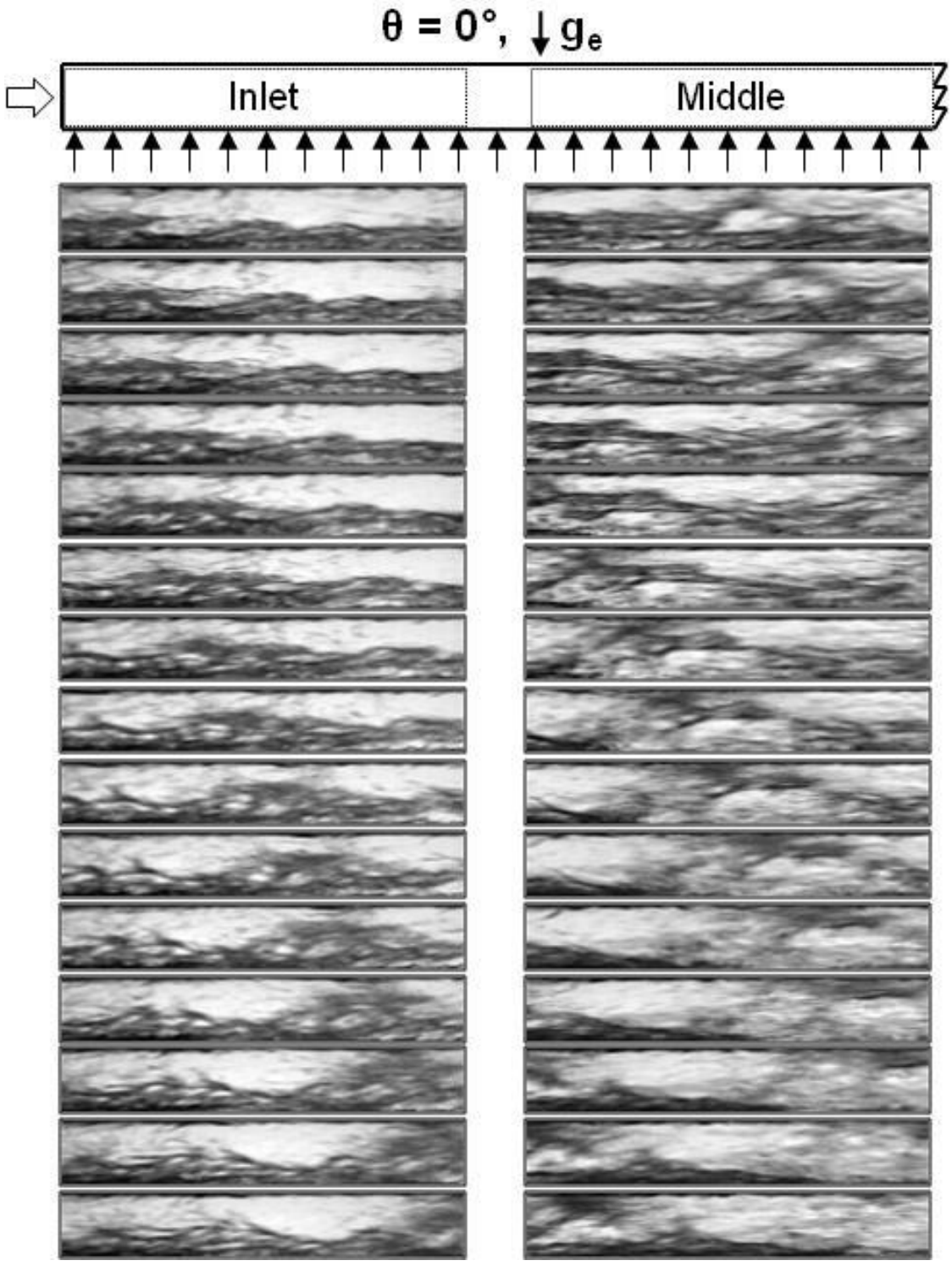

Figure 5.4(a): Sequential images of two-phase flow in inlet and middle regions of heated wall captured at CHF- for $G/\rho_f = 0.398$ m/s and $x_{e,in} = 0.01$ for $\theta = 0°$.

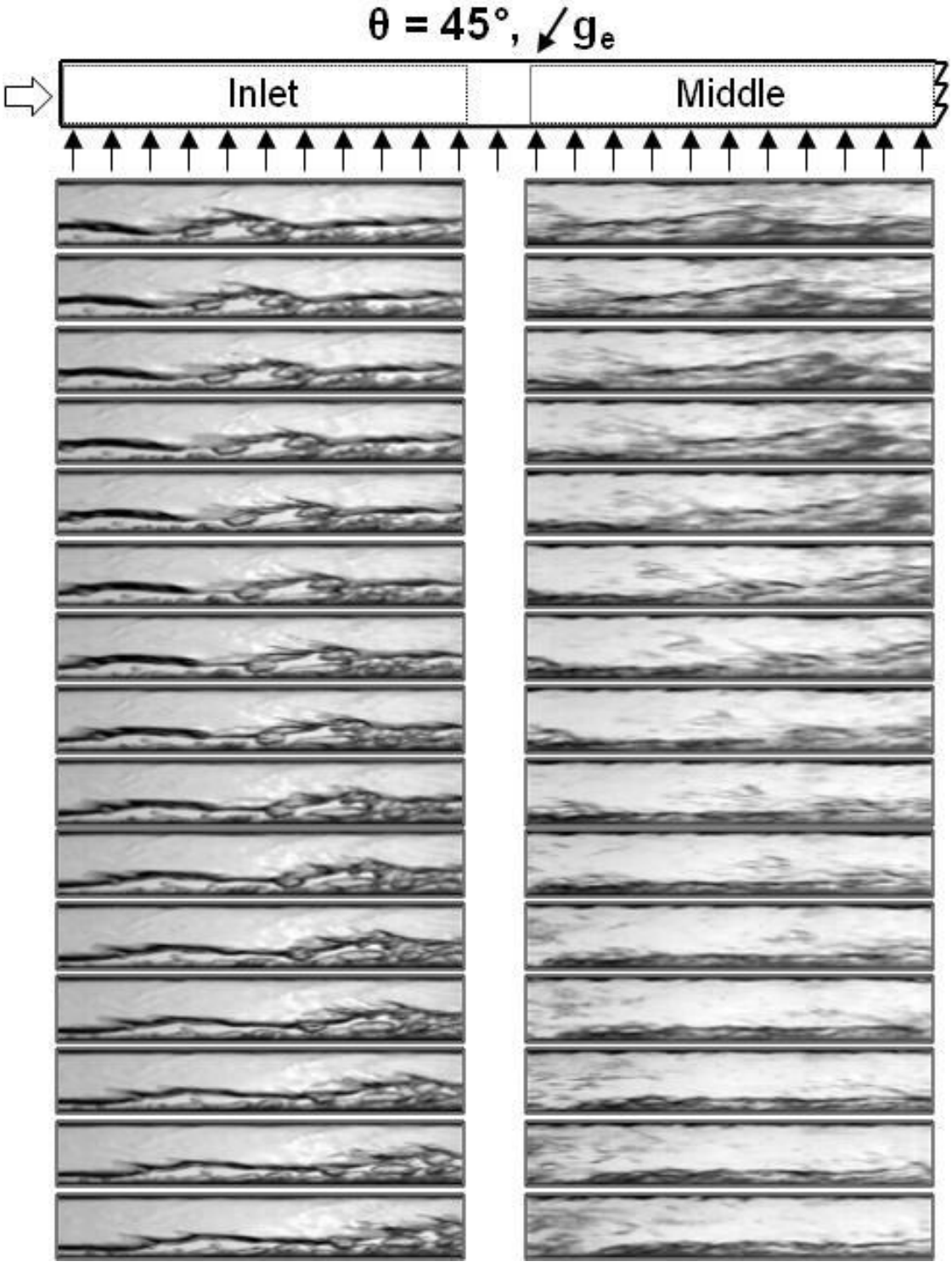

Figure 5.4(b): Sequential images of two-phase flow in inlet and middle regions of heated wall captured at CHF- for G/ρ_f = 0.398 m/s and $x_{e,in}$ = 0.01 for θ = 45°.

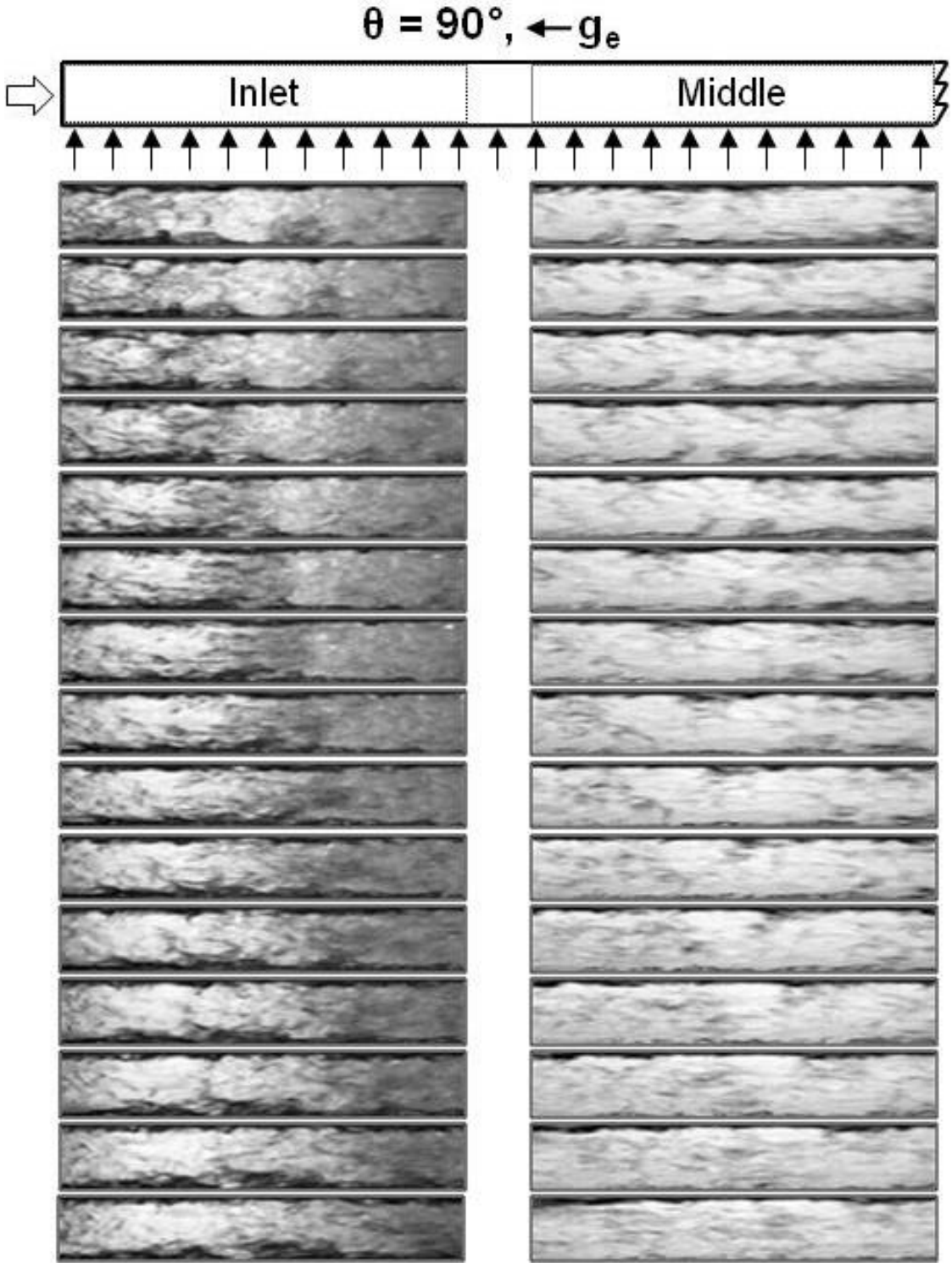

Figure 5.4(c): Sequential images of two-phase flow in inlet and middle regions of heated wall captured at CHF- for $G/\rho_f = 0.398$ m/s and $x_{e,in} = 0.01$ for $\theta = 90°$.

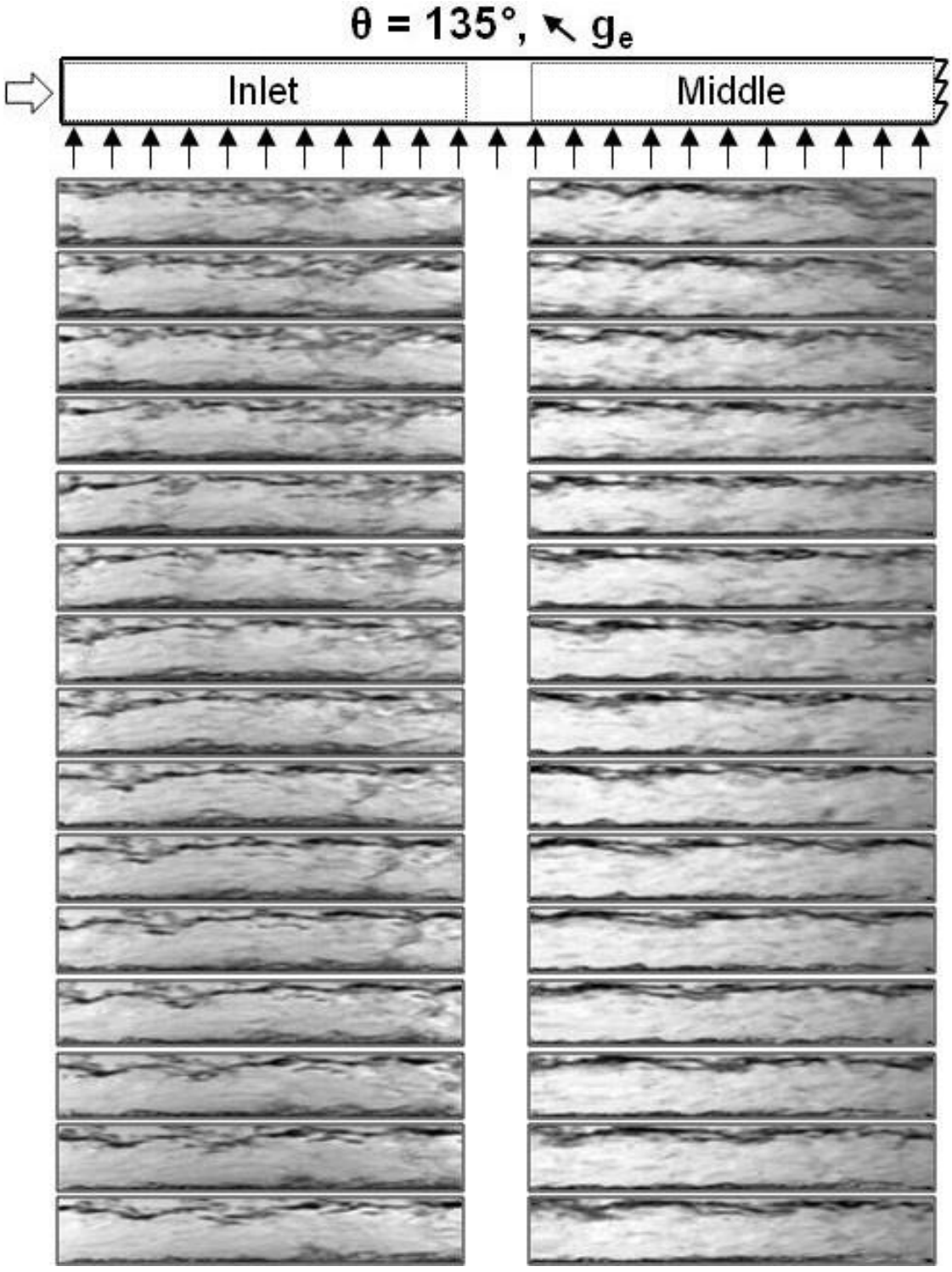

Figure 5.4(d): Sequential images of two-phase flow in inlet and middle regions of heated wall captured at CHF- for G/ρ_f = 0.398 m/s and $x_{e,in}$ = 0.01 for θ = 135°.

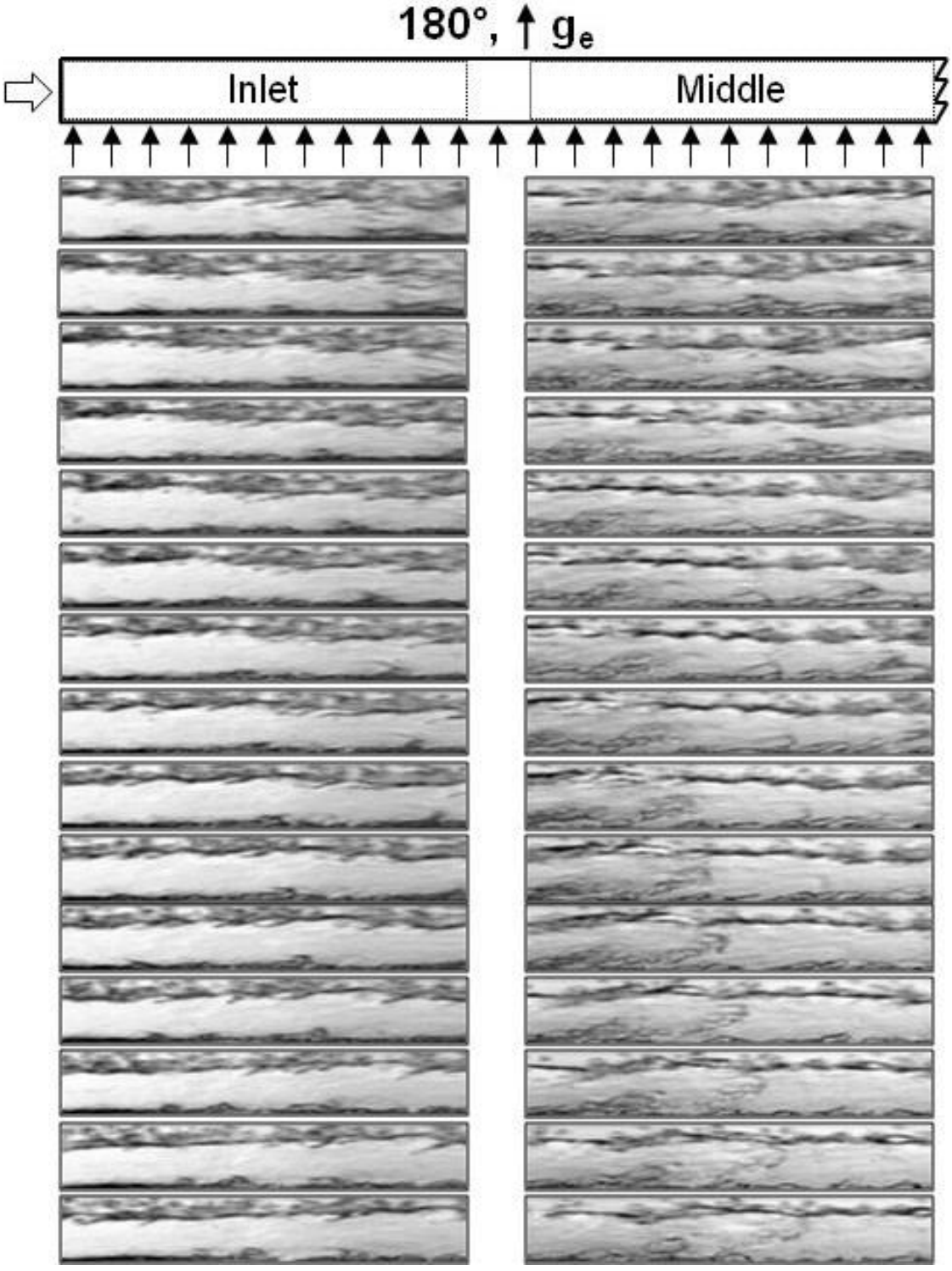

Figure 5.4(e): Sequential images of two-phase flow in inlet and middle regions of heated wall captured at CHF- for $G/\rho_f = 0.398$ m/s and $x_{e,in} = 0.01$ for $\theta = 180°$.

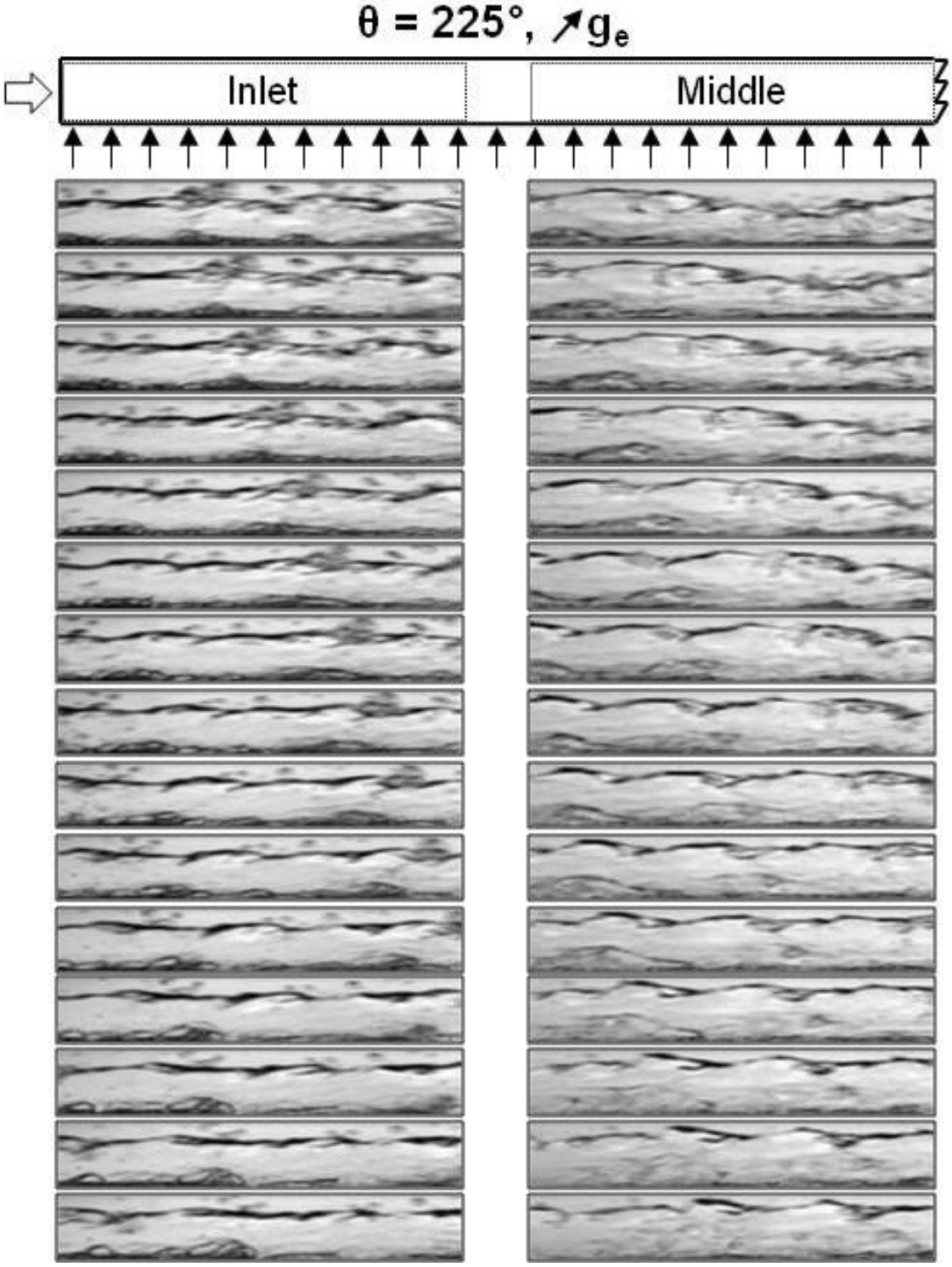

Figure 5.4(f): Sequential images of two-phase flow in inlet and middle regions of heated wall captured at CHF- for G/ρ_f = 0.398 m/s and $x_{e,in}$ = 0.01 for θ = 225°.

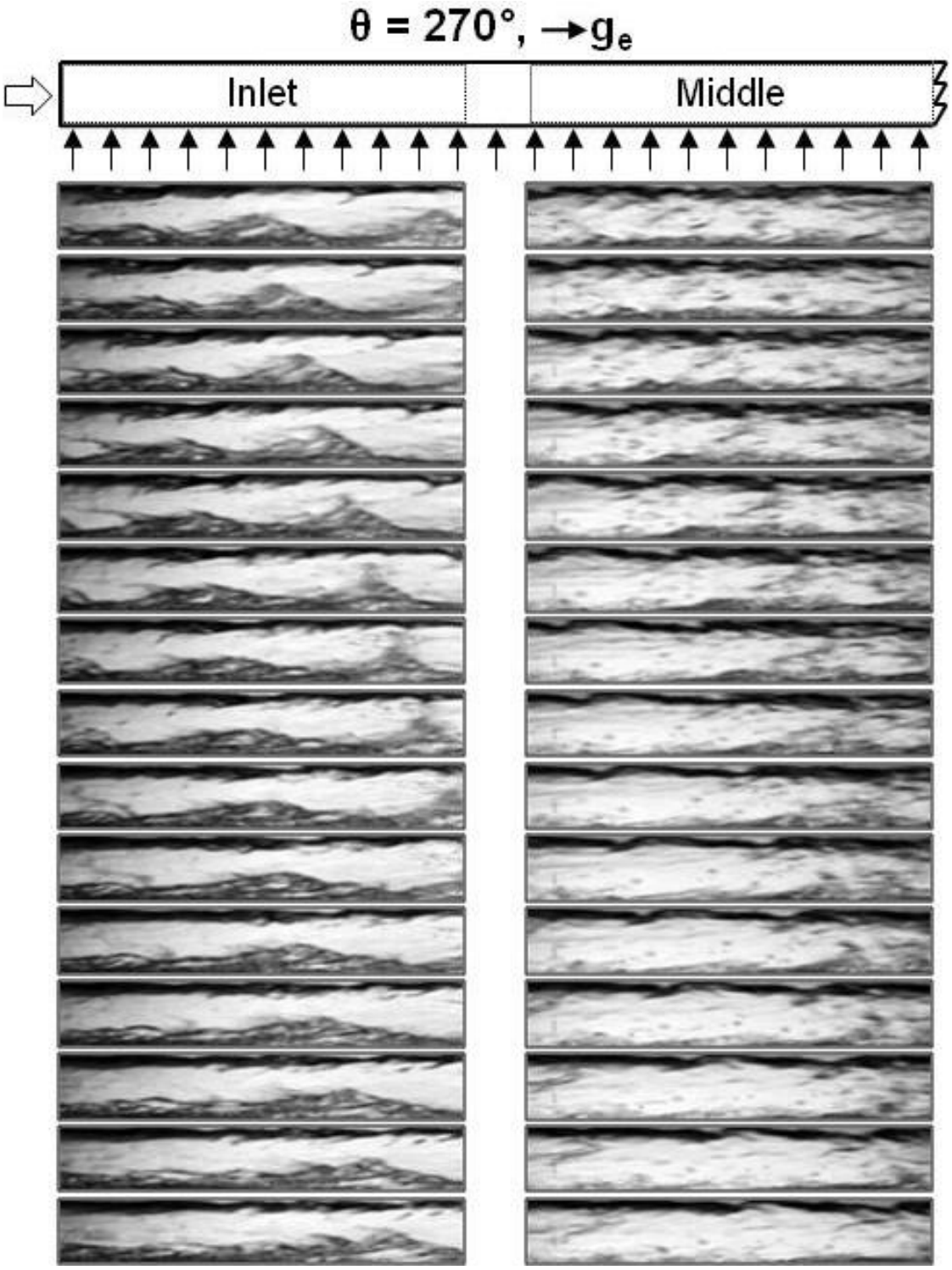

Figure 5.4(g): Sequential images of two-phase flow in inlet and middle regions of heated wall captured at CHF- for G/ρ_f = 0.398 m/s and $x_{e,in}$ = 0.01 for θ = 270°.

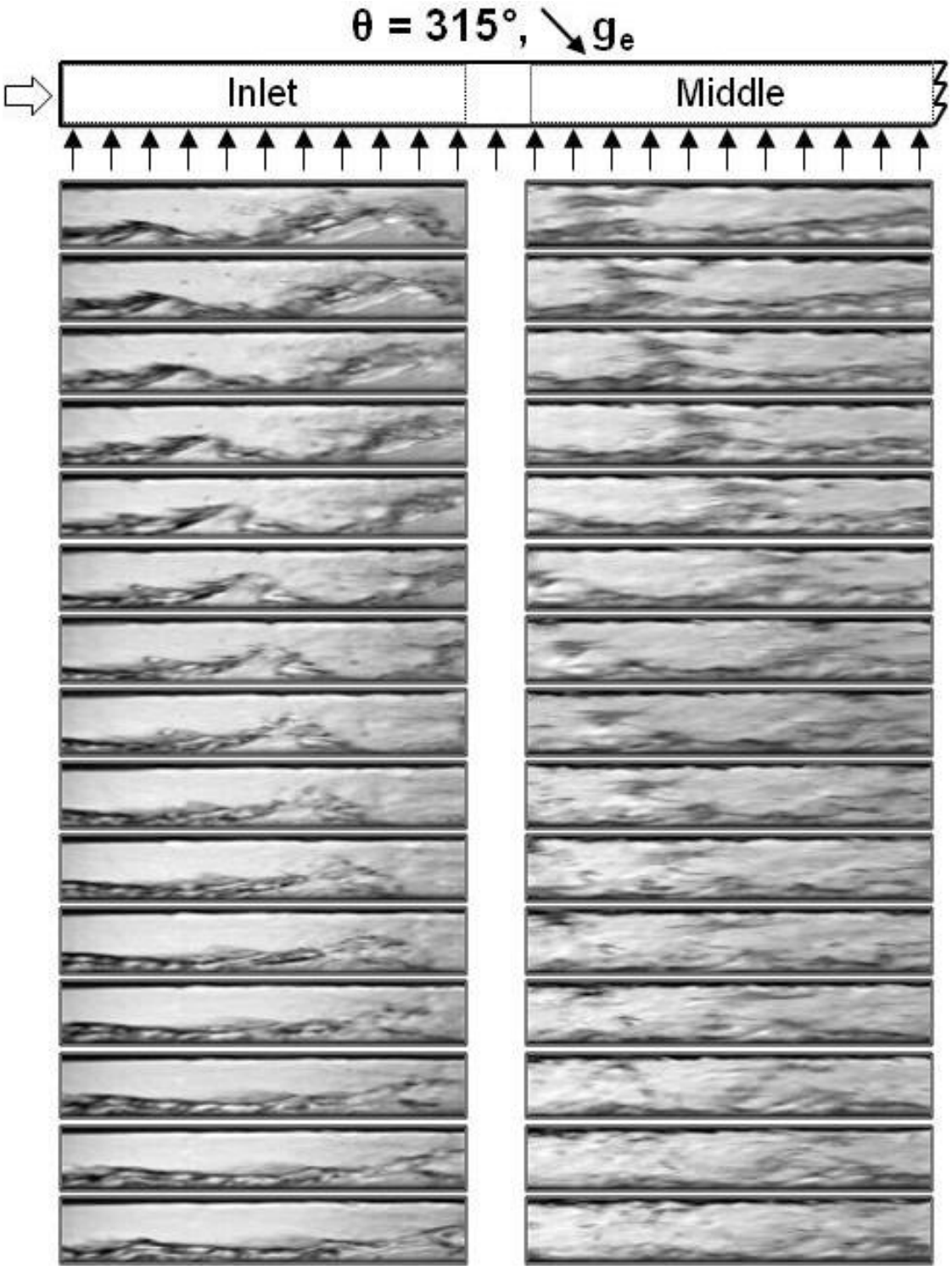

Figure 5.4(h): Sequential images of two-phase flow in inlet and middle regions of heated wall captured at CHF- for G/ρ_f = 0.398 m/s and $x_{e,in}$ = 0.01 for θ = 315°.

vertical upflow, $\theta = 90°$, CHF- is associated with the *Wavy Vapor Layer Regime,* similar to that observed for $G/\rho_f = 0.224$ m/s and $x_{e,in} = 0.01$. Interestingly, this behavior is also prevalent at $G/\rho_f = 0.398$ m/s for all downward-facing heated wall orientations ($\theta = 135°$, 180° and 225°), as well as for vertical downflow ($\theta = 270°$). These findings prove that increasing mass velocity imparts uniformity in CHF mechanism regardless of orientation.

5.2 CHF Results and Predictions

Figures 5.5(a) and 5.5(b) show CHF variations with orientation for $x_{e,in} = 0.01$ and 0.19, respectively, for different mass velocities. There are obvious similarities in these variations for different values of G/ρ_f and $x_{e,in}$, with higher CHF values achieved for upward-facing heated wall orientations (θ = 315°, 0°, and 45°) and low values for downward-facing heated wall orientations (θ = 135°, 180° and 225°). These trends are consistent in trend with those of Zhang *et al.* [4,5] for $x_{e,in} \leq 0$. Another obvious trend for each $x_{e,in}$ is the significant variation in CHF for low compared to high G/ρ_f. For example, the data in Fig. 5.5(a) corresponding to the two lowest mass velocities of G/ρ_f = 0.126 and 0.224 m/s, show appreciable reduction in CHF for several orientations. For all downward-facing heated wall orientations (θ = 135°, 180° and 225°), weak inertia at the two lowest mass velocities allows buoyancy to stratify the vapor along the heated wall, resulting in very low CHF values. CHF is also low for vertical downflow (θ = 270°), where buoyancy causes the vapor flow to impede that of the liquid, and compromises liquid replenishment of the wall. The trends in Figure 5.5(b) for $x_{e,in} = 0.19$ are similar to those for $x_{e,in}$ = 0.01. However, CHF values are higher for the higher inlet quality. Notice also that the influence of orientation on CHF for G/ρ_f = 0.398 m/s is greatly reduced for $x_{e,in} = 0.19$ compared to $x_{e,in} = 0.01$. These trends point to increasing mass velocity and inlet quality as two very effective means at combating the influence of buoyancy on flow boiling CHF.

Figure 5.6 shows the variation of measured CHF with orientation for the limiting mass velocities of G/ρ_f = 0.126 and 0.995 m/s and $x_{e,in} = 0.01$. Also shown for G/ρ_f = 0.995 m/s are CHF predictions based on the *Interfacial Lift-off Model*, which are in good

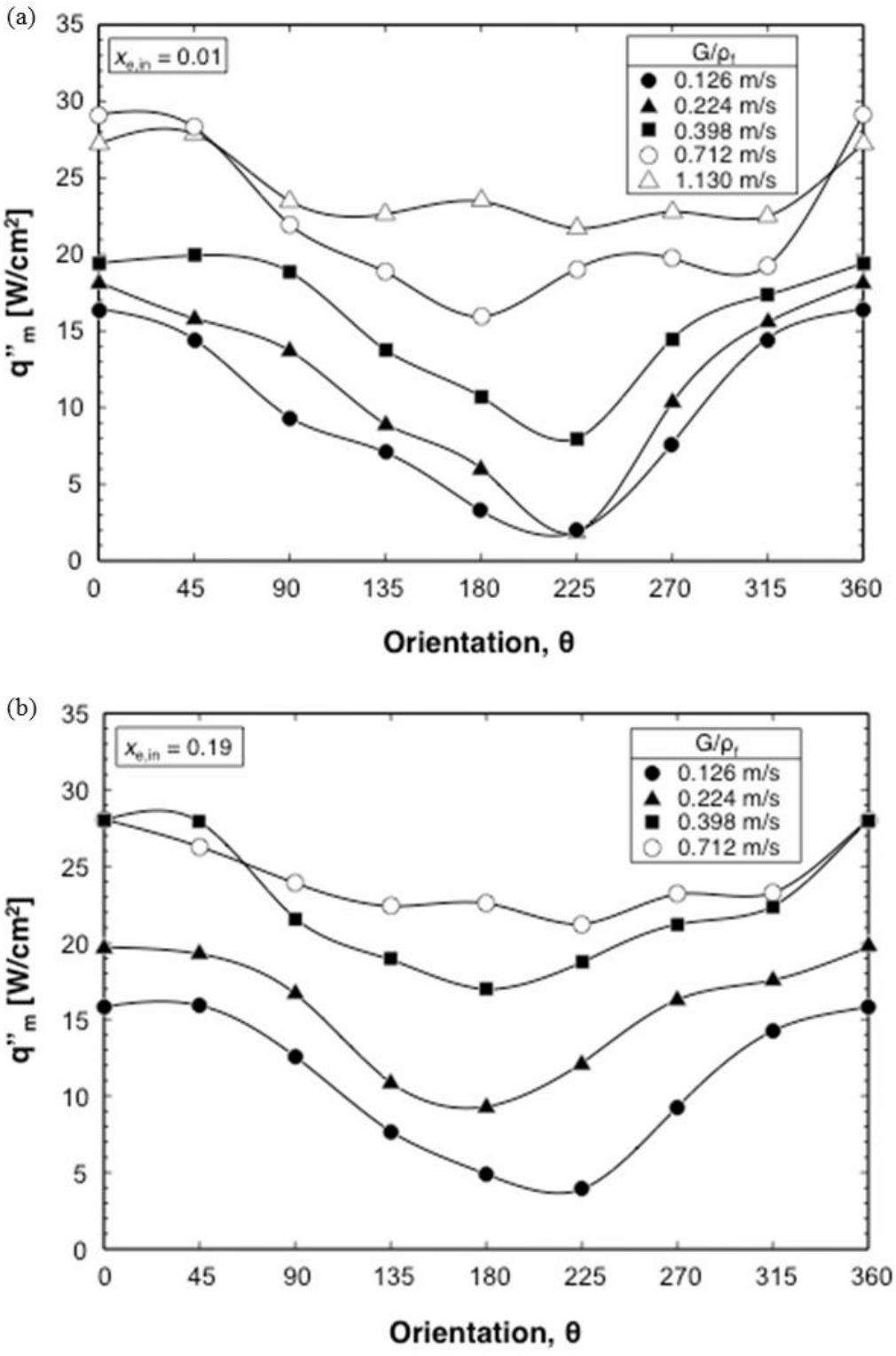

Figure 5.5: Variation of CHF with flow orientation for different mass velocities at (a) $x_{e,in}$ = 0.01 and (b) $x_{e,in}$ = 0.19.

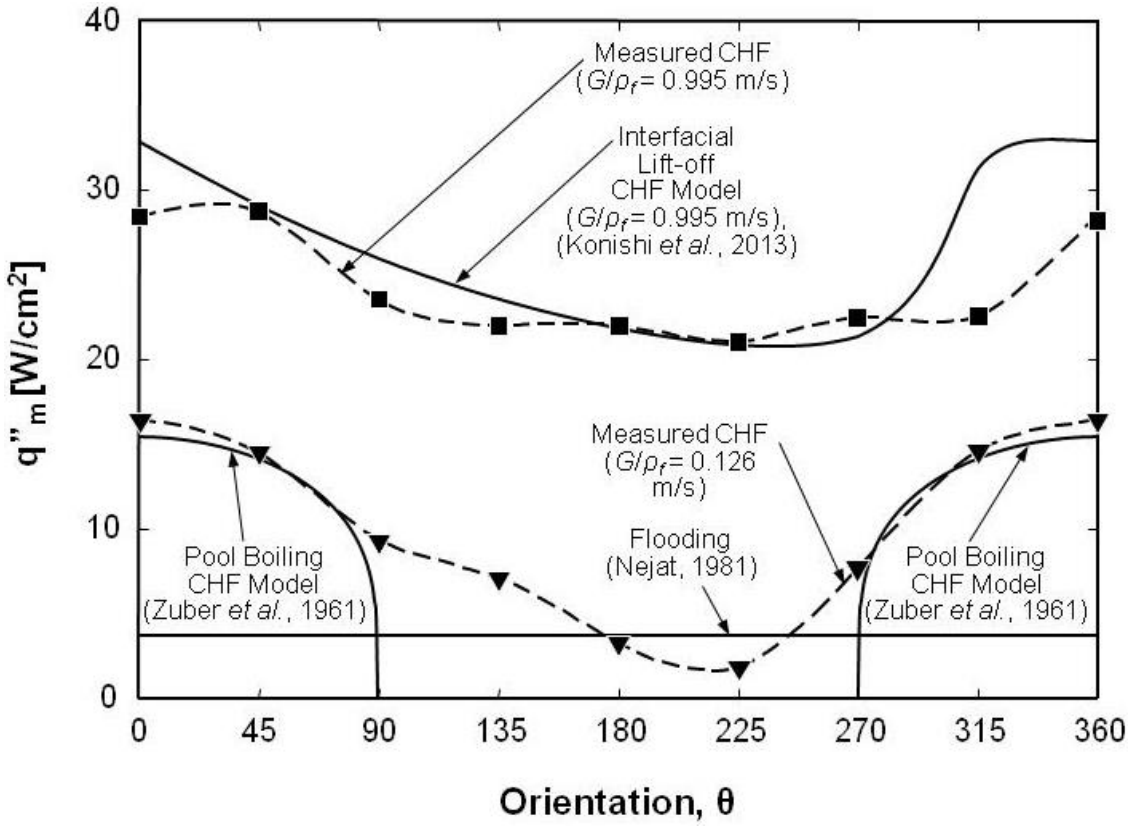

Figure 5.6: Comparison of CHF data for lowest and highest mass velocities and $x_{e,in}$ = 0.01 with predictions based on previous models and correlations.

agreement with the experimental data. For G/ρ_f = 0.126 m/s, Figure 5.6 also shows predictions of the classical pool boiling model of Zuber *et al.* [7],

$$q''_m = 0.131\rho_g h_{fg}\left[\frac{\sigma(\rho_f-\rho_g)g_e\cos\theta}{\rho_g^2}\right]^{1/4}. \tag{5.1}$$

Figure 5.6 includes predictions based on a relation by Nejat [58] for CHF resulting from flooding,

$$q''_m = 0.36\left(\frac{L}{D_h}\right)^{0.1}\left(\frac{A}{A_h}\right)\rho_g h_{fg}\left[\frac{(\rho_f-\rho_g)g_e D_h}{\rho_g}\right]^{1/2}\left[1+\left(\frac{\rho_g}{\rho_f}\right)^{1/4}\right]^{-2}, \tag{5.2}$$

where L, D_h, A, and A_h are the heated length, hydraulic diameter, channel cross-sectional area, and heated area, respectively. Notice how, for the low mass velocity, the Zuber *et al.* model provides good predictions for horizontal and near-horizontal upward-facing heated wall orientations (θ = 315°, 0° and 45°).

5.3 Overall Methodology for Overcoming Influence of Gravity on Flow Boiling CHF

The method used to develop criteria for overcoming the effects of gravity on flow boiling CHF with $x_{e,in} > 0$ is based on the technique developed by Zhang *et al.* [5] for $x_{e,in} \leq 0$. The present criteria for $x_{e,in} > 0$ are complicated by the influence of inlet void fraction. Introduced below are criteria for:

(1) Overcoming the influence of gravity perpendicular to the heated wall based on hydrodynamic instability analysis of the vapor-liquid interface,

(2) Overcoming the influence of gravity opposite to the fluid flow. This gravity component governs vapor removal (or flooding for low mass velocities and downflow orientations) along the flow direction, and

(3) Ensuring that the wavelength of the liquid-vapor interface is smaller than the heated length to facilitate liquid contact with wall.

5.3.1 Criterion for Negating Influence of Component of Gravity Perpendicular to Heated Wall

Classical instability theory are based on the assumption of a sinusoidal vapor-liquid interface. Potential flow relations coupled with appropriate velocity boundary

conditions are imposed for each phase as well as along the interface in between [55,56]. Another interfacial boundary condition is that pressure difference due to the sinusoidal perturbation is balanced by surface tension. This method results in the following relation for the critical wavelength, λ_c, corresponding to a neutrally stable wave.

$$\frac{2\pi}{\lambda_c}\frac{\sigma(\rho_f+\rho_g)}{\rho_f\rho_g(U_g-U_f)^2}=\frac{1}{2}\left\{1+\sqrt{1+4\frac{(\rho_f-\rho_g)(\rho_f+\rho_g)^2\sigma g_e\cos\theta}{\rho_f^2\rho_g^2(U_g-U_f)^4}}\right\}. \tag{5.3}$$

Eq. (5.3) indicates that interfacial instability is governed by the combined influences of inertia, surface tension, and component of gravity that is perpendicular to the heated wall. Eq. (5.3) also reveals that the influence of gravity becomes negligible when

$$\left|\frac{(\rho_f-\rho_g)(\rho_f+\rho_g)^2\sigma g_e\cos\theta}{\rho_f^2\rho_g^2(U_g-U_f)^4}\right|<<\frac{1}{4}, \tag{5.4}$$

which reduces Eq. (5.3) to

$$\lambda_c=\frac{2\pi\sigma(\rho_f+\rho_g)}{\rho_f\rho_g(U_g-U_f)^2}. \tag{5.5}$$

Equation (5.4) can also be presented in terms of the Bond and Weber numbers,

$$\left|\frac{Bo}{We^2}\right|=\left|\frac{(\rho_f-\rho_g)(\rho_f+\rho_g)^2\sigma g_e\cos\theta}{\rho_f^2\rho_g^2(U_g-U_f)^4}\right|<<\frac{1}{4}, \tag{5.6}$$

where

$$Bo=\frac{(\rho_f-\rho_g)g_e\cos\theta L^2}{\sigma} \tag{5.7}$$

and

$$We=\frac{\rho_f\rho_g(U_g-U_f)^2L}{(\rho_f+\rho_g)\sigma}. \tag{5.8}$$

Because the present data correspond to saturated inlet conditions, the criterion for negating the influence of gravity perpendicular to the heated wall is a function of inlet quality, $x_{e,in}$. To develop a criterion that a designer can employ without solving the detailed two-phase flow field, a two-step approach is used. First, the criterion is examined by replacing ($U_g - U_f$) in Eqs. (5.6) and (5.8) by the known G/ρ_f. Next, the criterion is modified to account for $x_{e,in}$.

Figures 5.5(a) and 5.5(b) showed how CHF is greatly influenced by orientation for low values of G/ρ_f, especially for low inlet quality. By increasing inlet velocity and

quality, the variation in CHF between orientations is shown to diminish. To develop a systematic criterion for negating the influence of orientation, CHF data such as those shown in Figs. 5.5(a) and 5.5(b) are filtered to determine, for each value of G/ρ_f and $x_{e,in}$, if the CHF variations with orientation falls within ±25% of the average CHF for all orientations. Evidenced by the trends in Figs. 5.5(a) and 5.5(b), low values of G/ρ_f do not satisfy this criterion. Figure 5.7 shows, for all test conditions, the locus of minimum G/ρ_f values that satisfy the ±25% criterion decreases with increasing $x_{e,in}$. Also shown in the same figure are the data points that do satisfy the minimum CHF variation. Notice that G/ρ_f = 1.13 and 0.995 m/s show minimum dependence on orientation for all inlet qualities. For G/ρ_f = 0.853 m/s, the influence of orientation is negligible for $x_{e,in} \geq 0.03$ but begins to fall outside of the ±25% bounds at $x_{e,in}$ = 0.01. Proceeding to G/ρ_f = 0.712 and 0.542 m/s, the quality required to negate the influence of orientation increases to $x_{e,in}$ = 0.07 and 0.13, respectively. For $G/\rho_f \leq$ 0.398 m/s, fluid inertia is far too weak to overcome orientation effects even at high inlet qualities. The locus of minimum G/ρ_f values necessary to negate orientation effects is fitted by the relation

$$\left.\frac{G}{\rho_f}\right|_{\min} = 0.584e^{(-15.75x_{e,in})} + 0.496, \tag{5.9}$$

with a mean absolute error (MAE) of 2.17%. For $x_{e,in}$ = 0, Eq. (5.9) predicts a minimum G/ρ_f of 1.08 m/s.

Figures 5.8(a) and 5.8(b) show the variations of Bo/We^2 with orientation and velocity, where $(U_g - U_f)$ is substituted by G/ρ_f. For a fixed G/ρ_f, the magnitude of Bo/We^2 is highest for horizontal flows, θ = 0° and 180°, where $|cos\theta| = 1$, and lowest for vertical flows, θ = 90° and 270°, where $cos\theta = 0$. Notice in Fig. 13(a) how the influence of gravity is quite pronounced for G/ρ_f = 0.126 and 0.224 m/s but decreases appreciably for $G/\rho_f \geq$ 0.398 m/s. Figure 5.8(b) shows variations of Bo/We^2 for $G/\rho_f \geq$ 0.398 m/s, where low values of Bo/We^2 point to a very weak influence of orientation for high mass velocities.

Zhang *et al.* [5] developed a Bo/We^2 criterion for negating the influence of body force perpendicular to the heated wall for $x_{e,in} \leq 0$ based on G/ρ_f = 1.5 m/s, for which their database showed minimum CHF dependence on orientation. Since the present database

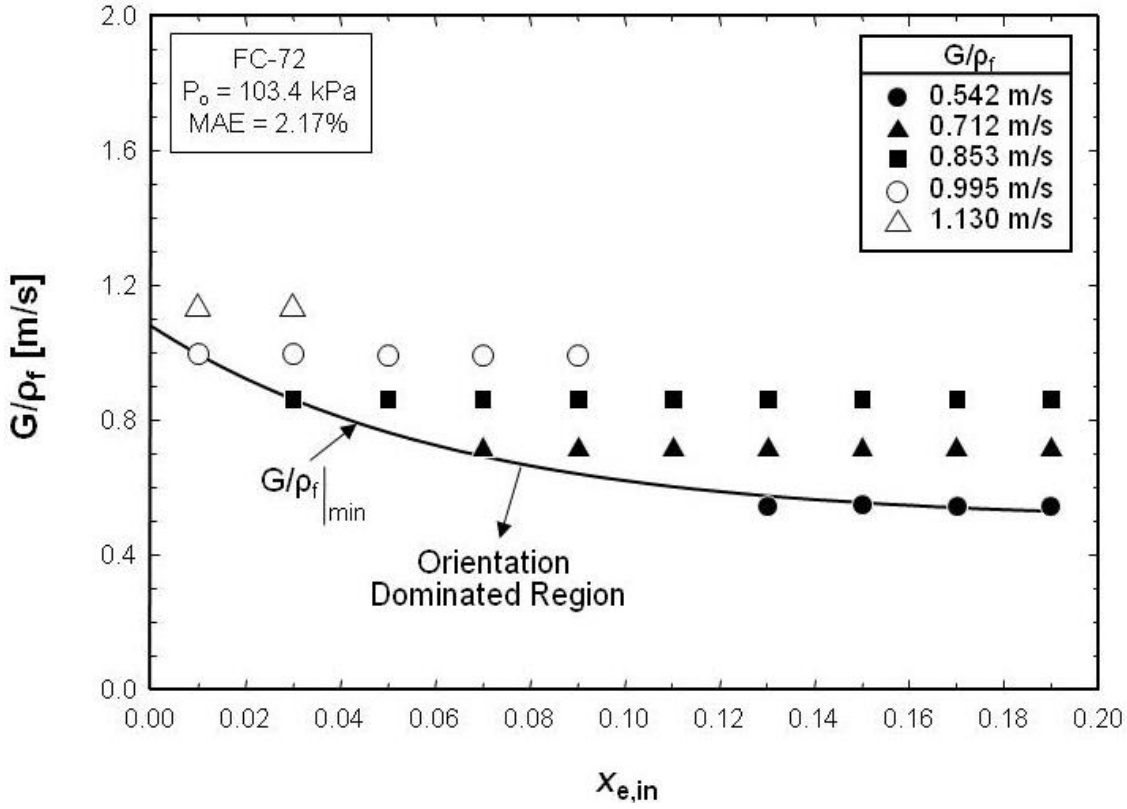

Figure 5.7: Determination of minimum G/ρ_f necessary to negate effects of orientation on CHF for different inlet qualities.

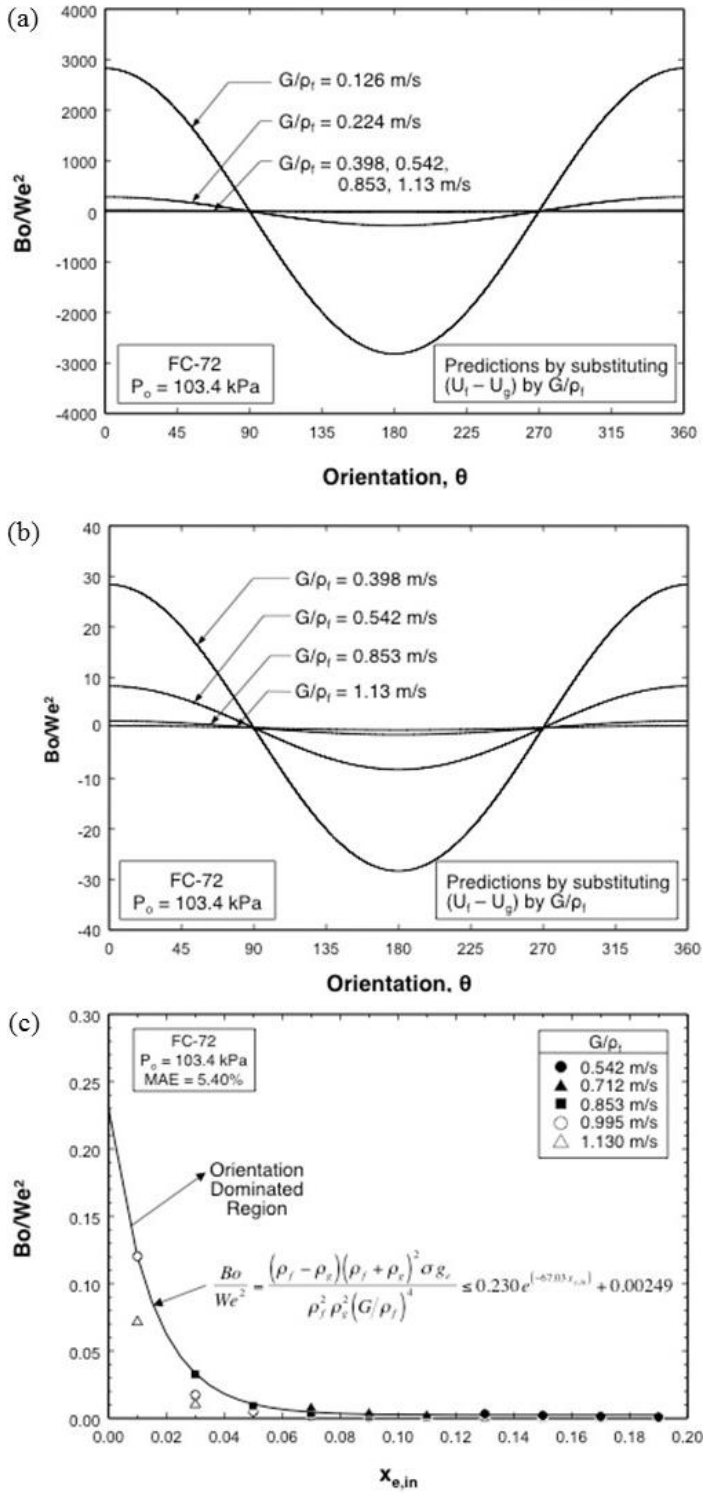

Figure 5.8: Variation of Bo/We^2 with mass velocity and orientation for (a) all mass velocities and (b) $G/\rho_f \geq 0.398$ m/s. (c) Determination of Bo/We^2 criterion for negating influence of gravity perpendicular to heated wall.

encompasses a broad range of $x_{e,in}$, a new Bo/We^2 criterion is developed using only data for which G/ρ_f exceeds the minimum criterion given by Eq. (5.9). Figure 5.8(c) shows values of Bo/We^2 for conditions that negate orientation effects are represented for $|cos\theta| = 1$ (corresponding to strongest orientation influence) by the relation

$$\frac{Bo}{We^2} = \frac{(\rho_f - \rho_g)(\rho_f + \rho_g)^2 \sigma g_e}{\rho_f^2 \rho_g^2 (G/\rho_f)^4} \leq 0.230 e^{(-67.03 x_{e,in})} + 0.00249. \quad (5.10)$$

5.3.2 Criterion for Negating Influence of Gravity Component Parallel to Heated Wall

Zhang *et al.* [5] developed a criterion for negating the influence of gravity parallel to the heated wall and opposite to the fluid flow using an expression for rise velocity for a large coalescent slug bubble relative to liquid [59],

$$U_\infty = 0.35 \frac{\left[(\rho_f - \rho_g) g_e |sin\ \theta| D_h\right]^{1/2}}{\rho_f^{1/2}}. \quad (5.11)$$

When U_∞ exceeds the liquid velocity, $U_{f,in}$, the vapor tends to flow backwards relative to the liquid, and vapor stagnation along the channel will occur when the two velocities are equal. The *Vapor Backflow* and *Vapor Stagnation Regimes* are associated with flooding as indicated for G/ρ_f = 0.126 m/s in Figure 5.6. A sufficient criterion for negating flooding regimes $U_\infty < U_{f,in}$, which, for $sin\ \theta = 1$ (corresponding to strongest orientation influence), can be presented in terms of the Froude number,

$$\left|\frac{1}{Fr}\right| = \left|\frac{(\rho_f - \rho_g)\sigma g_e D_h}{\rho_f U_{f,in}^2}\right| \leq 8.16. \quad (5.12)$$

As discussed earlier, because $x_{e,in} > 0$ in the present study, determining $U_{f,in}$ in Eq. (5.12) requires solving the detailed two-phase flow field. Therefore, the $1/Fr$ criterion is developed in a two-step approach. First, the criterion is examined by replacing $U_{f,in}$ by the known G/ρ_f. Next, the criterion is modified to account for $x_{e,in}$.

Figures 5.9(a) and 5.9(b) show the variations of $1/Fr$ for different flow velocities and orientations in the range of $180° < \theta < 360°$ prone to flooding, where $U_{f,in}$ is replaced by G/ρ_f. The two figures show the influence of gravity on $1/Fr$ greatly decreases with increasing G/ρ_f. Like the Bo/We^2 criterion, this proves that high mass velocity is the most

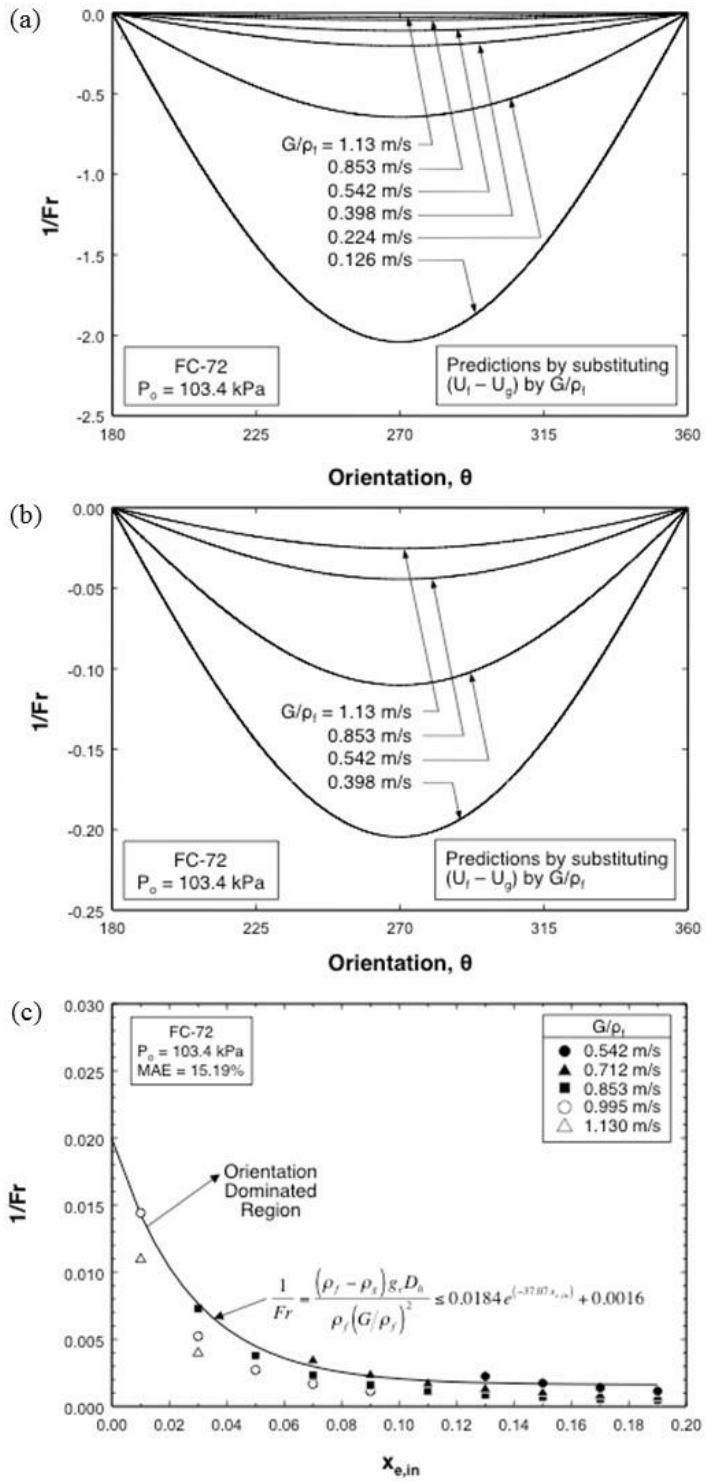

Figure 5.9: Variation of *1/Fr* with mass velocity and orientation in the range of 180° to 360° for (a) all mass velocities and (b) $G/\rho_f \geq 0.398$ m/s. (c) Determination of *1/Fr* criterion for negating influence of gravity parallel to heated wall.

effective means to overcoming flooding effects. Figure 5.9(c) shows values of $1/Fr$ for G/ρ_f values that negate orientation effects are represented, for $\sin\theta = 1$ (corresponding to strongest orientation influence), by the relation

$$\frac{1}{Fr} = \frac{\left(\rho_f - \rho_g\right) g_e D_h}{\rho_f \left(G/\rho_f\right)^2} \le 0.0184\, e^{\left(-37.07 x_{e,in}\right)} + 0.0016. \tag{5.13}$$

5.3.3 Criterion for Critical Wavelength compared to Heated Length

Even when the criterion for negating the influence of gravity perpendicular to the heated wall is satisfied, it is crucial that the interfacial wavelength be smaller than the heated length, *i.e.,* $\lambda_c \le L$, to enable liquid contact with the heated wall. Using the expression for λ_c from Eq. (5.5), this criterion can be expressed as a Weber number criterion,

$$We = \frac{\rho_f \rho_g \left(U_g - U_f\right)^2 L}{\left(\rho_f + \rho_g\right)\sigma} \ge 2\pi. \tag{5.14}$$

As with the previous two criteria, the heated length criterion is modified by replacing (U_g - U_f) in the definition of *We* by G/ρ_f. Next, the criterion is modified to account for $x_{e,in}$ by examining only G/ρ_f values that negate orientation effects as shown in Figure 5.10,

$$We = \frac{\rho_f \rho_g \left(G/\rho_f\right)^2 L}{\left(\rho_f + \rho_g\right)\sigma} \ge 1015\, e^{\left(8.682 x_{e,in}\right)} - 595.2. \tag{5.15}$$

5.3.4 Dominant Mechanism for Negating Gravity Effects

Notice that Eqs. (5.10), (5.13) and (5.15) point to increasing G/ρ_f as the most effective means to satisfying all three criteria for negating the influence of gravity on CHF. The same equations prove that a smaller G/ρ_f is required when increasing $x_{e,in}$. The three criteria are now combined to determine which criterion is dominant for different gravity fields, and the corresponding minimum G/ρ_f. This minimum value is of paramount importance to thermal management in both terrestrial and space applications since it corresponds to the minimum pumping power required to prevent CHF while avoiding the aforementioned flow anomalies.

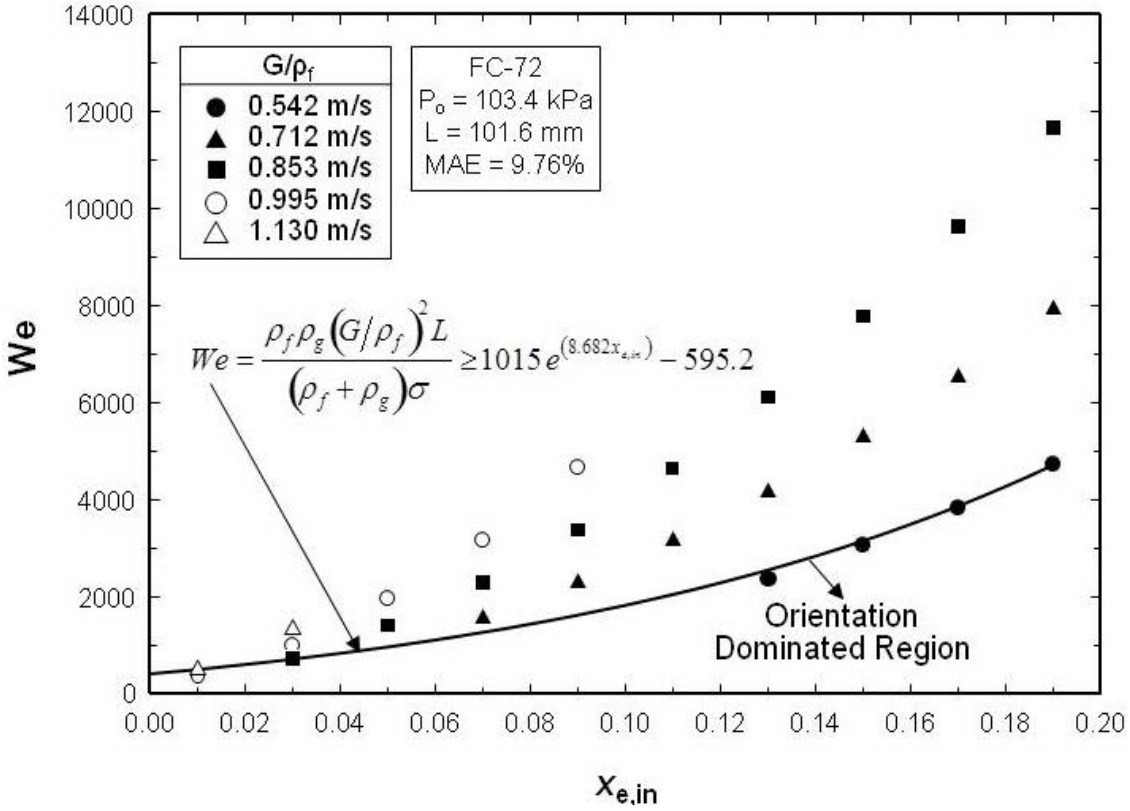

Figure 5.10: Determination of *We* criterion related to heated length versus critical wavelength.

Figure 5.11 shows the minimum mass velocity required to satisfy each of the three criteria as a function of g/g_e, the prevailing gravity nondimensionalized by Earth's gravity. For each of the three criteria, G/ρ_f is computed for a range of $x_{e,in}$ values. For subcooled conditions ($x_{e,in} \leq 0$), the minimum G/ρ_f is dominated by the flooding criterion (gravity component parallel to heated wall) for $g/g_e > 1.2$, and instability criterion (gravity component perpendicular to heated wall) for $g/g_e < 1.2$. The heated length criterion is dominant only for very small values of g/g_e, including microgravity, and the transition between this criterion and the instability criterion is a function of the heated length, with shorter length requiring a greater G/ρ_f. Notice that the minimum G/ρ_f in Lunar, Martian and Earth environments is dominated by the instability criterion. Figure 5.11 shows that the minimum G/ρ_f decreases monotonically with increasing $x_{e,in}$ for all three criteria.

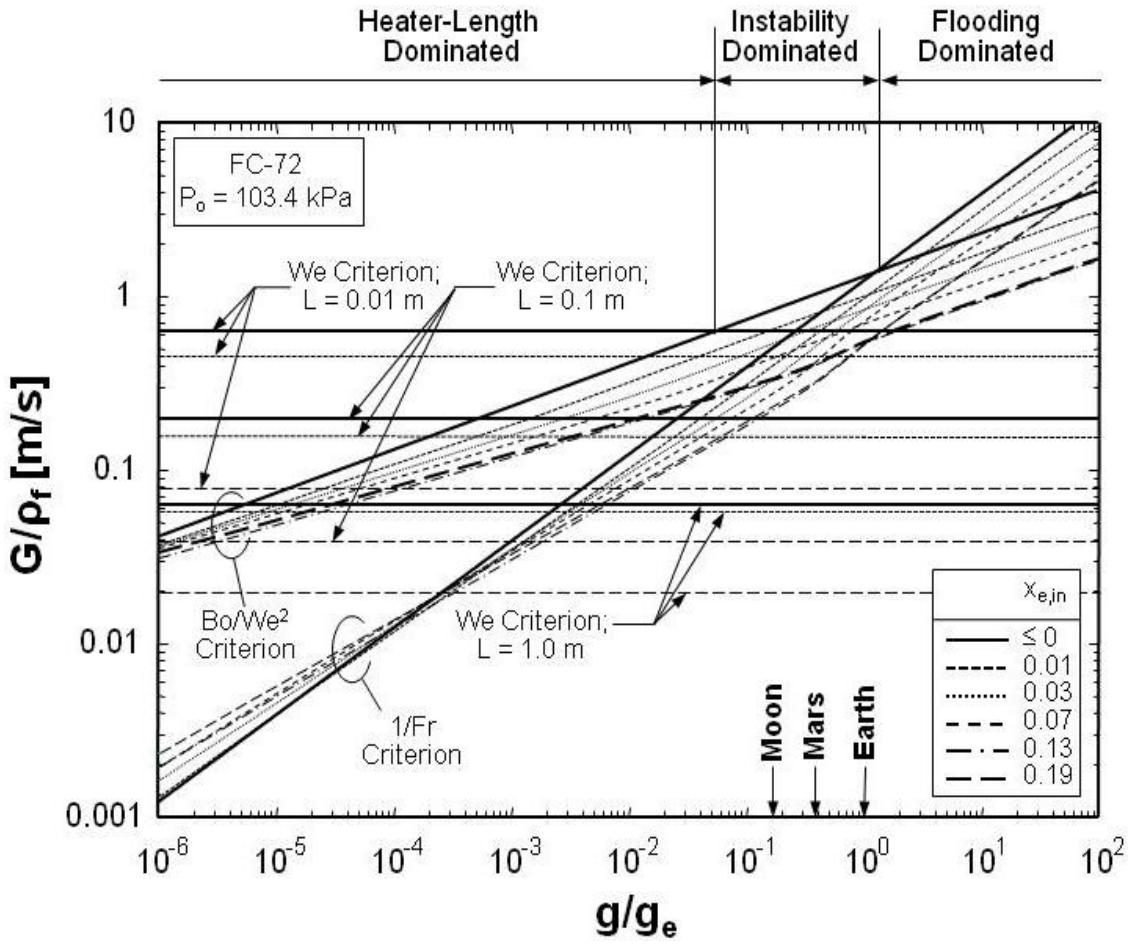

Figure 5.11: Determination of minimum G/ρ_f required to overcome all gravity effects on CHF.

CHAPTER 6. FLOW BOILING IN MICROGRAVITY

6.1 Flow Visualization Results

6.1.1 Interfacial Features for Single-Sided Heating

As indicated earlier, the operator of the microgravity facility could activate either one of the heated walls (*H1*) or both wall (*H1* and *H2*) simultaneously. Capturing single-wall interfacial images and data allows results from the present study to be compared to several prior studies that have been conducted at the PU-BTPFL that utilized one-sided heating wall. They include terrestrial studies on pool boiling on a short vertical wall [48], flow boiling on a short vertical wall [14,15], flow boiling on a long horizontal wall [16,17], and flow boiling on a long wall at different orientations relative to Earth gravity [4,5,46,47,52]. They also include flow boiling studies that were performed in parabolic flight to simulate microgravity [1,57]. A fundamental reason for using a single-sided heating wall in terrestrial experiments, particularly in flow boiling studies at different orientations relative to Earth gravity, is to isolate the influence of gravity component perpendicular to the heated wall on two-phase flow structure and heat transfer. It is important to emphasize that the present microgravity study is focused mostly on the high heat flux region of nucleate boiling, including CHF, rather than the single-phase liquid and low heat flux nucleate boiling regions.

Figure 6.1 shows individual images of flow boiling for single-sided heating along wall *H1* at inlet velocities ranging from U = 0.1 - 1.9 m/s and heat fluxes increasing to CHF. In the upstream region of the heated wall, the incoming liquid is slightly subcooled and requires a short distance to warm up to saturation temperature before beginning to generate small bubbles. The small bubbles are driven along the heated wall by liquid shear and drag forces, and grow in size because of further evaporation as well as

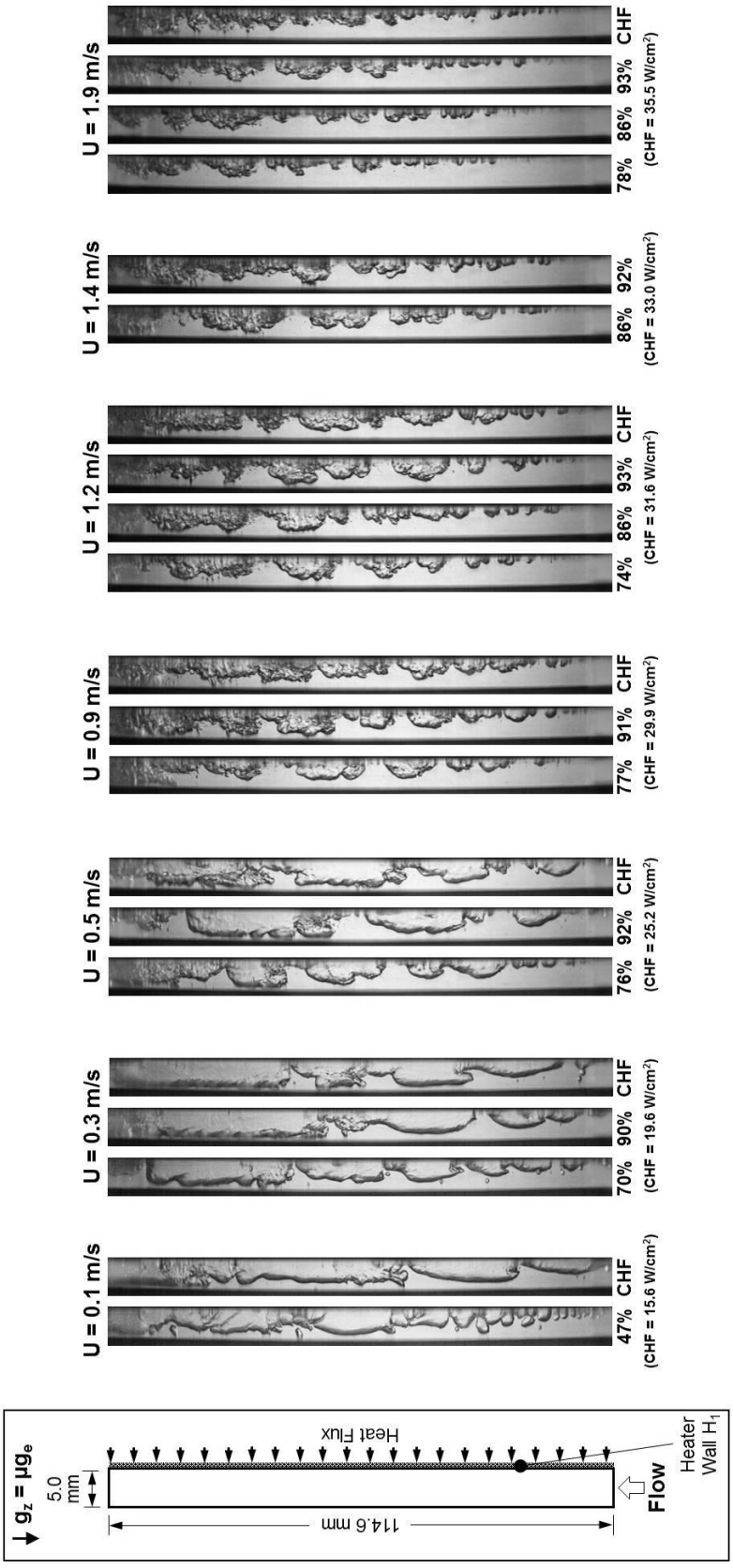

Figure 6.1: High-speed video images of heated wall *H1* from single-sided heating experiments for different inlet velocities and different heat fluxes leading to CHF.

coalescence with other bubbles. This upstream activity quickly develops into large vapor patches that mimic a continuous wavy vapor layer along the heated wall. Notice that boiling is sustained mostly in 'wetting fronts' where the wave troughs contact the wall, and abated within the large vapor patches or wave peaks. For each combination of velocity and heat flux, the mean thickness of the wavy vapor layer increases along the flow direction. Comparing images corresponding to different velocities shows the length of vapor patches decreases and number of wetting fronts increases with increasing velocity. These interfacial characteristics are consistent with wavelength trends predicted according to hydrodynamic instability theory as proposed by Galloway and Mudawar [14,15].

Figure 6.2 shows 15 sequential images captured for single-sided heating along *H1* for U = 0.1, 0.5, 0.9 and 1.9 m/s at the lowest recorded percentage of CHF value as well as close to but below CHF. The time elapsed between consecutive frames is 1.4 ms. Here too, the wavy vapor layer is observed for all flow velocities and heat fluxes from approximately 50% CHF to near CHF commencement. At U = 0.1 m/s, low liquid inertia fosters rapid growth of nucleating bubbles near the leading edge of the heated wall with immediate bubble coalescence. The vapor patches are shown propagating downstream along the heated wall, gradually increasing in thickness. The upstream bubble growth decreases with increasing flow velocity, and the onset of nucleation is shifted farther downstream, especially for U = 1.9 m/s, where bubble nucleation commences at approximately 20% of the heated length.

6.1.2 Interfacial Features for Double-Sided Heating

Figure 6.3 shows individual images of flow boiling during double-sided heating at inlet velocities ranging from U = 0.1 - 1.9 m/s and heat fluxes increasing to CHF. For each velocity tested, bubble generation culminates in formation of wavy vapor layers on both heated walls. Thickening of the vapor layers along the heated walls causes the two layers to merge downstream. The merger of vapor layers is observed to shift upstream with increasing heat flux because of the increased vapor production. On the other hand, increasing flow velocity shifts the merger downstream because increased liquid inertia

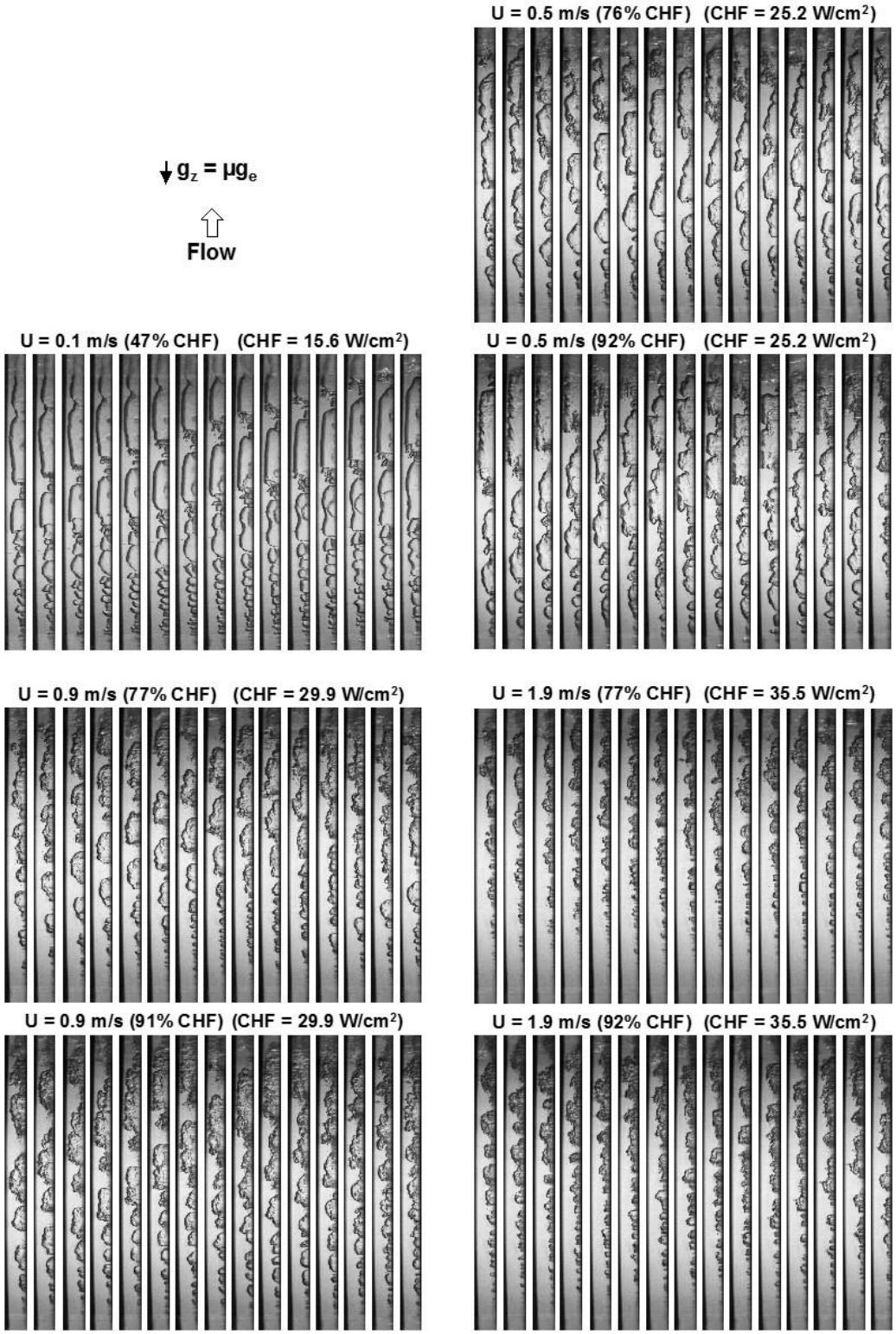

Figure 6.2: Sequential high-speed video images of heated wall *H1* from single-sided heating experiments for different inlet velocities and different heat fluxes.

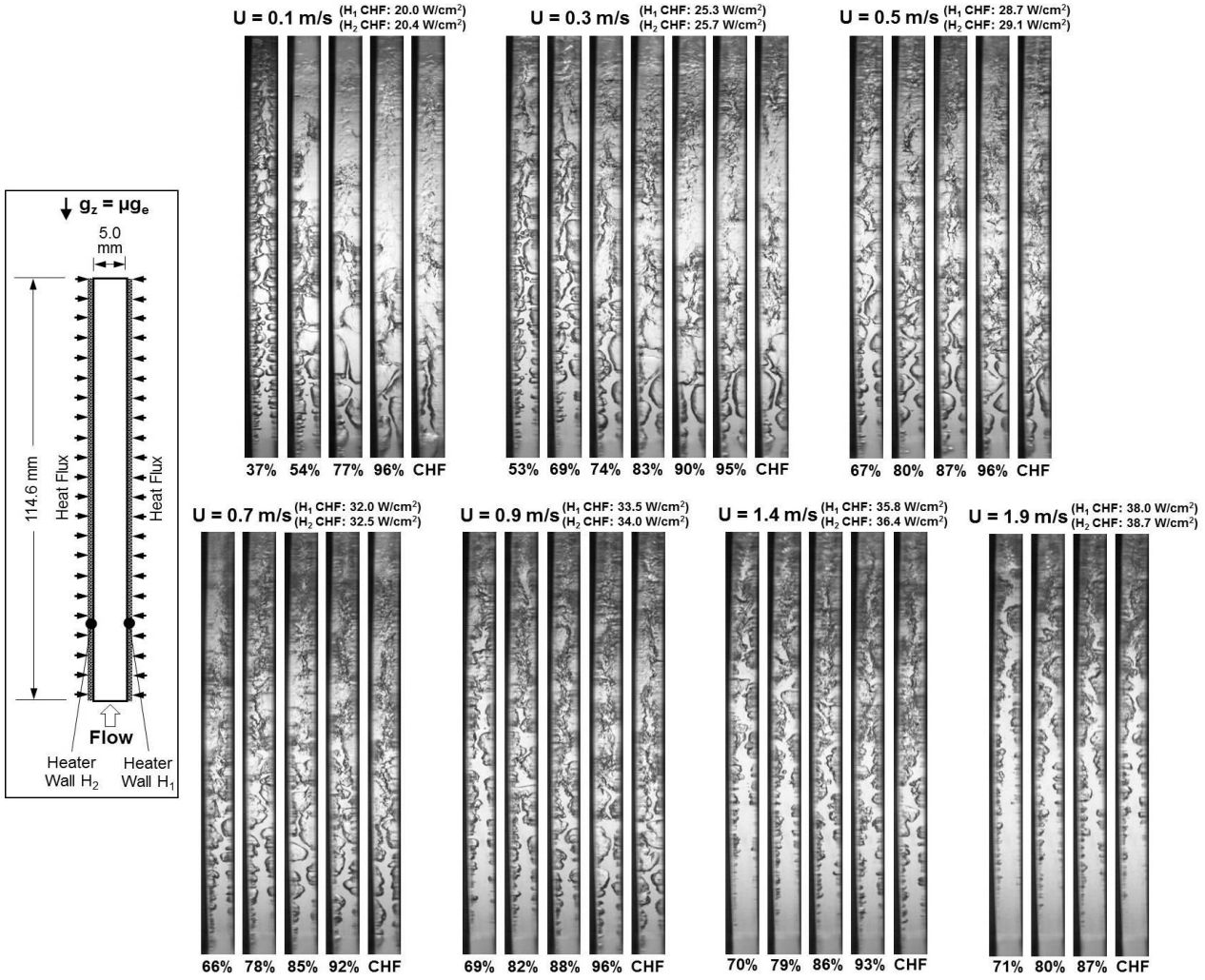

Figure 6.3: High-speed video images from double-sided heating experiments for different inlet velocities and different heat fluxes leading to CHF.

reduces the thicknesses of the individual layers. Notice for the lowest velocity of $U = 0.1$ m/s, a large downstream fraction of the heated length is occupied mostly by vapor, mixed with a few liquid ligaments. For most velocities, CHF occurs as fairly thick vapor layers insulate the downstream regions of the two walls, evidenced by wall temperature excursions in those regions.

Figure 6.4 shows 15 sequential high-speed images captured for double-sided heating for $U = 0.1$, 0.5, 0.9 and 1.9 m/s at the lowest recorded percentage of CHF value as well as close to but below CHF. The time elapsed between consecutive frames is 1.4 ms. A low heat flux of 37% CHF is tested only for $U = 0.1$ m/s, where bubbly flow is observed. For all conditions tested, bubble nucleation is initiated very close to the leading edge for both heated walls. The bubbles propagate along the heated walls, gradually growing in size because of both evaporation and coalescence with neighboring bubbles. Eventually, wavy vapor layers are formed on both walls, squeezing the bulk liquid layer in between. The existence of the central liquid layer prevents the two vapor layers from merging fully across the channel. Instead, some vapor bubbles are ejected from one or both heated walls, and are pulled into the bulk liquid layer, possibly by the liquid drag and shear forces. These bubbles are then compressed by the opposite wavy vapor layers and conveyed downstream with the bulk liquid layer. A very interesting behavior is observed as the two opposite wavy vapor layers compete in occupying the channel's cross-section. Upon close examination, the wave peak on one of the heated walls grows rapidly towards the trough (wetting front) between two wave peaks on the opposite wall. Immediately following this event, a wave peak on the second wall immediately upstream grows rapidly towards the trough between two wave peaks on the first heated wall. This phenomenon is constantly repeated, resembling the meshing of mechanical gear teeth between two rotating sprockets. The meshing action between the two opposite wavy vapor layers causes progressive mixing, and culminates in a downstream region occupied mostly by vapor, with remnants of liquid in the form of liquid ligaments. Notice for $U = 0.1$ m/s and 37% CHF, the wavy vapor layers grow at a slow rate, which causes the meshing to take place farther downstream. Increasing the heat input for $U = 0.1$ m/s from 37% to 96% causes the meshing to commence upstream.

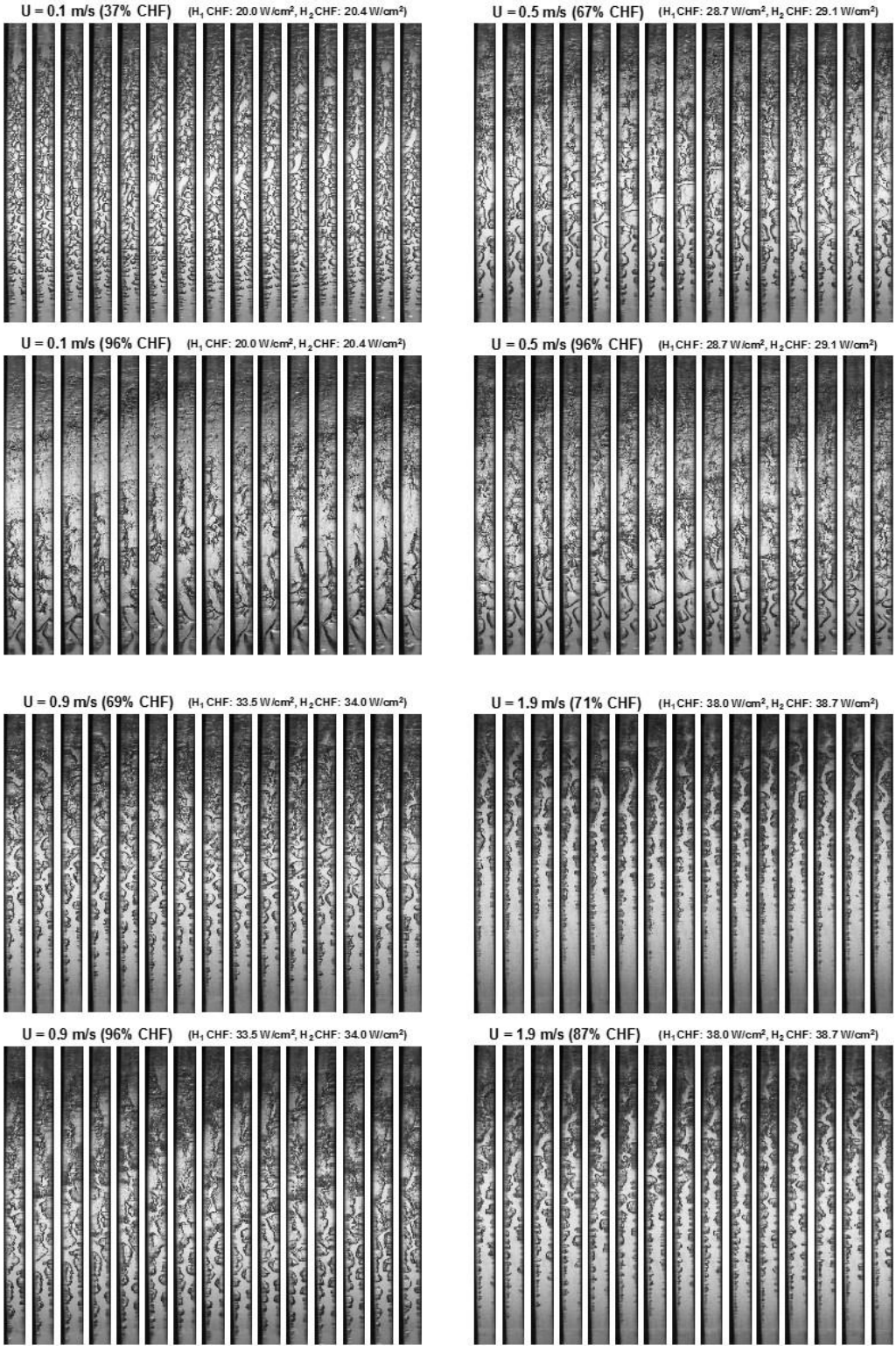

Figure 6.4: Sequential high-speed video images from double-sided heating experiments for different inlet velocities and different heat fluxes.

The same meshing trends are observed for U = 0.5, 0.9 and 1.9 m/s. For the highest velocity tested, U = 1.9 m/s, high flow inertia significantly delays bubble nucleation and growth of the wavy vapor layers, which causes the meshing to be shifted to the outlet region.

6.1.3 Idealized Depiction of Interfacial Features for Single-Sided and Double-Sided Heating

Figure 6.5(a) depicts an idealized representation of interfacial behavior for single-sided heating at high heat fluxes approaching CHF. Near the inlet, subcooled liquid is shown warming up to saturation temperature before bubbles begin to nucleate on heated wall *H1*. The bubbles grow quickly due to both evaporation and coalescence with other bubbles, culminating in the formation of a fairly continuous wavy vapor layer. As the vapor layer propagates along the heated wall, dryout occurs beneath the wave peaks, especially close to CHF, while vigorous boiling is sustained in the wave troughs. The mean thickness of the wavy vapor layer increases gradually along the heated wall. The axial thickening of the vapor layer is hastened by increasing the heat flux or decreasing the inlet liquid velocity.

Figure 6.5(b) depicts an idealized representation of the interfacial behavior captured at high heat fluxes approaching CHF for double-sided heating. Three distinct interfacial flow regions are identified: (1) wavy vapor layer developing region, (2) wavy vapor layer meshing region, and (3) wavy vapor layer merging region. In the upstream wavy vapor layer developing region, subcooled liquid is heated to above saturation temperature, initiating bubble nucleation on both heated walls. The bubbles grow rapidly and coalesce with other bubbles to form a fairly continuous wavy vapor layer. In the middle wavy vapor layer meshing region, wave peaks from one wall protrude towards a trough of the opposite vapor layer. Upon extensive examination of high-speed video records, this phenomenon is observed to occur when the maximum thickness of the wavy vapor layer grows to approximately one-third the distance between the heated walls. Because of the gradual increase in vapor mass flow rate due to evaporation, coupled with the large density differences between the two phases, the vapor layers propagate at a

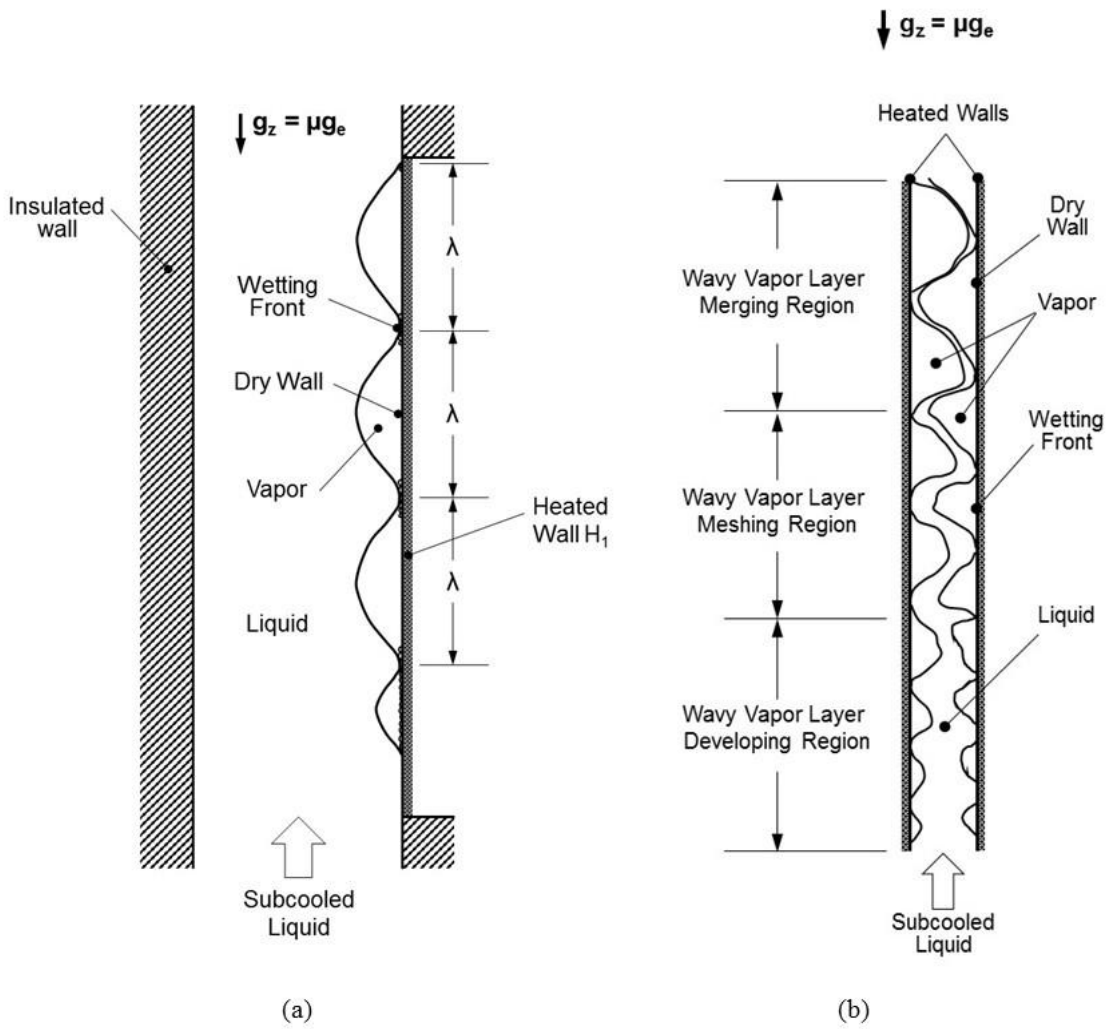

Figure 6.5: Schematic representation of pre-CHF interfacial behavior (a) along heated wall *H1* during single-sided heating experiments, and (b) along both walls during double-sided heating experiments.

faster rate than the bulk liquid. The combined effect of large interfacial curvature and high velocity difference is speculated to induce flow separation and low pressure zones, which draw in the wave peaks from opposite walls. The downstream wavy vapor layer merging region is characterized by opposite vapor layers virtually merging with one another. Due to low inertia, low flow velocities cause rapid vapor growth, shifting the wavy vapor layer meshing region upstream. Similarly, this region is shifted upstream when the wall heat flux is increased.

6.2 Heat Transfer Results

6.2.1 Experimental Heat Transfer Data Reduction

Experimental data are continuously recorded during every parabolic flight. Figures 6.6(a) – 6.6(c) show composite temporal plots of heated wall temperatures and heat fluxes, and gravity for double-sided heating at U = 0.1 m/s, single-sided heating at U = 1.9 m/s, and double-sided heating at U = 1.9 m/s, respectively. The temperatures are designated as $T_{w1,n}$ and $T_{w2,n}$, where *1* and *2* refer to heated walls *H1* and *H2*, respectively, and n is the thermocouple location along the heated wall. For U = 0.1 m/s, Figure 6.6(a) shows a slight drop in the heated wall temperatures as the aircraft enters the hypergravity phase of the parabola. The heated wall temperatures then increase slightly as the aircraft enters the microgravity phase, and decrease once again during the hypergravity descent. These temperature variations point to enhancement in flow boiling heat transfer with increasing gravity, and degradation in μg_e. These trends are consistent with those of parabolic flight experiments with FC-72 in a 6.0-mm diameter tube by Baltis *et al.* [61] corresponding to moderate to high heat fluxes. The temporal plots for U = 1.9 m/s in Figures 6.6(b) and 6.6(c) show heated wall temperature variations across the hypergravity ascent, microgravity and hypergravity descent are less pronounced than for U = 0.1 m/s, Figure 6.6(a), because of the reduced influence of gravity at higher velocities. It should be noted that the flow rate changes by approximately 5% while transitioning between different gravitational phases during a parabolic maneuver. This change is attributed to

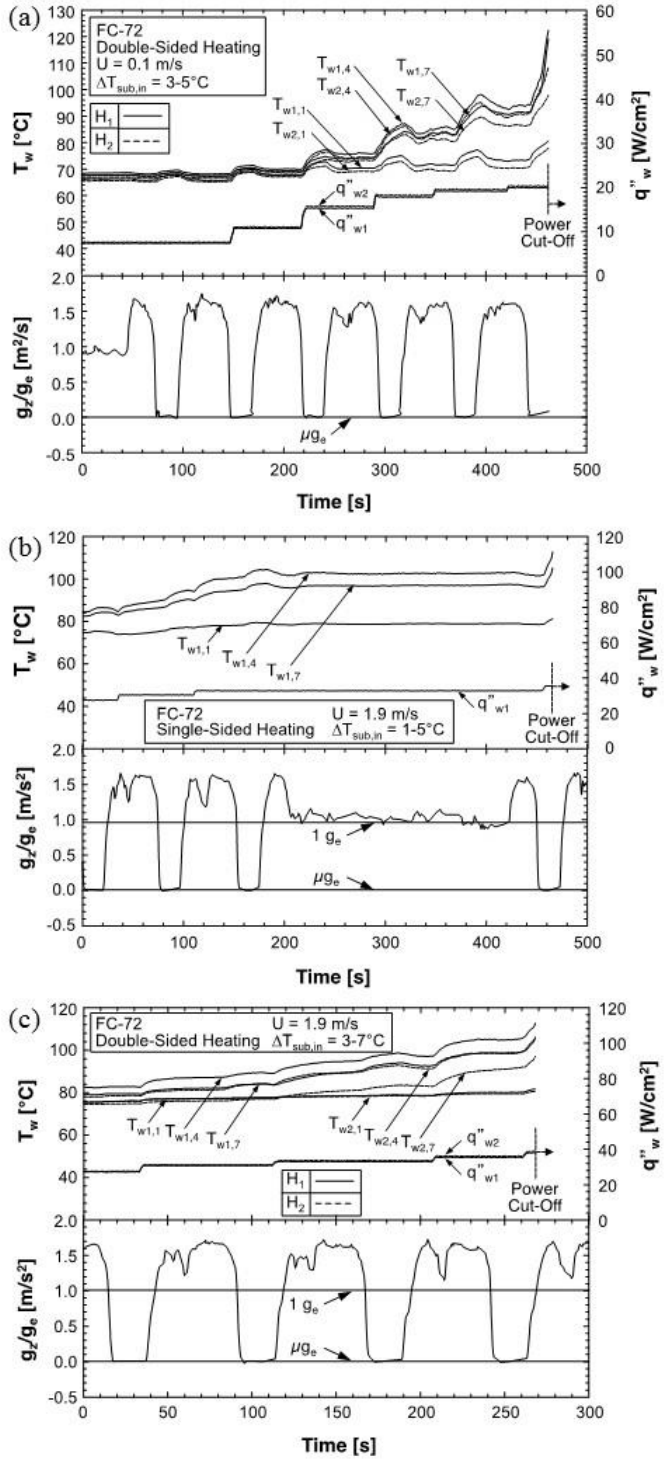

Figure 6.6: Temporal records of heated wall temperatures and heat fluxes, and gravity during series of parabolas for (a) double-sided heating at U = 0.1 m/s, (b) single-sided heating at U = 1.9 m/s, and (b) double-sided heating at U = 1.9 m/s.

changes in hydrostatic head within the flow loop with varying gravity, and is more pronounced at low velocities and decreases with increasing velocity.

Although data are measured throughout the parabolic maneuver, inconsistencies in the magnitude of hypergravity, coupled with *g*-jitter due to turbulence and short durations of hypergravity, preclude any reliable measurements during hypergravity. Therefore, all experimental results presented in this study concern the microgravity phase alone. Results are presented both for single-sided and double-sided heating.

6.2.2 Experimental Heat Transfer Trends

As indicated earlier, the present study is focused mostly on the upper region of the nucleate boiling curve depicted in Figure 6.7(a). Data obtained in this region, coupled with high-speed video motion analysis, help provide both qualitative and quantitative identification of mechanisms leading to CHF. Figures 6.7(b) and 6.7(c) provide, for different inlet velocities, data for the nucleate boiling region preceding CHF for single-sided and double-sided heating, respectively. The wall heat flux, q''_w, is plotted versus the difference between the average wall temperature, $T_{w,avg}$, and saturation temperature, T_{sat}. The single-sided and double-sided data exhibit similar monotonically increasing trends of heat flux with temperature difference, as well as a shift to higher heat fluxes with increasing velocity. Figure 6.7(c) shows slight differences in boiling data for heated walls *H1* and *H2*, which are attributed to small differences in electrical power input between the arrays of six thick-film resistors soldered to the two walls. These differences are the result of a 0.5-Ω (1.7%) greater equivalent electrical resistance for heated wall *H1* compared to *H2*. Comparing Figures 6.7(b) and 6.7(c) shows better flow boiling performance and as much as 22% higher CHF for double-sided compared to single-sided heating for equal velocities. This enhancement with the double-sided heating can be explained as follows. With both walls heated, far more vapor is being produced than with one heated wall. This causes the flow to accelerate much faster, and the heat transfer performance to be enhanced with double-sided versus single-sided heating. Interestingly, Figure 6.7(c) shows *H2*, which has a slightly higher heat flux, produces lower wall temperatures than *H1*. This unexpected trend is speculated to be the result of

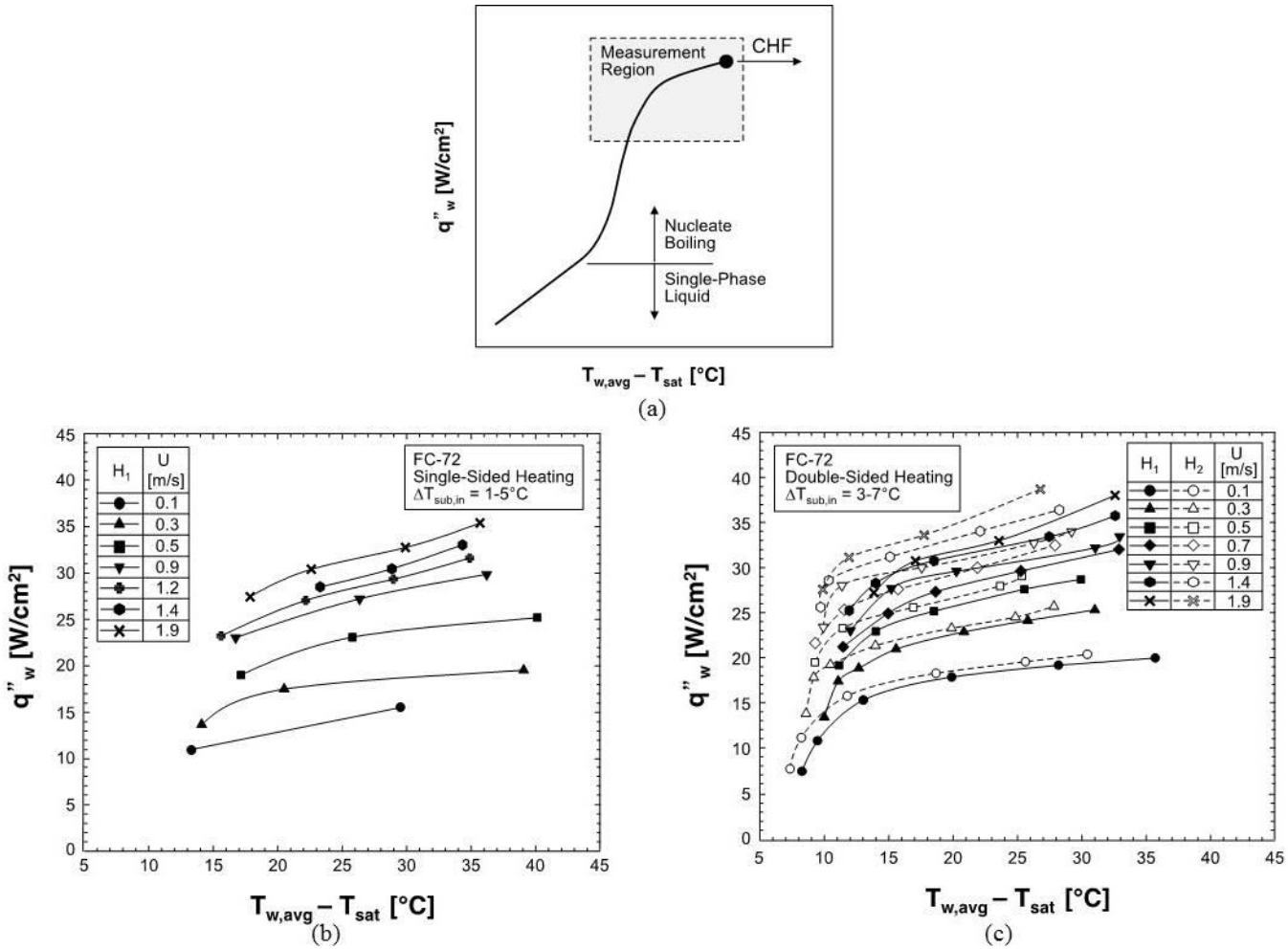

Figure 6.7: (a) Region of boiling curve of interest to present study. (b) Boiling curves for heated wall *H1* from single-sided heating experiments for different inlet velocities. (c) Boiling curves for both heated walls from double-sided heating experiments for different inlet velocities.

differences in evaporation rate between the two heated walls. Producing the higher heat flux, *H2* yields higher evaporation rates, increasing flow velocities locally more than along *H1*, therefore enhancing heat transfer more and resulting in lower wall temperatures.

Figures 6.8(a) and 6.8(b) show, for U = 0.1, 0.9 and 1.9 m/s, axial variations of wall temperature for different heat fluxes for single-sided and double-sided heating, respectively. The two heating configurations produce similar trends, with temperatures increasing with increasing heat flux, and, for a fixed heat flux, increasing from the leading edge of the heated wall ($T_{wm,1}$) wall to a maximum immediately downstream from the middle (T_{w5} or T_{w6}), before decreasing again towards the exit ($T_{wm,7}$). CHF is initiated in the vicinity of $T_{wm,5}$ or $T_{wm,6}$ where maximum wall temperature is achieved. The lowest wall temperatures at $T_{wm,1}$ are attributed to the fluid entering the heated region as subcooled liquid at the lowest temperature. The wall temperature initially increases downstream of $T_{wm,1}$ as a result of both gradual rise in liquid temperature and vapor layer development. However, the vapor generation also causes gradual acceleration of the flow, which helps enhance heat transfer and therefore decrease wall temperature. The net effect of these two opposing trends is to achieve maximum wall temperature shortly downstream of the middle, before acceleration dominates heat transfer and reduces wall temperature towards the exit. This process is also complicated by the development of the wavy vapor layer along the heated wall for single-sided heating, and both the vapor layer development and meshing between vapor layers for double-sided heating.

The local heat transfer coefficient at a wall thermocouple location is obtained from the following expression,

$$h_{m,n} = \frac{q''_w}{\left(T_{wm,n} - T_f\right)}, \tag{6.1}$$

where q''_w is the wall heat flux, $T_{wm,n}$ the wall temperature measured along heated wall m (m =1 for *H1* and 2 for *H2*), with n corresponding to thermocouple location z_n, and T_f the bulk fluid temperature. Subcooled liquid enters the heated portion of the channel and is heated up to T_{sat} before bubbles can begin to nucleate. For double-sided heating, axial

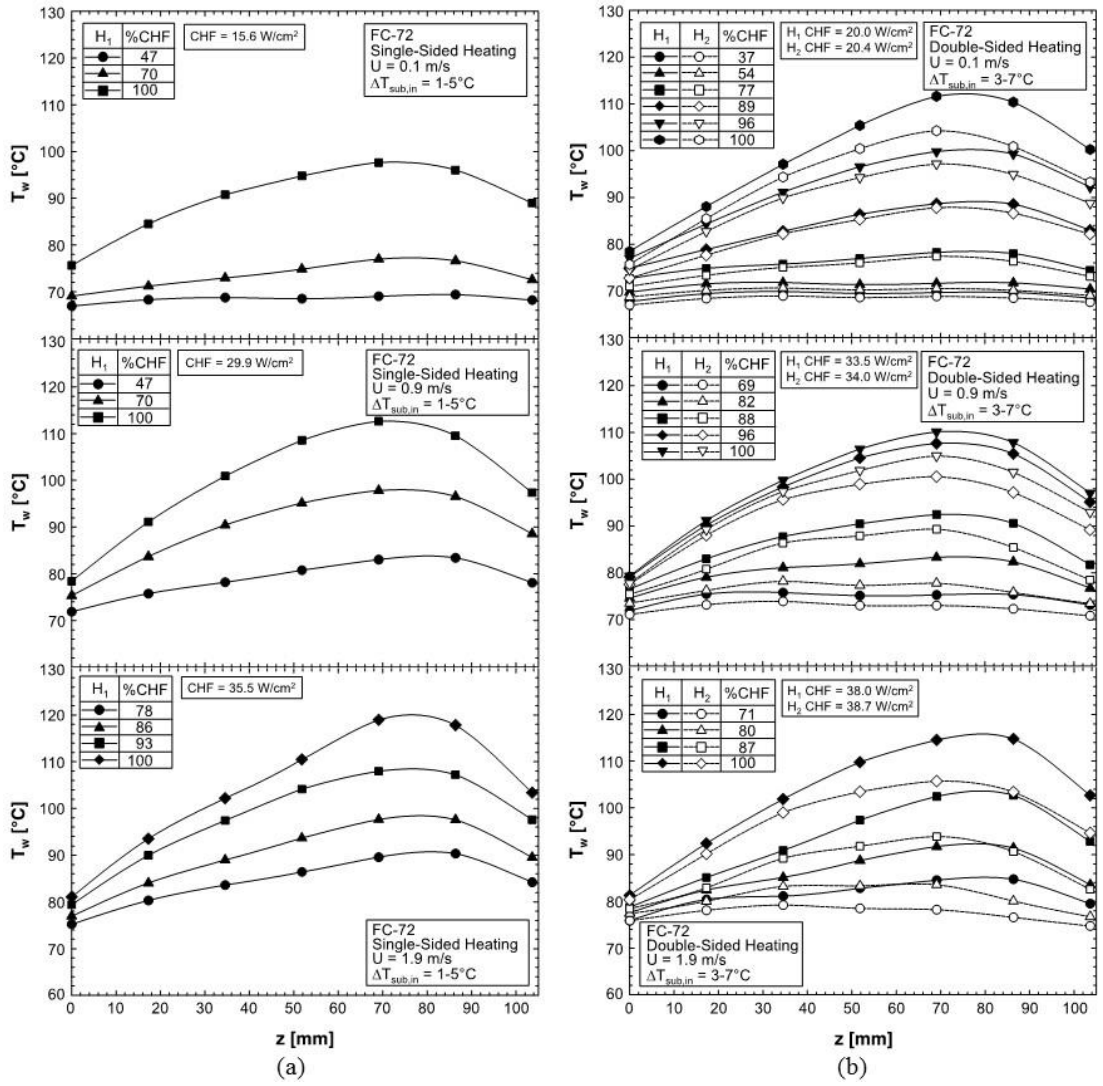

Figure 6.8: Variation of temperature along heated wall for different heat fluxes for (a) heated wall *H1* from single-sided heating experiments, and (b) both heated walls from double-sided heating experiments.

variations of the bulk fluid temperature, T_f, encompassing the subcooled and saturated regions are given, respectively, by

$$T_{f,n+1} = T_{f,n} + \frac{(q''_{w1} + q''_{w2})W\Delta z}{\dot{m}c_{p,f}} \quad \text{for } x_e < 0 \tag{6.2a}$$

and

$$T_f = T_{sat} \quad \text{for} \quad 0 \le x_e \le 1. \tag{6.2b}$$

The above equations are also used for single-sided heating by setting $q''_{w2} = 0$. A single value of the heat transfer coefficient is determined at each thermocouple location. These values are then spatially averaged to determine h_{avg}.

Figures 6.9(a) and 6.9(b) show variations of h_{avg} with inlet velocity at different heat fluxes for single-sided and double-sided heating, respectively. For single-sided heating, Figure 6.9(a) shows h_{avg} increases fairly monotonically with increasing velocity for fixed heat flux, and decreases, for fixed velocity, as heat flux increases towards CHF. For double-sided heating, Figure 6.9(b) shows h_{avg} generally increases with increasing inlet velocity for fixed heat flux, and decreases, for fixed velocity, as the heat flux is increased towards CHF. However, there is a slight decline in h_{avg} above 1.4 m/s for 80% and 85% of CHF. Like the boiling curves and temperature data, there are differences in h_{avg} between the two heated walls that generally increase with increasing velocity.

Figures 6.10(a) and 6.10(b) show the variations of h_{avg} with heat flux at different inlet velocities for single-sided and double-sided heating, respectively. Overall, h_{avg} increases with increasing velocity. But the variation of $h_{w,avg}$ with heat flux appears to be governed by evolution of the vapor layer along the heated length. As depicted in the video images, heat transfer from the heated wall to the bulk liquid is speculated to occur primarily in the wetting fronts separating less conductive vapor patches. While increasing the heat flux increases flow velocity due to increased evaporation, the wall regions beneath the vapor patches become increasingly dry, placing more pressure on the wetting fronts to dissipate the majority of the heat. This is also exasperated by increased vapor production netting more dryout downstream, which is especially problematic for double-sided heating because of the merging of vapor layers from opposite walls. These complex trends will be explored shortly with aid of a separated flow model that will track axial variations of mean velocities and mean thicknesses of the liquid and vapor layers, as

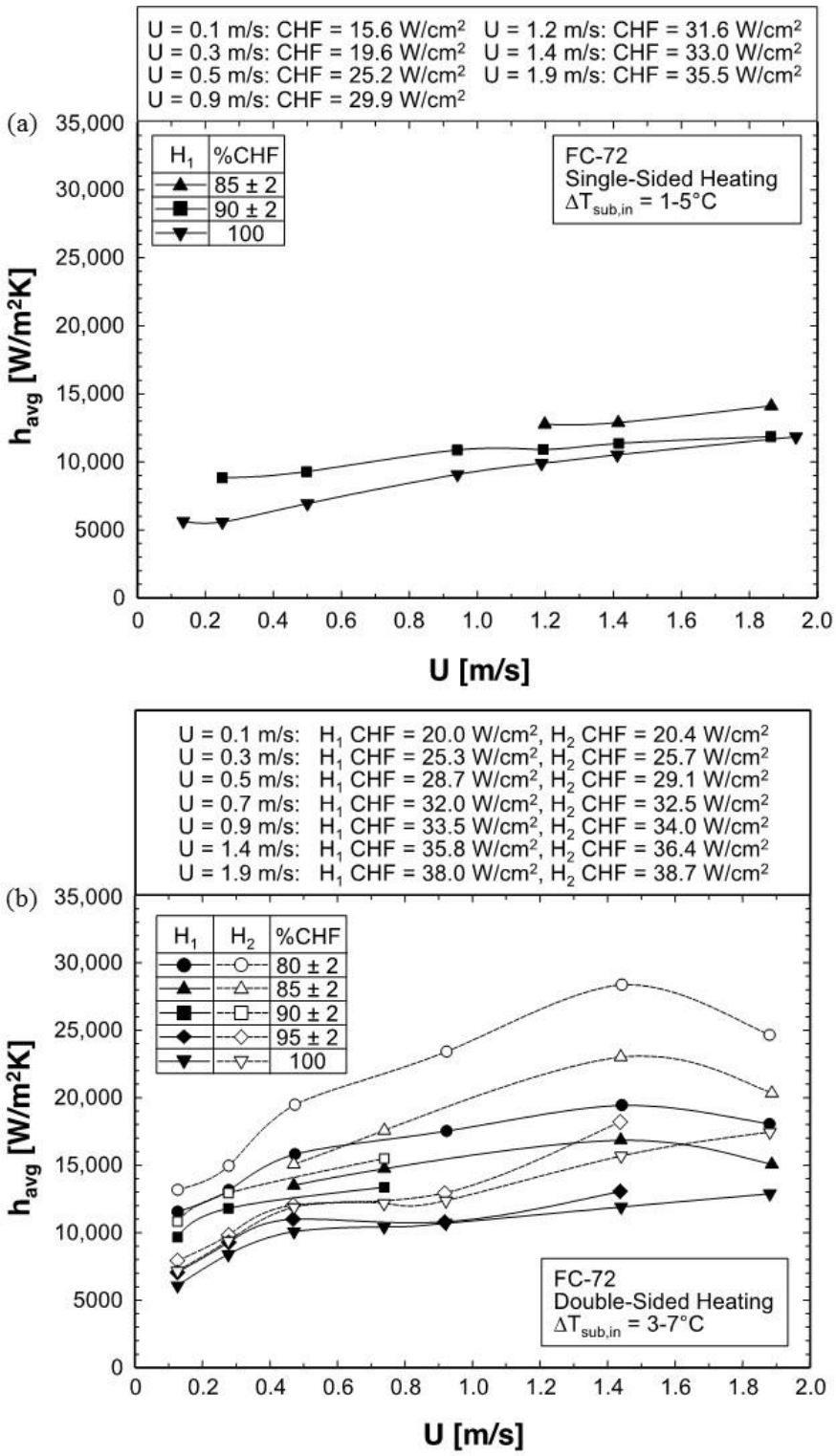

Figure 6.9: Variation of heat transfer coefficient with inlet velocity for different heat fluxes for (a) heated wall *H1* from single-sided heating experiments, and (b) both heated walls from double-sided heating experiments.

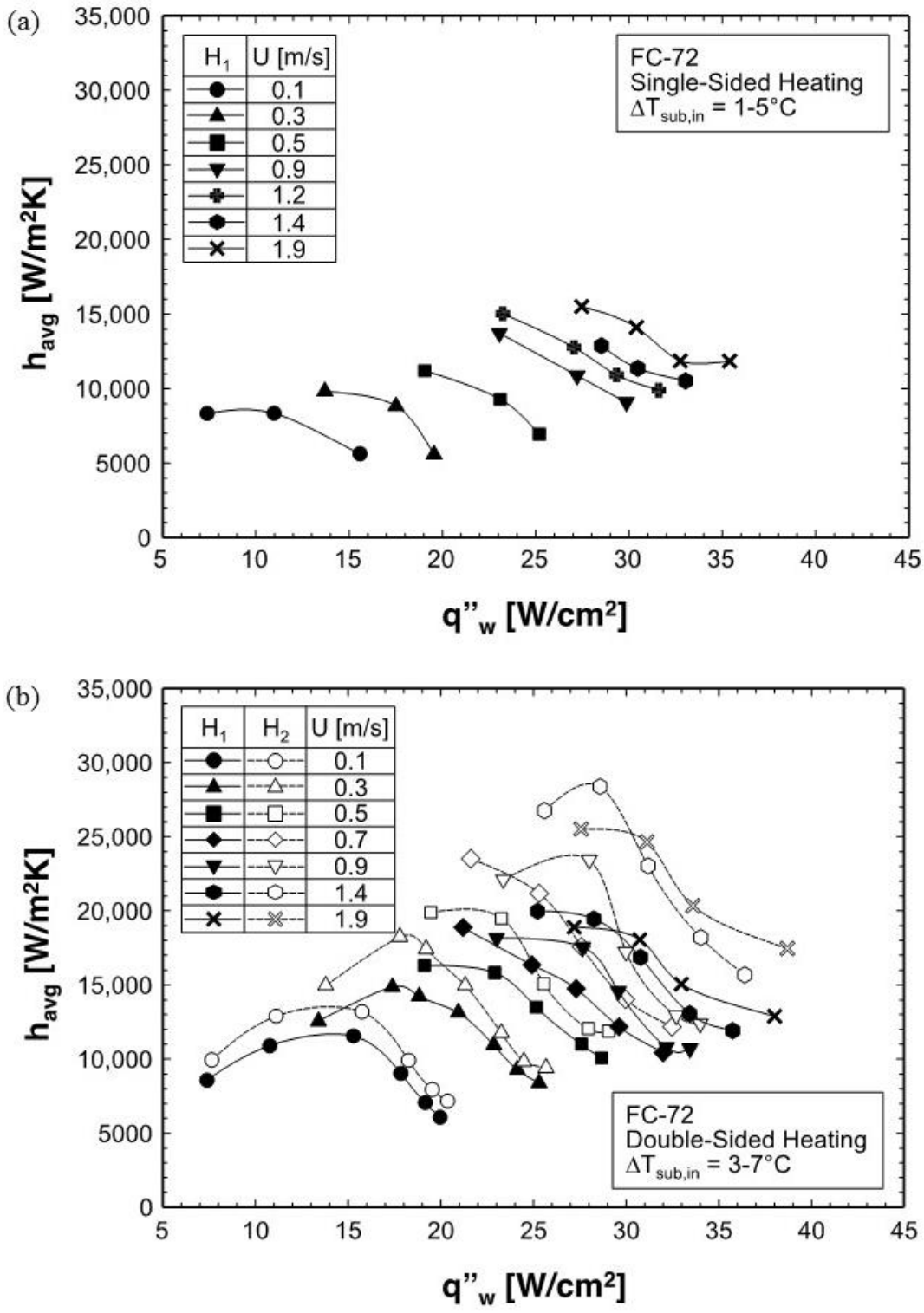

Figure 6.10: Variation of heat transfer coefficient with wall heat flux for different inlet velocities for (a) heated wall *H1* from single-sided heating experiments, and (b) both heated walls from double-sided heating experiments.

well as the theoretical Interfacial Lift-off Model that will assess the impact of these variations on flow boiling CHF.

The microgravity study points to the importance of both amassing large databases to better ascertain parametric trends as discussed in [8,62], and better characterizing interfacial behavior. Interfacial waves appear to play a dominant heat transfer role for all conditions tested. Better characterization of these waves will require conducting detailed measurements of liquid velocity and turbulence, and local instantaneous thicknesses of both the liquid and vapor layers. Liquid velocity and turbulence measurements have indeed been conducted in adiabatic, relatively thick wavy liquid films [63,64]. For small channels, liquid velocity measurements are possible with the aid of micro-particle image velocimetry (μ-PIV) [65]. Small channels also require miniaturized sensors to measure liquid and vapor layer thicknesses and characterize interfacial waves [63,64,66], as well as temperature profile across the liquid layer [67-70]. However, it is not known how such complex diagnostic tools might influence flow boiling structure and especially CHF.

6.3 Experimental Pressure Drop Trends

Pressure drop is measured by pressure transducers connected to taps in the channel immediately upstream and downstream of the copper heated walls. These pressures are measured continuously during every parabola. The operator of the flow boiling facility can activate either one of the heated walls (*H1*) or both walls (*H1* and *H2*) simultaneously. Figures 6.11(a) and 6.11(b) shows variations of the measured pressure drop across the heated length, Δp, with wall heat flux for different inlet velocities for single-sided and double-sided heating, respectively. Overall, Δp increases with increasing velocity for both heating configurations and, with less regularity, increases with increasing heat flux for a given velocity. However, double-sided heating produces greater pressure drop than single-sided heating for identical flow conditions. This is attributed to nearly twice the amount of vapor produced with double-sided heating greatly increasing the velocities of vapor and liquid.

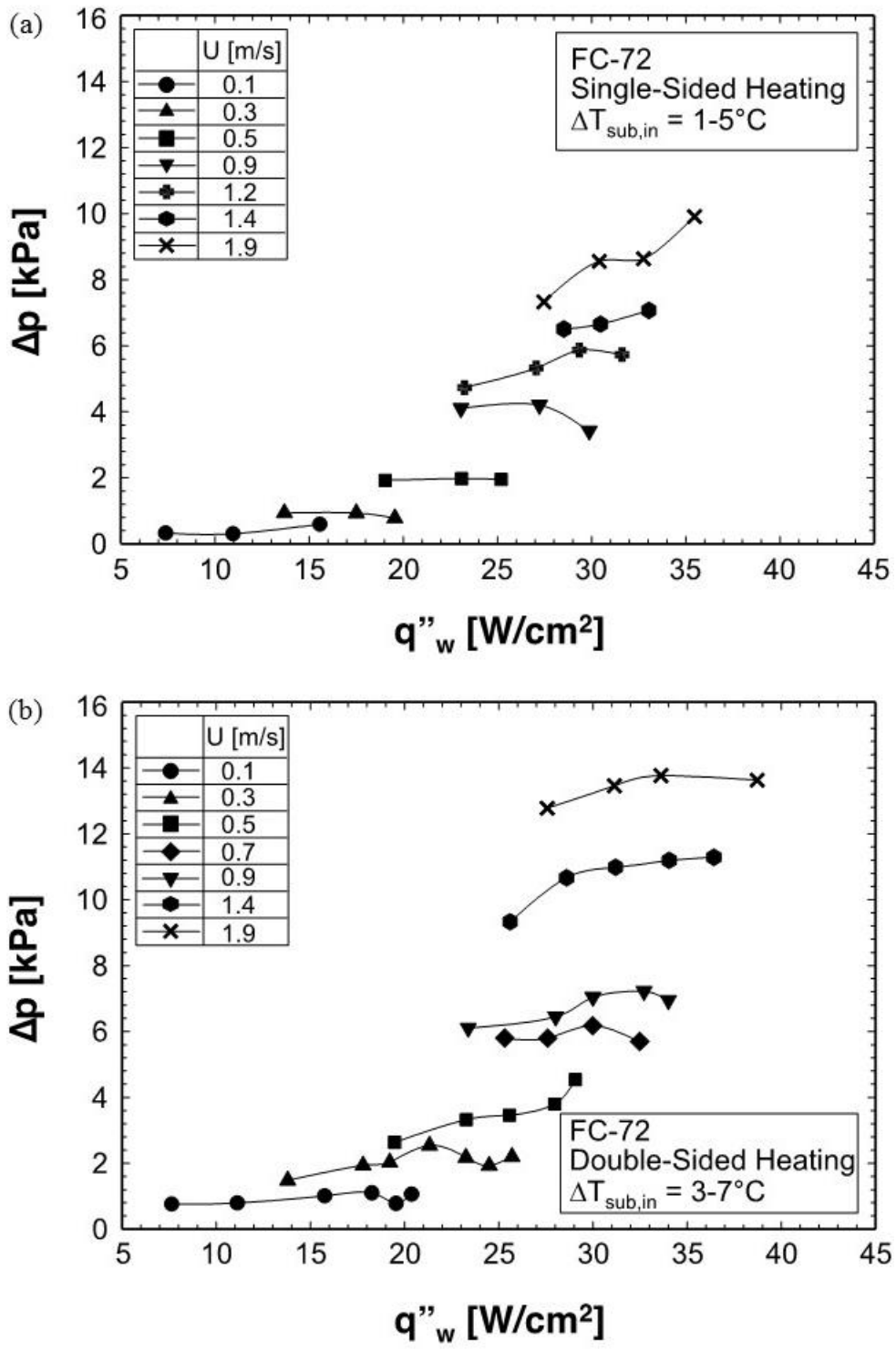

Figure 6.11: Variation of pressure drop across the heated portion of the channel with wall heat flux for different inlet velocities for (a) single-sided heating and (b) double-sided heating.

6.4 Experimental Critical Heat Flux Results

6.4.1 Video Images of Interfacial Behavior at CHF

As discussed earlier, a high-speed camera is used to capture interfacial behavior along the entire heated portion of the channel. Also included in the first part is the detailed evolution of interfacial behavior preceding CHF for both single-sided and double-sided heating. Discussed below are interfacial features captured immediately preceding CHF commencement, during the CHF transient, and shortly after CHF. These results are used to lay the groundwork for formulation of a CHF model for flow boiling in μg_e.

Figure 6.12 shows sequential images captured in μg_e during the CHF transient and immediately after CHF (CHF+) for single-sided heating at U = 0.1, 0.5, 0.9 and 1.9 m/s. The time elapsed between consecutive frames is 1.4 ms. This interfacial behavior agrees remarkably well with the μg_e flow boiling visualization results of Zhang *et al.* [1]. Figure 6.12 shows the heated wall during the CHF transient at U = 0.1 m/s covered by broad vapor patches separated by short wetting fronts. As time elapses, the wetting fronts sustaining heat transfer from the wall to the bulk liquid as well as liquid replenishment of the wall are gradually lifted from the wall. At CHF+, boiling activity in the wetting fronts appears to be fully extinguished, causing the heated wall to be completely encased by a continuous wavy vapor layer. Increasing the flow velocity to U = 0.5 m/s is shown decreasing the wavy vapor layer's mean thickness and wavelength while increasing the number of wetting fronts along the heated wall. The trends of decreasing mean thickness and wavelength, and increasing number of wetting fronts is evident at the two highest flow velocities of U = 0.9 and 1.9 m/s. The most noticeable change in interfacial behavior between the CHF transient and CHF+ is the gradual extinguishing of boiling activity in the wetting fronts. It appears that an initial wetting front is extinguished first, causing the same total amount of heat to be dissipated through a smaller number of wetting fronts. This causes the remaining wetting fronts to be extinguished even more rapidly. This chain reaction eventually culminates in the loss of cooling in all wetting fronts.

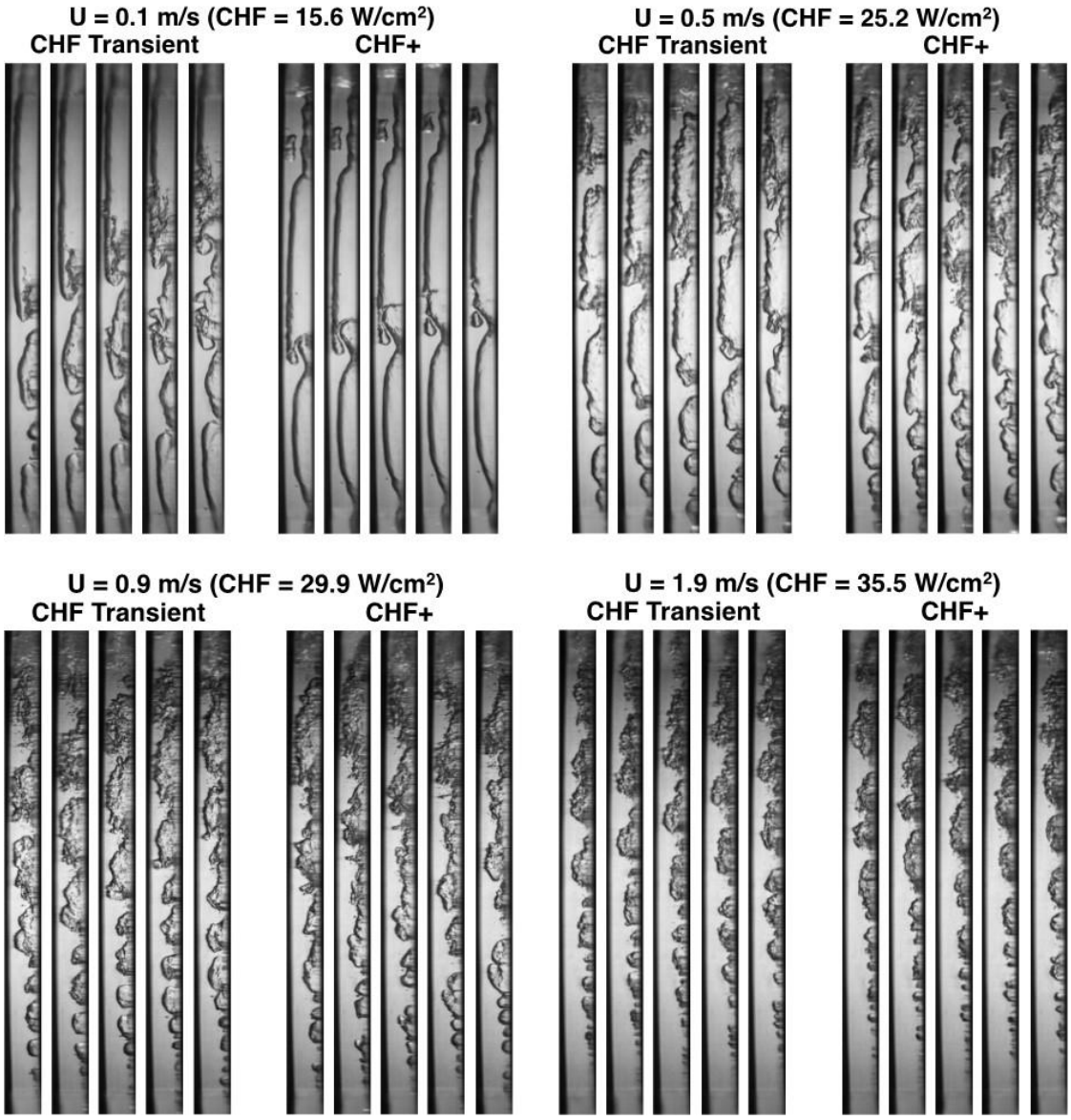

Figure 6.12: Sequential high-speed video images from single-sided heating experiments for different inlet velocities obtained during CHF transient and at CHF+.

Figure 6.13 depicts sequential images captured in μg_e just before (CHF-), during the CHF transient, and just after CHF (CHF+) for double-sided heating at U = 0.1, 0.5, 0.9 and 1.9 m/s, where CHF- corresponds to heat fluxes equal to 95 ± 1% of CHF value. Notice that the image sequences for the single-sided heating do not include CHF- because coarse heat flux increments during these tests caused the last pre-CHF value to fall below the 95 ± 1% range. The double-sided tests involved far smaller heat flux increments prior to CHF, allowing precise determination of CHF- conditions, as well as measurement of CHF values for both heated walls. For double-sided heating, Figure 6.13 shows CHF- for U = 0.1 m/s is associated with the development of wavy vapor layers staring immediately at the leading edge of the heated region. There is also appreciable meshing between wavy vapor layers from the opposite walls beginning near the leading edge, whereas the downstream region incurs merging of the wavy vapor layers, with both walls being replenished by liquid ligaments that are entrained in the coalescent vapor flow. During the CHF transient, the majority of the downstream region is covered with vapor, and cooling is concentrated in a few wetting fronts farther upstream. At CHF+, these upstream wetting fronts are extinguished, meaning no further regions are available for core liquid to cool or replenish the heated walls. As the inlet velocity is increased to 0.5 and 0.9 m/s, the mean thickness of the opposite wavy vapor layers decreases at CHF-, shifting both the meshing and merging of the two layers farther downstream; there is also a substantial increase in the number of wetting fronts. During the CHF transient, downstream regions begin to dry out, and, at CHF+, wetting fronts both upstream and in the middle of the heated region begin to be extinguished. At the highest inlet velocity of U = 1.9 m/s, CHF- conditions could not be captured by video within the 95 ± 1% range, but images during the CHF transient depict a substantial decrease in mean thickness of the opposite vapor layers and increase in the number of wetting fronts; the meshing between the two layers is also shifted farther downstream compared to lower velocities. At CHF+, there is downstream merging between the two layers and difficulty maintaining wetting fronts; both appear to contribute to wall dryout.

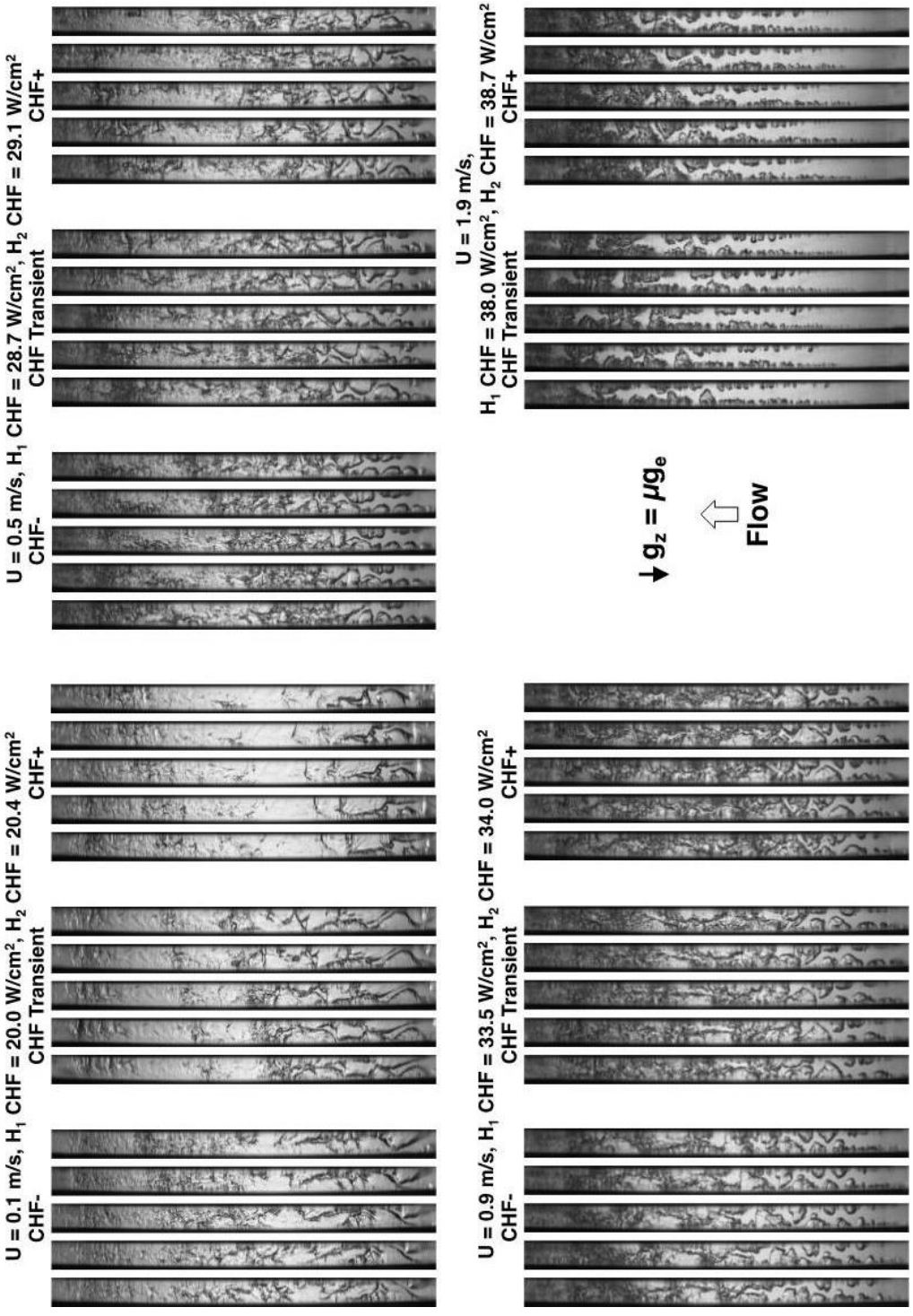

Figure 6.13: Sequential high-speed video images from double-sided heating experiments for different inlet velocities obtained at CHF-, during CHF transient and at CHF+.

6.4.2 Idealized Representation of Interfacial Behavior at CHF-

Figure 6.14(a) and 6.14(b) show idealized schematics of interfacial behavior observed at CHF- in the upstream region for single-sided and double-sided heating, respectively. A key feature of the interfacial behavior for both configurations is wavy vapor layer formation. This vapor layer is the result of both evaporation and bubble coalescence. Localized dryout occurs beneath the wave peaks as the wavy vapor layer propagates along the heated wall, while vigorous boiling is sustained in wetting fronts corresponding to the wave troughs. There is also a continuous wetting front upstream. The mean thickness of the wavy vapor layer increases along the flow direction due to evaporation. Notice that the meshing and merging of vapor layers from opposite walls for double-sided heating are purposely eliminated from Figure 6.14(b) to better represent the upstream evolution of the wavy vapor layer and wetting fronts as a prelude to development of the CHF model in the next section. The meshing and merging phenomena are depicted in Figure 6.5(b).

6.5 CHF Model

6.5.1 Model Rationale

Aside from the present findings, the CHF model presented in this section is also based on extensive photographic evidence from past 1-g_e [4,5,14-17,26,46,47,51,52,70-74] and μg_e flow boiling studies [1,57]. In all these studies, flow boiling was investigated along rectangular channels that were heated along a single wall. The most dominant interfacial feature observed in all these studies is a periodic wavy vapor layer that develops along the heated wall prior to CHF. The interfacial waviness is clearly a manifestation of hydrodynamic instability between liquid and vapor layers moving at different velocities. The second dominant feature is contact of the wavy interface with the wall in discrete "wetting fronts" corresponding to the wave troughs. At CHF-, vigorous boiling is observed in the wetting front, while portions of the vapor layer around the wave peaks appear dry. This points to the wetting fronts as the last source for cooling and liquid replenishment for the heated wall. Two forces control the formation of a

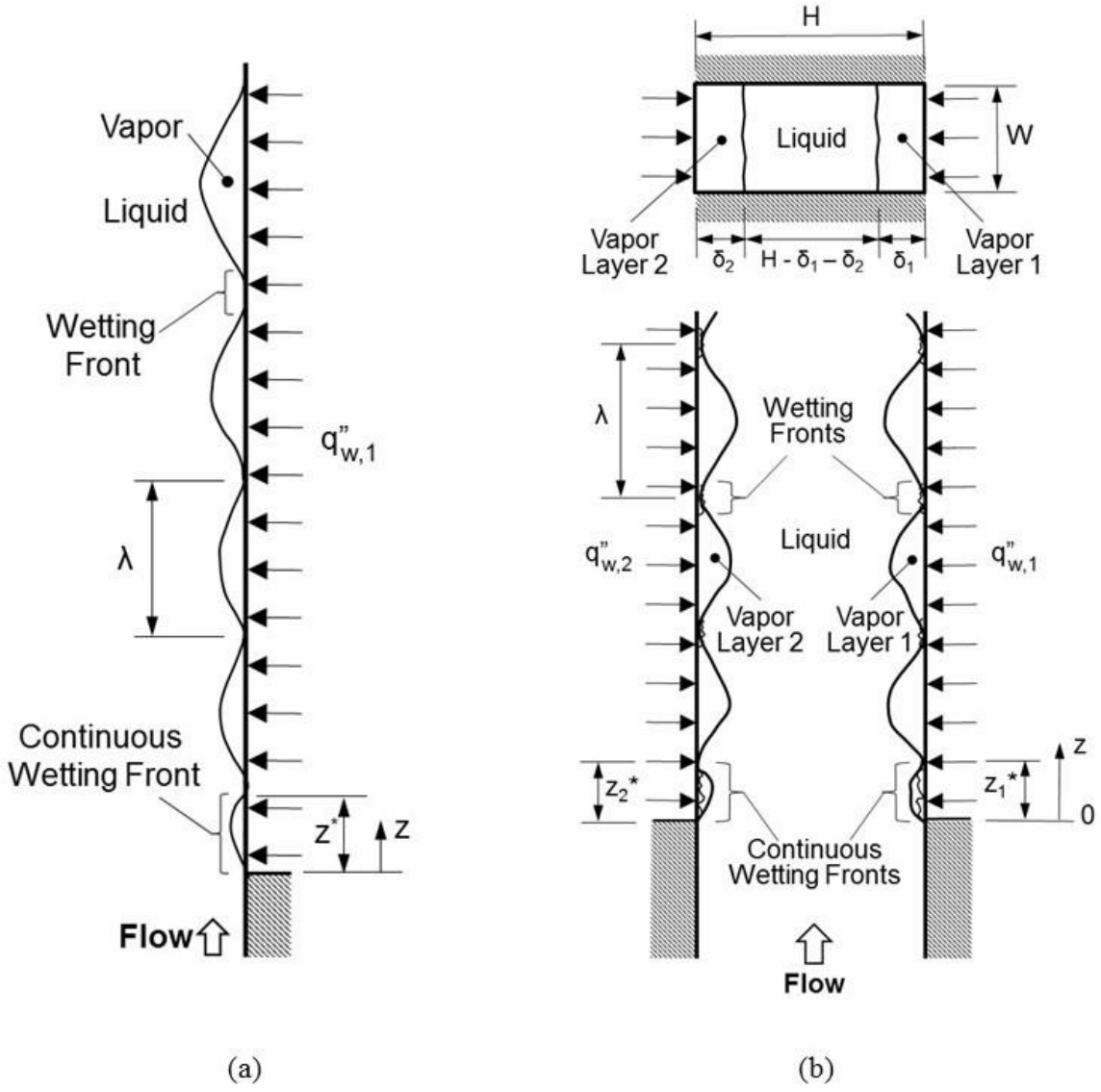

Figure 6.14: Schematics of upstream wavy vapor layer and wetting front development at CHF- for (a) single-sided heating and (b) double-sided heating. Downstream meshing and merging of vapor layers from the opposite walls for double-sided heating are purposely eliminated to better represent the upstream development of the vapor layers.

wetting front. A pressure force associated with interfacial curvature around the wave troughs pushes the interface towards the heated wall. The pressure force is opposed by momentum generated by intense vapor effusion in the wetting front normal to, and away from the wall. Interfacial contact with the wall is ensured and wetting fronts are maintained at CHF- because the pressure force exceeds the vapor momentum. CHF is postulated to commence when the vapor momentum increases to just overcome the pressure force. This event causes lifting of the interface from the wall, which extinguishes the wetting front. Heat that was dissipated at the just extinguished wetting front must now be conducted axially through the wall and dissipated to neighboring wetting fronts. This increases the momentum of vapor effusion in the neighboring wetting fronts, fostering rapid extinguishing of these wetting fronts as well. This process can best be described as a chain reaction, where wetting fronts are extinguished in succession and at an increasing rate. Loss of wetting fronts leaves the wall essentially dry, an event that is captured by the wall thermocouples in the form of a sharp and unsteady rise in the wall temperature. These interfacial events at CHF- are key components of the Interfacial Lift-off Model first proposed by Galloway and Mudawar [9,10] for single-sided heating.

However, the model sought here must tackle double-sided heating and accurately predict data for both 1 g_e and μg_e. Like the original Galloway and Mudawar model, the present model incorporates four major components: (1) a separated flow model to determine axial variations of mean liquid and vapor velocities, and mean thickness of the wavy vapor layers, (2) an instability model of the wavy vapor layer to determine the wavelength, wetting front axial span, and pressure force created by interfacial curvature, (3) an interfacial lift-off criterion – CHF trigger mechanism – to determine the heat flux in wetting fronts required to produce sufficient vapor momentum to exceed the curvature pressure force, and (4) a surface energy balance to relate the average wall heat flux for the entire heated wall to the heat flux concentrated in the wetting fronts propagating along the wall.

6.5.2 Separated Flow Model

A separated flow model is constructed to determine axial variations of mean liquid and vapor velocities, and mean thickness of the wavy vapor layers. Illustrated in Figure 6.15(a) is an idealized representation of vapor layers growing along both heated walls with the liquid flowing in between. The flow, therefore, consists of three clearly identifiable layers. The control volume method is used to apply mass, momentum and energy conservation to the individual phases and/or the entire flow. In Figure 6.15(a), $\Gamma_{fg,1}$ and u_{i1} represent the rate of evaporation per unit distance between the liquid layer and vapor layer 1, and streamwise velocity of the liquid-vapor interface in between. Similarly, $\Gamma_{fg,2}$ and u_{i2} represent the rate of evaporation per unit distance between the liquid layer and vapor layer 2 and the streamwise velocity of the liquid-vapor interface in between. The assumptions employed in the separated flow model are: (1) the heated walls provide equal heat fluxes, (2) the vapor layers are initiated at the leading edge (z = 0) for each heated wall (this assumption is justified by the slightly subcooled inlet liquid conditions), (3) velocities are uniform across the individual layers (*i.e,* the two-phase flow is one-dimensional), (4) pressure is uniform across the channel's cross-section, (5) the middle liquid layer preserves its subcooling in the axial direction, and (6) the vapor maintains saturation temperature corresponding to local pressure at every z location.

Applying mass conservation to a control volume of length Δz encompassing the entire cross-section yields $d\dot{m}/dz = 0$, which implies $\dot{m}$ is constant, also G is constant since $G = \dot{m}/A$ and A is constant. Applying energy conservation to the vapor layers yields the following relations for mean velocities, U_{g1} and U_{g2}, of the vapor layers along heated walls *H1* and *H2*, respectively, in terms of the mean thicknesses of the respective layers,

$$U_{g1} = \frac{q''_w \, z}{\rho_g \, \delta_1 \left(c_{p,f} \, \Delta T_{sub,in} + h_{fg} \right)} \tag{6.3a}$$

and

$$U_{g2} = \frac{q''_w \, z}{\rho_g \, \delta_2 \left(c_{p,f} \, \Delta T_{sub,in} + h_{fg} \right)}. \tag{6.3b}$$

Continuity is used to derive an expression for the mean velocity of the liquid layer. For equal heat flux, q''_w, applied along both heated walls,

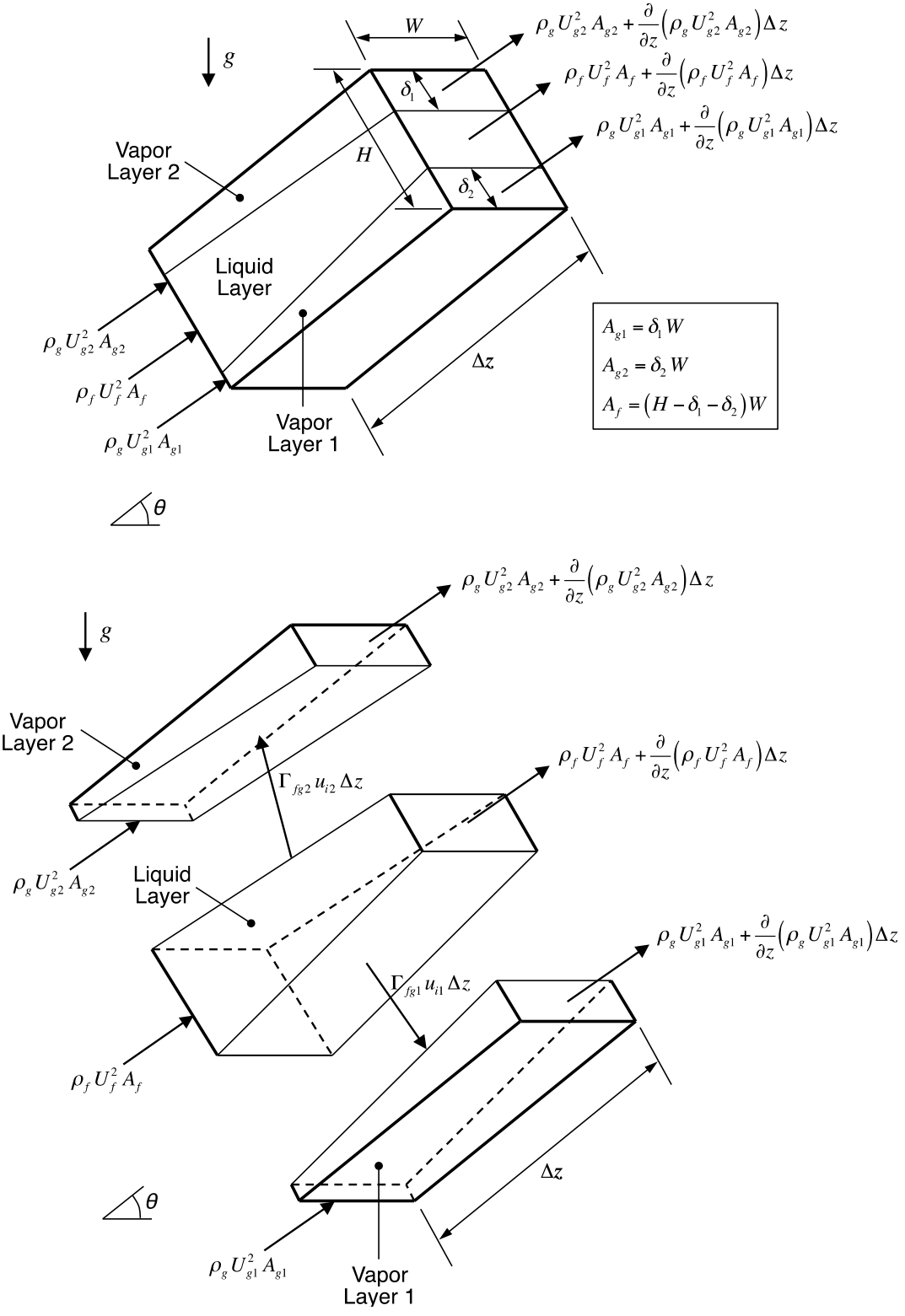

Figure 6.15(a): Mass conservation applied to control volumes of length Δz for combined two-phase flow and for individual layers.

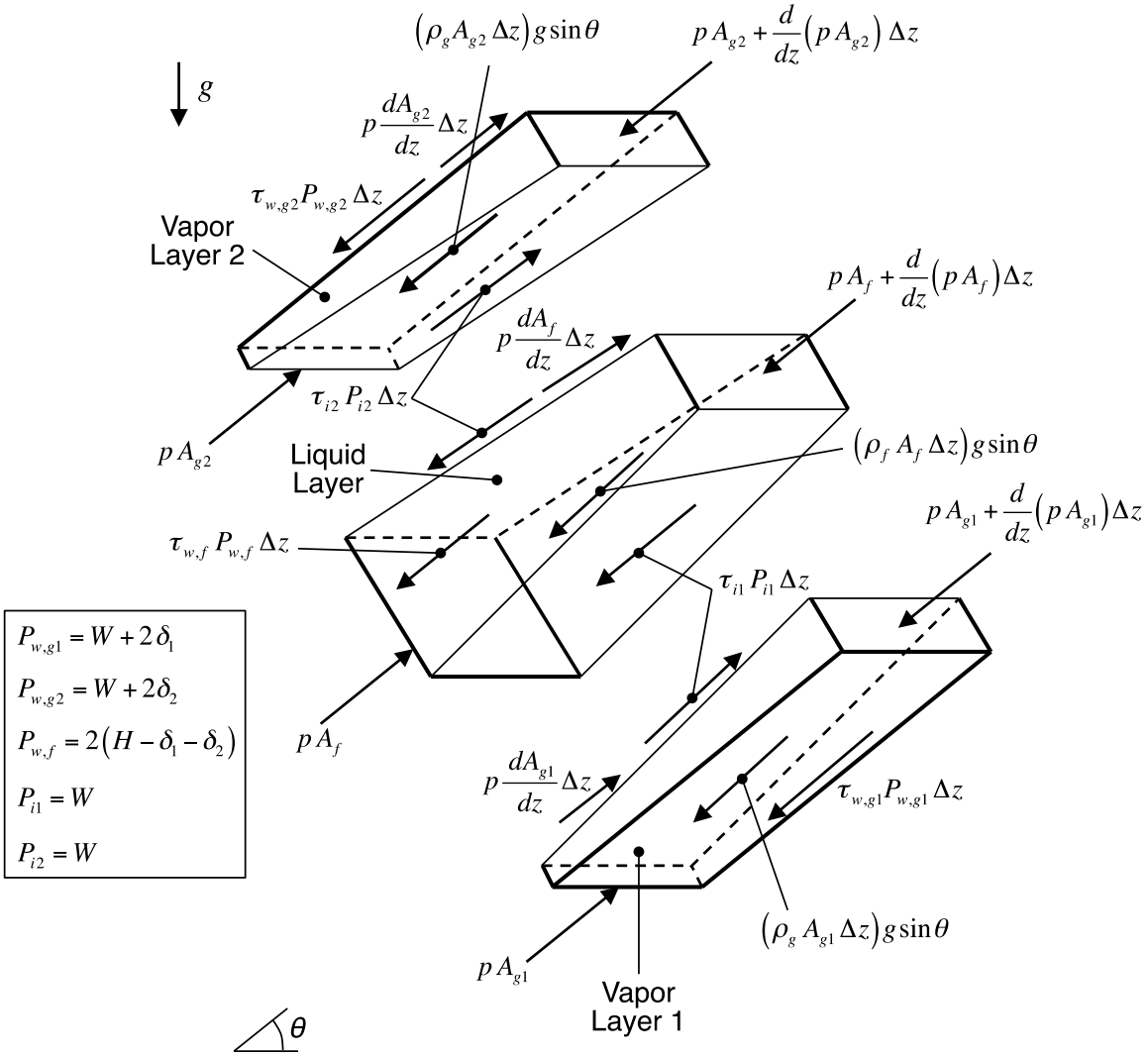

Figure 6.15(b): Momentum conservation applied to control volumes of individual layers.

$$U_f = \frac{UH}{H-\delta_1-\delta_2} - \frac{2q''_w\, z}{\rho_f (H-\delta_1-\delta_2)\left(c_{p,f}\Delta T_{sub,in} + h_{fg}\right)}. \tag{6.4}$$

Figure 6.15(b) shows momentum conservation for control volumes of length Δz encompassing the three individual layers of the flow. For now, an arbitrary body force per unit volume g is assumed with the channel oriented at angle θ relative to the horizontal plane, and $g \approx 0$ in microgravity. Summing momentum and force terms yields the following relations for heated wall vapor layer 1, liquid layer and heated wall vapor layer 2, respectively,

$$\frac{d}{dz}\left(\rho_g U_{g1}^2 A_{g1}\right) - \Gamma_{fg1} u_{i1} = -A_{g1}\frac{dp}{dz} - \tau_{w,g1} P_{w,g1} \mp \tau_{i1} P_{i1} - \rho_g A_{g1} g \sin\theta, \tag{6.5a}$$

$$\frac{d}{dz}\left(\rho_f U_f^2 A_f\right) + \Gamma_{fg1} u_{i1} + \Gamma_{fg2} u_{i2} = -A_f\frac{dp}{dz} - \tau_{w,f} P_{w,f} \pm \tau_{i1} P_{i1} \pm \tau_{i2} P_{i2} - \rho_f A_f g \sin\theta, \tag{6.5b}$$

and

$$\frac{d}{dz}\left(\rho_g U_{g2}^2 A_{g2}\right) - \Gamma_{fg2} u_{i2} = -A_{g2}\frac{dp}{dz} - \tau_{w,g2} P_{w,g2} \mp \tau_{i2} P_{i2} - \rho_g A_{g2} g \sin\theta, \tag{6.5c}$$

where A_{g1}, A_f, A_{g2}, u_{i1}, u_{i2}, $\tau_{w,g1}$, $\tau_{w,f}$, $\tau_{w,g2}$, $P_{w,g1}$, $P_{w,f}$, $P_{w,g2}$, τ_{i1}, τ_{i2}, P_{i1}, and P_{i2} are the flow area for vapor layer 1, flow area for the liquid layer, flow area for vapor layer 2, interfacial velocity between vapor layer 1 and the liquid layer, interfacial velocity between vapor layer 2 and the liquid layer, wall shear stress for vapor layer 1, wall shear stress for the liquid layer, wall shear stress for vapor layer 2, wall friction perimeter for vapor layer 1, wall friction perimeter for the liquid layer, wall friction perimeter for vapor layer 2, interfacial shear stress between vapor layer 1 and the liquid layer, interfacial shear stress between vapor layer 2 and the liquid layer, interfacial perimeter between vapor layer 1 and the liquid layer, and interfacial perimeter between vapor layer 2 and the liquid layer. The flow areas are defined in Figure 6.15(a) in terms of the channel dimensions (W and H) and thicknesses of vapor layer 1, δ_1, and vapor layer 2, δ_2. Figure 6.15(b) provides definitions for all wall friction and interfacial perimeters.

Visual observations from prior flow boiling studies [1,57] revealed the vapor generated at the leading edge of the heated wall has no initial streamwise velocity. Therefore, it is assumed the liquid-vapor interface does not contribute streamwise momentum to the control volumes ($u_{i1} = u_{i2} = 0$). Equations 6.5(a) – 6.5(c) can be

presented in terms of flow quality of vapor layer 1, x_1, void fraction of vapor layer 1, α_1, flow quality of vapor layer 2, x_2, and void fraction of vapor layer 2, α_2.

$$G^2 \frac{d}{dz}\left[\frac{x_1^2}{\rho_g \alpha_1}\right] = -\alpha_1 \frac{dp}{dz} - \frac{\tau_{w,g1} P_{w,g1}}{A} \mp \frac{\tau_{i1} P_{i1}}{A} - \rho_g \alpha_1 g \sin\theta, \tag{6.6a}$$

$$G^2 \frac{d}{dz}\left[\frac{(1-x_1-x_2)^2}{\rho_f (1-\alpha_1-\alpha_2)}\right] = -(1-\alpha_1-\alpha_2)\frac{dp}{dz} - \frac{\tau_{w,f} P_{w,f}}{A} \pm \frac{\tau_{i1} P_{i1}}{A} \pm \frac{\tau_{i2} P_{i2}}{A} - \rho_f (1-\alpha_1-\alpha_2) g \sin\theta, \tag{6.6b}$$

and

$$G^2 \frac{d}{dz}\left[\frac{x_2^2}{\rho_g \alpha_2}\right] = -\alpha_2 \frac{dp}{dz} - \frac{\tau_{w,g2} P_{w,g2}}{A} \mp \frac{\tau_{i2} P_{i2}}{A} - \rho_g \alpha_2 g \sin\theta, \tag{6.6c}$$

where $A = WH$ and the definitions for x_1, α_1, x_2, α_2, $\tau_{w,g1}$, $\tau_{w,f}$, $\tau_{w,g2}$, τ_{i1} and τ_{i2} are provided in Table 6.1.

Notice that, for equal heat flux, q''_w, along both heated walls, Eqs. 6.3(a) and 6.3(b) yield the following differential relations for flow qualities of the vapor layers.

$$\frac{dx_1}{dz} = \frac{dx_2}{dz} = \frac{q''_w W}{\dot{m}\left(c_{p,f} \Delta T_{sub,in} + h_{fg}\right)}. \tag{6.7}$$

Using a fourth-order Runge-Kutta numerical scheme, the separated flow model relations are solved simultaneously to determine axial variations of pressure, p, qualities, x_1 and x_2, mean velocity of vapor layer 1, U_{g1}, mean velocity of liquid velocity, U_f, mean velocity of vapor layer 2, U_{g2}, mean thickness of vapor layer 1, δ_1, and mean thickness of vapor layer 2, δ_2. The main input parameters of the model equations, which are defined at the inlet to the channel's heated length ($z = 0$) are inlet pressure, p_{in}, inlet temperature, T_{in}, mass velocity, G, and wall heat flux, q''_w.

6.5.3 Interfacial Instability Analysis

Visual observations from prior flow boiling studies corresponding to subcooled [4,5,14-17,46,47,60,71] and saturated [26,51,52,73,74] inlet conditions, showed the vapor at CHF- forms a wavy layer along the heated wall. Classical instability theory [15,55,56] is utilized to describe a sinusoidal liquid-vapor interface between two fluid layers moving at different velocities. The instability is governed by the relative influences of the inertia, surface tension and body force. Instability is postulated to be a necessary condition for the interface to contact the heated wall in order to establish wetting fronts. In the analysis

Table 6.1: Summary of relations used in conjunction with the separated flow model.

Quality relations for individual vapor layers:

$$x_1 = \frac{\rho_g U_{g1} \alpha_1}{G} \text{ and } x_2 = \frac{\rho_g U_{g2} \alpha_2}{G}$$

Wall shear stress relations:

$$\tau_{w,k,j} = \frac{1}{2} \rho_k U_{k,j}^2 f_{k,j}$$

$$f_{k,j} = C_1 + \frac{C_2}{\mathrm{Re}_{D,k,j}^{1/C_3}} = C_1 + \frac{C_2}{\left(\frac{\rho_k U_{k,j} D_{k,j}}{\mu_k} \right)^{1/C_3}}$$

where $k = f$ or g, and j = 1-2. $C_1 = 0$, $C_2 = 16$ and $C_3 = 1$ for laminar flow ($Re_{D,k,j} \leq 2100$), $C_1 = 0.0054$, $C_2 = 2.3 \times 10^{-8}$ and $C_3 = -2/3$ for transitional flow ($2100 < Re_{D,k,j} \leq 4000$), and $C_1 = 0.00128$, $C_2 = 0.1143$ and $C_3 = 3.2154$ for turbulent flow ($Re_{D,k,j} > 4000$) [54], where $D_{k,j} = 4A_{k,j}/P_{k,j}$

Interfacial shear stress relations:

$$\tau_{i1} = \frac{C_{f,i}}{2} \rho_g \left(U_{g1} - U_f \right)^2 \text{ and } \tau_{i2} = \frac{C_{f,i}}{2} \rho_g \left(U_{g2} - U_f \right)^2,$$

where $C_{f,i} = 0.5$ [15]

presented below, hydrodynamic instability analysis is used to determine (1) the wavelength of the vapor-liquid interface, which also dictates the length of the wetting front, and (2) the interfacial curvature above the wetting front, which dictates the magnitude of pressure force tending to secure attachment of the interface with the heated wall. Similar instability analysis has yielded remarkable success in predicting flow boiling CHF for single-sided heating [1,4,5,14-17,26,46,47,51,52,57,71-74].

Figure 6.16(a) and 6.16(b) show idealized instability representations of flow boiling at CHF- in Earth's gravity and microgravity, respectively. The vapor-liquid interfaces between vapor layer 1 and the liquid layer, and between vapor layer 2 and the liquid layer, are assumed to acquire the simple waveform $\eta(z,t)=\eta_0 e^{ik(z-ct)}$, where η_0 is the wave amplitude, k the wave number ($k = 2\pi/\lambda$), and c the wave speed. The wave speed is comprised of a real part, representing actual speed of the interface, and an imaginary part that characterizes interfacial stability, $c = c_r + \mathrm{i}\, c_i$. A disturbance normal to the interface associated with this waveform produces a pressure difference across the interface that can be expressed as

$$p_f - p_g = -\left[\rho_f''\left(c-U_f\right)^2+\rho_g''\left(c-U_{g,m}\right)^2+\left(\rho_f-\rho_g\right)\frac{g_{n,m}}{k}\right]k\eta_o e^{ik(z-ct)}, \tag{6.8}$$

where $\rho_f''=\rho_f \coth(kH_f)$ and $\rho_g''=\rho_g \coth(kH_g)$ are "modified density" terms, and g_n is the component of gravity normal to the heated wall. Equation (6.8) represents instability between a single liquid layer and single vapor layer, which is why the subscripts for heated walls *H1* and *H2* in mean vapor velocity are dropped for now. The mean liquid and vapor thicknesses, H_f and H_g, respectively, found in the modified density terms are obtained from the simple relations

$$H_g=\delta_1=\delta_2=\delta \tag{6.9a}$$

and

$$H_f=H-\delta_1-\delta_2=H-2\delta, \tag{6.9b}$$

which assume identical vapor behavior on both heated walls. Pressure difference across the vapor-liquid interface can also be approximated as the product of surface tension and curvature,

$$p_f - p_g \approx \sigma\frac{\partial^2\eta}{\partial z^2}=-\sigma\eta_o k^2 e^{ik(z-ct)}. \tag{6.10}$$

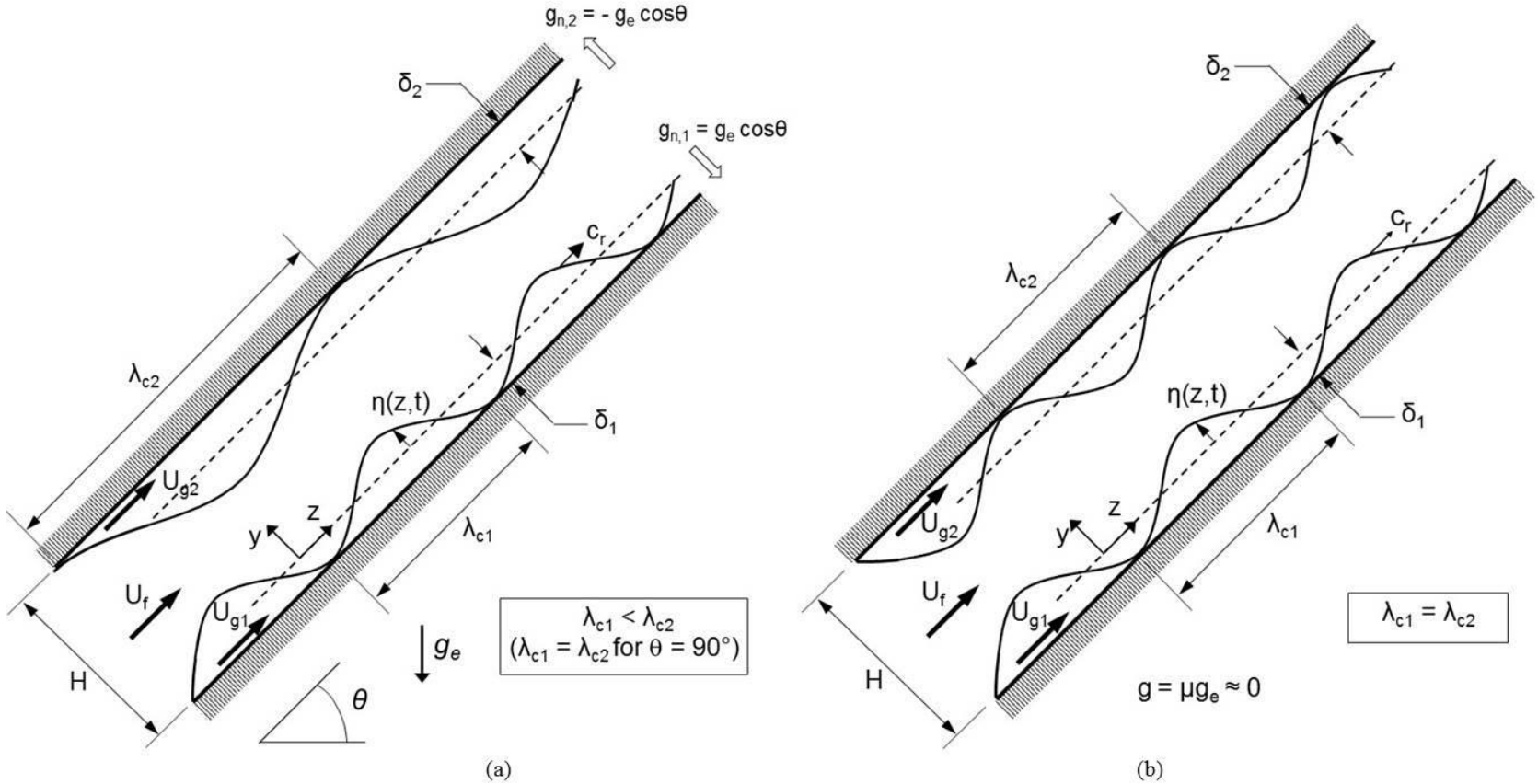

Figure 6.16: Hydrodynamic instability of wavy vapor layers along heated walls of double-sided heated channel at CHF- (a) for inclined channel at 1 g_e and (b) for microgravity.

Equating Eqs. (6.8) and (6.10) for pressure difference yields the following quadratic equation for wave speed,

$$\rho_f''\left(c-U_f\right)^2+\rho_g''\left(c-U_{g,m}\right)^2+\left(\rho_f-\rho_g\right)\frac{g_{n,m}}{k}-\sigma k=0\,, \tag{6.11}$$

whose solution is

$$c=\frac{\rho_f''U_f+\rho_g''U_{g,m}}{\rho_f''+\rho_g''}\pm\sqrt{\frac{\sigma k}{\rho_f''+\rho_g''}-\frac{\rho_f''\rho_g''\left(U_{g,m}-U_f\right)^2}{\left(\rho_f''+\rho_g''\right)^2}-\frac{\left(\rho_f-\rho_g\right)}{\left(\rho_f''+\rho_g''\right)}\frac{g_{n,m}}{k}}\,. \tag{6.12}$$

The terms under the radical in Eq. (6.12) represent different momentum and force components. The wave speed will acquire both real and imaginary components when the net for terms under the radical is negative. The real and imaginary components can be expressed, respectively, as

$$c_r=\frac{\rho_f''U_f+\rho_g''U_{g,m}}{\rho_f''+\rho_g''} \tag{6.13a}$$

and

$$c_i=\sqrt{\frac{\rho_f''\rho_g''\left(U_{g,m}-U_f\right)^2}{\left(\rho_f''+\rho_g''\right)^2}+\frac{\left(\rho_f-\rho_g\right)}{\left(\rho_f''+\rho_g''\right)}\frac{g_{n,m}}{k}-\frac{\sigma k}{\rho_f''+\rho_g''}}\,. \tag{6.13b}$$

In Eq. 6.13(b), the first term under the radical accounts for inertial, which is always destabilizing to the interface. The second term is associated with the gravitational body force, which in Earth's gravity may be stabilizing or destabilizing depending on orientation of the heated wall relative to gravity, while $g_n \approx 0$ in microgravity. The third term accounts for surface tension force, which tends to stabilize the interface.

The interface is stable when $c_i < 0$, which causes the amplitude of interfacial perturbation to decrease with time, preventing any contact of the interface with the heated surface. The interfacial contact essential to producing the wetting fronts requires that $c_i > 0$. Neutral stability, or the condition that initiates the contact is achieved when $c_i = 0$. The neutral stability condition is used to determine the value of critical wave number, k_c, associated with the critical wavelength, λ_c. This is achieved by setting Eq. (6.13b) equal to zero,

$$k_c=\frac{2\pi}{\lambda_c}=\frac{\rho_f''\rho_g''\left(U_{g,m}-U_f\right)^2}{2\sigma\left(\rho_f''+\rho_g''\right)}+\sqrt{\left[\frac{\rho_f''\rho_g''\left(U_{g,m}-U_f\right)^2}{2\sigma\left(\rho_f''+\rho_g''\right)}\right]^2+\frac{\left(\rho_f-\rho_g\right)g_{n,m}}{\sigma}}\,. \tag{6.14}$$

Aside from the magnitude of body force, there are fundamental differences between double-sided heating in microgravity and at different orientations in Earth gravity. In the latter, the components of gravity perpendicular to the heated walls yield different instability behavior for the two vapor layers. As shown in Figure 6.16(a), the gravitational components normal to the upward-facing heater (1) and the downward-facing heater (2) are expressed, respectively, as

$$g_{n,1} = g_e \cos\theta \tag{6.15a}$$

and

$$g_{n,2} = g_e \cos(\theta + \pi) = -g_e \cos\theta . \tag{6.15b}$$

For a particular flow orientation θ, the gravitational body force tends to destabilize the liquid-vapor interface adjacent to the upward-facing heated wall, and stabilize the interface on the downward-facing heated wall. Therefore, the interface along the downward-facing wall will be either stable or unstable, but with a critical wavelength larger than that of the upward-facing wall. For an unstable interface along the downward-facing wall, curvature near the wetting fronts is also weaker, causing CHF to be lower for the downward-facing wall compared to the upward-facing. It is important to note that these effects are more pronounced for low inlet velocities, where the influence of body force is most significant. However, by greatly increasing the inlet velocity, body force effects become comparatively insignificant, and CHF differences between the two walls less discernible. Notice that in Earth's gravity, vertical upflow produces zero gravitational body forces normal to the opposite heated walls and equal CHF values for both walls.

In microgravity, the body force component is negligible, which reduces Eq. (6.14) to

$$\lambda_c = \frac{2\pi\sigma\left(\rho_f'' + \rho_g''\right)}{\rho_f''\rho_g''\left(U_g - U_f\right)^2} \tag{6.16}$$

Also, in the absence of gravity, CHF is the same for the two opposite heated walls. Flow visualization results from [1,4,5,57,60,71,72] have demonstrated the existence of a continuous upstream liquid wetting region, z^*, defined as

$$z^* = z_0 + \lambda_c\left(z^*\right), \tag{6.17}$$

where z_0 is the distance from the leading edge of the heated wall to the location where the vapor velocity just exceeds the liquid velocity. Beyond z^*, the vapor velocity continues to increase faster than the liquid velocity, resulting in hydrodynamic instability of the wavy vapor-liquid interface. Determination of λ_c using Eq. (6.16) and z^* using Eq. (6.17) requires iteration. The separated flow model provides the flow parameters needed to calculate of critical wavelength.

6.5.4 Interfacial Lift-Off Criterion

As discussed earlier, CHF is postulated to occur when the momentum of vapor emanating in the wetting fronts normal to the heated wall overcomes the pressure force associated with interfacial curvature. Illustrated in Figure 6.17(a), the average pressure force over the wetting front is equated to the vapor momentum. Integrating the expression for pressure difference, Eq. (6.10), over the width of the wetting front, $b\lambda$,

$$\overline{p_f - p_g} = \frac{4\pi\sigma\delta}{b\lambda_c^2}\sin(b\pi), \tag{6.18}$$

where b is the ratio of wetting front length to the wavelength. Extensive video analysis of the wavy vapor layer at CHF- by Sturgis and Mudawar [16,17] revealed a consistent value of b = 0.2, which also used in the present study. The mean velocity of vapor produced in the wetting front normal to the heated wall is obtained by equating the heat concentrated in the wetting front to the energy of the generated vapor.

$$q''_{w,w} A_{w,w} = \left(c_{p,f}\,\Delta T_{sub,in} + h_{fg}\right)\rho_g U_{g,n} A_{w,w}, \tag{6.19}$$

where, $q''_{w,w}$ is the heat flux concentrated in the wetting front, $A_{w,w}$ the wetting front area, and $U_{g,n}$ the vapor velocity normal to the wall. Equation (6.19) is used to determine $U_{g,n}$. Then, equating the normal vapor momentum, $\rho_g U_{g,n}^2$, to the average pressure difference given by Eq. (6.18) yields the following relation for the lift-off heat flux concentrated in the wetting front,

$$q''_{w,w} = \rho_g\left(c_{p,f}\,\Delta T_{sub,in} + h_{fg}\right)\sqrt{\frac{\overline{p_f - p_g}}{\rho_g}} = \rho_g\left(c_{p,f}\,\Delta T_{sub,in} + h_{fg}\right)\left[\frac{4\pi\sigma}{\rho_g}\frac{\sin(b\pi)}{b}\right]^{1/2}\frac{\delta^{1/2}}{\lambda_c}. \tag{6.20}$$

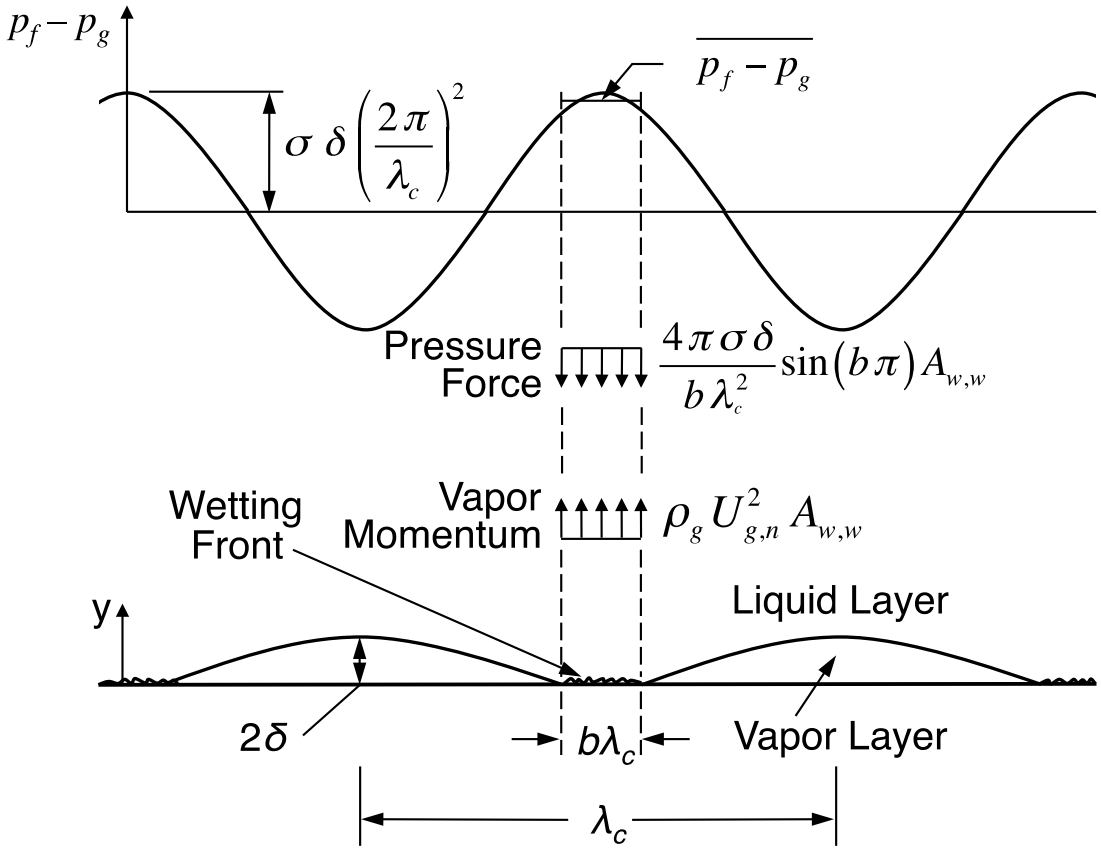

Figure 6.17(a): Schematic representation of interfacial lift-off from heated wall in wetting front at CHF.

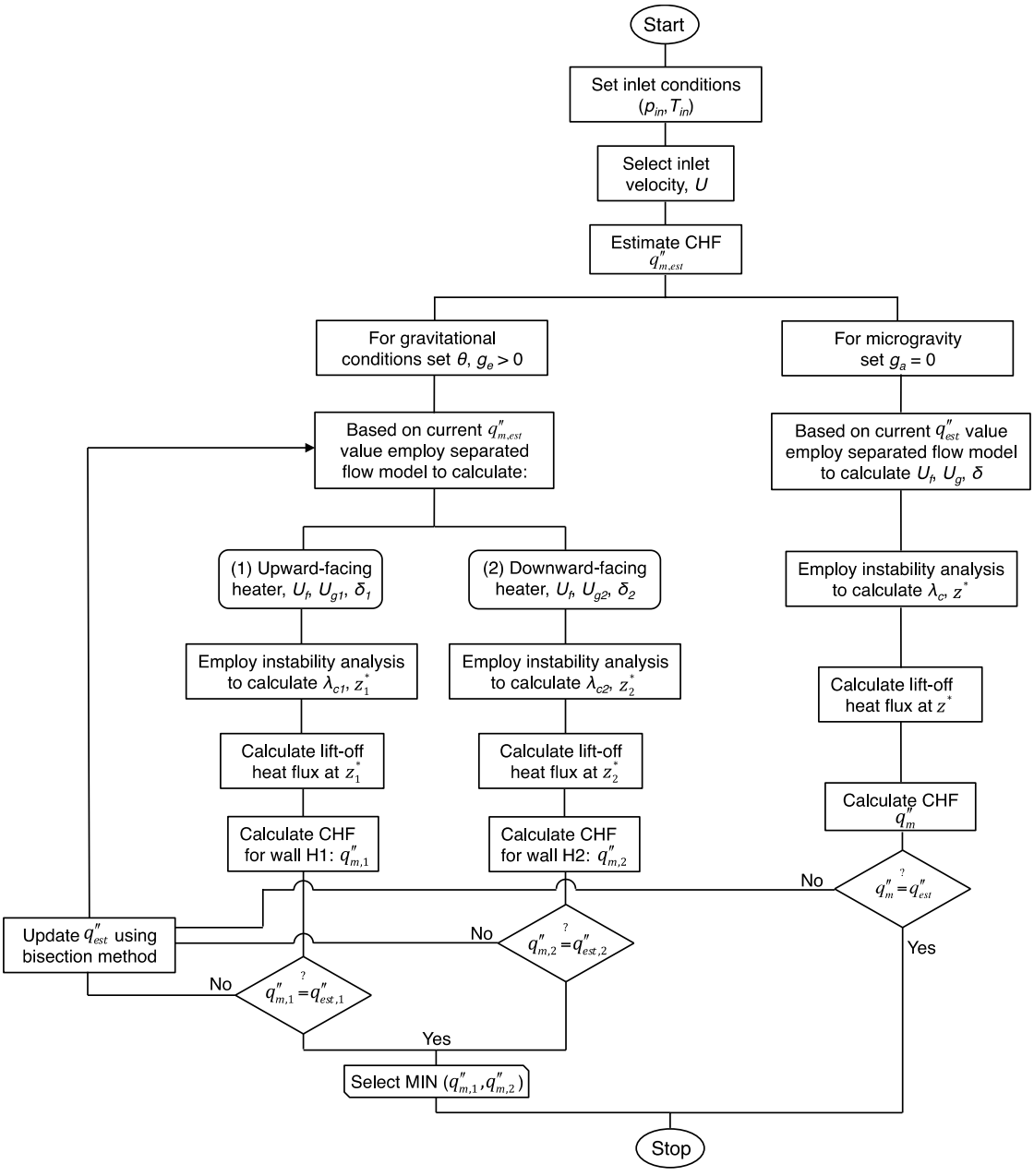

Figure 6.17(b): Procedure used to calculate CHF.

6.5.5 Heated Wall Energy Balance

An energy balance is applied in which the sum of heat dissipated at CHF- in all the wetting fronts is equal to the total heat supplied from the heated wall. The critical heat flux, q''_m, is based on the total wall heat input divided by the total wall area, therefore

$$q''_m = b q''_{w,w} . \tag{6.21}$$

Combining Eq. (6.21) with the expression for heat flux in the wetting front given by Eq. (6.20) gives the following relation for CHF.

$$q''_m = \rho_g \left(c_{p,f} \Delta T_{sub,in} + h_{fg} \right) \left[\frac{4\pi\sigma b \sin(b\pi)}{\rho_g} \right]^{1/2} \left. \frac{\delta^{1/2}}{\lambda_c} \right|_{z^*} , \tag{6.22}$$

where the vapor layer thickness, δ, and critical wavelength, λ_c, are calculated at z^*, where the wavy vapor layer is generated.

6.5.6 CHF Model Calculation Procedure

The CHF model is composed of four major components, and is capable of predicting CHF for subcooled flow boiling in terrestrial and microgravity environments. Combining the different equations associated with the four components requires multiple iterations to arrive at a convergent CHF value. Figure 6.17(b) provides a step-by-step procedure for this iterative solution. The procedure is initiated by setting the subcooled inlet conditions at the leading edge of the heaters (z = 0) in terms of temperature T_{in}, pressure p_{in}, and inlet flow velocity U. The computations begins with a guessed value for critical heat flux, $q''_{m,est}$, which is used in the separated flow model to determine mean liquid velocity, U_f, as well as mean vapor velocity, U_g, and mean vapor layer thickness, δ, for both heated walls. These parameters are obtained for every z location along the heated length using a fourth-order Runge-Kutta numerical scheme. Next, CHF is determined for subcooled flow boiling in either Earth gravity or microgravity. In Earth's gravity (g = 1 g_e), CHF is influenced by gravitational body force, therefore the interfacial lift-off model will yield different values for upward-facing and downward-facing heated

walls, and therefore different CHF values. In microgravity ($g \approx 0$), body force is negligible, therefore identical CHF values are predicted for both heated walls.

A key step in the iterative solution is to determine z_0, where $U_g = U_f$, using the separated flow model. This is followed by calculating critical wavelength, λ_c, and axial span of the upstream wetting front, z^*, which requires multiple iterations. Using the value of $b = 0.2$ recommended in [16,17], CHF is finally determined by evaluating fluid properties, λ_c and δ at z^*. The predicted CHF value, q''_m, is compared with the initial estimate $q''_{m,est}$. If the two values differ by a small pre-specified value, the procedure is terminated, otherwise the entire procedure is repeated using the updated estimate until convergence is achieved.

Notice that, when the model is used to predict CHF for terrestrial conditions, different CHF values will be realized for the two heated walls. The true CHF is chosen as the lowest of the two values. This is based on actual practice in performing flow boiling experiments, where, to avoid any physical damage to the flow channel components, the power to both walls must be simultaneously cut off once CHF is encountered in either wall.

6.5.7 Comparison of CHF Data and Model Predictions

To explore the effectiveness of the CHF model just presented, the model predictions are compared to the double-sided heating CHF data obtained in μg_e onboard the parabolic aircraft. Figure 6.18 shows both the measured and predicted variations of CHF with inlet velocity for double-sided heating in μg_e. Low velocities are shown yielding relatively small CHF values in μg_e, and CHF increases appreciably with increasing flow velocity. Also shown in Figure 6.18 are predictions of the CHF model. Both measured and predicted results show CHF increases appreciably with increasing inlet velocity. Moreover, the CHF data are predicted very well in both trend and value. The *MAE* for the double-sided heating CHF data is 5.0% for *H1* and 5.7% for *H2*.

It is important to emphasize that the CHF model is capable of tackling both μg_e and 1 g_e conditions. To further investigate CHF trends, predictions for 1-g_e vertical upflow with double-sided heating are also presented in Figure 6.18. The upflow

configuration is unique for 1 g_e in that it does not include body force effects normal to the heated walls, which yields equal CHF values for the two walls. Notice how the 1-g_e predictions tend to converge with the μg_e data and predictions above $U \sim 1$ m/s. These findings are consistent with single-sided μg_e heating results of Zhang *et al.* [1], namely: (1) low CHF in low velocity μg_e flow boiling, (2) increasing CHF with increasing velocity, and (3) convergence between μg_e and 1-g_e CHF values at high velocities, (4) prevalence of wavy vapor layer and wetting fronts along heated wall at CHF-, and (5) effectiveness of Interfacial Lift-off model in predicting μg_e flow boiling CHF data. The convergence of CHF data for μg_e and 1 g_e around 1 m/s is especially important since knowing the velocity at which convergence occurs allows designers of space systems to achieve inertia-dominated performance as well as to take advantage of prior data and correlations developed from terrestrial studies.

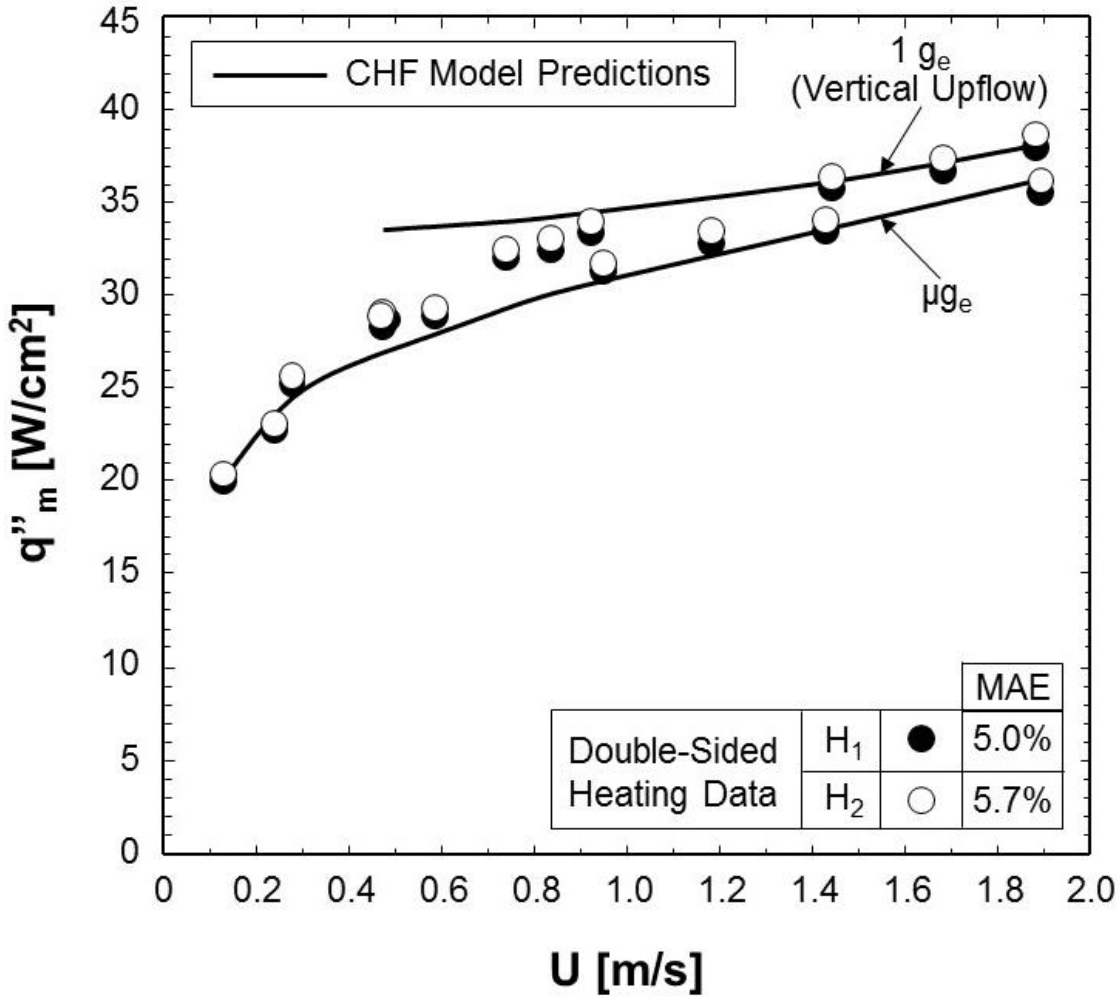

Figure 6.18: Comparison of measured and predicted variations of CHF with inlet velocity for double-sided heating in μg_e, along with predicted CHF for double-sided heating in vertical upflow at 1 g_e.

CHAPTER 7. CONCLUSIONS

7.1 Flow Boiling CHF with Inlet Void in Earth's Gravity

This study explored flow boiling CHF for FC-72 in a rectangular channel fitted along one side with a heated wall. The flow was supplied as a two-phase mixture and the channel was tested at different orientations relative to Earth's gravity. High-speed video imaging was used to explore interfacial behavior at heat fluxes up to and including CHF to capture the CHF trigger mechanism for different orientations, mass velocities and inlet qualities. The CHF data were compared to predictions of the Interfacial Lift-off Model. Key findings from the study are as follows.

(1) For low mass velocities ($G/\rho_f \leq 0.224$ m/s) and small inlet qualities, orientation has a significant influence on CHF. The orientations surrounding horizontal flow with upward-facing heated wall cause buoyancy to separate the flow with liquid flowing along the heated wall and the vapor flowing above. CHF for these orientations is triggered when intense vapor production separates the liquid layer from the heated wall. On the other hand, orientations surrounding horizontal flow with downward-facing heated wall cause stratification of the vapor towards the heated wall and yield very small CHF values.

(2) High mass velocities ($G/\rho_f \geq 0.398$ m/s) cause appreciable diminution in the influence of orientation on CHF, which is evidenced by similar flow separation patterns and CHF trigger mechanism regardless of orientation. This behavior can be explained by the higher mass velocities increasing the magnitude of shear and drag forces compared to buoyancy, especially for high inlet qualities.

(3) Excluding the combination of very low velocities and downward-facing heated wall orientations, the influence of orientation on CHF is predicted with good accuracy in both trend and magnitude by the Interfacial Lift-off Model. The model points to the

(4) effectiveness of inertia at overcoming buoyancy effects and helping produce CHF values insensitive to orientation.

7.2 Localized Dryout Versus CHF

This terrestrial-based study investigated the interfacial phenomena preceding the occurrence of CHF for flow boiling with a finite inlet vapor void. Temporal records of the heated wall temperatures were used to track the complex transient response of the heated wall, and identify differences between temperature excursions associated with momentary localized dryout and those with true CHF. Key findings from the study are as follows.

(1) The flow enters the channel fully separated, with a liquid layer sheathing all four channel walls surrounding a central vapor core. At high heat fluxes, a wavy vapor layer begins to form beneath the heated wall liquid layer, and cooling is available mostly through wetting fronts in accordance with the Interfacial Lift-off Model. However, certain operating conditions cause monetary dryout well below true CHF.

(2) Localized dryout is observed prior to CHF for upward-facing heated wall orientations (θ = 315°, 0° and 45°) in the inlet region of the heated wall for low inlet mass velocities ($G/\rho_f \leq 0.315$ m/s), and the outlet region for mid-range velocities ($0.542 \geq G/\rho_f \geq 0.315$ m/s). This phenomenon is associated with breakup of the heated wall liquid layer into ligaments that are entrained in the vapor core. The wall is able to recover from this dryout by a combination of reattachment of ligaments with the heated wall and heat conduction.

(3) Breakup into ligaments is the result of axial thinning of the heated wall liquid layer caused by both evaporation and axially increasing shear stresses. The separated flow model is an effective tool for describing this thinning effect and eventual evaporation of the heated wall liquid layer.

(4) Experimental studies must adopt minimum heated wall thickness criteria and consistent temperature detection methods to achieve reliable CHF data.

7.3 Assessment of Body Force on Flow Boiling CHF

This study explored the influence of orientation on flow boiling CHF with two-phase inlet conditions in Earth's gravity.. Using FC-72 as working fluid, different CHF regimes were identified for different orientations, mass velocities and inlet qualities. These results were used to develop dimensionless criteria for negating the influence of gravity on CHF. Key findings from the study are as follows.

(1) Orientation has an appreciable influence on CHF for low mass velocities ($G/\rho_f \leq$ 0.224 m/s), resulting in a number of CHF regimes, including *Pool Boiling, Stratification* and *Wavy Vapor Layer*. On the other hand, only the *Wavy Vapor Layer Regime* is prevalent at high mass velocities. Overall, the influence of orientation on CHF is insignificant in the limit of very high mass velocity, especially with high inlet quality.

(2) Negating the influence of orientation on CHF is achieved by simultaneously satisfying three separate criteria: overcoming the influence of gravity perpendicular to the heated wall, overcoming the influence of gravity parallel to the heated wall, and ensuring that the wavelength of the liquid-vapor interface is smaller than the heated wall to facilitate liquid contact with wall.

(3) The three criteria for negating the influence of orientation on CHF can be combined to determine the minimum mass velocity required to negate gravity effects in any gravitational environment. This minimum is crucial to the design of thermal management systems in both terrestrial and space applications since it corresponds to the minimum pumping power required to operate safely below CHF.

7.4 Review of Flow Boiling and CHF in Microgravity

The appendix consists of a study which reviewed published literature concerning two-phase flow and heat transfer in reduced gravity. Discussed are the different methods and platforms dedicated to exploring the influence of reduced gravity, including ground flow boiling experiments performed at different orientations relative to Earth gravity, as well as adiabatic two-phase flow, pool boiling, flow boiling and CHF reduced gravity experiments. Key observations from this review can be summarized as follows.

(1) Despite the important fundamental knowledge gained from microgravity pool boiling experiments, there is general agreement that, because of unusually large bubble size and appreciable reduction in CHF compared to terrestrial data, pool boiling will be difficult to implement in future space applications.

(2) By relying on fluid inertia to overcome body force effects, flow boiling provides an effective means for controlling bubble growth and sustaining liquid replenishment of the heater surface to boast CHF. This renders flow boiling a very suitable cooling configuration for future space applications.

(3) Many of the published microgravity heat transfer databases are measured using heater designs that fail to satisfy the asymptotic wall thickness limit, and therefore produce measurements that are heater specific rather than represent metallic surfaces of practical interest.

(4) Despite the extensive microgravity data and flow visualization results available in the literature, there is a severe shortage of useful correlations, mechanistic models and/or computational models, which compromises readiness to adopt flow boiling in future space systems.

(5) Emphasis in future microgravity studies should be placed on operating conditions, particularly mass velocity, that ensure inertia-dominated performance independent of gravity. Exceeding the minimum mass velocity necessary to achieve this goal allows data, correlations, and/or models developed at 1 g_e to be safely implemented in the design of space systems.

(6) Most reduced gravity experiments have been performed in short duration drop tower, drop shaft or parabolic flight platforms. Lack of ability to achieve steady state in short duration experiments brings into question the validity of a significant portion of this literature. Following the retirement of NASA's Space Shuttle program, the ISS constitutes the ideal testing platform for future flow boiling experiments. However, ISS experiments are very complex and costly, and require many years of development and safety certification. To maximize return on investment in space research, future ISS flow boiling experiments will require close cooperation among

space agencies worldwide on the design of ISS facilities, performance of experiments, sharing of data, and development of predictive correlations and models.

(7) Emphasis should also be placed on microgravity fluid flow and heat transfer associated with condensation, which is expected to be used concurrently with flow boiling in future space thermal management systems.

7.5 Flow Boiling in Microgravity

This study explored flow boiling heat transfer of FC-72 in microgravity, which was simulated in a series of parabolic flight maneuvers. A rectangular flow channel was used, which was fitted with two opposite heating walls, allowing either one or both walls to be activated during a given test. The study involved both high-speed video analysis of interfacial features and heat transfer measurements. The main objectives of this study are to capture the trigger mechanism for CHF and develop a mechanistic model for double-sided heating. Key findings from the study are as follows.

(1) Bubbly flow is encountered with double-sided heating only at the lowest flow velocity (U = 0.1 m/s) and lowest heat flux (37% CHF) tested. For all remaining conditions, which include velocities as high as 1.9 m/s and moderate to high heat fluxes, a dominant wavy vapor layer is encountered with both single-sided and double-sided heating. Boiling is sustained mostly in 'wetting fronts' where the wave troughs contact the wall, and abated near the wave peaks. The mean thickness of the vapor layer increases along the heated wall, but the wavelength decreases and number of wetting fronts increases with increasing velocity.

(2) Double-sided heating produces complex interactions between the opposite wavy vapor layers, resulting in three distinct regions: wavy vapor layer developing region, wavy vapor layer meshing region, and wavy vapor layer merging region. The wavy vapor layer is formed initially in the upstream developing region. In the middle meshing region, wave peaks from one wall protrude towards troughs in the opposite vapor layer, mimicking the engagement of gear teeth. The downstream merging region is characterized by opposite vapor layers virtually merging with one another with liquid ligaments squeezed in between.

(3) During a flight parabola, heated wall temperatures decrease slightly as the aircraft enters the hypergravity phase of the parabola. The heated wall temperatures then increase slightly as the aircraft enters the microgravity phase, and decrease once again during the hypergravity descent. These temperature variations point to enhancement in flow boiling heat transfer with increasing gravity, and degradation in μg_e.

(4) For identical inlet velocities and equal heat fluxes, double-sided heating produces better heat transfer compared to single-sided. This enhancement is attributed to higher vapor production, with double-sided heating resulting in faster fluid motion.

(5) CHF- interfacial behavior is consistent with the single-sided heating behavior proposed by Galloway and Mudawar [14,15], where a dominant wavy vapor layer covers the heated walls, with liquid access to the walls sustained only in wetting fronts corresponding to the troughs of the wave. CHF is associated with successive lift-off of wetting fronts from the walls, which is also consistent with the Interfacial Lift-off Model of Galloway and Mudawar.

(6) Data for both single-sided and double-sided heating configurations show CHF increases appreciably with increasing inlet velocity, with double-sided heating providing higher CHF than single-sided for identical inlet conditions and wall heat fluxes. Higher CHF for double-side heating is attributed to formation of two vapor layers compared to one vapor layer for single-sided increasing the velocities of the flow layers more with double-sided heating.

(7) The Interfacial Lift-off Model, which has been validated extensively in past studies using single-sided heating in both μg_e and 1 g_e, shows remarkable success in predicting μg_e double-sided heating CHF data in both trend and magnitude. Additionally, applying the same model for double-sided heating in vertical upflow at 1 g_e points to convergence of CHF values for μg_e and 1 g_e for inlet velocities greater than about 1 m/s. Therefore, using velocities above this threshold allows designers of space systems to achieve inertia-dominated performance as well as to adopt prior data and correlations developed from terrestrial studies.

LIST OF REFERENCES

LIST OF REFERENCES

[1] H. Zhang, I. Mudawar, M.M. Hasan, Flow boiling CHF in microgravity, Int. J. Heat Mass Transfer 48 (2005) 3107-3118.

[2] F.P. Chiaramonte, J.A. Joshi, Workshop on critical issues in microgravity fluids, transport, and reaction processes in advanced human support technology - final report, NASA TM-2004-212940, 2004.

[3] The National Academies, Recapturing a future for space exploration: life and physical sciences research for a new era, National Academies Press, Washington, DC, 2011.

[4] H. Zhang, I. Mudawar, M.M. Hasan, Experimental assessment of the effects of body force, surface tension force, and inertia on flow boiling CHF, Int. J. Heat Mass Transfer 45 (2002) 4079-4095.

[5] H. Zhang, I. Mudawar, M.M. Hasan, A method for assessing the importance of body force on flow boiling CHF, ASME J. Heat Transfer 126 (2004) 161-168.

[6] I. Mudawar, Recent advances in high-flux, two-phase thermal management, J. Thermal Science and Engineering Applications – Trans. ASME, in press.

[7] N. Zuber, M., Tribus, J.W. Westwater, The hydrodynamic crisis in pool boiling of saturated and subcooled liquids, Int. Dev. Heat Transfer: Proc. 1961-62 Int. Heat Transfer Conf., Boulder, CO (1961) 230-236.

[8] D.D. Hall, I. Mudawar, Critical heat flux (CHF) for water flow in tubes - I. Compilation and assessment of world CHF data, Int. J. Heat Mass Transfer 43 (2000) 2573-2604.

[9] S.S. Kutateladze, A.I. Leont'ev, Some applications of the asymptotic theory of the turbulent boundary layer, Proc. 3rd Int. Heat Transfer Conf., Chicago, Illinois, Vol. 3 (1966) 1-6.

[10] L.S. Tong, Boundary-layer analysis of the flow boiling crisis, Int. J. Heat Mass Transfer 11 (1968) 1208-1211.

[11] W. Hebel, W. Detavernier, M. Decreton, A contribution to the hydrodynamics of boiling crisis in a forced flow of water, Nuclear Engng Design 64 (1981) 443-445.

[12] J. Weisman, B.S. Pei, Prediction of critical heat flux in flow boiling at low qualities, Int. J. Heat Mass Transfer 26 (1983) 1463-1477.

[13] C.H. Lee, I. Mudawar, A mechanistic critical heat flux model for subcooled flow boiling based on local bulk flow conditions, Int. J. Multiphase Flow 14 (1988) 711-728.

[14] J.E. Galloway, I. Mudawar, CHF mechanism in flow boiling from a short heated wall-part 1. Examination of near-wall conditions with the aid of photomicrography and high-speed video imaging, Int. J. Heat Mass Transfer 36 (1993) 2511-2526.

[15] J.E. Galloway, I. Mudawar, CHF mechanism in flow boiling from a short heated wall-part 2. Theoretical CHF model, Int. J. Heat Mass Transfer 36 (1993) 2527-2540.

[16] J.C. Sturgis, I. Mudawar, Critical heat flux in a long, rectangular channel subjected to onesided heating - I. Flow visualization, Int. J. Heat Mass Transfer 42 (1999) 1835-1847.

[17] J.C. Sturgis, I. Mudawar, Critical heat flux in a long, rectangular channel subjected to onesided heating - II. Analysis of critical heat flux data, Int. J. Heat Mass Transfer 42 (1999) 1849–1862.

[18] S.M. Kim, I. Mudawar, Universal approach to predicting saturated flow boiling heat transfer in mini/micro-channels-Part I. Dryout incipience quality, Int. J. Heat Mass Transfer, in press.

[19] Y. Katto, General features of CHF of forced convection boiling in uniformly heated rectangular channels, Int. J. Heat Mass Transfer 24 (1981) 1413–1419.

[20] C. Martín-Callizo, Flow boiling heat transfer in single vertical channel of small diameter, Ph.D. Thesis, Royal Institute of Technology, Sweden, 2010.

[21] R. Ali, B. Palm, Dryout characteristics during flow boiling of R134a in vertical circular minichannels, Int. J. Heat Mass Transfer 54 (2011) 2434-2445.

[22] W.P. Baek, S.H. Chang, KAIST CHF data, Personal communication, Korea Advanced Institute of Science and Technology, Taejon, South Korea, December 8, 1997.

[23] G.M. Roach Jr., S.I. Abdel-Kahlik, S.M. Ghiaasiaan, M.F. Dowling, S.M. Jeter, Low-flow critical heat flux in heated microchannels, Nucl. Sci. Eng. 131 (1999) 411-425.

[24] K.M. Becker, Burnout measurements in vertical round tubes, effect of diameter, AE-TPM-RL-1260, Aktiebolaget Atomenergi, 1970.

[25] W.Yu, D.M. France, M.W. Wambsganss, J.R. Hull, Two-phase pressure drop, boiling heat transfer, and critical heat flux to water in a small-diameter horizontal tube, Int. J. Multiphase Flow 28 (2002) 927-941.

[26] C.R. Kharangate, I. Mudawar, M.M., Hasan, Experimental and theoretical study of critical heat flux in vertical upflow with inlet vapor void, Int. J. Heat Mass Transfer 55 (2012) 360-374.

[27] G. Guglielmini, E. Nannei, On the effect of heating wall thickness on pool boiling burnout, Int. J. Heat Mass Transfer 19 (1976) 1073-1075.

[28] H.S. Lee, H. Merte, Spherical vapor bubble growth in uniformly superheated liquids, Int. J. Heat Mass Transfer 39 (1996) 2427-2447.

[29] Y. Ma, J.N. Chung, An experimental study of forced convection boiling in microgravity, Int. J. Heat Mass Transfer 41 (1998) 2371-2382.

[30] Y. Ma, J.N. Chung, A study of bubble dynamics in reduced gravity forced-convection boiling, Int. J. Heat Mass Transfer 44 (2001) 399-415.

[31] I. Mudawar, Two-phase micro-channel heat sinks: theory, applications and limitations, ASME J. Electronic Packaging 133 (2011) 041002-2.

[32] I. Mudawar, K.A. Estes, Optimizing and predicting CHF in spray cooling of a square surface, ASME J. Heat Transfer 118 (1996) 672-680.

[33] L. Lin, R. Ponnappan, Heat transfer characteristics of spray cooling in a closed loop, Int. J. Heat Mass Transfer 46 (2003) 3737-3746.

[34] J.R. Rybicki, I. Mudawar, Single-phase and two-phase cooling characteristics of upward-facing and downward-facing sprays, Int. J. Heat Mass Transfer 49 (2006) 5-16.

[35] Y. Katto, M. Kunihiro, Study of the mechanism of burn-out in boiling system of high burn-out heat flux, Bulletin JSME 16 (1973) 1357-1366.

[36] I. Mudawar, D.C. Wadsworth, Critical heat flux from a simulated electronic chip to a confined rectangular impinging jet of dielectric liquid, Int. J. Heat Mass Transfer 34 (1991) 1465-1480.

[37] D.C. Wadsworth, I. Mudawar, Enhancement of single-phase heat transfer and critical heat flux from an ultra-high-flux simulated microelectronic heat source to a rectangular impinging jet of dielectric liquid, ASME J. Heat Transfer 114 (1992) 764-768.

[38] M.E. Johns, I. Mudawar, An ultra-high power two-phase jet-impingement avionic clamshell module, ASME J. Electronic Packaging 118 (1996) 264-270.

[39] T.C. Willingham, I. Mudawar, Forced-convection boiling and critical heat flux from a linear array of discrete heat sources, Int. J. Heat Mass Transfer 35 (1992) 2879-2890.

[40] M.B. Bowers, I. Mudawar, High flux boiling in low flow rate, low pressure drop mini-channel and micro-channel heat sinks, Int. J. Heat Mass Transfer 37 (1994) 321-332.

[41] T.N. Tran, M.W. Wambsganss, D.M. France, Small circular- and rectangular-channel boiling with two refrigerants, Int. J. Multiphase Flow 22 (1996) 485-498.

[42] H.J. Lee, S.Y. Lee, Heat transfer correlation for boiling flows in small rectangular horizontal channels with low aspect ratios, Int. J. Multiphase Flow 27 (2001) 2043-2062.

[43] V. Khanikar, I. Mudawar, T. Fisher, T., Effects of carbon nanotube coating on flow boiling in a micro-channel, Int. J. Heat Mass Transfer 52 (2009) 3805-3817.

[44] R.J. Simoneau, F.F. Simon, A visual study of velocity and buoyancy effects on boiling Nitrogen, NASA Tech Note TN D-3354, 1966.

[45] K. Mishima, H. Nishihara, The effect of flow direction and magnitude on CHF for low pressure water in thin rectangular channels, Nuclear Engineering Design 86 (1985) 165-181.

[46] C.O. Gersey, I. Mudawar, Effects of heater length and orientation on the trigger mechanism for near-saturated flow boiling critical heat flux - I. Photographic study and statistical characterization of the near-wall interfacial features, Int. J. Heat Mass Transfer 38 (1995) 629-641.

[47] C.O. Gersey, I. Mudawar, Effects of heater length and orientation on the trigger mechanism for near-saturated flow boiling critical heat flux - II. Critical heat flux model, Int. J. Heat Mass Transfer 38 (1995) 643-654.

[48] I. Mudawar, A.H. Howard, C.O. Gersey, An analytical model for near-saturated pool boiling CHF on vertical surfaces, Int. J. Heat Mass Transfer 40 (1997) 2327-2339.

[49] A.H. Howard, I. Mudawar, Orientation effects on pool boiling CHF and modeling of CHF for near-vertical surfaces, Int. J. Heat Mass Transfer 42 (1999) 1665-1688.

[50] A.H. Howard, I. Mudawar, Photographic study of pool boiling CHF from a downward-facing convex surface, Int. Communications Heat Mass Transfer 35 (2008) 793-799.

[51] C.R. Kharangate, I. Mudawar, M.H. Hasan, Photographic study and modeling of critical heat flux in horizontal flow boiling with inlet vapor void, Int. J. Heat Mass Transfer, 55 (2012) 4154-4168.

[52] C. Konishi, I. Mudawar, M.M. Hasan, Investigation of the influence of orientation on critical heat flux for flow boiling with two-phase inlet, Int. J. Heat Mass Transfer 61 (2013) 176-190.

[53] C.O. Gersey, I. Mudawar, Orientation effects on critical heat flux from discrete, in-line heat sources in a flow channel, ASME J. Heat Transfer, Vol. 115 (1993) 973-985.

[54] M.S. Bhatti, R.K. Shah, Turbulent and transitional convective heat transfer in ducts, in Handbook of single-phase convective heat transfer, S. Kakac, R.K. Shah, R.k., W. Aung, eds, John Wiley and Sons, NY(1987).

[55] H. Lamb, Hydrodynamics, 6th ed., Dover Publications, NY (1945).

[56] L. M. Milne-Thompson, Theoretical Hydrodynamics, 4th ed., Macmillan, NY (1960).

[57] H. Zhang, I. Mudawar, M.M. Hasan, CHF model for subcooled flow boiling in Earth gravity and microgravity, Int. J. Heat Mass Transfer 50 (2007) 4039-4051.

[58] Z. Nejat, Effect of density ratio on critical heat flux in closed end vertical tubes, Int. J. Multiphase Flow 7 (1981) 321-327.

[59] G.B. Wallis, One-dimensional two-phase flow, New York, McGraw Hill Book Company (1969).

[60] H. Zhang, I. Mudawar, M.M. Hasan, Photographic study of high-flux subcooled flow boiling and critical heat flux, Int. Communications Heat Mass Transfer 34 (2007) 653-660.

[61] C. Baltis, G.P. Celeta, M. Cumo, L. Saraceno, G. Zummo, Gravity influence on heat transfer rate in flow boiling, Multiphase Sci. Tech. 24 (2012) 203-213.

[62] DD. Hall, I. Mudawar, Ultra-high critical heat flux (CHF) for subcooled water flow boiling - II. High-CHF database and design parameters, Int. J. Heat Mass Transfer 42 (1999) 1429-1456.

[63] I. Mudawar, R.A. Houpt, Mass and momentum transport in smooth falling liquid films laminarized at relatively high Reynolds numbers, Int. J. Heat Mass Transfer 36 (1993) 3437-3448.

[64] I. Mudawar, R.A. Houpt, Measurement of mass and momentum transport in wavy-laminar falling liquid films, Int. J. Heat Mass Transfer 36 (1993) 4151-4162.

[65] W. Qu, I. Mudawar, S.-Y. Lee, S.T. Wereley, Experimental and computational investigation of flow development and pressure drop in a rectangular micro-channel, J. Electronic Packaging – Trans. ASME 128 (2006) 1-9.

[66] J.E. Koskie, I. Mudawar, W.G. Tiederman, Parallel-wire probes for measurement of thick liquid films, Int. J. Multiphase Flow 15 (1989) 521-530.

[67] J.A. Shmerler, I. Mudawar, Local heat transfer coefficient in wavy free-falling turbulent liquid films undergoing uniform sensible heating, Int. J. Heat Mass Transfer 31 (1988) 67-77.

[68] J.A. Shmerler, I. Mudawar, Local evaporative heat transfer coefficient in turbulent free-falling liquid films, Int. J. Heat Mass Transfer 31 (1988) 731-742.

[69] T.H. Lyu, I. Mudawar, Statistical investigation of the relationship between interfacial waviness and sensible heat transfer to a falling liquid film, Int. J. Heat Mass Transfer 34 (1991) 1451-1464.

[70] T.H. Lyu, I. Mudawar, Determination of wave-induced fluctuations of wall temperature and convective heat transfer coefficient in the heating of a turbulent falling liquid film, Int. J. Heat Mass Transfer 34 (1991) 2521-2534.

[71] H. Zhang, I. Mudawar, M.M. Hasan, Experimental and theoretical study of orientation effects on flow boiling CHF, Int. J. Heat Mass Transfer 45 (2002) 4463-4478.

[72] H. Zhang, I. Mudawar, M.M. Hasan, Investigation of interfacial behavior during the flow boiling CHF transient, Int. J. Heat Mass Transfer 47 (2004) 1275-1288.

[73] C. Konishi, I. Mudawar, M.M. Hasan, Criteria for negating the influence of gravity on flow boiling critical heat flux with two-phase inlet conditions, Int. J. Heat Mass Transfer 65 (2013) 203-218.

[74] C. Konishi, I. Mudawar, M.M. Hasan, Investigation of localized dryout versus CHF in saturated flow boiling, Int. J. Heat Mass Transfer 67 (2013) 131-146.

[75] H. Lee, I. Mudawar, M.M. Hasan, M.M., 2013, Experimental and theoretical investigation of annular flow condensation in microgravity, Int. J. Heat Mass Transfer 61 (2013) 293-309.

[76] N.J. Penley, C.P. Schafer, J.D.F. Bartoe, The International Space Station as a microgravity research platform, Acta Astronautica 50 (2002) 691-696.

[77] C.R. Class, J.R. DeHaan, M. Piccone, R.B. Cost, Boiling heat transfer to liquid hydrogen from flat surfaces, Advances Cryogenic Engng, K.D. Timmerhaus (ed.), Vol. 5, Plenum Press, New York, NY, 1960.

[78] P.M. Githinji, R.H. Sabersky, Some effects of orientation of the heating surface in nucleate boiling, J. Heat Transfer – Trans. ASME 85 (1963) 379.

[79] W.R. Marcus, D. Dropkin, The effect of surface configuration on nucleate boiling heat transfer, Int. J. Heat Mass Transfer 6 (1963) 863-867.

[80] L.T. Chen, Heat transfer to pool-boiling Freon from inclined heating plate, Letters Heat Mass Transfer 5 (1978) 111-120.

[81] K. Nishikawa, Y. Fujita, S. Uchida, S., H. Ohta, Effect of heating surface orientation on nucleate boiling heat transfer, Proc. ASME-JSME Thermal Engineering Joint Conf., Y. Mori and W.J. Yang (eds.), Vol. 1, Honolulu. HI, pp. 129-136, 1983.

[82] V. Kumar, M. Prasad, M.K. Verma, N.S. Garg, Effect of inclination on pool boiling heat transfer from a flat plate, Indian Chemical Engineer 32, (1990) 61-64.

[83] H. Lee, I. Park, I. Mudawar, M.M. Hasan, Micro-channel evaporator for space applications – 1. Experimental pressure drop and heat transfer results for different orientations in Earth gravity, Int. J. Heat and Mass Transfer, in press.

[84] H. Lee, I. Park, I. Mudawar, M.M. Hasan, Micro-channel evaporator for space applications – 2. Assessment of predictive tools, Int. J. Heat and Mass Transfer, in press.

[85] Y. Abe, A. Iwasaki, Pool boiling under microgravity, Advances Space Research 13 (1993) 165-168.

[86] T. Oka, Y. Abe, Y.H. Mori, A. Nagashima, Pool boiling of n-Pentane, CFC-113, and water under reduced gravity: parabolic flight experiments with a transparent heater, J. Heat Transfer – Trans. ASME 117 (1995) 408-417.

[87] T. Oka, Y. Abe, Y.H. Mori, A. Nagashima, Pool boiling heat transfer in microgravity (experiments with CFC-113 and water utilizing a drop shaft facility), JSME Int. J. 39 (1996) 798-807.

[88] H.S. Lee, H. Merte, Hemispherical vapor bubble growth in microgravity: experiments and model, Int. J. Heat Mass Transfer 39 (1996) 2449-2461.

[89] H. Ohta, K. Kawaji, H. Azuma, K. Kawasaki, H. Tamaoki, K. Ohta, S. Okada, S. Yoda, T. Nakamura, TR-1A rocket experiment on nucleate pool boiling heat transfer under microgravity, in Heat transfer in microgravity systems, ASME HDT 354 (1997) 249-256.

[90] J. Straub, G. Picker, M. Steinbichler, Boiling and bubble dynamics at a small hemispherical heater under microgravity and Earth conditions, University of Tokyo, 2nd Japanese-German Symp. Multi-Phase-Flow, Tokyo, Japan, pp. 169-176, 1997.

[91] J. Straub, Microscale boiling heat transfer under 0g and 1g conditions, Int. J. Therm. Sci. 39 (2000) 490-497.

[92] J. Straub, Origin and effect of thermocapillary convection in subcooled boiling. Observations and conclusions from experiments performed at microgravity, Annals N.Y. Acad. Sci. 974 (2002) 348-363.

[93] H. Ohta, K. Kawasaki, S. Okada, H. Azuma, S. Yoda, T. Nakamura, On the heat transfer mechanisms in microgravity nucleate boiling, Advances Space Research 24 (1999) 1325-1330.

[94] Y. Abe, A. Iwasaki, Single and dual vapor bubble experiments in microgravity, Proc. Int. Conf. Microgravity Fluid Physics Heat Transfer, Oahu, HI, pp. 55-61, 1999.

[95] J. Kim, J.F. Benton, D. Wisniewski, Pool boiling heat transfer on small heaters: effect of gravity and subcooling, Int. J. Heat Mass Transfer 45 (2002) 3919-3932.

[96] C.D. Henry, J. Kim, A study of the effects of heater size, subcooling, and gravity level on pool boiling heat transfer, Int. J. Heat Fluid Flow 25 (2004) 262-273.

[97] H. Merte, Momentum effects in steady nucleate pool boiling during microgravity, Annals N.Y. Acad. Sci. 1027 (2004) 196-216.

[98] H. Merte, Some parameter boundaries governing microgravity pool boiling modes, Annals N.Y. Acad. Sci. 1077 (2006) 629-649.

[99] C. Sodtke, J. Kern, N. Schweizer, P. Stephan, High resolution measurements of wall temperature distribution underneath a single vapour bubble under low gravity conditions, Int. J. Heat Mass Transfer 49 (2006) 1100-1106.

[100] J.F. Zhao, S.X. Wan, G. Liu, Z.D. Li, W.R. Hu, Pool boiling heat transfer in microgravity, Microgravity Sci. Tech. 19 (2007) 135-136.

[101] J.F. Zhao, G. Liu, S.X. Wan, N. Yan, Bubble dynamics in nucleate pool boiling on thin wires in microgravity, Microgravity Sci. Tech. 20 (2008) 81-89.

[102] J.F. Zhao, J. Li, N. Yan, S.F. Wang, Bubble behavior and heat transfer in quasi-steady pool boiling in microgravity, Microgravity Sci. Tech. 21 (2009) 175-183.

[103] R. Raj, J. Kim, J. McQuillen, Subcooled pool boiling in variable gravity environments, J. Heat Transfer – Trans. ASME 131 (2009) 1-10.

[104] O. Kannengieser, C. Colin, W. Bergez, Pool boiling with non-condensable gas in microgravity: results of a sounding rocket experiment, Microgravity Sci. Tech. 22 (2010) 447-454.

[105] Y.F. Xue, J.F. Zhao, J.J. Wei, J. Li, D. Guo, S.X. Wan, Experimental study of nucleate pool boiling of FC-72 on smooth surface under microgravity, Microgravity Sci. Tech. 23 (2011) (Suppl. 1) S75-S85.

[106] R. Raj, J. Kim, J. McQuillen, Pool boiling heat transfer on the International Space Station: experimental results and model verification, J. Heat Transfer – Trans. ASME 134 (2012) 1-14.

[107] V.K. Dhir, G.R. Warrier, E. Aktinol, D.F. Chao, J. Eggers, W. Sheredy, W. Booth, Nucleate pool boiling experiments (NPBX) on the International Space Station, Microgravity Sci. Tech. 24 (2012) 307-325.

[108] R.R. Souza, J.C. Passos, E.M. Cardoso, Confined and unconfined nucleate boiling under terrestrial and microgravity conditions, Appl. Thermal Engng 51 (2013) 1290-1296.

[109] G. Son, V.K. Dhir, N. Ramanuju, Dynamics and heat transfer associated with a single bubble during nucleate boiling on a horizontal surface, J. Heat Transfer – Trans. ASME 121 (1999) 623–631.

[110] B.N. Antar, Gas-liquid, two phase flow dynamics in low gravity, 27th AIAA Dynamics Conf., New Orleans, LA, 1996.

[111] H. Ohta, A. Baba, K. Gabriel, Review of existing research on microgravity boiling and two-phase flow, future experiments on the International Space Station, Annals N.Y. Acad. Sci. 974 (2002) 410-427.

[112] G.P. Celeta, Flow boiling heat transfer in microgravity: recent progress, Microgravity Sci. Tech. 19 (2007) 13-17.

[113] G.P. Celata, G. Zummo, Flow boiling heat transfer in microgravity: recent progress, Multiphase Sci. Tech. 21 (2009) 187-212.

[114] J.F. Zhao, Two-phase flow and pool boiling heat transfer in microgravity, Int. J. Multiphase Flow 36 (2010) 135-143.

[115] P. Di Marco, Influence of force fields and flow patterns on boiling heat transfer performance: a review, J. Heat Transfer – Trans. ASME 134 (2012) 1-15.

[116] H. Ohta, S. Baba, Boiling experiments under microgravity conditions, Exp. Heat Transfer 26 (2013) 266-295.

[117] C. Baldassari, M. Marengo, Flow boiling in microchannels and microgravity, Prog. Energy Combustion Sci. 39 (2013) 1-36.

[118] D.B. Hepner, C.D. King, J.W. Littles, Zero gravity experiments in two-phase fluids flow regimes, ASME Intersociety Conf. Environmental Systems, San Francisco, CA, 1975.

[119] L. Zhao, K.S. Rezkallah, Gas-liquid flow patterns at microgravity, Int. J. Multiphase Flow 19 (1993) 751-763.

[120] B. Choi, T. Fujii, H. Asano, K. Sugimoto, A study of gas-liquid two-phase flow in a horizontal tube under microgravity, Annals N.Y. Acad. Sci. 974 (2002) 316-327.

[121] A.E. Dukler, J.A. Fabre, J.B. McQuillen, R. Vernon, Gas-liquid flow at microgravity conditions: Flow patterns and their transitions, Int. J. Multiphase Flow 14 (1988) 389-400.

[122] W.S. Bousman, Studies of two-phase gas-liquid flow in microgravity, Ph.D. thesis, University of Houston, TX, 1994.

[123] W.S. Bousman, J.B. McQuillen, Characterization of annular two-phase gas-liquid flows in microgravity, Proc. 2nd Microgravity Fluid Physics Conf., Cleveland, OH, pp. 227-232, 1994.

[124] W.S. Bousman, J.B. McQuillen, L.C. Witte, Gas-liquid flow patterns in microgravity: Effects of tube diameter, liquid viscosity and surface tension, Int. J. Multiphase Flow 22 (1996), 1035-1053.

[125] C. Colin, J. Fabre, A.E. Dukler, Gas-liquid flow at microgravity conditions – I. Dispersed bubble and slug flow, Int. J. Multiphase Flow 17 (1991) 533-544.

[126] C. Colin, A. Kamp, J. Fabre, Influence of gravity on void distribution in two-phase gas-liquid flow in pipe, Advances Space Research 13 (1993) 141-145.

[127] C. Colin, J. Fabre, Gas-liquid pipe flow under microgravity conditions: Influence of tube diameter on flow patterns and pressure drops, Advances Space Research 16 (1995) 137-142.

[128] C. Colin, J. Fabre, J. McQuillen, Bubble and slug flow at microgravity conditions: state of knowledge and open questions, Chemical Engng Communications 141-142 (1996) 155-173.

[129] C. Colin, J. Fabre, A. Kamp, Turbulent bubble flow in pipe under gravity and microgravity conditions, J. Fluid Mechanics 711 (2012) 469-515.

[130] D. Lee, Thermohydraulic and flow regime analysis for condensing two-phase flow in a microgravity environment, Ph.D. thesis, Texas A&M University, TX, 1987.

[131] D. Lee, F.R. Best, N. McGraw, Microgravity two-phase flow regime modeling, Proc. 3rd Nuclear Thermal Hydraulics Winter Meeting, Los Angeles, CA, 1987.

[132] T.R. Reinarts, Adiabatic two phase flow regime data and modeling for zero and reduced (horizontal flow) acceleration fields, Ph.D. thesis, Texas A&M University, TX, 1993.

[133] C.S. Huckerby, K.S. Rezkallah, Flow pattern observations in two-phase gas-liquid flow in a straight tube under normal and microgravity conditions, AIChE Symp. Ser. 88 (1992) 139-147.

[134] R. Rite, K.S. Rezkallah, Heat transfer in two-phase flow through a circular tube at reduced gravity, J. Thermophysics Heat Transfer 8 (1994) 702-708.

[135] J.F. Zhao, W.R. Hu, Slug to annular flow transition of microgravity two-phase flow, Int. J. Multiphase Flow 26 (2000) 1295-1304.

[136] S.S. Jayawardena, V. Balakotaiah, L.C. Witte, Flow pattern transition maps for microgravity two-phase flows, AIChE J. 43 (1997) 1637-1640.

[137] A.M. Shephard, C. Kurwitz, F.R. Best, Microgravity bubbly-to-slug flow regime transition theory and modeling, Microgravity Sci. Tech. 25 (2013) 161-177.

[138] L. Zhao, K.S. Rezkallah, Pressure drop in gas-liquid flow at microgravity conditions, Int. J. Multiphase Flow 21 (1995) 837-849.

[139] R.W. Lockhart, R.C. Martinelli, Proposed correlation of data for isothermal two-phase, two-component flow in pipes, Chemical Engng Progress 45 (1949) 39–48.

[140] I. Chen, R. Downing, E.G. Keshock, M. Al-Sharif, Measurements and correlation of two-phase pressure drop under microgravity conditions, J. Thermophysics Heat Transfer 5 (1991) 514-523.

[141] J.F. Zhao, H. Lin, J.C. Xie, W.R. Hu, Pressure drop of bubbly two-phase flow in a square channel at reduced gravity, Advances Space Research 29 (2002) 681-686.

[142] R. Siegel, C. Usiskin, A photographic study of boiling in the absence of gravity, J. Heat Transfer – Trans. ASME 81 (1959) 230-236.

[143] C.M. Usiskin, R. Siegel, An experimental study of boiling in reduced and zero gravity field, J. Heat Transfer – Trans. ASME 83 (1961) 251-252.

[144] S.S. Papell, An instability effect on two-phase heat transfer for subcooled water flowing under conditions of zero gravity, NASA Tech Note TN D-2259, 1964.

[145] M. Misawa, An experimental and analytical investigation of flow boiling heat transfer under microgravity conditions, Ph.D. thesis, University of Florida, 1993.

[146] M. Saito, N. Yamaoka, K. Miyazaki, M. Kinoshita, Y. Abe, Boiling two-phase flow under microgravity, Nuclear Engng Design 146 (1994) 451-461.

[147] H. Ohta, Experiments on microgravity boiling heat transfer by using transparent heaters, Nuclear Engng Design 175 (1997) 167-180.

[148] Y. Ma, J.N. Chung, An experimental study of critical heat flux (CHF) in microgravity forced-convection boiling, Int. J. Multiphase Flow 27 (2001) 1753-1767.

[149] D.T. Westheimer, G.P. Peterson, Visualization of flow boiling in an annular heat exchanger under microgravity conditions, J. Thermophysics Heat Transfer 15 (2001) 333-339.

[150] G.P. Celata, M. Cumo, M. Gervasi, G. Zummo, Flow pattern analysis of flow boiling in microgravity, Multiphase Sci. Tech. 19 (2007) 183-210.

[151] S. Luciani, D. Brutin, C. Le Niliot, O. Rahli, L. Tadrist, Flow boiling in minichannels under normal, hyper-, and microgravity: local heat transfer analysis using inverse methods, J. Heat Transfer – Trans. ASME 130 (2008) 1-13.

[152] C. Baltis, G.P. Celeta, M. Cumo, L. Saraceno, G. Zummo, Gravity influence on heat transfer rate in flow boiling, Multiphase Sci. Tech. 24 (2012) 203-213.

[153] D. Brutin, V.S. Ajaev, L. Tadrist, Pressure drop and void fraction during flow boiling in rectangular minichannels in weightlessness, Appl. Thermal Eng. 51 (2013) 1317-1327.

[154] M. Narcy, E. De Malmazet, C. Colin, Flow boiling in straight heated tubes under microgravity conditions, Proc. 8th Int. Conf. Multiphase Flow, Jeju, Korea, 2013.

[155] G.P. Celeta, M. Cumo, M. Gervasi,G. Zummo, Quenching experiments inside 6.0 mm tube at reduced gravity, Int. J. Heat Mass Transfer 52 (2009) 2807-2814.

[156] G.P. Celeta, M. Cumo, F. D'Annibale, L. Saraceno, G. Zummo, Rewetting velocity in quenching at reduced gravity, Int. J. Thermal Sci. 49 (2010) 1567-1575.

[157] S. Luciani, D. Brutin, C. Le Niliot, O. Rahli, Boiling heat transfer in a vertical microchannel: local estimation during flow boiling with a non intrusive method, Multiphase Sci. Tech. 21 (2009) 297-328.

APPENDIX

APPENDIX
REVIEW OF FLOW BOILING AND CHF IN MICROGRAVITY

A.1 Introduction

This appendix provides a review of published literature concerning two-phase flow and heat transfer in reduced gravity. Discussed are the different methods and platforms dedicated to exploring the influence of reduced gravity, including ground flow boiling experiments performed at different orientations relative to Earth gravity, as well as reduced gravity adiabatic two-phase flow, pool boiling, flow boiling and CHF experiments. Despite the extensive data and flow visualization results available in the literature, it is shown that there is a severe shortage of useful correlations, mechanistic models and computational models, which compromises readiness to adopt flow boiling in future space systems. Key recommendations are provided concerning platform, heater design, and operating conditions for future studies to expedite the deployment of two-phase thermal management in future space missions.

A.1.1 Microgravity Testing Platforms

Performing boiling experiments in reduced gravity, especially microgravity, is a challenging and costly endeavor. Several types of testing platforms have been used for this purpose. Microgravity can be achieved by placing an experimental package in a state of freefall in an above ground *drop tower* or below ground *drop shaft*. These platforms provide high quality microgravity ($<1\text{x}10^{-4}\ g_e$) for relatively short durations between 2.2 and 10 s (2.2 s for NASA Glenn Research Center's 24-m drop tower, 5.2 s for NASA Glenn Research Center's 132-m drop shaft, 4.6 s for NASA Marshall Space Flight Center's 105-m drop tower, 4.72 s for Germany Drop Tower Bremen's (ZARM's) 110-m drop tower, and 10 s for Japan Microgravity Center's (JAMIC's) 700-m drop shaft) [75].

Key disadvantages of drop towers and drop shafts are (1) inability to reach steady-state for many types of experiments because of the short test duration, (2) need to perform many repetitive drops to acquire sufficient data (since only one set of operating conditions can be tested in a single drop), and (3) inability to interact manually with the experimental package during the drop. Due to short microgravity duration and low operational cost, drop towers and shafts are primarily used for initial validation of experiments before more comprehensive testing is carried out on long-duration microgravity platforms.

Sounding rockets provide another platform to achieving microgravity during a sub-orbital flight. They provide 3 to 13 minutes of testing with high quality microgravity ($< 1x10^{-4}\ g_e$) [75]. Sounding rockets share the disadvantages of drop towers and shafts in their inability to interact with the experimental package, or to perform multiple experiments at different operating conditions; they also cannot accommodate large experimental packages.

Parabolic flight aircraft provide a cost effective means to achieving microgravity with durations of 15 - 30 s. Through a series of parabolic maneuvers, varying gravitational conditions can be achieved, including microgravity (μg_e), Lunar gravity and Martian gravity. Parabolic flight experiments offer considerable advantages over drop towers and drop shafts and sounding rockets, including ability to (1) accommodate larger experimental packages, (2) test many different operating conditions in multiple parabolas during the same flight, and (3) grant the experimenter manual access to the facility. Their key drawback is relatively low quality microgravity (+/- 0.01 g_e) and '*g-jitter,*' which are influenced by pilot skills and weather related turbulence [75].

A few studies were privileged use of NASA's Space Shuttles for microgravity experimentation. During their active years, Space Shuttles satisfied virtually all testing needs, including (1) ability to perform long duration experiments, (2) high quality microgravity ($< 1x10^{-4}\ g_e$), (3) operator access to the experimental package, and (4) both automatic and remote control capabilities. However, the process of granting testing onboard Space Shuttles required long periods of development and safety certification, let alone the very high cost.

With the retirement of NASA's Space Shuttle program, the International Space Station (ISS) presently provides the ultimate testing environment for microgravity research, sharing benefits similar to those of the Space Shuttles [76]. But like Space Shuttle experiments, ISS experiments are very costly and require many years of development and safety certification. These drawbacks pose major obstacles to meeting researchers' needs for microgravity flow boiling data.

A.2 Terrestrial Studies on Influence of Body Force on Flow Boiling CHF

A.2.1 Method for Achieving Reduced Component of Gravity Perpendicular to Heated Wall

A common method to simulating reduced gravity in terrestrial experiments is boiling on a heated wall that is tilted relative to Earth gravity. This provides a partial component of gravity perpendicular to the heated wall. However, a fundamental weakness this approach is the inability to achieve true reduced gravity since tilting the heated wall also results in a finite component of gravity parallel to the wall. Nonetheless, terrestrial boiling experiments are far less expensive than microgravity counterparts, and provide valuable insight into the CHF mechanism.

A.2.2 Influence of Heated Wall Orientation on Pool Boiling

Class *et al.* [77], Githinji and Sabersky [78], Marcus and Dropkin [79], Chen [80], Nishikawa *et al.* [81], and Kumar *et al.* [82] examined the influence of wall orientation on pool boiling. These studies demonstrated both drastic variations of CHF value and vast differences in CHF trigger mechanism with orientation, which implies that different CHF models must be pursued for the different orientations. Interestingly, these studies also prove that the classical pool boiling CHF model by Zuber *et al.* [7] is valid only for horizontal or near-horizontal upward-facing orientations. The strong influence of orientation on pool boiling CHF is also evident from studies by Mudawar *et al.* [48] and Howard and Mudawar [49], who conducted extensive measurements and photographic studies of interfacial behavior for different orientations. Overall, they divided pool

boiling wall orientation effects into three regions: near-horizontal upward-facing, near-vertical, and downward-facing as depicted in Figure 1.6(b). In the near-horizontal upward-facing region, buoyancy forces were observed to remove the vapor vertically off the heated wall in accordance with the Zuber *et al*. model. The near-vertical orientations produced a wavy vapor layer that swept along the heater wall, closely resembling the interfacial lift-off mechanism for vertical flow boiling CHF illustrated in Figure 1.2. The downward-facing wall orientations caused the vapor to stratify on the heated wall, greatly reducing CHF relative to all other orientations.

A.2.3 Influence of Flow and Heated Wall Orientations on Flow Boiling CHF

Several terrestrial studies were also conducted to explore flow boiling CHF for different orientations. These studies point to orientations effects far more complex that those for pool boiling because of the strong influence of velocity. Simoneau and Simon [44] showed that vapor motion in vertical nitrogen downflow changes from concurrent at high liquid velocities to countercurrent at low velocities, and CHF values for downflow are lower than for upflow at the same velocity. Additionally, CHF differences between upflow and downflow decrease with increasing inlet velocity because of a gradual diminution of buoyancy effects relative to liquid inertia. Mishima and Nishihara [45] suggested flooding is the cause of CHF for downflow of water at very low velocities. Increasing the velocity from a flooded downflow state caused bubbles to stagnate as the drag force exerted by liquid just balanced buoyancy force. This bubble stagnation produced an even lower CHF than with flooding at lower velocities. By increasing the flow velocity further, bubbles began to flow concurrently downward with the liquid, causing an increase in flow boiling CHF. Gersey and Mudawar [46,47] also demonstrated strong sensitivity of flow boiling CHF of FC-72 to orientation. This sensitivity gradually decreased with increasing flow velocity and increasing subcooling. Like Mishima and Nishihara, they observed vapor flowing opposite to liquid in downflow at very low velocities, stagnating at slightly higher velocities, and moving concurrently with liquid in downflow upon further increases in velocity.

Zhang *et al.* [4,71,72] performed extensive studies of the influence of orientation and velocity for flow boiling of FC-72 in a 5.0 x 2.5 mm^2 rectangular channel heated along one short side. Experiments were performed in different orientations, Figures A.1(a) and A.1(b), including $\theta = 0°$ and 180° corresponding to horizontal flow with the heated wall facing upwards and downwards, respectively, and $\theta = 90°$ and 270° corresponding to vertical upflow and downflow, respectively. Figure A.1(a) shows vapor behavior captured by Zhang *et al.* [4] at CHF- (conditions just preceding CHF) for near-saturated flow ($\Delta T_{sub,o} = 3°C$) at $U = 0.1$ m/s. This low velocity greatly reduced liquid drag force compared to buoyancy, causing orientation to have a profound influence on CHF mechanism and magnitude. Shown in Figure A.1(a) are four different CHF regimes: (1) *Pool-Boiling Regime* for $\theta = 0°$, (2) *Wavy Vapor Layer Regime* for $\theta = 90°$, (2) *Stratified Regime* for $\theta = 180°$, and (4) *Vapor Stagnation Regime* for $\theta = 270°$. Notice that, because of the low flow velocity, the first three CHF regimes correspond very closely with the pool boiling regimes observed by Howard and Mudawar [49] and depicted in Figure 1.6(a). In the Pool Boiling Regime ($\theta = 0°$), bubbles coalesce along the heated wall before being detached by buoyancy and driven into the liquid core, with weak tendency to flow with the liquid. The Wavy Vapor Layer Regime ($\theta = 90°$) is associated with bubble coalescence into vapor patches that propagate along the heated wall mimicking a continuous wavy vapor layer, closely resembling the interfacial lift-off mechanism for vertical flow boiling CHF illustrated in Figure 1.2. The Stratification Regime ($\theta = 180°$) occurs when vapor stratifies above the liquid in the form of a thick, fairly smooth layer that covers nearly the entire heated wall. The Vapor Stagnation Regime ($\theta = 270°$) is the result of buoyancy force just balancing the drag force exerted by liquid on the vapor. Two additional CHF regimes were observed at low flow velocities that are not shown in Figure A.1(a). A *Separated Concurrent Vapor Flow Regime* was encountered at velocities slightly greater than $U = 0.1$ m/s, when liquid drag began to exceed buoyancy. Conversely, a *Vapor Counter Flow Regime* was detected at velocities below 0.1 m/s, where buoyancy exceeded liquid drag, pushing the vapor backwards towards the channel inlet. Aside from these drastic differences in vapor behavior, Figure A.1(a) shows the large differences in CHF magnitude among the four orientations at $U = 0.1$ m/s.

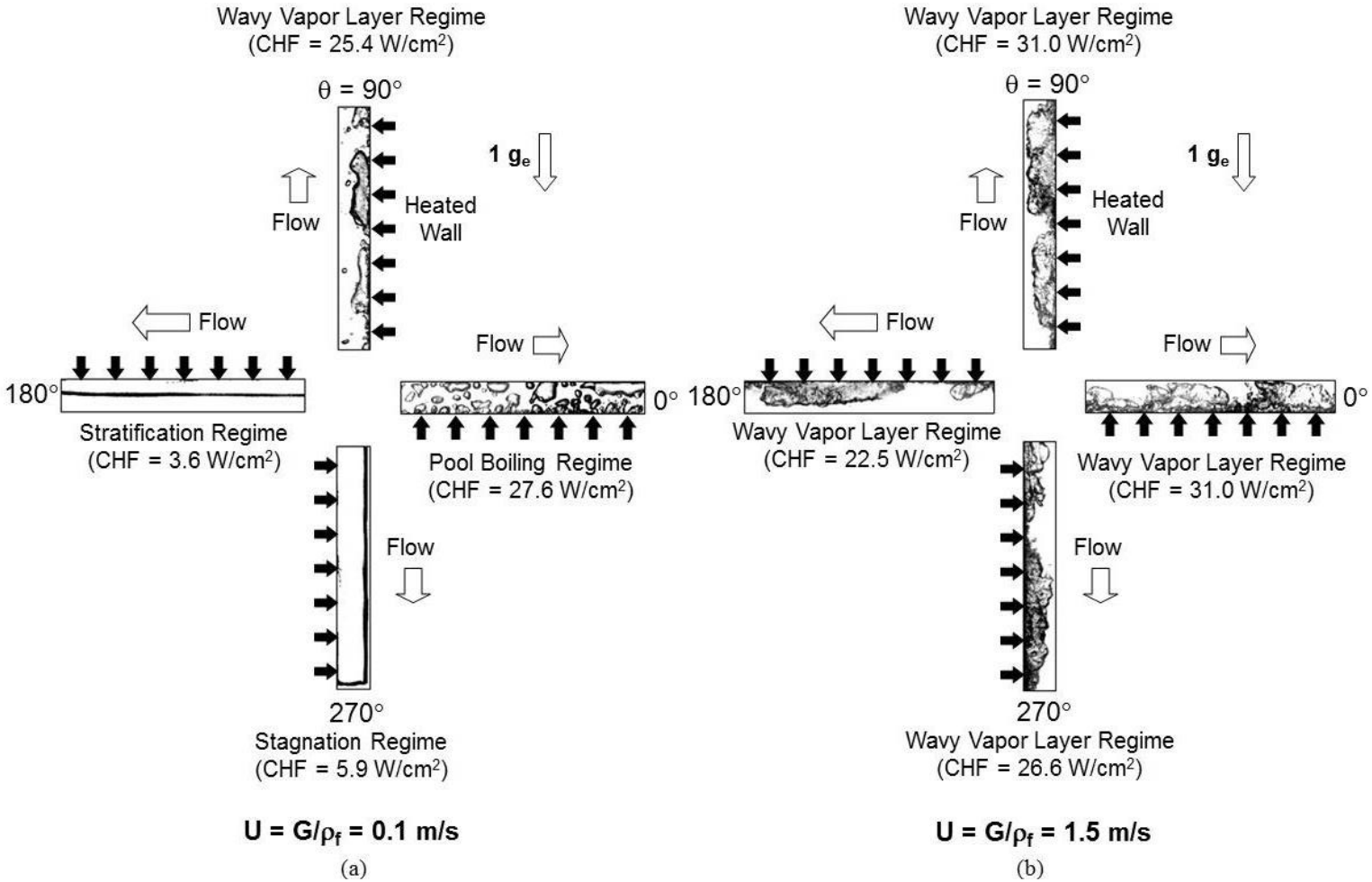

Figure A.1: Near saturated ($\Delta T_{sub,o}$ = 3°C) flow boiling CHF regimes at 1 g_e corresponding to different flow orientations for inlet liquid velocities (a) $U = G/\rho_f$ = 0.1 m/s and (b) $U = G/\rho_f$ = 1.5 m/s. CHF regime and magnitude are highly dependent on orientation for the lower velocity and independent of orientation for the higher velocity [4].

Figure A.1(b) depicts vapor behavior captured by Zhang *et al.* [4] for near-saturated flow ($\Delta T_{sub,o}$ = 3°C) at U = 1.5 m/s. This high velocity greatly increases drag forces, dwarfing any buoyancy effects, which is manifest by all four orientations yielding the same Wavy Vapor Layer Regime and fairly equal CHF values. Overall, these findings demonstrate the importance of high flow velocity as a means to overcome body force effects.

Another important parameter that influences CHF is subcooling. High subcooling serves to greatly reduce the size of coalescent vapor masses, thereby decreasing the influence of body force for a given velocity [57,60]. Figure A.2 shows increasing velocity and subcooling increase both CHF magnitude and the sensitivity of CHF to velocity [60].

Kharangate *et al.* and Konishi *et al.* extended the flow boiling CHF experiments of Zhang *et al.* to operating conditions where the fluid enters the channel as a saturated two-phase mixture for vertical upflow [26], horizontal flow with the heated wall upward facing [51], and for eight orientations [52,73,74]. They utilized the same experimental apparatus as Zhang *et al.* excepting the use of a preheater upstream from the flow channel to condition the working fluid, FC-72, to the desired inlet quality $x_{e,in}$. Compared to the flow regimes captured earlier by Zhang *et al.* for pure liquid inlet conditions, only the *Pool Boiling Regime*, *Stratification Regime* and *Wavy-Vapor Layer Regime* were observed. Kharangate *et al.* and Konishi *et al.* hypothesized that the increasing inlet quality increases the velocities of vapor and liquid and the shear force in between, thereby overcoming the influence of body force more effectively than with a pure liquid inlet. Figure 3.4(a) shows a polar plot of CHF data measured by Konishi *et al.* [52] for eight orientations and velocities ranging from G/ρ_f = 0.126 to 1.130 m/s with an inlet quality of $x_{e,in}$ = 0.01. The influence of orientation is quite pronounced for the two lowest velocities of G/ρ_f = 0.126 and 0.224 m/s, especially at θ = 225°, where CHF values are vanishingly small. There is a diminution of orientation effects starting at the middle velocity of G/ρ_f = 0.398 m/s, and further diminution at the two higher velocities of G/ρ_f = 0.712 and 1.130 m/s. Overall, orientations involving a combination of upflow and/or upward-facing heated wall (θ = 0°, 45° and 90°) produce higher CHF than downflow

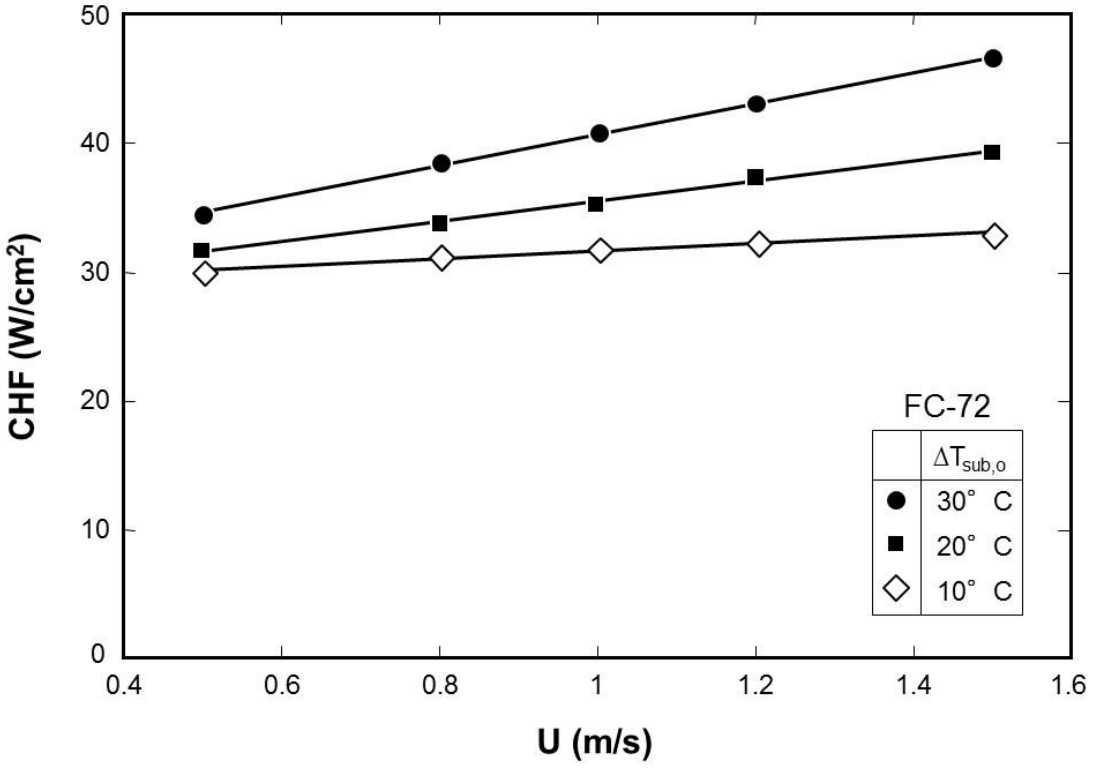

Figure A.2: Variation of CHF with mean inlet liquid velocity for three subcoolings [60].

and/or downward-facing heated wall (θ = 180°, 225° and 270°). Figure 3.4(b) shows CHF data for velocities ranging from G/ρ_f = 0.126 to 0.72 m/s at a much larger inlet quality of $x_{e,in}$ = 0.19. Like Figure 3.4(a), the influence of orientation for the lowest velocity of G/ρ_f = 0.126 m/s is quite pronounced and yields a vanishingly small CHF value for θ = 225°. But unlike Figure 3.4(a), orientation effects are markedly weaker for G/ρ_f = 0.224 m/s at $x_{e,in}$ = 0.19 compared to $x_{e,in}$ = 0.01. The influence of orientation is further degraded for the two higher velocities of G/ρ_f = 0.398 and 0.712. Comparing Figures 3.4(a) and 3.4(b) shows that, for equal G/ρ_f, increasing inlet quality reduces the sensitivity of CHF to orientation. This reduced sensitivity can be explained by higher velocities of the two phases increasing the magnitude of shear and drag forces compared to buoyancy.

A.2.4 Using Tilted Flow Boiling Experiments to Derive Criteria for Negating Body Force Effects

Zhang *et al.* [5] developed criteria for negating the influence of body force on flow boiling CHF with $x_{e,in} \leq 0$. Three separate criteria were proposed: (a) overcoming the influence of the component of gravity perpendicular to the heated wall, (b) overcoming the influence of the component of gravity opposite to the direction of fluid flow, (c) ensuring that the wavelength associated with instability of the liquid-vapor interface is smaller than the heated length to facilitate liquid contact with wall.

The criterion for negating the influence of the component of gravity perpendicular to the heated wall is derived as follows. The *Wavy-Vapor Layer Regime* that is dominant for near vertical orientations at low velocities and for all orientations at high velocities can be described with the aid of classical instability theory based on the assumption of a sinusoidal vapor-liquid interface. The critical wavelength, λ_c, of the interface, which is used to describe the vapor-liquid interface adjacent to the heated wall, is given by

$$\frac{2\pi}{\lambda_c}\frac{\sigma\left(\rho_f+\rho_g\right)}{\rho_f\rho_g\left(U_g-U_f\right)^2}=\frac{1}{2}\left\{1+\sqrt{1+4\,\frac{\left(\rho_f-\rho_g\right)\left(\rho_f+\rho_g\right)^2\sigma g_e\cos\theta}{\rho_f^2\rho_g^2\left(U_g-U_f\right)^4}}\right\}. \tag{A.1}$$

where U_g and U_f are the mean velocities of the vapor and liquid layers, respectively, and $g_e\cos\theta$ the component of gravity perpendicular to the heated wall. Equation (A.1)

indicates that interfacial instability is governed by the combined influences of inertia, surface tension, and component of gravity perpendicular to the heated wall. Notice that the influence of gravity becomes negligible when

$$\left|\frac{\left(\rho_f-\rho_g\right)\left(\rho_f+\rho_g\right)^2\sigma g_e\cos\theta}{\rho_f^2\rho_g^2\left(U_g-U_f\right)^4}\right| << \frac{1}{4}, \tag{A.2}$$

which reduces Eq. (A.1) to

$$\lambda_c = \frac{2\pi\sigma\left(\rho_f+\rho_g\right)}{\rho_f\,\rho_g\left(U_g-U_f\right)^2}\ , \tag{A.3}$$

regardless of body force. Equation (5) can also be presented in terms of the Bond and Weber numbers,

$$\left|\frac{Bo}{We^2}\right| = \left|\frac{\left(\rho_f-\rho_g\right)\left(\rho_f+\rho_g\right)^2\sigma g_e\cos\theta}{\rho_f^2\rho_g^2\left(U_g-U_f\right)^4}\right| << \frac{1}{4}, \tag{A.4}$$

where

$$Bo = \frac{\left(\rho_f-\rho_g\right)g_e\cos\theta L^2}{\sigma} \tag{A.5}$$

and

$$We = \frac{\rho_f\,\rho_g\left(U_g-U_f\right)^2 L}{\left(\rho_f+\rho_g\right)\sigma}. \tag{A.6}$$

This criterion was examined by substituting the phase velocity difference by the characteristic velocity of the flow channel, U, and the component of gravity perpendicular to the heated wall by the maximum value of the same component, g. Since the CHF data of Zhang *et al.* showed little dependence on orientation for $U \sim 1.5$ m/s, the magnitude of Bo/We^2 corresponding to $U = 1.5$ m/s was used as a criterion for overcoming body force effects on CHF, which, for any gravity field, g, can be simplified to

$$\frac{Bo}{We^2} = \frac{\left(\rho_f-\rho_g\right)\left(\rho_f+\rho_g\right)^2\sigma g}{\rho_f^2\rho_g^2U^4} \le 0.09\cdot \tag{A.7}$$

The criterion for negating the influence of gravity parallel to the heated wall and opposite the direction of fluid flow uses an expression for rise velocity of a large coalescent slug flow bubble relative to liquid [66],

$$U_\infty = 0.35\frac{\left[\left(\rho_f-\rho_g\right)g_e|\sin\theta|D_h\right]^{1/2}}{\rho_f^{1/2}}, \tag{A.8}$$

where D_h is the hydraulic diameter of the channel. When U_∞ exceeds the liquid velocity, the vapor tends to flow backwards relative to the liquid inducing flooding, and when the two velocities are equal the vapor stagnates along the channel. A sufficient criterion for preventing flooding is $U_\infty << U$, which, for $sin\ \theta = 1$ (corresponding to strongest orientation influence), can be presented in terms of the Froude number,

$$\left|\frac{1}{Fr}\right| = \left|\frac{\left(\rho_f - \rho_g\right)\sigma g_e D_h}{\rho_f U^2}\right| \le 8.16. \tag{A.9}$$

Since the CHF data of Zhang *et al.* showed flooding is avoided for $U \ge 0.5$ m/s, the criterion for precluding the occurrence of this anomaly in any gravity, g, can be reduced to

$$\frac{1}{Fr} = \frac{\left(\rho_f - \rho_g\right) g D_h}{\rho_f U^2} \le 0.13. \tag{A.10}$$

To enable liquid contact with the heated wall, it is crucial that the interfacial wavelength be smaller than the heated length, *i.e.,* $\lambda_c \le L$. This comprises the third criterion for negating the influence of body force. Using the expression for λ_c from Eq. (A.3), this criterion can be expressed as a Weber number criterion,

$$We = \frac{\rho_f \rho_g \left(U_g - U_f\right)^2 L}{\left(\rho_f + \rho_g\right)\sigma} \ge 2\pi. \tag{A.11}$$

Figure A.3 shows the minimum velocity required to satisfy the above three criteria as a function of g/g_e, the ratio of prevailing gravity to Earth gravity. Avoiding all body force effects requires that flow velocity exceed values predicted by each of the three criteria; only one of these criteria is dominant for a given value of g/g_e. Figure A.3 shows fairly appreciable flow velocities are required to overcome flooding, should a large gravitational field of $g/g_e > 75$ be present in a direction opposite to the liquid flow. Instability effects are dominant for $g/g_e < 75$ in a direction perpendicular to the heated wall; this is where surface tension effects become increasingly important. Notice that this instability criterion spans Earth, Lunar and Martian environments. The heater length criterion is dominant for very low values of g/g_e. The g/g_e value associated with transition between the instability-dominated and heater-length-dominated regimes is a function of the heated length, with shorter heaters requiring higher velocities to decrease

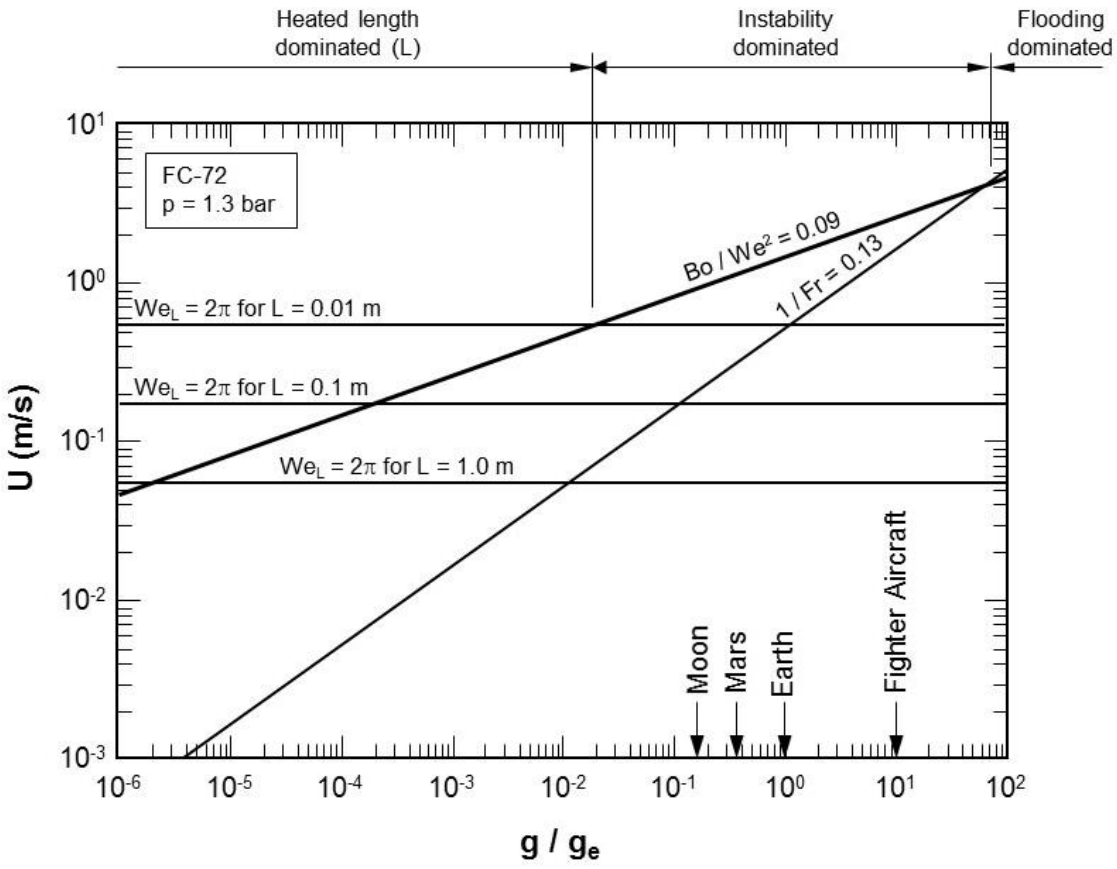

Figure A.3: Determination of minimum flow velocity required to satisfy all criteria for negating gravity effects on flow boiling CHF [5].

critical wavelength below the heated length. In general, the heater-length-dominated regime is more significant for microgravity conditions.

Recall that the criteria developed by Zhang *et al.* are based on their own data for which $x_{e,in} \leq 0$. Recently, Konishi *et al.* [73] extended these criteria to two-phase inlet conditions, $x_{e,in} \geq 0$. Here, flow velocities increase with increasing $x_{e,in}$. Therefore, stronger inertial effects serve to combat gravity more effectively and satisfy the criteria for negating gravity effects at lower inlet velocities than for $x_{e,in} \leq 0$.

A.2.5 Advantages of Micro-Channels in Helping Negate Body Force Effects

Decreasing hydraulic diameter of the flow channel increases flow velocity for a given flow rate. This is a key feature of two-phase flow in micro-channels, which provide important advantages to space systems by greatly increasing flow inertia for a given flow rate to help resist body forces effects. These advantages were recently examined by Lee *et al.* [83,84] who explored flow boiling of FC-72 in a test module containing 80 of 231-μm wide × 1000-μm deep micro-channels in three flow orientations: horizontal, vertical upflow and vertical downflow. Their data showed gravity effects are negated altogether at velocities far smaller than those for macro-channels.

A.3 Pool Boiling in Reduced Gravity

Before reviewing reduced gravity flow boiling, it is useful to examine findings from reduced gravity pool boiling studies concerning such fundamental processes as bubble nucleation, growth and coalescence on a heated wall in the absence of gravity, and the impact of these processes on both nucleate boiling heat transfer and CHF. Table A.1 summarizes prior reduced gravity pool boiling studies.

Oka and coworkers performed microgravity pool boiling experiments with n-Pentane, R-113 and water in parabolic flight [86], and R-113 and water in a drop shaft [87]. In both types of tests, the fluid's surface tension and latent heat of vaporization had a profound influence on bubble nucleation, growth and coalescence, and on heat transfer effectiveness. Tests with n-Pentane and R-113, which possess relatively low surface tension and low heat of vaporization, showed bubbles rarely detach from the heater

Table A.1: Summary of prior reduced gravity pool boiling studies.

Author(s)	Microgravity Platform	Test Fluid	Heater Geometry	Test Conditions	Remarks
Abe & Iwasaki (1993) [85]	Sounding rocket (TR-1A) (2×10^{-4} g_e , ~ 6 min)	n-pentane	BK-7 glass A_h = 30 x 30 mm^2 5 Artificial cavities (100 μm diameter)	p = 100, 160 kPa ΔT_{sub} = 11.1, 25.7 K q'' = 5-50 kW/m^2	– Minimal isolated bubble departure promotes coalescence into a large bubble encompassing majority of heater surface – Nucleate heat transfer is degraded in μg_e
Oka *et al.* (1995) [86]	Parabolic flight (Caravelle 234) (10^{-2} g_e)	n-Pentane, R-113, water	BK-7 glass-/indium tin oxide (ITO) transparent coated heater A_h = 50 × 50 mm^2	p = 81-183 kPa ΔT_{sub} = 2-17 K T_b = 29.2-94.5°C q'' = 30-119 kW/m^2	– Bubbles generated in water are spherical in shape, allowing minimal contact, or are expelled from heater surface; bubbles in other fluids are attached to heater surface over a large contact area – Boiling heat transfer is deteriorated for water over entire nucleate boiling regime, but for other fluids only at high heat fluxes – CHF for organic fluids is degraded by 40% in μg_e compared to terrestrial data
Oka *et al.* (1996) [87]	Drop shaft (JAMIC) (10^{-5} g_e , ~ 10 s)	R-113, water	Aluminum plate/stainless steel foil coating A_h = 40, 80 mm square and Pryex/ITO coated A_h = 30 mm square	ΔT_{sub} = 6-22 K q'' < 64 kW/m^2	– For water, capillarity-driven bubble detachment sustains nucleate boiling over a range of heat flux up to CHF – Periodic bubble formation in R-113 occurs on relatively small fraction of heater surface, excluding discrete areas encompassed by larger vapor masses – CHF is degraded by 20 – 30% – CHF dependence on liquid subcooling is stronger in μg_e than in terrestrial conditions
Lee & Merte (1996) [88]	NASA Space Shuttle (STS-47, 57, 60) (10^{-4} g_e)	R-113	Quartz/semi-transparent gold film A_h = 19.05 × 38.1 mm^2	p = 107.7-117.3 kPa ΔT_{sub} = 0.7-3.2 K T_b = 48.6°C q'' = 1.8-6.5 W/cm^2	– Hemispherical models developed to globally describe bubble growth in μg_e and determine upper and lower bounds of the growth

Table A.1: Summary of prior reduced gravity pool boiling studies – continued.

Author(s)	Microgravity Platform	Test Fluid	Heater Geometry	Test Conditions	Remarks
Ohta *et al.* (1997) [89]	Parabolic flight (MU-300) (10^{-2} g_e, 2 g_e)	Water/ ethanol	Sapphire glass/ITO coated D_h = 50 mm	p = 100, 20 kPa ΔT_{sub} = 3-11 K q'' = 30-290 kW/m^2	– At low heat fluxes, nucleate boiling heat transfer coefficient in μg_e is larger than in 2 g_e, but no differences are observed at high fluxes – Enhancement or deterioration of local heat transfer dictated by microlayer formation beneath primary bubbles just after their formation
Straub *et al.* (1997), Straub (2000, 2002) [90-92]	Spacelab (Mission IML-2, STS-65) (10^{-4} g_e)	R-11	Thermistor D_h = 0.26 mm	p = 650 kPa T_b = 30-70°C T_w = 150-200°C $q'' \leq$ 900 kW/m^2	– There is no observable influence of gravity on heat transfer in nucleate boiling regime – With moderate subcooling, heat transfer coefficient in film boiling and transition boiling is degraded by 50% in μg_e compared to terrestrial conditions – With moderate subcooling, a thermocapillary jet is formed in the film boiling regime on a primary vapor bubble, which effectively transports high heat fluxes into the bulk liquid
Ohta *et al.* (1999) [93]	Sounding rocket (TR-1A)	Ethanol	Sapphire glass/ITO coated D_h = 50 mm	p = 11, 20 kPa ΔT_{sub} = 3-11 K T_b = 27°C q'' = 30 kW/m^2	– Steady-state nucleate boiling is attainable in μg_e except for high heat fluxes or very low liquid subcooling – At high heat fluxes or low liquid subcooling, a large coalescent vapor bubble is formed which lifts off the heater surface because of generation of bubbles at the base; this is speculated to be the dominant mechanism for nucleate boiling heat transfer
Abe & Iwasaki (1999) [94]	Drop shaft (JAMIC) (10^{-5} g_e, ~ 10 s)	R-113, R-122/R-12, water/ethanol	TEMPAX glass/ITO coated A_h = 20 × 30 mm^2	ΔT_{sub} = 3-18 K	– The Marangoni effect is more pronounced with increased liquid subcooling – Interferograms captured during the bubble evolution suggest the Marangoni effect is governed by temperature gradients in the early stages of bubble growth and later by concentration gradients

Table A.1: Summary of prior reduced gravity pool boiling studies – continued.

Author(s)	Microgravity Platform	Test Fluid	Heater Geometry	Test Conditions	Remarks
Kim *et al.* (2002), Henry & Kim (2004) [95,96]	Parabolic flight (KC-135) (0.01 g_e, 1.7 g_e)	FC-72	Platinum resistance heater A_h = 0.65 - 7.29 mm^2	ΔT_{sub} = 23.1-31.2 K T_b = 35-54.8°C q'' ~ 0-30 W/cm^2	– In low gravity, CHF increases with increasing subcooling if the dry area beneath the primary bubble is smaller than the heater surface area – Thermocapillary convection at higher superheats and subcooling decreases the size of the primary bubble – In high gravity, bubble departure frequency decreases for the smallest heater array, but is significantly smaller compared to low gravity conditions – For the larger heaters, increased subcooling decreases departure frequency of the primary bubble, but the time and surface averaged heat transfer is unaffected
Merte (2004, 2006) [97,98]	NASA Space Shuttle (STS-47, 57, 60, 72, 77) (10^{-4} g_e)	R-113	Quartz/semi-transparent gold film A_h = 19.05 × 38.1 mm^2	ΔT_{sub} = 0.3-22.2 K q'' = 0.5-8 W/cm^2	– High subcooling produces small vapor bubbles within the vicinity of heater surface; these bubbles are driven along the surface by thermocapillary effects – Computations show momentum transfer of the small nucleating bubbles bombarding the primary vapor bubble are countered only by the thermocapillary force on the primary bubble
Sodtke *et al.* (2006) [99]	Parabolic flight (ESA A-300)	FC-72	Aluminum plate/stainless steel foil (10 μm) A_h = 11.76 cm^2	ΔT_{sub} = 3-5 K q = 12-15 W	– High resolution wall temperature distribution close to the thin liquid film near the base of the vapor bubble in nucleate boiling is captured using unencapsulated thermochromic liquid crystals – A strong wall temperature drop occurs close to the thin liquid film where the liquid-vapor interface approaches the heater surface

Table A.1: Summary of prior reduced gravity pool boiling studies – continued.

Author(s)	Microgravity Platform	Test Fluid	Heater Geometry	Test Conditions	Remarks
Zhao *et al.* (2007, 2008) [100,101]	22nd Chinese recoverable satellite ($10^{-3} \sim 10^{-5}$ g_e)	R-113	Platinum wire 60 μm diameter, 30 mm long	p = 101 kPa ΔT_{sub} = 26.2 K T_b = 21.3°C	– The two-phase heat transfer coefficient is enhanced in μg_e – Lateral bubble oscillation along the wire leads to bubble coalescence and causes bubble departure – A thorough dynamic analysis of departure criteria is performed for bubbles growing in μg_e
Zhao *et al.* (2009) [102]	Chinese recoverable satellite (SJ-8) ($10^{-3} \sim 10^{-5}$ g_e)	FC-72	AL_2O_3 ceramic A_h = 15 × 15 mm^2	p = 57.2-111.7 kPa ΔT_{sub} = 18.4-36.9 K T_b = 16.7-43.3°C ΔT_{sat} = 11-76 K	– Both the two-phase heat transfer coefficient and CHF increase with increases in subcooling or pressure – CHF is degraded by about a third in μg_e compared to terrestrial conditions
Raj *et al.* (2009) [103]	Parabolic flight (ESA Airbus A300) (0.01 g_e, 1.8 g_e)	nPFH	Platinum resistance heater A_h = 12.25 - 49.0 mm^2	p = 1 atm ΔT_{sub} = 26°C T_w = 65-100°C	– Drastic variations of heat flux between low and high gravity preclude the possibility of deriving a unified power law dependence across all gravity levels – High dissolved gas concentrations cause nucleate boiling heat transfer to be enhanced in high gravity and degraded in low gravity – Nucleation site density remains fairly constant under gravity levels that foster capillary lengths significantly smaller than the characteristic length of the heater
Kannengi-eser *et al.* (2010) [104]	Sounding rocket (Maser 11) (5×10^{-4} g_e, ~ 6.5 min)	HFE-7000	Copper A_h = 1 cm^2	p = 120-330 kPa T_b = 25°C q = 0-5 W	– Boiling is dominated by formation of a large primary bubble due to coalescence of smaller bubbles on the heater surface, driven by Marangoni convection – For $T_w < T_{sat}$, bubble growth is impeded because of weak evaporation, and heat transfer is governed mainly by Marangoni convection – For $T_w > T_{sat}$, significant bubble growth is intensified by enhanced bubble nucleation at the wall, and heat transfer is governed mainly by evaporation

Table A.1: Summary of prior reduced gravity pool boiling studies – continued.

Author(s)	Microgravity Platform	Test Fluid	Heater Geometry	Test Conditions	Remarks
Xue *et al.* (2011) [105]	Drop tower (Beijing NMLC) (10^{-2} g_e, ~ 3.6 s)	FC-72	Silicon chip A_h = 10 × 10 mm^2	p = 102 kPa ΔT_{sub} = 41 K T_b = 14.6°C q'' = 3.38-11.59 W/cm^2	– At low heat fluxes, there is minimum coalescence amongst nucleating bubbles, which maintain contact with the heater surface because of strong thermocapillary convection around the bubbles – Upon increasing heat flux, bubble size and frequency increase – At high heat fluxes, a large coalescent bubble rapidly forms and completely covers the heater surface, leading to local dryout at the bubble base and deterioration of nucleate boiling heat transfer
Raj *et al.* (2012) [106]	International Space Station (ISS) (10^{-6} g_e)	nPFH	Platinum resistance heater A_h = 17.6 - 49.0 mm^2	p = 0.58-1.86 atm ΔT_{sub} = 1-26°C T_w = 55-107.5°C	– A gravity scaling parameter for μg_e pool boiling heat flux developed earlier by the same authors is modified and shows excellent agreement with experimental results
Dhir *et al.* (2012) [107]	International Space Station (ISS) (1.2×10^{-7} - 6×10^{-7} g_e)	nPFH	Aluminum D_h = 89.5 mm 5 Artificial cavities (10 μm diameter)	p = 51-243 kPa T_b = 30-59°C T_w = 40-80°C	– Low wall superheat promotes lateral coalescence of bubbles into a single coalescent bubble that grows progressively on the heater surface
Souza *et al.* (2013) [108]	Sounding rocket (Brazil VSB 30) (10^{-6} g_e , ~ 6.5 min)	n-Pentane	Copper disks D_h = 12 mm	p = 117-132 kPa ΔT_{sub} = 14.3-15.8 K T_b = 25.6-28.3°C $q \leq$ 60 kW/m^2	– Subcooled nucleate boiling behavior is investigated for different bulk temperatures and gap sizes – For the smallest gap size, the two-phase heat transfer coefficient is degraded by about 20% in μg_e compared to terrestrial conditions – For the largest gap size, the two-phase heat transfer coefficient decreases with increasing heat flux

surface at moderate subcoolings. At low heat fluxes, isolated bubbles slid slowly across the heater surface, constantly coalescing with neighboring bubbles. This sliding motion facilitated liquid replenishment to dryout regions of the surface originally inhabited by the bubbles. At high heat fluxes and/or near-saturated conditions, isolated bubbles grew larger and coalesced with other sliding bubbles with greater frequently, culminating in the formation of a single large bubble that encompassed the majority of the heater surface. Dryout beneath the large bubble ensued, resulting in unsteady rise in the surface temperature. As shown in Figure A.4(a), nucleate boiling is far less effective and CHF significantly smaller for R-113 in microgravity was than in Earth gravity. In microgravity tests with water, whose surface tension and heat of vaporization are significantly greater than those of n-Pentane and R-113, Oka *et al.* observed isolated bubbles detaching from the heater surface almost immediately upon generation, and growing to significantly larger size compared to terrestrial tests. At moderate subcooling, the detached bubbles immediately collapsed into the bulk liquid due to increased condensation. When detached bubbles were propelled into the bulk liquid at saturated or nearly saturated conditions, they remained within the vicinity of the heater surface, constantly coalescing with each other to form a single large vapor bubble, which continued to grow in size by engulfing newly formed bubbles. The high latent heat of vaporization of water delayed the complete evaporation of the thin liquid film beneath the large bubble, evidenced by absence of wall temperature excursions, especially for near-saturated conditions. Continued liquid supply to the thin film at the bubble contact area was confirmed by generation of a secondary bubble within the large bubble, a phenomenon later confirmed for microgravity pool boiling of water by Abe and Iwasaki [94].

Some investigators postulated that thermocapillary or Marangoni convection, typically masked by dominant buoyancy-driven convection in terrestrial conditions, plays a significant role in bubble nucleation and growth in microgravity, and therefore influences heat transfer effectiveness. These convection effects are the result of fluid motion along the vapor-liquid interface and away from the heater surface, induced by surface tension gradients. Predominantly observed in subcooled boiling, these

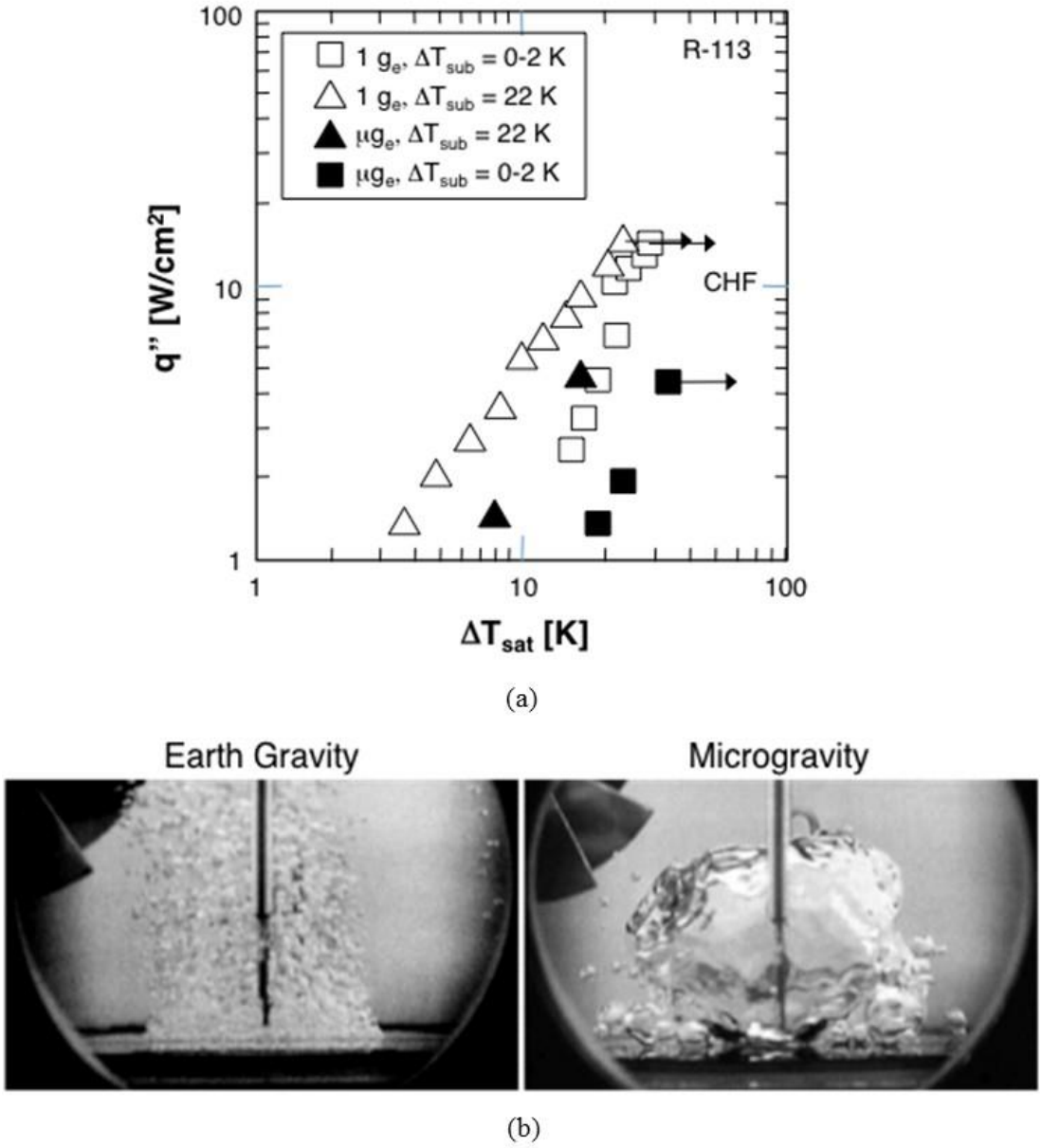

Figure A.4: (a) Pool boiling curves for R-113 in microgravity and Earth gravity at two levels of subcooling (adapted from Oka *et al.* [87]). (b) Photos of pool boiling of R-113 in Earth gravity and microgravity (courtesy NASA).

convection effects resulted in jet streams around the nucleating bubbles, which assisted the transport of heat from the bubbles to the bulk liquid. These effects were identified by Straub [91] in long-duration microgravity pool boiling experiments with R-11 on a hemispherical heater that were performed in Spacelab mission IML-2. Straub [92] later performed a thorough heat transfer analysis of the contributions of thermocapillary convection in microgravity. Overall, the strength of the thermocapillary jet, which was measured by particle image velocimetry (PIV), increased with increasing heat flux. However, this behavior was highly influenced by the degree of subcooling. In saturated conditions, they measured zero jet velocity. Upon slightly increasing the subcooling, the jet velocity increased rapidly to a maximum level, but decreased back to zero at high subcooling. In subcooled boiling, they postulated bubble growth is dictated by a balance between evaporation at the bubble base and condensation at the bubble cap. Differences between the two rates resulted in temperature gradients that induced vapor flow within the bubble. Straub proposed that thermocapillary convection observed in subcooled conditions is induced by accumulation of minute amounts of inert gases that are driven by the internal bubble vapor flow towards condensation region.

Merte and co-workers [97,98] also conducted long-duration microgravity pool boiling experiments with R-113 onboard NASA's Space Shuttle (STS-47, 57, 60, 72, 77). They used a flat 19.05 x 38.1 mm^2 rectangular heater consisting of a semi-transparent gold film deposited on a quartz substrate. Their experiments covered subcoolings of ΔT_{sub} = 0.3-22.2 K and heat fluxes of q'' = 0.5-8 W/cm^2. For moderate subcoolings and low heat fluxes, a large vapor bubble formed and hovered in the vicinity of the heater surface while smaller bubbles nucleated underneath. For low heat fluxes, they postulated that the thermocapillary reaction force that would otherwise push the large vapor bubble towards the heater surface and cause dryout is opposed by momentum of small bubbles coalescing into the large bubble. This helps maintain liquid replenishment of the heater surface, permitting steady nucleate boiling and even yielding heat transfer coefficients at low heat fluxes that are greater than those realized in terrestrial conditions. Excepting their highest subcooling condition, all tests conducted at the highest heat flux culminated in partial or complete dryout as a large vapor bubble engulfed the entire heater surface

leading to unsteady rise in the surface temperature and appreciable reduction in the heat transfer coefficient. Figure A.4(b) shows photos of bubble formation in microgravity obtained in Space Shuttle experiments compared to those in Earth gravity. Notice how a single large bubble is formed in microgravity engulfing the entire heater surface without a tendency to depart from the surface. On the other hand, many smaller discrete bubbles are formed in Earth gravity, which are pulled away from the surface by buoyancy.

A common observation in the above and other microgravity pool boiling experiments is formation of an unusually large bubble, which often engulfs the entire heater surface, a phenomenon rarely encountered in terrestrial conditions. This phenomenon can be explained by the Capillary or Laplace length, which dictates the size of a bubble in response to surface tension and gravity. In microgravity, Capillary length is unusually large, which explains the formation of the unusually large bubble. Another important consideration is how the Capillary length compares to heater size.

Kim and co-workers conducted microgravity pool boiling experiments with FC-72 in several parabolic flight campaigns, and recently with nPFH onboard the ISS, and addressed the influence of Capillary length. They obtained impressive high-speed video images of pool boiling in both microgravity and high gravity (1.7 g_e) onboard NASA's KC-135 jet [95,96]. They developed a unique heater surface consisting of several arrays of platinum resistance heaters that were controlled by a bank of feedback circuitry to achieve constant surface temperature. Subcooled pool boiling of FC-72 was achieved using three heater sizes, 0.65, 2.62 and 7.29 mm^2. In microgravity, absence of buoyancy allowed surface tension to play a dominant role, culminating in the formation of a single large bubble regardless of heater size. On the other hand, tests at 1.7 g_e showed a dependence on heater size, with the smallest heater yielding a single primary bubble due to proximity of this heater's size to the Capillary length, while the largest heater was able to accommodate multiple nucleation sites and generate a primary bubble with neighboring satellite bubbles. Kim's team later performed long-duration microgravity tests onboard the ISS utilizing the Boiling eXperiment Facility (BXF) [106], which incorporated two experiments within a single apparatus: Kim and co-workers' Microheater Array Boiling Experiment (MABE), and the Nucleate Pool Boiling

Experiment of Dhir *et al.* [107]. Experimental results from MABE led to the following important findings concerning pool boiling in microgravity: (1) the onset of nucleate boiling (ONB) in microgravity occurs at lower surface superheat compared to terrestrial data, (2) increasing system pressure decreases the superheat required for ONB, which enhances heat transfer throughout the nucleate boiling regime up to CHF, (3) heat transfer is enhanced with increased subcooling and degraded with decreased subcooling, where a large bubble engulfs the entire heater surface, (4) the boiling curve for high gravity is heater size dependent, and (5) with decreasing heater size, heat transfer is enhanced at high subcooling and degraded at low subcooling.

Dhir and co-workers [107] conducted long-term nucleate boiling experiments onboard the ISS. Testing was performed with nPFH on an aluminum wafer equipped with an array of strain gage heaters and thermistors, and featuring five 10-μm diameter artificial cavities. They compared single and multiple bubble dynamics and heat transfer data with predictions of numerical simulation tools developed earlier by Son *et al.* [109]. The numerical model accounts for interfacial condensation at the bubble cap as well as dissolved gasses present in the liquid. Numerical single-bubble nucleation results predicted the experimental transient bubble shape and size remarkably well. Like previous investigators, Dhir and co-workers observed the formation of single large primary bubble from coalescence of lateral bubbles merging on the heater surface. At high superheats, the large bubble was able to lift off the heater surface and hover within close proximity of the surface, continuously growing in size by pulling in additional bubbles generated on the surface.

Despite the important fundamental knowledge gained from microgravity pool boiling experiments, two overriding concerns point to serious challenges in implementing pool boiling in space applications: (i) formation of an unusually large bubble that engulfs the entire heater surface, and (ii) appreciable reduction in CHF compared to terrestrial data. These concerns point to the need for another force to overcome these effects. By relying on fluid inertia to dwarf other forces, flow boiling systems provide an effective means for controlling bubble growth and maintaining liquid replenishment of the heater surface to boast CHF.

A.4 Two-Phase Flow and Heat Transfer in Reduced Gravity

A.4.1 Types of Two-Phase Flow and Heat Transfer Microgravity Studies and Prior Review Articles

Three different types of studies have been undertaken to assess the influence of microgravity on two-phase flow and heat transfer: (1) adiabatic experiments aimed at identifying dominant two-phase flow patterns and measuring two-phase pressure drop, (2) steady-state heat transfer experiments that explore bubble nucleation and growth, and measure nucleate boiling heat transfer and CHF, and (3) quenching experiments that measure the same parameters but in transient experiments.

Several articles have recently been published to review the limited literature concerning these studies. They include an early article by Antar [110] on two-phase flow dynamics, followed by a series of reviews on two-phase heat transfer [111-114]. More recently, Di Marco [115] reviewed the mechanisms governing both pool boiling and flow boiling in microgravity, with added focus on the influence of electrical field on boiling. Ohta and Baba [116] highlighted their microgravity boiling research and discussed an experimental facility to be launched in a few years to the ISS to conduct long-duration flow boiling experiments. Baldassari and Marengo [117] summarized findings from both terrestrial and microgravity flow boiling literature, with particular focus on the influence of the Eötvös number for flow boiling in terrestrial small-channel experiments and in low gravity.

A.4.2 Adiabatic Two-Phase Flow Studies

Since the early adiabatic two-phase microgravity experiments of Hepner *et al.* [118], researchers quickly realized the vast differences in interfacial behavior between terrestrial and reduced gravity environments. Only three of the classical flow patterns in tubes are commonly achieved in reduced gravity: bubbly, slug and annular flows, with a fourth frothy slug-annular flow pattern observed in a few studies, as depicted in Figure A.5(a), based on combinations of superficial velocities of vapor and liquid, j_g and j_f, respectively [119]. Choi e*t al.* [120] compared air-water flow patterns along a 10-mm

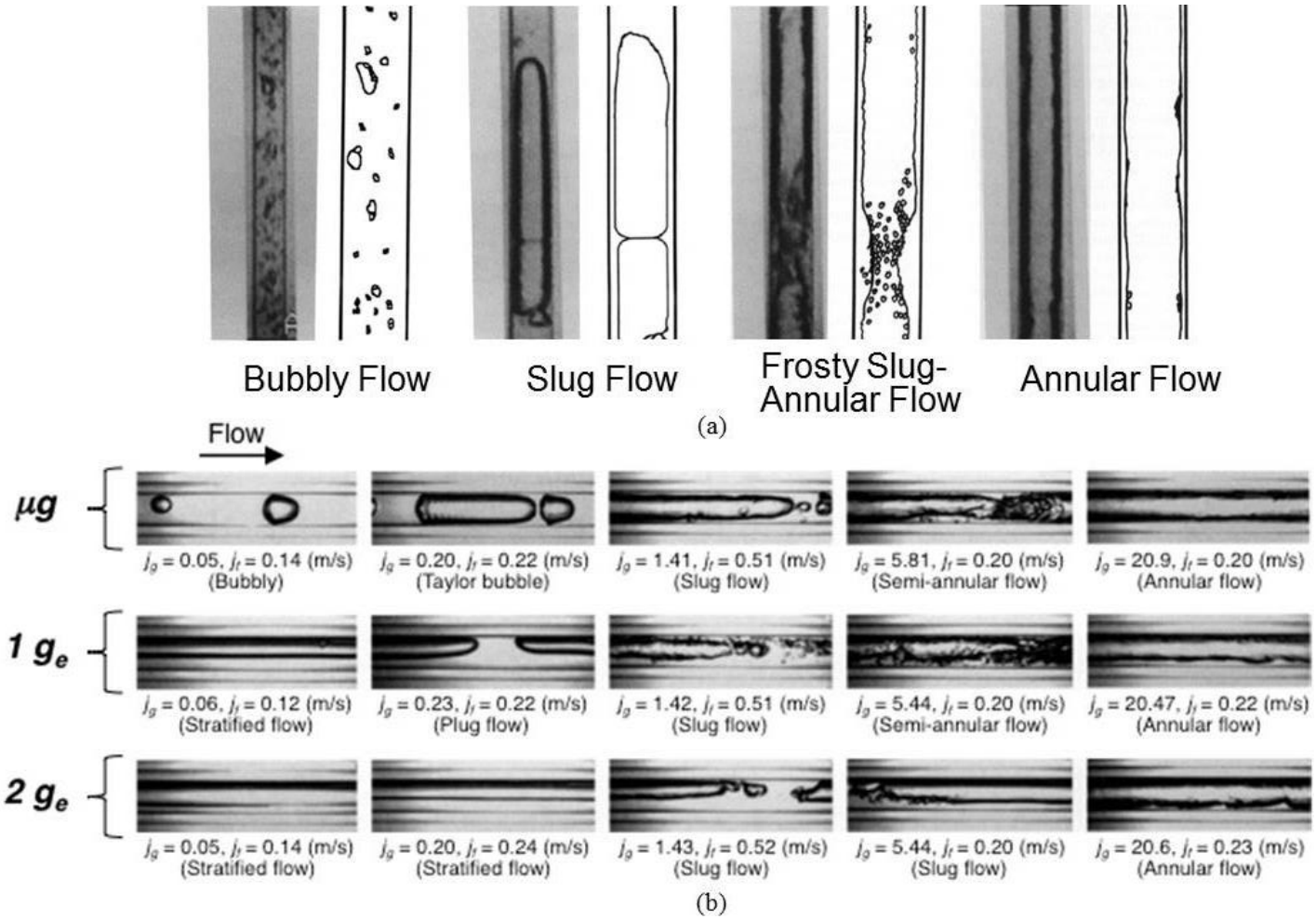

Figure A.5: (a) Air-water two-phase flow patterns in microgravity (adapted from Zhao and Rezkallah [119]). (b) Air-water flow patterns along a 10-mm diameter tube in microgravity (μg_e), terrestrial gravity (1 g_e), and hypergravity (2 g_e) (adapted from Choi *et al.* [120]).

diameter tube in microgravity (μg_e) and hypergravity (2 g_e) aboard an MU-300 aircraft, and in terrestrial gravity (1 g_e). Their findings point to the important role of flow velocities in influencing, not only flow pattern, but also the relative importance of body force. As shown in Figure A.5(b), low flow velocities allow surface tension forces to play a dominant role in μg_e, yielding bubbly flow, whereas 1-g_e and 2-g_e environments produce stratified and plug flows, respectively, for the same velocities. On the other hand, high velocities cause flow inertia to dwarf any surface tension or gravity effects, yielding similar flow patterns for all gravity levels.

Dukler *et al.* [121] performed adiabatic air-water two-phase flow experiments in a 9.52-mm diameter and 0.475-m long horizontal tube in the NASA Lewis 100-ft drop tower and in parabolic flight onboard the NASA Lewis Learjet. Three classical flow patterns were observed: bubbly, slug and annular flow. Transition from bubbly to slug flow was based on bubble size and concentration in bubbly flow that promotes coalescence, which was estimated to occur at $\alpha = 0.45$. In the absence of drift between the phases in microgravity bubbly flow, the mean velocities of vapor and liquid are equal. Using $\alpha = 0.45$, this yields the following relation for transition from bubbly to slug flow.

$$j_f = j_g\left(\frac{1-\langle\alpha\rangle}{\langle\alpha\rangle}\right) = 1.22\, j_g, \tag{A.12}$$

where $\langle\alpha\rangle$ is the void fraction averaged over the cross-sectional area of the tube. For transition from slug to annular flow, they postulated that increased gas flow rate promotes elongation of Taylor bubbles in the axial direction. As the liquid slugs separating these bubbles become relatively short, variations in the local velocity or adjacent film thickness cause the slugs to rupture, allowing surface tension forces to draw the liquid towards the wall and establish the characteristic annular flow. The slug-annular transition was obtained by equating the following Drift-Flux relations for slug and annular flow, respectively.

$$\frac{j_g}{j_f + j_g} = C_0\langle\alpha\rangle \tag{A.13a}$$

and

$$\frac{\langle\alpha\rangle^{5/2}}{\left(1-\langle\alpha\rangle\right)^2} = \left(\frac{f_i}{f_w}\right)\left(\frac{\rho_g}{\rho_f}\right)\left(\frac{j_g}{j_f}\right)^2, \tag{A.13b}$$

where C_o is the distribution parameter in the Drift Flux model. The interfacial friction factor, f_i, in Eq. (A.13b) is determined from the empirical correlation [59]

$$\frac{f_i}{f_g} = 1 + 150\left(1-\alpha^{1/2}\right), \tag{A.14}$$

and the wall friction factor, f_w, and gas layer friction factor, f_g, using the Blausius relation with a Drift Flux distribution parameter of $C_o = 1.25$.

Bousman *et al.* [122-124] continued the work of Dukler *et al.* by conducting parabolic flight adiabatic tests using two horizontal tubes: a smaller tube (D =12.7 mm) in NASA's Learjet Model 25, and larger tube (D = 25.4 mm) in NASA's KC-135 jet. In addition to investigating the influence of tube diameter, they explored surface tension effects by testing three different fluid combinations: air-water, air- 50-50 wt% water/glycerin, and air-water/Zonyl FSP. Observations of interfacial behavior proved turbulent oscillations are more pronounced in the larger tube, which enhanced bubble coalescence, causing a significant shift in void fraction corresponding to bubbly-slug transition; this shift was less pronounced for the reduced surface tension liquids (glycerin, Zonyl FSP). Therefore, different relations were recommended for bubbly-slug transition based on different fluid combinations. For both tubes, they estimated slug-annular transition to occur at $\alpha = 0.75$ for air-water and air-water/Zonyl FSP, and $\alpha = 0.70$ for air-water/glycerin. They used the same general methodology proposed by Dukler *et al.* to derive an alternative Drift-Flux relation for slug-annular transition.

Colin and coworkers [125-129] performed several adiabatic air-water two-phase flow experiments in microgravity. Colin *et al.* [125] compared flow patterns in a 40-mm, 3.14-m long tube in parabolic flight with those in vertical upflow at 1 g_e. Comparing results with those of Dukler *et al.* [121] and Bousman *et al.* [124] revealed a dependence of flow pattern transitions on tube diameter. In reduced gravity, bubbles in the 40-mm diameter tube of Colin *et al.* were concentrated more in the central region of the tube, compared to a more uniform distribution in the smaller tubes of Dukler *et al.* and Bousman *et al*. This behavior was attributed to greater turbulence in the larger tube causing increased bubble coalescence. Colin *et al.* [126] showed bubbles produce maximum concentration along the center of the tube in μg_e compared to near the wall in 1

g_e. They also observed bubbly-slug transition to occur at a lower transitional void fraction of $\alpha = 0.20$, for which Eq. (14) becomes

$$j_f = 3.2\, j_g. \tag{A.15}$$

Later, Colin *et al.* [128] proposed the dimensionless parameter $N_D = \sigma D \big/ \left(\rho_f v_f^2\right) = Re^2/We$ to ascertain the influence of tube diameter and fluid properties on bubbly-slug transition.

Lee [130,131] also developed flow pattern transitional models for μg_e. Though intended for condensation, the same models were later adopted by several investigators in conjunction with adiabatic two-phase flow. Formulation of these models is based on the premise that the transitions are dictated by forces dominating each flow pattern, including surface tension, gravity, fluid inertia, friction, and turbulent fluctuations. They postulated that bubbly-slug transition is dominated by the surface tension force tending to preserve Taylor bubbles in slug flow, and turbulent fluctuations to rupture the liquid-vapor interface to form smaller bubbles. On the other hand, vapor inertia and surface tension dictated the slug-annular transition.

Reinarts [132] conducted two-phase flow experiments with R-12 in two horizontal tubes with diameters of 4.7 and 10.5 mm. Tests were conducted aboard NASA's KC-135 aircraft to simulate μg_e as well as Lunar (1.7 m/s^2) and Martian (3.7 m/s^2) environments, and were compared with 1-g_e ground tests. The influence of body force was prevalent in Lunar and Martian tests in the form of stratified and plug flow patterns not observed in μg_e, where only bubbly, slug, and annular flows were observed. Reinarts developed flow pattern transition models based on formulations proposed earlier by Lee [130,131].

More recently, several additional efforts were undertaken to capture adiabatic two-phase flow regimes in μg_e, and to predict flow pattern transitions using a variety of models and dominant dimensionless groups [133-137].

Another key focus of adiabatic microgravity studies is two-phase pressure drop. The total pressure drop in two-phase flow is composed of frictional, accelerational, and gravitational components. Notice that the accelerational component is zero for adiabatic flow. Also, the gravitational component is zero in μg_e. Therefore, adiabatic two-phase

flow experiments in microgravity enable the measurement of the frictional component alone.

Because of the aforementioned concentration of bubbles along the center of large diameter tubes with almost pure liquid flow near the wall, Colin *et al.* [125] showed μg_e wall friction data agree well with predictions of the Blasius correlation for single-phase turbulent flow. On the other hand, Colin *et al.* [127,128] detected an increase in wall friction for low Reynolds numbers in smaller tubes from single-phase relations, which was attributed to the small diameters causing bubbles to approach the wall. Zhao and Rezkallah [138] also observed an increase in wall friction at low flow rates, fostering bubbly and slug flows.

Bousman [122] found the Homogeneous Equilibrium Model (HEM) and Separated Flow Model (SFM) incapable of accurately predicting the majority of their pressure drop data corresponding to the bubbly and slug flow regimes. However, the Lockhart-Martinelli model [139] provided fairly good predictions of annular flow data.

Both Chen *et al.* [140] and Choi *et al.* [120] showed pressure drop in μg_e is significantly larger than in 1 g_e. Zhao *et al.* [141] showed classical 1-g_e empirical pressure drop models yield poor predictions of μg_e data. Such deviations, which demonstrate the fundamental differences in two-phase behavior between μg_e and 1 g_e, have prompted investigators to devise new correlations or modified models specific to microgravity.

A.4.3 Flow Boiling Studies

A.4.3.1 Two-Phase Flow Boiling Patterns and Transitions

Although microgravity flow boiling experiments have been conducted since the late 1950s, far fewer studies have investigated flow boiling that pool boiling and adiabatic two-phase flow. The earliest investigation of microgravity flow boiling is attributed to Siegel and Usiskin [142,143]. Table A.2 provides a summary of more recent studies concerning this topic. Overall, these studies show striking differences in interfacial behavior and heat transfer mechanisms between μg_e and 1 g_e.

Table A.2: Summary of prior reduced gravity flow boiling studies.

Author(s)	Microgravity Platform	Test Fluid	Flow/Heater Geometry	Test Conditions	Remarks
Papell (1964) [144]	Parabolic flight	Water	Circular (nickel-alloy) D = 7.9 mm, L_h = 165.1 mm, Vertical	p = 3.4 bar ΔT_{sub} = 79.4-92.2°C $\dot{m}$ = 0.09 kg/s q'' = 2289.6 kW/m^2	– Flow patterns observed in μg_e: bubbly and slug
Misawa (1993) [145]	Drop tower (University of Florida) (0.02 g_e, 1.25 s)	R-113	Rectangular (Pyrex) A = 5 ×5 mm^2, L = 500 mm, CL_2Sn film heater on 4 sides	ΔT_{sub} = 4.6-16.9°C G = 37.7-114.4 kg/m^{2}s q'' = 2.9 kW/m^2 $x_{e,o}$ = -0.045 - 0.175	– Flow patterns observed in μg_e: bubbly, slug, slug-frothy, annular, annular-frothy – Bubbles significantly larger in μg_e than 1 g_e – Flow pattern transition occurs at smaller values of void fraction in μg_e than 1 g_e – Data agree well with flow pattern transitional maps of Dukler *et al.* [121] and Colin *et al.* [125] – Void fraction rapidly increases in subcooled region in μg_e compared to 1 g_e – Heat transfer deteriorates in μg_e compared to 1 g_e – For bubbly flow, turbulence generated by bubbles is weakened in μg_e – Wall shear stress in μg_e is 1.18 times larger than in 1 g_e due to large bubbles in low-quality region – Homogeneous model predicts bubbly flow pressure drop well
Saito *et al.* (1994) [146]	Parabolic flight (MU-300)	Water	Rectangular A = 25×25 mm^2, L = 600 mm, Rod-type electric heater, D = 8 mm, L = 200 mm, Horizontal	p = 90-204 kPa T_{in} = 86.1-112.8°C U = 3.7-22.9 cm/s q'' = 5.3-18.6 W/cm^2	– In 1 g_e at low inlet flow velocity and high heat flux, bubbles detach frequently from heated rod then stratify in upper portion of flow channel due to buoyancy – Stratification is not observed in μg_e due minimal detachment of bubbles, which propagate along heated rod, continuously growing and coalescing with neighboring bubbles, especially at low inlet velocity, low inlet subcooling, and high heat flux

Table A.2: Summary of prior reduced gravity flow boiling studies – continued.

Author(s)	Microgravity Platform	Test Fluid	Flow/Heater Geometry	Test Conditions	Remarks
Ohta (1997) [147]	Parabolic flight (MU-300)	R-113	Circular (Pyrex) D = 8 mm, L = 100 and 300 mm, L = 70 and 255 mm, Gold film heater (0.01 μm), Vertical upflow	p = 0.11-0.22 MPa G = 150-600 kg/m^{2}s $x_{e,in}$ = 0 - 0.8 q'' = 5-150 kW/m^2	– Heat transfer regimes in μg_e are segregated based on mass velocity, heat flux, and quality, with the relative significance of body force identified for each regime
Ma & Chung (2001) [148]	Drop tower (Washington State University) (10^{-3} g_e, 2.1s)	FC-72	Square (Pyrex) A_h = 1×1 mm^2 Gold film heater (0.045 μm), Horizontal	p = 112 kPa T_{in} = 30°C $\Delta T_{sub,in}$ = 26°C U = 6.5-30 cm/s q'' = 5.4, 39.7 kW/m^2	– Bubbles are larger and acquire semi-spherical shape on heated surface in μg_e compared to 1 g_e – In μg_e, increasing flow rate suppresses growth of bubble before departure because of dominance of convective heat loss at exposed liquid-vapor interface compared to evaporation rate at bubble base – In 1 g_e, greater frequency of bubble generation increases with increasing flow rate compared to μg_e, but this difference is minimal at very high flow rates ($Re \geq$ 16,821)
Ma & Chung (2001) [148]	Drop tower (Washington State University) (10^{-3} g_e, 2.1s)	FC-72	Platinum wire D = 0.254 mm, L = 20 mm, Horizontal	p = 112 kPa T_{in} = 30 °C $\Delta T_{sub,in}$ = 26°C U = 6.5-30 cm/s q'' = 0-600 kW/m^2	– Heat transfer enhancement is greater in μg_e at lower flow rates – Degradation in heat transfer occurs in transition boiling regime up to CHF in μg_e, resulting in significantly lower CHF compared to 1 g_e
Westheimer & Peterson (2001) [149]	Parabolic flight (NASA KC-135)	R-113	Circular (Borosilicate glass) Annular countercurrent heat exchanger, D = 10 mm, L = 584 mm, Vertical upflow	p = ambient R-113: Q = 100 mL/min Water: Q = 24 mL/min R-113: q = 0-11W Water: q = 266-356 W	– Flow patterns observed in μg_e: bubble, slug and annular – Bubble speed decreases in μg_e due to absence of buoyancy – Lower heat input is required to initiate flow regime transition in μg_e – 1-g_e flow pattern maps predict experimental data poorly – Highest local heat transfer coefficient is achieved at axial location corresponding to transition from bubbly to slug flow

Table A.2: Summary of prior reduced gravity flow boiling studies – continued.

Author(s)	Microgravity Platform	Test Fluid	Flow/Heater Geometry	Test Conditions	Remarks
Celeta *et al.* (2007) [150]	Parabolic flight (Zero-G Airbus A300)	FC-72	Circular (Pyrex) D = 4.0 and 6.0 mm, L = 165 and 145 mm, Joule effect through metallic tape, Vertical upflow	p = 1.6-1.8 bar $\Delta T_{sub,in}$ = 9-30°C G = 47.5-520 kg/m^{2}s q'' ≤ 100 kW/m^2 $x_{e,o}$ ≤ 0.22	– Flow patterns observed in μg_e: bubbly, intermittent (slug-plug) and annular – Flow pattern map of Dukler *et al.* [121] shows reasonable agreement with μg_e data for 4.0 mm tube – Modified criterion based on Dukler *et al.* [121] map is proposed to correlate μg_e data for 6.0 mm tube
Luciani *et al.* (2008) [151]	Parabolic flight (A300)	HFE-7100	Rectangular (Inconel) D_h = 0.49, 0.84, 1.18 mm, H/W = 0.04-0.11, L = 50 mm, Vertical upflow	T_{sat} = 54°C $\Delta T_{sub,in}$ = 2°C $\dot{m}$ = 0.26 g/s q'' = 33 kW/m^2	– Heat transfer is enhanced in μg_e – For all gravity conditions tested (μg_e, 1 g_e, 1.8 g_e), two-phase heat transfer coefficient is highest at the inlet and decreases in the flow direction – No noticeable difference observed between 1 g_e and 1.8 g_e data
Baltis *et al.* (2012) [152]	Parabolic flight (Zero-G Airbus A300)	FC-72	Circular (Pyrex) D = 2.0, 4.0, 6.0 mm, L = 0.2 m Joule effect through metallic tape	p = 1.2-1.8 bar $\Delta T_{sub,in}$ = -9 to -30°C G = 47.5-570.0 kg/m^{2}s q'' ≤ 100.0 kW/m^2 $x_{e,o}$ ≤ 0.22	– Bubbly flow pattern exhibits heat transfer enhancement predominantly at the tube inlet, which is degraded at the outlet – Increasing vapor quality and/or mass velocity diminishes body force effects – The largest tube tested (D = 6.0 mm) shows body force effects are dominant for G < 425 kg/m^{2}s – Smaller tubes show diminishing influence of body force, but greater flow instabilities occur in the smallest tube (D = 2.0 mm)
Brutin *et al.* (2013) [153]	Parabolic flight (A300)	HFE-7100	Rectangular (Inconel) D_h = 0.84 mm, H/W = 0.08, L = 50 mm, Vertical upflow	T_{sat} = 54°C $\Delta T_{sub,in}$ = 2°C G = 30-248 kg/m^{2}s q'' = 15-55 kW/m^2	– Up to 50% deterioration of frictional pressure drop is achieved in μg_e compared to 1 g_e, the pressure drop in 1.8 g_e is 1.3 times higher than in 1 g_e – Local two-phase heat transfer coefficient is enhanced in μg_e due to smaller film thickness

Table A.2: Summary of prior reduced gravity flow boiling studies – continued.

Author(s)	Microgravity Platform	Test Fluid	Flow/Heater Geometry	Test Conditions	Remarks
Narcy *et al.* (2013) [154]	Parabolic flight	HFE-7000	Circular (sapphire) D = 6 mm, L = 200 mm, ITO film heater, Vertical upflow	P = 1-2 bar G = 50-1200 kg/m^{2}s q'' ≤ 45 kW/m^2 $x_{e,in}$ ≤ 0.9	– Flow patterns observed in μg_e: bubbly, slug and annular flow – Bubbly and slug flows transition to annular flow earlier in μg_e than in 1 g_e due to increased bubble coalescence – Thinner liquid film is measured in annular flow and transitional flow (slug-to-annular region) in μg_e compared to 1 g_e – Adiabatic pressure drop downstream of the heated section is correlated well for bubbly and annular flow using the Lockhart-Martinelli [139] correlation – At low mass velocity, the two-phase heat transfer coefficient is degraded in μg_e compared to 1 g_e for x_e < 0.2, and enhanced for x_e > 0.2

Misawa [145] investigated subcooled and saturated flow boiling of R-113 in both drop tower (1.25 s at 0.02 g_e) and NASA's Learjet experiments. Using a film heated square channel (A = 5×5 mm^2, L = 500 mm), and two electrically heated coiled tubes (D = 4 and 12.8 mm, L = 500 and 480 mm), flow patterns were shown to transition earlier in μg_e compared to 1 g_e, but differences in flow behavior diminished at high vapor quality. They identified bubbly, slug, slug-frothy, annular and annular-frothy patterns, whose transitions were in good agreement with the μg_e maps of Dukler *et al.* [121] and Colin *et al.* [125].

Saito *et al.* [146] performed parabolic flight water flow boiling experiments in a 25×25 mm^2 and 600-mm long square channel that was fitted with an electrically heated rod (D = 8 mm, L = 200) along its central axis. Figure A.6(a) shows differences in interfacial behavior between μg_e and 1 g_e tests. Notice how body force effects are prevalent at 1 g_e and low flow rates, where bubbles generated on the heated rod detached and stratified in the upper portion of the flow channel. On the other hand, the absence of buoyancy in μg_e subdued bubble detachment, causing bubbles to continue to propagate along the heated surface and to grow from downstream bubble generation as well as coalescence with neighboring bubbles.

Ohta *et al.* [147] conducted parabolic flight microgravity flow boiling experiments using R-113 in 8-mm diameter pyrex tubes coated internally with thin heating gold film (L = 70 and 255 mm). Experimental data for subcooled and saturated inlet conditions were obtained for μg_e and 2 g_e, and compared with 1 g_e vertical upflow tests. As shown in Figure A.6(b), bubbly flow was observed in all gravity levels for subcooled inlet conditions and relatively low mass velocity of G = 150 kg/m^{2}s. And like μg_e pool boiling, bubbles in μg_e flow boiling flow were significantly larger than in 1 g_e and 2 g_e. But for the highest mass velocity of G = 600 kg/m^{2}s, similar bubble detachment diameters were observed for all gravity levels. This similarity was attributed to increased fluid inertia dwarfing body force effects by providing sufficient interfacial shear to detach bubbles from the heated surface before further growth due to evaporation could take effect. Figure A.6(b) shows body force effects were also suppressed for high inlet quality

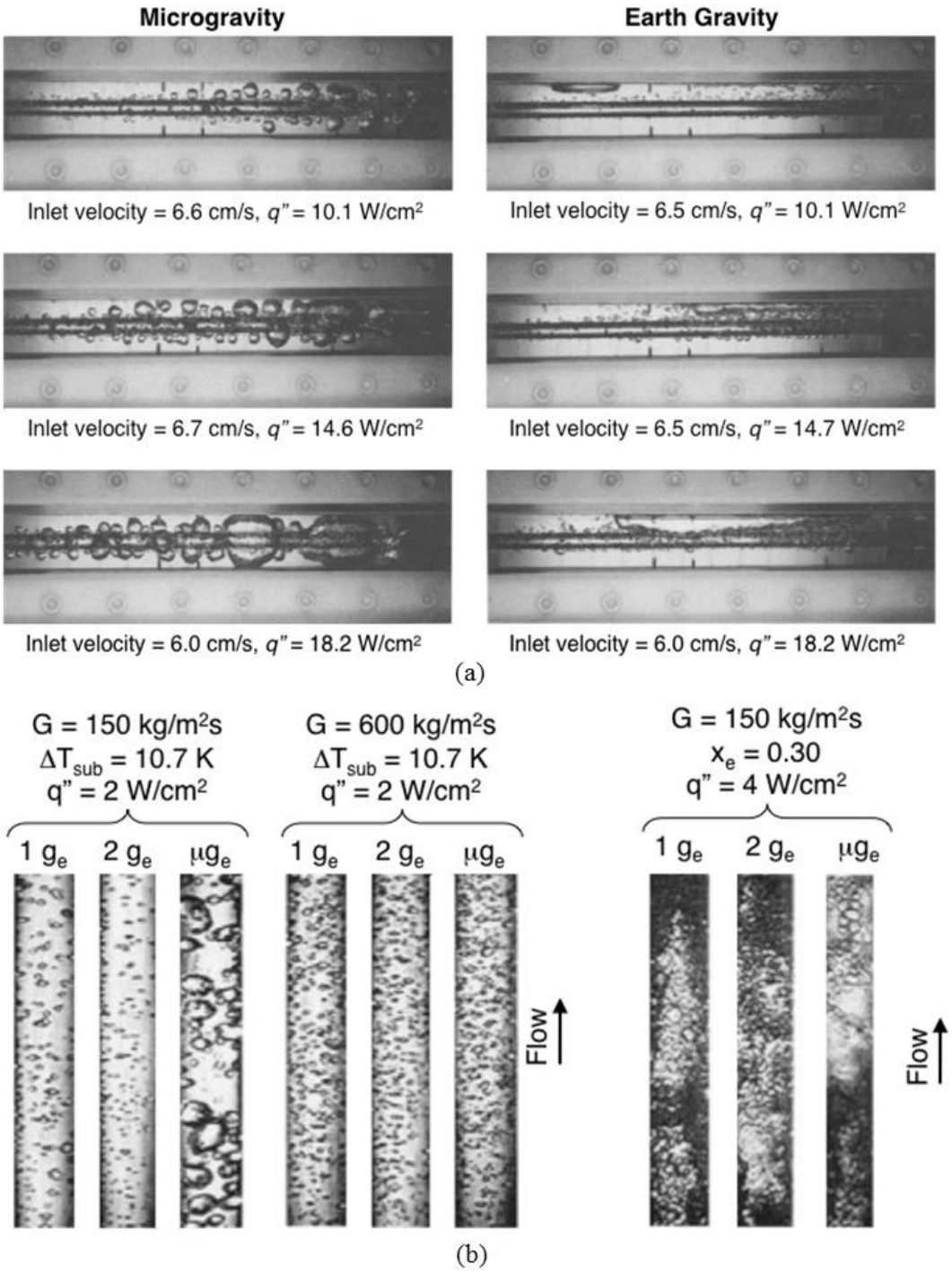

Figure A.6: (a) Comparison of water flow boiling behavior in microgravity and Earth gravity along a square channel fitted with a central cylindrical heating rod (adapted from Satto *et al.* [146]). (b) Comparison of flow boiling of R-113 in vertical upflow in 1 g_e, 2 g_e and μg_e for subcooled inlet conditions at low and high mass velocities, and for low mass velocity and high inlet quality (adapted from Ohta [147]).

and high heat flux conditions, where similar annular flow behavior was observed for all gravity levels.

Celeta *et al.* performed multiple parabolic flight experiments to investigate flow boiling [150] and quenching [155,156] in μg_e. Their flow boiling experiments involved subcooled FC-72 introduced through circular glass tubes (D = 4 and 6 mm) that were heated by metallic tape helically coiled on their outer surfaces. Interfacial behavior in μg_e for the 4-mm tube agreed with that for 1-g_e vertical upflow, where bubbly flow was encountered at low mass velocities and low heat fluxes. They speculated that the absence of buoyancy in μg_e prolonged bubble growth during nucleation, resulting in larger bubble detachment diameters compared to 1-g_e. Intermittent (plug-slug) flow patterns were achieved with an increase in heat flux in μg_e, whereas churn flow was observed at 1 g_e for the same conditions. Overall, similar interfacial behavior was observed at high mass velocities and high heat fluxes, indicating independence of body force effects, and the observed interfacial behavior and heat transfer characteristics were similar to those of Ohta *et al.* [147]. Similar flow patterns were observed by Celeta *et al.* in the 6.0-mm tube with the exception of annular flow. For bubbly flow in μg_e, this larger tube promoted greater bubble nucleation, which enhanced coalescence frequency and led to the formation of larger bubbles. Transition from bubbly to intermittent flow occurred at lower heat fluxes in μg_e compared to 1 g_e. Celata *et al.* also explored the effectiveness of prior μg_e flow pattern maps in predicting their own data. The transitional criteria proposed by Dukler *et al.* [121] showed good agreement with their 4.0-mm tube data.

Luciani *et al.* [151,157] investigated subcooled flow boiling of HFE-7100 in three narrow rectangular channels (6.0×0.254, 6.0×0.454, 6.0×0.654 mm^2) with a heated length of 50 mm. Tests were conducted in parabolic flight to simulate μg_e and 1.8 g_e, and later compared with 1-g_e vertical upflow tests. They detected some upstream heat transfer enhancement in μg_e, but similar interfacial behavior in 1 g_e and 1.8 g_e.

A.4.3.2 Two-Phase Heat Transfer and Pressure Drop

Misawa [145] investigated the contributions of turbulence in bubbly flow. Because of the absence of drift in μg_e, they postulated that turbulence induced by bubble

agitation is compromised, leading to deterioration in heat transfer in μg_e compared to 1 g_e.

Ohta *et al.* [147] performed flow boiling experiments in parabolic flight at μg_e and 2 g_e, which they compared with ground 1 g_e vertical upflow tests. They monitored wall temperature during parabolic flight in response to varying gravity. For all mass velocities fostering bubbly flow, changes in gravity during parabolic flight had minimum effects on heat transfer, suggesting a dominant nucleate boiling heat transfer mechanism for bubbly flow that is both local and confined to the heated wall. For conditions yielding annular flow with moderate inlet quality, heat transfer at low heat fluxes was governed by two-phase forced convection and strongly influenced by gravity, and heat transfer deteriorated in low-*g* compared to high-*g*. Waves in the liquid film caused film thickness to decrease at high-*g* and increase in μg_e. For annular flow and high heat flux, nucleate boiling was observed within the annular liquid film, yielding similar heat transfer coefficients through the varying gravity event. Yet, the influence of gravity on annular heat transfer diminished at high inlet quality, where greater shear forces resulting from increased vapor core velocity appeared to overcome body force effects.

Celeta *et al.* [155] and Baltis *et al.* [152] also explored wall temperature variations in a 6.0-mm tube with varying gravity during parabolic maneuvers. At low mass velocity and low exit vapor quality, the hypergravity phase produced bubbly flow with small bubbles detaching from the wall. Entering the μg_e phase, heat transfer was enhanced significantly in the inlet and reduced in the outlet. The upstream enhancement was attributed to greater mixing and turbulence brought about by larger bubble diameters in μg_e. With increased mass velocity, no significant variations in wall temperature were detected, proving these operating conditions greatly reduced the influence of body force. At low mass velocity and high exit quality, which yielded intermittent/annular flow, slight gravitational effects were detected.

Luciani *et al.* [151,157] employed inverse methods to estimate the local heat transfer coefficient. They reported heat transfer enhancement in all μg_e conditions, with average heat transfer coefficients as much as 30% higher than terrestrial data. For all gravity levels, large heat transfer coefficients were measured near the inlet, which

dropped sharply to fairly constant value from about the middle of the channel to the exit. Brutin *et al.* [153] continued the work of Luciani *et al.* by examining void fraction and frictional two-phase pressure drop. The frictional pressure drop increased with increasing gravity, which they explained by a decrease in void fraction with increasing gravity causing more of the channel cross-section to be occupied by liquid, thereby increasing friction.

Overall, the influence of body force on two-phase heat transfer appears to be highly dependent on mass velocity, inlet quality and heat flux, which also dictate flow pattern. Also, some of the findings by different investigators appear quite contradictory.

A.4.4 Flow Boiling Critical Heat Flux

As mentioned earlier, the ability to predict CHF is of paramount importance to the functionality of any heat-flux controlled flow boiling system. Also, as discussed earlier, several microgravity pool boiling studies point to an appreciable decrease in CHF in μg_e as compared to 1 g_e. In the absence of a body force to remove growing vapor bubbles, this decrease was attributed mostly to bubble coalescence into an unusually large bubble encompassing the entire heated wall. Flow boiling constitutes a practical and effective means to precluding this massive vapor coalescence by relying on liquid inertia to flush bubbles away from the heated wall and providing a path for bulk liquid to replenish the heated wall. Despite these important facts, very few studies have been devoted exclusively to flow boiling CHF in reduced gravity.

Ohta [147] obtained limited flow boiling CHF measurements in μg_e at high inlet quality, but noted that the CHF couldn't be accurately measured in the absence of local wall temperature measurements along the heated wall. Ma and Chung [148] investigated subcooled flow boiling of FC-72 across a heated 0.254-mm platinum wire in a 2.1-s drop tower. They measured an appreciable shift in the μg_e boiling curve to lower heat fluxes compared to 1 g_e, indicating significant reduction in heat transfer effectiveness. Additionally, CHF in μg_e was significantly lower than in 1 g_e. However, differences in both heat transfer rate and CHF decreased with increasing flow rate.

Zhang *et al.* [1] conducted subcooled flow boiling CHF experiments with FC-72 onboard NASA's KC-135 jet. CHF data were measured in μg_e, Lunar gravity (0.17 g_e) and Martian gravity (0.38 g_e), which were achieved with different parabolic maneuvers, and later compared with 1-g_e CHF data. Their study featured a 2.5×5.0 mm^2 rectangular polycarbonate flow channel that was fitted on one of the 2.5-mm sides with a 101.6-mm long electrically heated copper plate. As discussed earlier in relation to Figures. A.1(a) and A.1(b), prior experiments by Zhang *et al.* involving flow boiling at different orientations in Earth gravity showed drastically different CHF mechanisms at low velocities, but the same wavy vapor layer behavior at high velocity regardless of orientation. Unlike this terrestrial behavior, Figure A.7(a) shows flow-boiling CHF in μg_e follows the same mechanism at both low and high velocities. For near-saturated flow at both G/ρ_f = 0.25 and 1.4 m/s, bubbles coalesced along the heated wall into vapor patches resembling a continuous wavy vapor layer. Figure A.7(a) also shows similar CHF behavior at G/ρ_f = 0.14 m/s and a high subcooling of 22.8°C.

Figure A.7(b) depicts sequential images of flow boiling at low velocities and 1.8 g_e for both low and high subcooling. Because of the large buoyancy force perpendicular to the heated wall, the images to the left show bubbles being removed from the surface before they have the opportunity to coalesce, and boiling behavior seems to mimic pool boiling at 1 g_e. The images to the right show high subcooling reduces the size of vapor bubbles considerably during growth and detachment as a result of strong condensation effects.

Zhang *et al.* [1] also conducted a few μg_e tests in which high-speed video imaging captured interfacial behavior during the CHF transient. Figure A.8 shows for G/ρ_f = 0.15 m/s and $\Delta T_{sub,o}$ = 3°C, how, just before CHF, vapor patches grow into a wavy vapor layer that propagates along the wall as vigorous boiling in wetting fronts between the vapor patches maintains heat transfer from the heated wall to the liquid. Notice the wetting front in the middle images beginning to lift off from the heated wall as the CHF transient progresses. This lift-off triggered a chain reaction in which upstream wettings fronts began to detach from the surface, as depicted in the right images, until the entire heated wall was engulfed in a continuous insulating wavy vapor layer. This behavior is

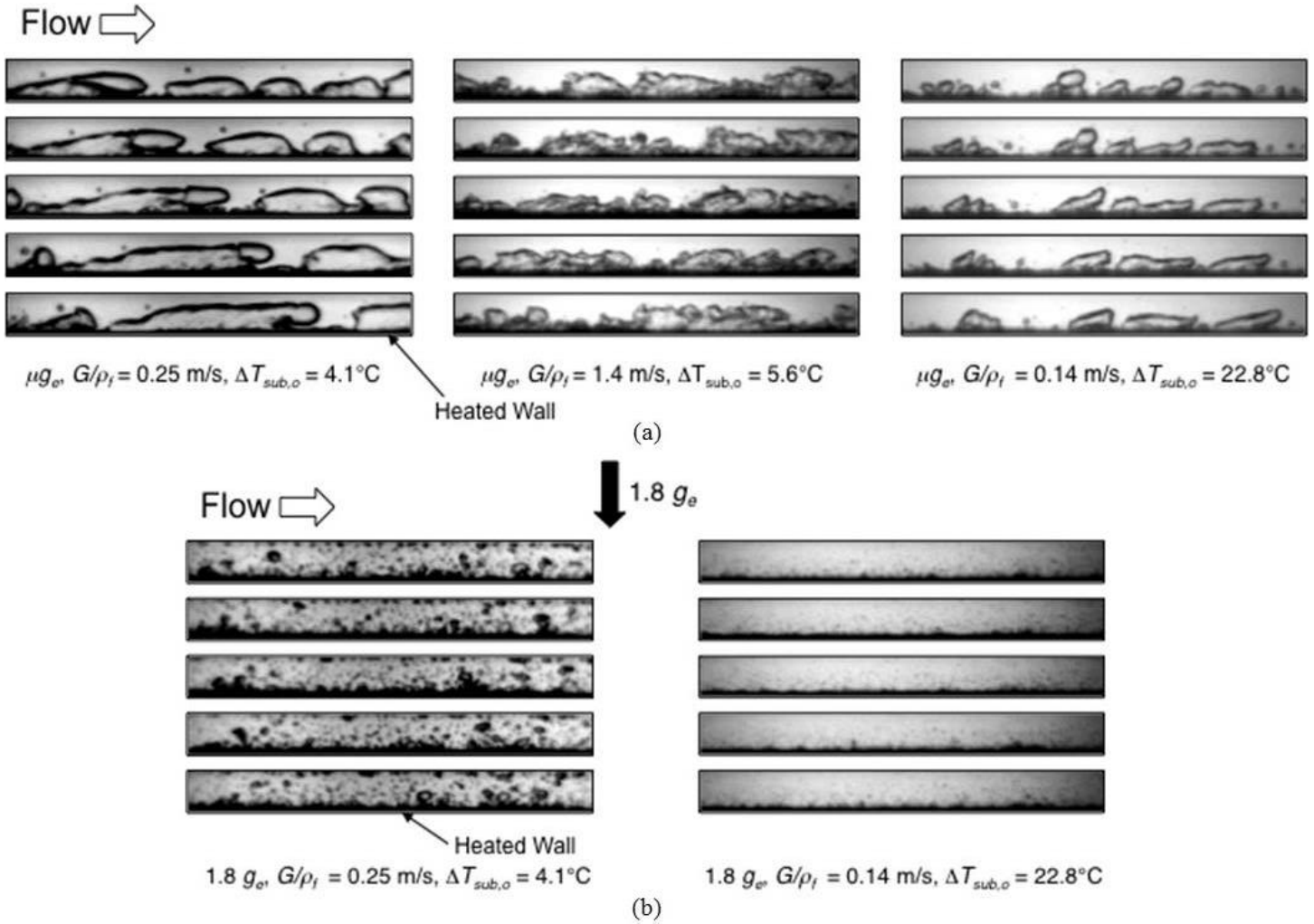

Figure A.7: (a) Wavy Vapor Layer CHF Regime prevalent in μg_e at both low and high velocities as well as near-saturated and subcooled conditions. (b) Low velocity pool-boiling-like flow boiling at 1.8 g_e [1].

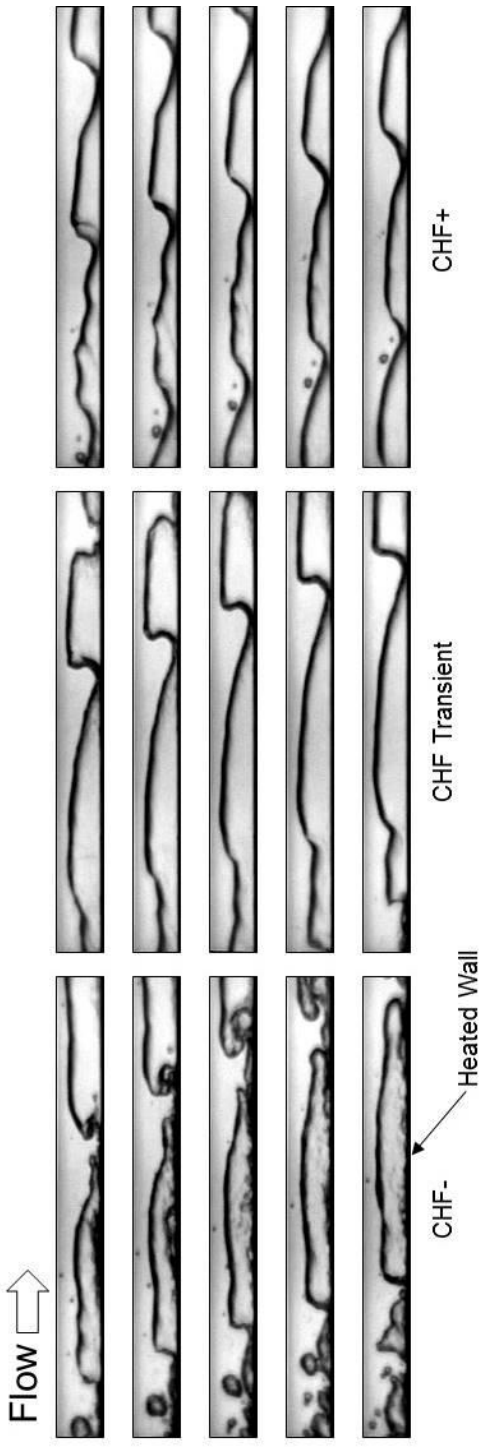

Figure A.8: CHF transient in μg_e for $G/\rho_f = 0.15$ m/s and $\Delta T_{sub,o} = 3.0$°C [1].

consistent with the Interfacial Lift-off CHF Model originally proposed by Galloway and Mudawar [14,15]. The Interfacial Lift-off Model uses hydrodynamic instability to describe the wavy interface between a liquid layer of mean velocity U_f and mean thickness H_f, and a vapor layer of mean velocity U_g and mean thickness H_g, as shown in Figure A.9(a). Wetting front formation requires that the interfacial wavelength exceed the critical wavelength, λ_c, which is given by

$$k_c = \frac{2\pi}{\lambda_c} = \frac{\rho_f'' \rho_g'' (U_g - U_f)^2}{2\sigma(\rho_f'' + \rho_g'')} + \sqrt{\left[\frac{\rho_f'' \rho_g'' (U_g - U_f)^2}{2\sigma(\rho_f'' + \rho_g'')}\right]^2 + \frac{(\rho_f - \rho_g) g_n}{\sigma}}, \tag{A.16}$$

where $\rho_f'' = \rho_f \coth(kH_f)$ and $\rho_g'' = \rho_g \coth(kH_g)$ are 'modified density' terms, and g_n is the component of gravity perpendicular to the heated wall. Equation (A.16) proves large velocity differences tend to destabilize the interface, while surface tension helps preserve interfacial stability. Depending on flow orientation relative to gravity, body force can be stabilizing or destabilizing.

The second part of the Interfacial Lift-off Model concerns the process of separation of wetting fronts from the wall, which is the trigger mechanism for CHF. Notice that the curvature of the liquid-vapor interface produces a pressure force that promotes interfacial contact with the heated wall, which is the process necessary for maintaining liquid replenishment. CHF occurs when the normal momentum of vapor generated in the wetting front just exceeds the pressure force. For an interfacial wave of the form $\eta(z,t) = \eta_o e^{ik(z-ct)}$, pressure difference perpendicular to the wall is expressed as

$$p_f - p_g = -\left[\rho_f''(c - U_f)^2 + \rho_g''(c - U_g)^2 + (\rho_f - \rho_g)\frac{g_n}{k}\right] k\eta_0 e^{ik(z-ct)}. \tag{A.17}$$

Assuming the wetting front occupies a fixed fraction b of the critical wavelength, the average pressure force for a wetting front is determined by averaging the pressure difference over $b\lambda_c$.

$$\overline{p_f - p_g} = \frac{4\pi\sigma\delta}{b\lambda^2}\sin(b\pi), \tag{A.18}$$

where δ is the mean vapor layer thickness. Figure A.9(b) shows the pressure force is opposed by vapor momentum $\rho_g U_{g,n}^2$ emanating from the wetting front normal to the heated wall.

Using extensive video records and statistical averaging techniques, Sturgis and Mudawar [27,28] showed that b = 0.2 over a broad range of flow conditions. They detected a continuous wetting region of length z^*, defined as $z^* = z_o + \lambda_c(z^*)$, where z_o is the distance from the leading edge of the heated wall to the location where U_g just surpasses U_f. The wavy interface is therefore generated at z^* and propagates downstream.

Considering flow boiling with a subcooled inlet, the heat concentrated in a wetting front is consumed by vaporizing liquid, $q''_w A_w = \left(c_{p,f}\Delta T_{sub,in} + h_{fg}\right)\rho_g U_{g,n} A_w$, where A_w is the wetting front area. The local heat flux required to push the interface away from the wall is determined by equating the vapor momentum, $\rho_g U_{g,n}^2$, to the pressure force obtained from Eq. (A.17).

$$q''_w = \rho_g\left(c_{p,f}\Delta T_{sub,i} + h_{fg}\right)\sqrt{\frac{\overline{p_f - p_g}}{\rho_g}} = \rho_g\left(c_{p,f}\Delta T_{sub,in} + h_{fg}\right)\left[\frac{4\pi\sigma}{\rho_g}\frac{\sin(b\pi)}{b}\right]^{1/2}\left.\frac{\delta^{1/2}}{\lambda_c}\right|_{z^*}. \qquad \text{(A.19)}$$

The critical heat flux, q''_m, is defined as the average heat flux over the entire heated area, which is related to the wetting front heat flux by the relation $q''_m = bq''_w$. This gives the following analytical expression for CHF corresponding to subcooled inlet conditions.

$$q''_m = \rho_g\left(c_{p,f}\Delta T_{sub,in} + h_{fg}\right)\left[\frac{4\pi\sigma b\sin(b\pi)}{\rho_g}\right]^{1/2}\left.\frac{\delta^{1/2}}{\lambda_c}\right|_{z^*}. \qquad \text{(A.20)}$$

Notice that δ and λ_c in Eq. (A.20) are calculated at z^*. These two parameters are determined from a separated flow model that is used to predict $U_f(z)$, $U_g(z)$, and $d(z)$. Table A.3 provides detailed relations for the separated flow model.

Figure A.9(c) shows variations of the CHF data of Zhang *et al.* with velocity in μg_e and l g_e. In μg_e, CHF increases appreciably with increasing velocity. However, this dependence is far weaker at l g_e. At the lowest velocity, CHF in μg_e is only 50% of that at 1 g_e. Increasing velocity is shown reducing differences between the two gravitational environments, with the CHF data converging around 1.5 m/s. Also included in Figure A.9(c) are CHF predictions based on the Interfacial Lift-off Model. Notice that this model provides predictions for μg_e over the entire velocity range, while only high velocity predictions are possible for 1 g_e because horizontal flow at lower velocities at 1 g_e is associated with the 'Pool Boiling' CHF regime, Figure A.1(a), which is

Table A.3: Summary of separated flow model relations (Zhang *et al.* [71]).

Quality and area fraction relations:

$$x_e = \frac{\rho_g U_g \alpha}{G}, \quad \alpha = \frac{\delta}{H}, \quad A = H \text{ x } W \text{ (channel height x channel width)}$$

Momentum conservation:

$$G^2 \frac{d}{dz}\left[\frac{(1-x_e)^2}{\rho_f (1-\alpha)}\right] = -(1-\alpha)\frac{dp}{dz} - \frac{\tau_{w,f} P_{w,f}}{A} + \frac{\tau_i P_i}{A} - \rho_f (1-\alpha) g_{II}$$

$$G^2 \frac{d}{dz}\left(\frac{x_e^2}{\rho_g \alpha}\right) = -\alpha \frac{dp}{dz} - \frac{\tau_{w,g} P_{w,g}}{A} - \frac{\tau_i P_i}{A} - \rho_g \alpha g_{II}$$

Wall shear stress relations ($k = g$ or f):

$$\tau_{w,k} = \frac{1}{2}\rho_k U_k^2 f_k$$

$$f_k = 0.184\left(\frac{\rho_k U_k D_{h,k}}{\mu_k}\right)^{-1/5}$$

Interfacial shear stress:

$$\tau_i = \frac{C_{f,i}}{2}\rho_g \left(U_g - U_f\right)^2$$

where $C_{f,i} = 0.5$

fundamentally different from the Wavy Vapor Layer regime for which the model is intended. The CHF predictions point to very important implications to future space missions. First, unlike 1 g_e, CHF in μg_e is dominated by the Wavy Vapor Layer regime regardless how small is the flow velocity. Second, flow boiling CHF in μg_e can be accurately predicted by the Interfacial Lift-off Model. Third, convergence of μg_e and 1 g_e data at about 1.5 m/s proves it is possible to design inertia-dominated space systems by maintaining flow velocities above this velocity threshold. Inertia-dominated systems allow data, correlations, and/or models developed at 1 g_e to be safely implemented in the design of space systems.

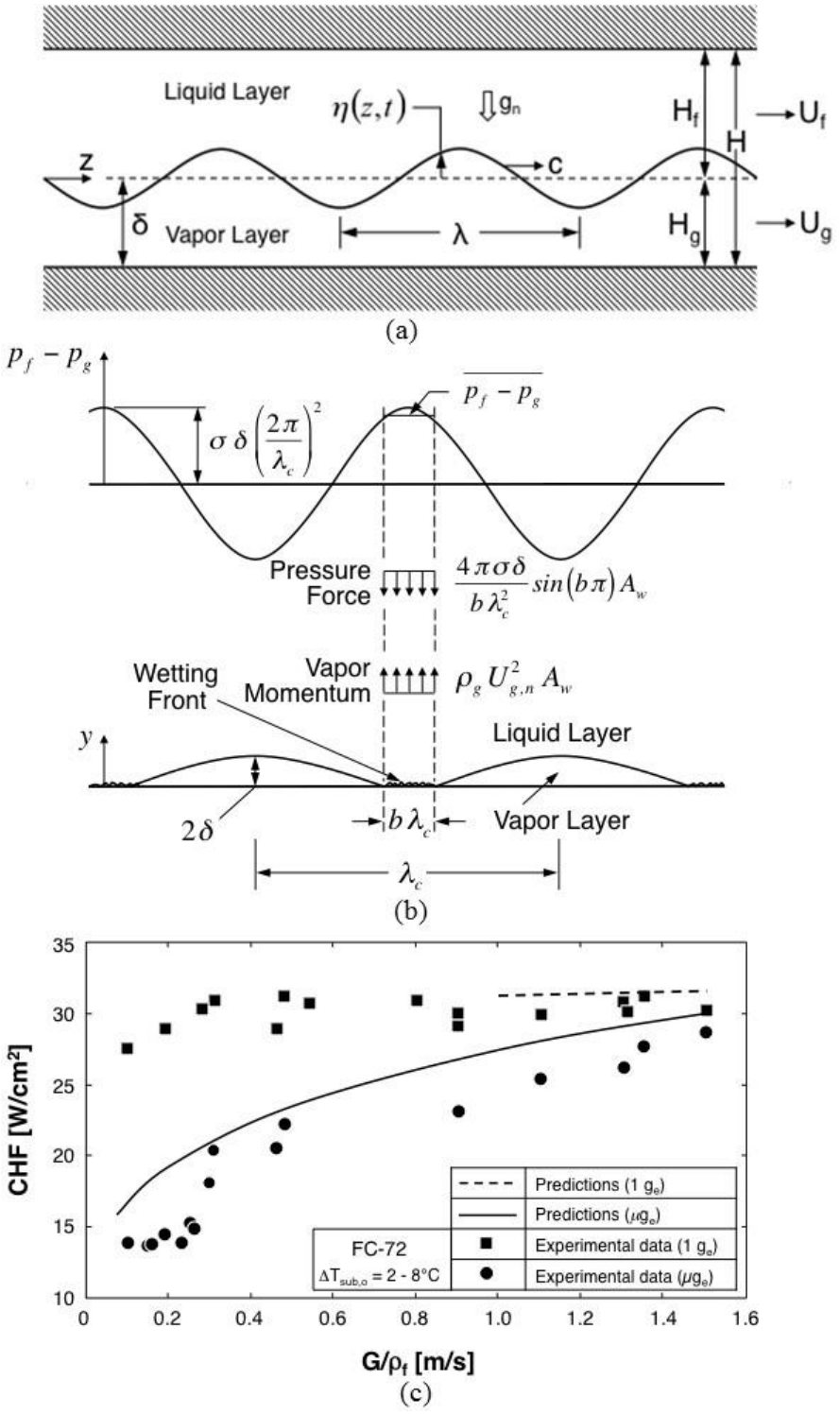

Figure A.9: (a) Wavy interface between liquid and vapor layers [71]. (b) Interfacial lift-off of wetting front at CHF [71]. (c) Comparison of CHF data and Interfacial Lift-off Model predictions for μg_e and horizontal 1 g_e flow boiling [1].

VITA

VITA

Christopher Alan Konishi

School of Mechanical Engineering
Purdue University, West Lafayette, IN 47907
E-mail: *c.konishi808@gmail.com*

EDUCATION

Doctor of Philosophy December 2014
Mechanical Engineering, Purdue University, West Lafayette, IN
Dissertation Title: Investigation of the Influence of Gravitational Body Force Effects on Critical Heat Flux for Flow Boiling with Subcooled and Two-Phase Inlet.

Master of Science August 2011
Mechanical Engineering, University of Hawaii, Honolulu, HI
Thesis Title: Hydraulic Characteristics of Single-Phase and Two-Phase Flow Across Micro-Pin-Fin Arrays.

Bachelor of Science August 2006
Mechanical Engineering, University of Hawaii, Honolulu, HI

RESEARCH AND WORK EXPERIENCE

Boiling and Two-Phase Flow Laboratory, Purdue University May 2009 − August 2014
Project: Effects of Body Force Effects on Flow Boiling Critical Heat Flux, NASA Glenn Research Center
Teaching Assistant, Purdue University August 2011 − May 2014
Research Assistant, University of Hawaii August 2007 − August 2009
Project: Investigation of Two-Phase Pressure Drop Across Staggered Micro-Pin-Fin Arrays
Pipeline-Micro, Honolulu, HI July 2008 − July 2009
Teaching Assistant, University of Hawaii August 2007 − December 2007

AWARDS

1. Donald English Endowment Fellowship, Purdue University, 2012
2. Dean's List, University of Hawaii, Spring 2007 & Fall 2006
3. Eagle Scout Award, 2001

PUBLICATIONS

Journal papers:

1. C. Konishi, H. Lee, I. Mudawar, M.M. Hasan, H.K. Nahra, N.R. Hall, J.D. Wagner, R.L. May, J.R. Mackey, " Flow boiling in microgravity: Part 1 – Interfacial behavior and experimental heat transfer results, *Int. J. Heat Mass Transfer*, in review.
2. C. Konishi, H. Lee, I. Mudawar, M.M. Hasan, H.K. Nahra, N.R. Hall, J.D. Wagner, R.L. May, J.R. Mackey, " Flow boiling in microgravity: Part 2 – Critical heat flux interfacial behavior, experimental data, and model, *Int. J. Heat Mass Transfer*, in review.
3. C. Konishi, I. Mudawar, "Review of flow boiling and critical heat flux in microgravity," *Int. J. Heat Mass Transfer* (2014), *Int. J. Heat Mass Transfer*, in review.
4. H. Lee, I. Park, C. Konishi, I. Mudawar, R.I. May, J.R. Juergens, J.D. Wagner, N.R. Hall, H.K. Nahra, M.M. Hasan, J.R. Mackey, "Experimental investigation of flow condensation in microgravity," *ASME J. Heat Transfer* 136 (2014) 1-11.
5. C. Konishi, I. Mudawar, M.M. Hasan, "Investigation of localized dryout versus CHF in saturated flow boiling," *Int. J. Heat Mass Transfer* 67 (2013) 131-146.
6. C. Konishi, I. Mudawar, M.M. Hasan, "Criteria for negating the influence of gravity on flow boiling critical heat flux with two-phase inlet conditions*," Int. J. Heat Mass Transfer* 65 (2013) 203-218.
7. C. Konishi, I. Mudawar, M.M. Hasan, "Investigation of the influence of orientation on critical heat flux for flow boiling with two-phase inlet," *Int. J. Heat Mass Transfer* 61 (2013) 176-190.
8. C. Konishi, W. Qu, F.E. Pfefferkorn, "Experimental study of water liquid-vapor two-phase pressure drop across an array of staggered micropin-fins," *ASME J. Electron. Packag*. 131 (2009) 1-8.

Conference Presentations:

1. Mudawar, H. Lee, C. Konishi, C. Kim, N. Hall, M.M. Hasan, H.K. Nahra, "Flow boiling and condensation experiment (FBCE) for the International Space Station - Predictive Tools," American Society for Gravitational and Space Research (ASGSR) 29th Annual Meeting, Orlando, FL, November 3-8, 2013.
2. H.K. Nahra, N. Hall, M.M. Hasan, J. Wagner, R. May, J. Mackey, J. Kolacz, R. Butcher, B. Frankenfield, I. Mudawar, C. Konishi, H. Lee, "Development of flow boiling and condensation experiment on the International Space Station I. Normal and low gravity flow boiling experiment development and test results," American Society for Gravitational and Space Research (ASGSR) 29th Annual Meeting, Orlando, FL, November 3-8, 2013.
3. C. Konishi, W. Qu, F.E. Pfefferkorn, "Experimental study of adiabatic water liquid-vapor two-phase pressure drop across an array of staggered micro-pin-fins," Proceedings of ASME International Mechanical Engineering Congress and Exposition, Paper IMECE2008-69051, Boston, MA, 2008.